VILNIUS UNIVERSITY
CENTRE FOR PHYSICAL SCIENCES AND TECHNOLOGY

Rokas
ŽALNĖRAVIČIUS

Synthesis, characterization and antimicrobial properties of metallic and semiconductor nanoparticles

DOCTORAL DISSERTATION

Natural sciences,
Chemistry N 003

VILNIUS 2020

This dissertation was written between 2015 and 2019 in Center for Physical Sciences and Technology.
The research was supported by Research Council of Lithuania and Lithuanian national agency Education Exchanges Support Foundation.
Stipends - DOK-17046, P-DAP-18-282, P-DAP-19-101.
Mobility funding – DOC-17095, P-DAK-18-62, 09.3.3.-LMT-K-712-07-0075, 09.3.3.-LMT-K-712-06-0158.
Part-time studies – DD-2018-LT-1594.

Academic supervisor:
Dr. Arūnas Jagminas (Center for Physical Sciences and Technology, Natural Sciences, Chemistry, N 003).
This doctoral dissertation will be defended in a public meeting of the Dissertation Defence Panel:
Chairman – **Prof. Habil. Dr. Emeritus Juozas Kulys** (Vilnius University, Natural Sciences, Biochemistry, N 004).
Members:
Habil. Dr. Zenonas Jusys (Ulm University, Natural Sciences, Chemistry, N 003).
Prof. Habil. Dr. Aivaras Kareiva (Vilnius University, Natural Sciences, Chemistry, N 003).
Dr. Šarūnas Meškinis (Kaunas University of Technology, Natural Sciences, Physics, N 002).
Prof. Habil. Dr. Almira Ramanavičienė (Vilnius University, Natural Sciences, Chemistry, N 003).

The dissertation shall be defended at a public meeting of the Dissertation Defence Panel at 11 a. m. on 28th February 2020 in meeting room D401 of the Center for Physical Sciences and Technology.

Address: Saulėtekio av. 3, D 401, Vilnius, Lithuania
Tel. +37052648884; e-mail: office@ftmc.lt

The text of this dissertation can be accessed at the libraries of Center for Physical Sciences and Technology and Vilnius University, as well as on the website of Vilnius University: www.vu.lt/lt/naujienos/ivykiu-kalendorius

VILNIAUS UNIVERSITETAS
FIZINIŲ IR TECHNOLOGIJOS MOKSLŲ CENTRAS

Rokas
ŽALNĖRAVIČIUS

Metalinių ir puslaidininkinių nanodalelių sintezė, charakterizavimas ir antimikrobinių savybių tyrimai

DAKTARO DISERTACIJA

Gamtos mokslai,
Chemija N 003

VILNIUS 2020

Disertacija rengta 2015 – 2019 metais Fizinių ir technologijos mokslų centre. Mokslinius tyrimus rėmė Lietuvos mokslo taryba ir Švietimo mainų paramos fondas:
Stipendija – DOK-17046, P-DAP-18-282, P-DAP-19-101.
Parama išvykoms – DOC-17095, P-DAK-18-62, 09.3.3.-LMT-K-712-07-0075, 09.3.3.-LMT-K-712-06-0158.
Dalinės studijos – DD-2018-LT-1594.

Mokslinis vadovas:
dr. Arūnas Jagminas (Fizinių ir technologijos mokslų centras, gamtos mokslai, chemija N 003).

Gynimo taryba:
Pirmininkas – prof. habil. dr. emeritas Juozas Kulys (Vilniaus universitetas, gamtos mokslai, biochemija N 004).
Nariai:
habil. dr. Zenonas Jusys (Ulmo universitetas, gamtos mokslai, chemija N 003).
prof. habil. dr. Aivaras Kareiva (Vilniaus universitetas, gamtos mokslai, chemija N 003).
dr. Šarūnas Meškinis (Kauno technologijos universitetas, gamtos mokslai, fizika N 002).
prof. habil. dr. Almira Ramanavičienė (Vilniaus universitetas, gamtos mokslai, chemija N 003).

Disertacija ginama viešame Gynimo tarybos posėdyje 2020 m. vasario mėn. 28 d. 11 val. Fizinių ir technologijos mokslų centro D 401 auditorijoje.

Adresas: Saulėtekio al. 3, Vilnius, Lietuva tel. +37052648884; el. paštas: office@ftmc.lt.

Disertaciją galima peržiūrėti Fizinių ir technologijos mokslų centro bei Vilniaus universiteto bibliotekose ir VU interneto svetainėje adresu: https://www.vu.lt/naujienos/ivykiu-kalendorius

Acknowledgments/Padėka

Studijų metu sutikti profesoriai, mokslų daktarai ir doktorantai, kiti kolegos negailėdami savo laiko stengėsi išaiškinti man kilusius klausimus ir vienaip ar kitaip prisidėjo prie galutinio šios disertacijos varianto. Nuoširdžiai jiems dėkoju.

Ačiū mamai ir tėčiui, kad gražiai užauginote mane ir visada visur mane palaikėte. Ačiū savo sesėms, Jūratei ir Živilei už visas gyvenimiškas pamokas ir mokykloje pakeltą „kartelę“. Ačiū Inetai, už kantrumą, rūpestį, sugaudytus kablelius ir palaikymą siekti savo tikslų.

Nuoširdus ačiū savo moksliniam darbo vadovui dr. Arūnui Jagminui už visokeriopą pagalbą, palaikymą, padrąsinimą, nuoširdumą žmogiškumą, ir galimybę iš arčiau susipažinti su nano-metrinio dydžio objektais.

Širdingas ačiū visiems savo kolegoms: Agnei ir Simonui – už draugiškumą ir pagalbą visais gyvenimo klausimais, Arnui, Audriui ir Rokui – už gražias nuotraukas, bei Ping-Pong‘o pamokas, Marijai už vertingus patarimus, Vaclovui už prasklaidytą tamsą elektrochemijos moksle, Giedrei ir Pauliui už draugiškumą ir moralinį palaikymą. Ačiū visiems Nanostruktūros laboratorijos kolegoms už žinias ir palaikymą.

Nuoširdus ačiū Vidui, Gediminui, Kęstučiui ir Vitalijai už atliktus XRD, Raman, magnetinius ir XPS matavimus bei pagalbą analizuojant gautus duomenis.

Nuoširdus ačiū dr. Algimantui Paškevičiui už galimybę bendradarbiauti, vertingus patarimus ir pagalbą analizuojant duomenis. Širdingas ačiū Jurgitai ir Eglei už naudingus patarimus, pagalbą ir pamokas dirbant su mikroorganizmais. Širdingas ačiū visiems Gamtos tyrimų centro, Biodestruktorių tyrimų laboratorijos skyriaus kolegoms už šiltą darbo aplinką ir palaikymą.

Nuoširdus ačiū prof. Tautgirdui Ruzgui už galimybę padirbėti pasaulinio lygio laboratorijoje, visas pamokas ir naudingus patarimus, visokiariopą pagalbą ir nuoširdumą. Taip pat norėčiau padėkoti savo kolegoms Skaidrei ir Dainiui už palaikymą, draugiškumą ir malonią darbo aplinką.

I would also like to thank Atefeh and Pannawich for great collaboration, clever ideas, shared sweets and many more things. I would like to thank people at the Department of Biomedical Sciences for creating wonderful working atmosphere and helping me out during my stay in Malmö university.

Abbreviations

AAO Anodic aluminium oxide
AC Alternating current
AFM Atomic force microscopy
Ag Silver
AMR Antimicrobial resistance
CAF Chloramphenicol
CE Counter electrode
CFU Colony forming unit
CV Cyclic voltammetry
DC Direct current
DLS Dynamic light scattering
DNA Deoxyribonucleic acid
EDTA Ethylenediaminetetraacetic acid
EDX Energy dispersive X-ray spectroscopy
FCC Face-centred cubic
FTIR Fourier-transform infrared spectroscopy
G Relative centrifugal force
GCE Glassy carbon electrode
GDP Gross domestic products
HR-TEM High-resolution transmission electron microscopy
ICP-OES Inductively coupled plasma - optical emission spectroscopy
ITO Indium tin oxide
MFC Microbial fuel cell
MIC Minimum inhibitory concentration
MRSA Methicillin-resistant *Staphylococcus aureus*
NFC Near-field communication
NPs Nanoparticles
OCP Open circuit potential
OD Optical density
PBS Phosphate-buffered saline
RE Reference electrode
RFID Radio frequency identification system
ROS Reactive oxygen species
SCE Saturated calomel electrode
SAED Selected area electron diffraction
SEM Scanning electron microscopy
SPE Screen-printed electrode
TEM Transmission electron microscopy
TiNT Titania nanotube
WE Working electrode
WHO World Health Organization
XRD X-ray diffraction
YEPD Yeast extract peptone dextrose

CONTENTS

INTRODUCTION

Infectious disease is caused by various microorganisms including bacteria, fungi and viruses. Today, drug-resistant infections are responsible for approximately 700.000 deaths per year globally. However, it is estimated, that antimicrobial resistant (AMR) caused deaths will increase to 10 million by 2050 [1]. This AMR infections would be responsible for costs as high as 100 trillion USD worldwide [2]. Furthermore, treats of AMR infections are growing exponentially, especially in Africa, Russia and Asia including China. Nowadays, AMR infections kill around 25 000 patients in Europe each year with associated cost in European Union of 1.5 billion EUR per year [3]. If no action is taken, this would also affect Europe's economy and could lead in a decrease of the total GDP from 1% to 4.5% by 2050. In order to prevent the multidrug-resistant bacteria caused infections, the development of novel antimicrobials is required.

The rising numbers of drug-resistant pathogens is one of the greatest challenges facing the research community. According to the Römling et al., up to 80 % of human infections caused by bacteria involve biofilm-assisted microorganism. For instance, the biofilm-forming bacteria are responsible for tissue infections, such as chronic wound infection, chronic otitis media, endocarditis, cystic fibrosis-associated lung infections, etc. [4]. Recently, WHO released the list of 12 antibiotic resistant bacteria, including species such as *Acinetobacter baumannii*, *Pseudomonas aeruginosa* or *Staphylococcus aureus* MRSA, etc. that pose the greatest threat to human health and for which new antimicrobial agents are desperately needed [5]. It is urgently necessary to find out a smart solutions or novel antimicrobial agents which could help to solve this problem.

One of the promising strategy that helps to combat with these highly resistant bacteria is the usage of engineered nanoparticles (NPs). These nanometre-scale materials have unique properties compared to their bulk composites. Due to their large surface to volume ratio, NPs could enhance the treatment efficiency minimizing side effects through their precise targeting mode of action [6]. It is commonly accepted that NPs with biocidal properties as ZnO, Cu, CuO, Cu_2O, Ag, Au, MgO offer novel applications, including prevention of biofilm formation and control of microbial colonization on different surfaces [7]. Current investigations supported that transition metal ferrite NPs as well as their metal-substituted forms could possess antimicrobial activity against various microorganisms and might be used as the promising antimicrobial agent. Despite the remarkable properties of these magnetic NPs, the antimicrobial activity against broad spectrum of bacteria

and fungi, especially those attributed to antidrug-resistant strains, is still unknown. In order to enlarge the existing knowledge and stimulate further works regarding the metallic and semiconductor NPs and their potency for antimicrobial activity, these nanostructures were fabricated and investigated herein and the main results are highlighted in this dissertation.

Major goal

To synthesize the metallic and semiconductor NPs and investigate their antimicrobial activity against various bacteria and fungi species.

Objectives

- ✓ To compare the antimicrobial activity of titanium oxide-based coatings, decorated with copper (I) oxide NPs with anodically formed copper (II) oxide films on the Cu substrate.
- ✓ To provide the anticorrosion, decorative and antimicrobial properties for food packing alumina foil *via* depositing Ag nanowire arrays.
- ✓ To synthesize different in size cobalt ferrite NPs using the hydrothermal approach and to prove their size-dependant antimicrobial behaviour.
- ✓ To fabricate the novel L-lysine amino acid stabilized iron-substituted cobalt ferrite NPs and to determine their antimicrobial activity dependence on the cobalt content in the NPs.
- ✓ To investigate the influence of stabilizing shell of superparamagnetic cobalt ferrite NPs on their antimicrobial efficacy against several bacteria and fungi strains.
- ✓ To synthesize ultra-small gold and magnetite-gold NPs stabilized with D,L-methionine amino acid and asses their antimicrobial behaviour against antibiotic resistant bacteria, in particular *S. enterica*, *S. aureus* MRSA and *A. baumannii*.

Scientific novelty

- ✓ Cu_2O/TiO_2, Cu_2O/TiNT and CuO/Cu coatings were tested as potential antimicrobial surfaces for the first time. It was found that anodically oxidized copper surfaces possessed higher antimicrobial activity than Cu_2O/TiO_2, Cu_2O/TiNT coatings against several micromycetes.

- ✓ The extremely thin porous AAO films (thickness ≤ 1 μm) have been grown on the food packing Al foil and further decorated in gold tints *via* Ag nanowires electrodeposition. For the first time, antimicrobial activity of this film was highlighted as a promising way to improve the food storage.
- ✓ For the first time, the dependency of antimicrobial behaviour of cobalt ferrite NPs on their size, chemical composition and shell has been shown.
- ✓ It has been shown for the first time, that ultra-small gold and magnetite-gold hybrid NPs exhibit the potential antimicrobial properties against multidrug resistant bacteria such as *S. enterica*, *S. aureus* MRSA and *A. baumannii*.

Statements of defence

- ✓ Black copper (II) oxide coatings possess the higher antimicrobial activity against micromycetes than copper (I) oxide-based coatings.
- ✓ Thin porous AAO films with encapsulated metallic Ag nanowires, as thin as ≤ 1.0 μm, provide the antimicrobial, decorative and anticorrosive properties for food packing alumina foil.
- ✓ Cobalt ferrite NPs are promising antimicrobial agent and exhibit the size, core and shell composition-dependent antimicrobial activity against various bacteria and fungi strains.
- ✓ Ultra-small gold (~2 nm) and magnetite-gold hybrid NPs inhibit the multidrug-resistant bacteria, such as *Salmonella enterica*, *Staphylococcus aureus* MRSA and *Acinetobacter baumannii* with the final concentration of 30 mg L^{-1}.

Contribution of the author

All coatings and NPs were fabricated, fractioned and collected by the author of this dissertation. Author also conducted all antimicrobial assessments and MIC determinations, as well as preparation the samples for SEM, TEM and confocal microscopy analysis. Furthermore, author took part in the analysis of experimental results, design of graphical illustration and preparation of scientific publications. Additionally, the obtained results were referenced by author in numerous international conferences and, of course, author wrote this dissertation himself. All non-original works are referenced.

Publications

The main results of the doctoral thesis were published in 6 scientific publications (P: 1-6) and 17 conference reports (C: 1-15).

Scientific publications

P1. **Žalnėravičius R**., Paškevičius A., Kovger J., Jagminas A. Fabrication by AC Deposition and Antimicrobial Properties of Pyramidal-Shaped Cu_2O-TiO_2 Heterostructures. *Nanomaterials and Nanotechnology*, 2014, DOI: 10.5772/59997, (**IF** = 1.6).

P2. Jagminas A., **Žalnėravičius R**., Rėza A., Paškevičius A., Selskienė A. Design, optical and antimicrobial properties of extremely thin alumina films colored with silver nanospecies. *Dalton Transactions*, 2015, 44, 4512-4519 DOI: 10.1039/c4dt03644a, (**IF** = 4.052).

P3. **Žalnėravičius R**., Paškevičius A., Kurtinaitienė M., Jagminas A. Size-dependent antimicrobial properties of the cobalt ferrite nanoparticles. *Journal of Nanoparticle Research*, 2016, 18, 300-310. DOI: 10.1007/s11051-016-3612-x, (**IF** = 2.009).

P4. **Žalnėravičius R**., Paškevičius A., Mažeika K., Jagminas A. Fe(II)-substituted cobalt ferrite nanoparticles against multidrug resistant microorganisms. *Applied Surface Science*, 2018, 435, 141-148. DOI: 10.1016/j.apsusc.2017.11.028, (**IF** = 5.155).

P5. Ramanavičius S., **Žalnėravičius R**., Drabavičius A., Jagminas A. Shell-Dependent Antimicrobial Efficiency of Cobalt Ferrite Nanoparticles. *Nano-Structures & Nano-Objects*, 2018, 15, 40–47, DOI: 10.1016/j.nanoso.2018.03.007.

P6. **Žalnėravičius R**., Mikalauskaite A., Niaura G., Paškevičius A., Jagminas A. Ultra-small methionine-capped Au^0/Au^+ nanoparticles as efficient drug against the antibiotic-resistant bacteria, *Materials Science and Engineering C-Materials for Biological Applications*, 2019, 102, 646-652. DOI: 10.1016/j.msec.2019.04.062, (**IF** = 4.959).

Other publications

O1. Jagminas A., Naujokaitis A., **Žalnėravičius R**., Jasulaitiene V., Valušis G. Tuning the Activity of Nanoplatelet MoS_2-Based Catalyst for Efficient Hydrogen Evolution via Electrochemical Decoration with Pt Nanoparticles. *Applied Surface Science*, 2016, 385, 56-62 DOI:10.1016/j.apsusc.2016.05.094.

O2. Jagminas A., Niaura G., **Žalnėravičius R**., Trusovas R., Račiukaitis G., Jasulaitienė V. Laser Light Induced Transformation of Molybdenum

Disulphide-Based Nanoplatelet Arrays. *Scientific reports*, 2016, 6, 37514-37523. DOI:10.1038/srep37514.

O3. Naujokaitis A., **Žalnėravičius R**., Pakštas V., Arlauskas K., Jagminas A. MoS_2 Nanoplatelet Arrays as a Support for Decoration with Pt Nanoparticles and its Effect on Electrochemical Water Splitting. *Journal of nanomaterials & Molecular nanotechnology*, 2017, 6, 1. DOI: 10.4172/2324-8777.1000208.

O4. **Žalnėravičius R**., Gedminas A., Ruzgas T., Jagminas A. Nanoplatelet MoS_2 arrays decorated with Pt nanoparticles for nonenzymatic detection of hydrogen peroxide. *Journal of electroanalytical chemistry*, 2019, 839, 274-282. DOI: 10.1016/j.jelechem.2019.03.032.

Conference reports

C1. **Žalnėravičius R**., Bružaitė I., Paškevičius A., Jagminas A. *Bacterial activity of extremely thin porous alumina films gold-colored by silver nanowire arrays.* Chemistry and technology of inorganic materials, Kaunas, Lithuania, 2013, 98-103, (PP).

C2. **Žalnėravičius R**., Paškevičius A., Jagminas A. *Fabrication and antimicrobial properties of Cu_2O-TiO_2 heterostructures*. FizTech2014, Vilnius, Lithuania, 2014, (OP).

C3. **Žalnėravičius R**., Jagminas A. *Anodically oxidation of Ti surfaces and decoration the obtained surfaces with Cu_2O nanoparticles for antimicrobial coatings*. Chemistry and chemical technology, Klaipeda, Lithuania, 2015, 157-161, (OP).

C4. **Žalnėravičius R**., Naujokaitis A., Jagminas A. *Nanoplatelet MoS_2 films decorated with Pt quantum dots for effective hydrogen production*. Chemistry and chemical technology. Vilnius, Lithuania, 2016, (PP).

C5. **Žalnėravičius R**., Jagminas A. *Size-dependent antimicrobial properties of the cobalt ferrite nanoparticles*. 18th International conference, Advanced Materials and Technologies, Palanga, Lithuania, 2016, 51, (PP).

C6. **Žalnėravičius R**., Jagminas A. *Synthesis and antimicrobial activity of $CoFe_2O_4$ nanoparticles*. FizTech2016, Vilnius, Lithuania, 2016, (OP).

C7. **Žalnėravičius R**., Naujokaitis A., Jagminas A. and Homs N. *Ultra-highly efficient MoS_2/Pt nanoplatelet arrays on Ti substrate for electrocatalytic hydrogen evoliution reaction*. 9th International Nanoconference, Advances in Bioelectrochemistry and Nanomaterials, Vilnius, Lithuania, 2016, 43-45, (PP).

C8. **Žalnėravičius R**., Jagminas A. *L-lysine coated Fe-doped magnetic nanoparticles are promising material for multidrug resistant microorganisms*

threat. [19]th International conference, Advanced Materials and Technologies, Palanga, Lithuania, 2017, 56, (PP).

C9. Naujokaitis A., Arlauskas K., **Žalnėravičius R.**, Jagminas A. *Electrochemical decoration of MoS_2 nanoplatelet arrays with Pt quantum dots for high efficient water splitting*. [11]th International Conference on Advanced materials & Processing, Edinburgh, Scotland, 2017, 91, (PP).

C10. **Žalnėravičius R.**, Jagminas A. *Synthesis, characterization and antimicrobial activity of superparamagnetic $CoFe_2O_4$ nanoparticles*. FizTech2017, Vilnius, Lithuania, 2017, (OP). **Awarded for the best oral presentation**.

C11. **Žalnėravičius R.**, Jagminas A., Paškevičius A. *Cobalt ferrite nanoparticles against multi-drug resistant microorganisms*. Biomedical and Life Sciences Meeting Collaborative Conference on Antimicrobial Resistance. Victoria, Canada, 2018, (OP).

C12. **Žalnėravičius R.**, Jagminas A., Paškevičius A. *Ultra-small nanoparticles as efficient antibiotics*. [23]th ISE topical meeting Electrochemistry for Investigation of Biological Objects: from Functional Nanomaterials to Micro/Nano-Electrodes, Vilnius, Lithuania, 2018, (OP).

C13. **Žalnėravičius R.**, Kurtinaitienė M., Paškevičius A., Jagminas A. *Ultra-small Gold Nanoparticles as a Promising Antimicrobial Agent*. Advanced materials and technologies, Palanga, Lithuania, 2018, (PP).

C14. **Žalnėravičius R.**, Jagminas A., Kurtinaitienė M., Klimas V., Paškevičius A., *Gold Nanoparticles Against Clinically Isolated Pathogens*, Nano Bio, International conference on nanotechnologies and Bionanoscience, Heraklion, Greece, 2018, (PP).

C15. Ruzgas T., Shafaat A., **Žalnėravičius R.**, Pham A.D., Gonzalez J.F., Sotres J. *Plugging redox reactions into wireless devices: RFID-based biosensor tag*, XXV International Symposium on Bioelectrochemistry and Bioenergetics, Limerick, Ireland, 2019, 139 (OP).

C16. Thirabowonkitphithan P., Laiwattanapaisal W., **Žalnėravičius R.**, Shafaat A., Neilands J., Jakubauskas D., Ruzgas T. *Wireless sensing of biofilms of medically relevant bacteria and fungi*. [6]th International Conference on Bio-Sensing Technology, Kuala Lumpur, Malaysia, 2019, (OP).

C17. **R. Žalnėravičius**, A. Jagminas. *Ultra-small Methionine-Capped Au^0/Au^+ Nanoparticles as efficient drug against most dangerous bacteria*. [3]rd Global summit on Nanotechnology, Nanomedicine & Material science, Barcelona, Spain, 2019, (PP).

1. LITERATURE REVIEW

1.1. Synthesis of nanomaterials

The history of nanomaterials usage has started even before Christ (BC). In fact, humans started to use ceramic matrixes, consisting of natural asbestos nanofiber more than 4500 years ago [8]. Furthermore, the ~ 5 nm in diameter PbS NPs were used as a hair dye in the Ancient Egypt [9]. However, people were not be able to understand process in nm scale at this period of life, therefore the usage of such nanomaterial was more incidental. Since the first report by Michael Faraday in scientific area of colloidal gold NPs synthesis in 1857, a large number of publications based on NPs, nanomaterials and nanocomposites preparation, stabilization and new synthesis routes have been written by many scientific groups. In the broadest term, the fabrication of nanomaterials refers to the design, construction and manipulation of materials with dimensions that are typically in the range of 1 to 100 nm. Basically, the nanoscale materials are synthesized by different techniques, which usually can be classified into two main ways: “top-down” and “bottom up” [10]. Since the approach of nanomaterials fabrication starts from bulk materials, in generally it belongs to the top down techniques (Fig. 1).

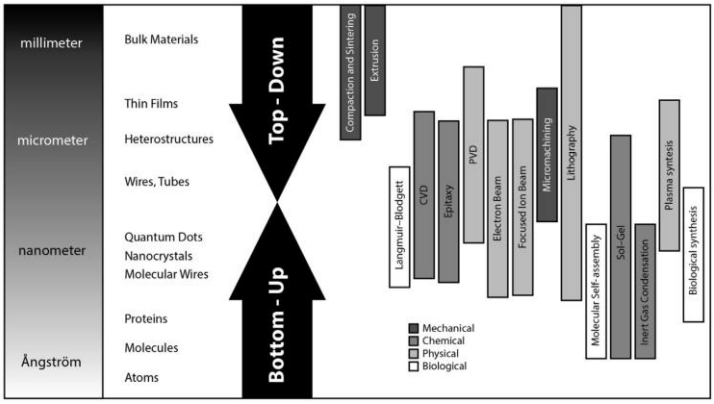

Figure 1. Schematic illustration of various fabrication route of nanomaterials [10].

Top-down synthesis approach belongs to technologies, which involves fabrication of nanomaterials by breaking down certain parts from larger or bulk material (macro-crystalline) substrate. It employs several methods as mechanical (crushing, milling or grinding), physical (optical lithography, direct laser writing), chemical (templated etching, anisotropic dissolution), and others depending on the requirements of the novel architectures [11]. Worth noticing that the physical top-down routes remain irreplaceable in the field of microelectronics and are still using to produce highly-ordered patterns

on the semiconductor substrates. However, this methods usually are not suitable for fabrication of uniformly shaped materials, especial very small NPs (1-20 nm). The main disadvantages of this synthesis route are the imperfection of the surface structure, insufficient homogenous chemical composition, the crystallographic structure damage, and high amount of defects. These limitations has a negative impact on the surface chemistry and physical properties of the final nanostructured product.

During the last few years, the fabrication of nanomaterial *via* bottom-up approach has been increasingly utilized [12]. Contrary to top-down method, bottom-up technology involves the synthesis routes, which start by stacking atoms onto each other on the top of a base substrate. Due to this process, atoms gives rise of crystal planes, which also stack further onto each other, resulting in the formation of nanostructures. This synthesis route is used more often due the possibility to form uniformly sized, shaped, and distributed nanomaterials. It should be noticed that fabricated nanoscale materials can possess significantly different properties depending on the synthesis route applied. Three widely known chemical (molecular self-assembly, sol-gel, hydrothermal, solvothermal, co-precipitation, thermal decomposition, electrodeposition), physical (microwave irradiation, ion beam techniques, physical vapour deposition) and biological (use a bacteria, fungi or plants to reduce metal ions) classes of methods, which belong to bottom-up techniques are used for synthesis of NPs [13]. As can be observed from Fig. 2, approximately 90 % of magnetic NPs are fabricated using chemical synthesis route, whereas the physical and biological approach take place with 8 and 2 % respectively. The most reported processes for the synthesis of ferrites are chemical, including several types as co-precipitation (28 %), thermal decomposition (9%), hydrothermal (26%), and microemulsion (20%) [14].

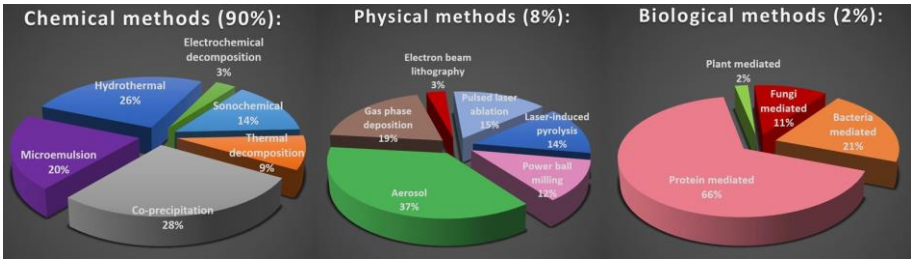

Figure 2. Methods used for magnetic NPs synthesis, divided into three main categories and their percentage usage.

Hydrothermal, co-precipitation, thermal decomposition and electrodeposition methods, which were used in this work, will be described in the following section in more detail.

1.1.1. Hydrothermal and co-precipitation synthesis route

The hydrothermal technique has been one of the most attractive synthesis route, garnering interest from different kind of scientists and technologists of various disciplines, particularly from 1990s [15]. Hydrothermal synthesis is usually defined as the heterogeneous chemical reaction or crystal growth process in aqueous or non-aqueous solutions under high temperature (> 100 °C) and pressure (greater than a few atmospheres) conditions [16]. In case of hydrothermal fabrication the solvent plays very important role due to the physical action as the P, T, and chemical action, as reactant or solvent. In order to control the nucleation of a desired phase or its homogeneity, size, shape or dispersity the surfactants, chelates and other capping agent additives are used, which play the key role. The surface of fabricated nanomaterials could be altered to hydrophobic or hydrophilic depending upon the applications [15]. During the crystal growth process, the presence of surfactant helps to control the crystal size and morphology. Besides that, in surface modification the pH of the mixture, isoelectric point (pI) and dissociation constant (pK_a) of the surface modifiers are very important in the surface modification too. If the pH are less than (pK_a), the surfactant molecules do not dissociate. Furthermore, below pI, the surface of metal oxide NPs is surrounded by positive charge and hydroxyl groups. There is no chemical reactions occurring between modifier and the nanomaterial surface, but it can attach to the NPs surface through a strong hydrogen bonding. On the other hand, at higher pH than pK_a value, dissociation of surfactant starts resulting in a chemical interaction between the dissociated part of surface modifier and OH_2 from the surface of metal oxides NPs [17]. Thus, the modifier molecules attach to the NPs surface by dehydration reaction. In fact, mass transfer, charge balance, pH, and the surfactant of the actual system might be fixed for most of the synthesis by considering the chemical reactions [15].

Returning to the hydrothermal synthesis operations in laboratory, it's necessary to discuss about the apparatus required for this work. Nanomaterials growth under hydrothermal conditions requires a corrosion-resistant vessel capable withstand high temperature and pressure. On top of that, these facilities must operate routinely and reliably in such extreme conditions. The highly corrosive solvent (reaction mixture) is placed into the container called autoclave, which is usually designed with corrosion resistant materials such as quartz, stainless steel, cobalt, nickel or others. Furthermore, in order to protect the main part of autoclave from highly corrosive mixture and extreme pH conditions, the Teflon-lined capsules or noble metal tubes are used during the hydrothermal treatments. The Teflon lined autoclave containing the

reaction mixture is placed into the electrically heated furnace for providing desired temperature. Recently, the hydrothermal synthesis were combined with other physical and chemical techniques such as microwaves, ultrasonic, mechanical or electrochemical assisted reactions in order to enhance the process kinetics and reduce the experiments duration, which is important from the economical aspect. With an increasing demand for new advanced composite nanostructures, the hydrothermal approach offers a unique method for coating of various compounds such as metals, plastics, ceramics or polymers as well as for fabrication of powders or nano-scale materials (Fig. 3). Hence, the hydrothermal method is becoming, probably, one of the most valuable fabrication ways in recent years due to a high quality of nanostructured products. However, the knowledge on the nucleation, crystallization, self-assembly, and growth mechanism on the nanomaterial, especially those combined with additional energy physical-chemical techniques in hydrothermal synthesis solution are still complicated and are not well understood [18].

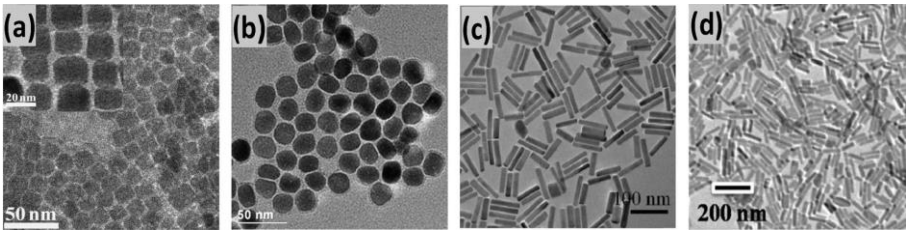

Figure 3. TEM images of upconversion nanocrystals synthesized *via* hydrothermal treatment: (a) NaYF4: Mn/Yb/Er, (b) NaYF4: Gd/Yb/Er, (c) NaGdF4: Yb/Er, (d) NaLuF4: Gd/Yb/Er [19].

Another synthesis technique, which is very similar to hydrothermal synthesis and belongs to aqueous solution approaches is called co-precipitation. Co-precipitation is one of the nanomaterials synthesis route, mostly cited in the literature as method used for magnetic, iron-based NPs fabrication. From the paper published in 1981 about magnetic NPs synthesis in acidic and alkaline aqueous solutions, this approach is still used in many laboratories for magnetic NPs, especial iron oxides or ferrites synthesis [20]. For the fabrication of iron oxide and metal ferrite NPs by co-precipitation route, Fe(III) and Me(II) salts (where the Me(II) is a d-block transition metal as Co, Fe, Mn, Ni and others) are suspended into alkaline solution (usually consisting of NaOH, NH_3OH, $N(CH_3)_4OH$), at the temperature below 100 °C, thus resulting in the formation of magnetic NPs. This process can be described by following equation:

$$Fe^{2+}\,(aq) + Fe^{3+}\,(aq) + 8OH^{-}\,(aq) \rightarrow Fe_3O_4\,(s) + 4H_2O\,(l) \quad (1)$$

The size, shape and composition of obtained nano-scaled products highly depend on the parameters such as temperature, ionic strength, pH, type/concentration of alkaline agent and the molar ratio between Me(II) and Fe(III) cations [21]. Kerroum et al., have shown that varying the pH of the synthesis mixture in the range between 9 and 12 both structure (mainly size and shape as illustrated in Fig. 4) and magnetic properties have been changed.

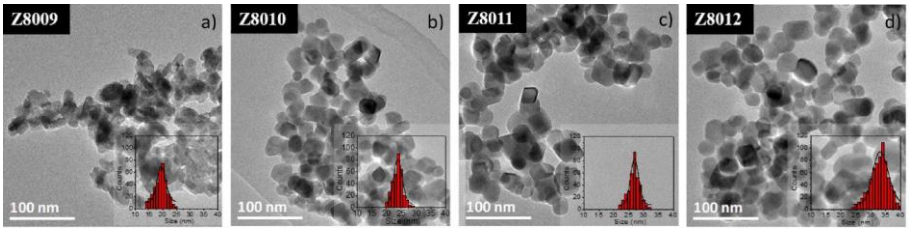

Figure 4. TEM images of $ZnFe_2O_4$ NPs fabricated by co-precipitation method at different pH values: a) 9, b) 10, c) 11 and d) 12 [22].

As highlighted by Pereira et al., it is possible to reduce the particle size at least 6 times *via* changing the sodium hydroxide base to alkanol amines in particular to isopropanolamine and diisopropanolamine [23]. More recently, Vikram and co-workers have showed that stability and size differences of fabricated citric acid stabilized Fe_3O_4, γ-Fe_2O_3 and γ-FeOOH NPs strongly depend on Fe^{2+}/Fe^{3+} ratio [24]. However, the NPs obtained by this route tend to form agglomerates and hence should be stabilized by low molecular weight surfactants or functionalized polymers. On the other hand this method has some advantages as low cost, fast, and reproducible for fabrication of high purity products. In addition, by this synthesis way it is not necessary to use hazardous organic solvents as well as treatments under the high pressure or temperature [25].

1.1.2. The synthesis by thermal decomposition route

Another popular wet synthesis route for iron oxide NPs fabrication is based on the thermal decomposition of organometallic precursors in the absence of oxygen at elevated temperatures in high-boiling point organic solvents bath containing stabilizing agents [21]. This method has been demonstrated to be the most successful approach for the synthesis of iron oxide or metal ferrite NPs due to better controls of their size and shape and high-quality monodispersion [14].

Iron oxide NPs have been fabricated using pyrolysis of different precursors such as pentacarbonyl iron ($Fe(CO)_5$) [26], iron acetylacetonate ($Fe(acac)_3$) [27], Prussian blue ($Fe_4[Fe(CN)_6 \cdot 14H_2O]$), iron oleate complex [28], ferrocene ($Fe(C_5H_5)_2$) [29], and others [30]. In these syntheses, organic solvents containing fatty acids or amines, such as oleic acid and

hexadecylamine are usually used as stabilizing agents. These solvents possess a high-boiling point value required for effective thermal decomposition reaction, which normally occur at temperatures between 200-320 ℃ [21]. In fact, the morphology of obtained products (especially size and shape) highly correlate with the selected ratio between the concentration of organometallic precursors, stabilizing agents and solvent. Besides that, the reaction time, temperature, aging period also plays an important role for thermal decomposition reaction being the important factors that influence the final nanomaterials morphology [30]. The reactivity of precursors, as well as their concentrations, may also be crucial for the precise control on the size and shape of nanoobjects. In general, the longer chain length of applied fatty acid leads to the slower reaction rate [30]. In order to accelerate it and decrease the reaction temperature, the alcohols or primary amine additives have been used.

The thermal decomposition method is superior compared to others synthesis methods due to a simple possibility to prepare the highly monodispersed magnetic NPs with a narrow size distribution. For instance, Chen et al., fabricated iron oxide NPs *via* decomposition of ferric oxyhydroxide, oleic acid, and 1-octadecene. The obtained NPs was further coated with polysiloxane-containing copolymer (Fig. 5 a) and was used as effective mediators for photothermal therapy [31].

Lu et al., have successfully synthesized the spherical and cubic-shaped (Fig. 5 a, b, respectively) magnetic cobalt ferrite ($CoFe_2O_4$) NPs by thermal decomposition of Fe(III) and Co(II) acetylacetonate compounds in the presence of oleic acid and oleyamine as surfactants and octadecanol as an accelerating agent. The reaction of $CoFe_2O_4$ NPs production are described by following equation [32]:

$$Co(acac)_2 + Fe(acac)_3 \rightarrow CoFe_2O_4\ (s) + CH_3COCH_3 + CO_2 \quad (2)$$

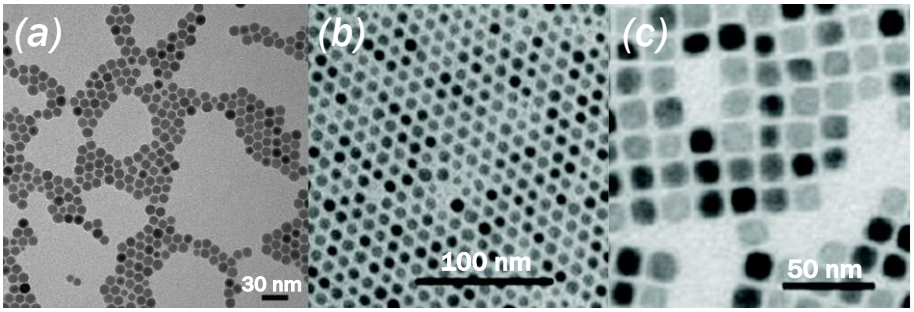

Figure 5. TEM images of Fe_3O_4 (a) [31] and $CoFe_2O_4$ (b, c) [33] NPs fabricated by thermal decomposition route.

They also found that NPs shape can be varied between the sphere, cube and star-like in the range of 4-30 nm *via* changing the surfactant concentration,

precursor ratio and the reaction time. The obtained NPs were applied for production of oriented carbon nanotubes. The authors also suggest to use as-obtained NPs for biomedical applications, however the fabricated products are mainly dispersible in organic solvents. The iron oxide or metal ferrite NPs produced by thermal decomposition method are usually hydrophobic and prone to aggregation under the physiological conditions. This disadvantage implied that these NPs are not applicable for biomedical applications, requiring more procedures and further surface modification rendering them soluble in aqueous solution, which increase the price of final products. Nevertheless, the synthesis of iron oxide and metal ferrite NPs by thermal decomposition way still receive a great deal of scientists' attention due to their promising applications in biomedicine, catalysis, and magnetic data storage [33].

1.1.3. Electro-inspired techniques for fabrication of nanostructures

Electrodeposition is a unique fabrication method whereby many kinds of nanomaterials including metals, metal oxides, bimetals, alloys, polymers, etc. can be successfully synthesized [34]. Several electrochemical methods can be assessed for fabrication of nanostructured materials, such as AC, DC, CV deposition. In general, this technique is associated with the electro-inspired redox reactions on the electrode surface, which usually is immersed in the solutions containing the metal ions. The electrons act herein as a "fuel" for the synthesis of nanomaterials and can reduce or oxidize atoms, ions or molecules in the solution bulk as well as at the conductive. During electrodeposition, the reduction reactions take place at the cathode, whereas those occurring at the anode are called oxidation reactions. In some cases the electrodeposition is carried out in the 3-electrodes cell configuration, consisting of working, counter, and reference electrodes. During the electrochemical process, the WE is negatively polarized with respect to the auxiliary electrode, resulting in positively charged metal ions reduction to their metallic form at the electrode surface in the electrolyte bath. The as-synthesized products possess high purity compact film, dense and strongly adhered to the substrate. Furthermore, the electrodeposition process can be easily adapted to industry due to its following characteristics – low cost, fast production rate and high reproducibility and thus play a huge role in nowadays coating and surface technology [35].

In order to control the electrodeposition at the nanoscale dimensions, the fundamentals about the formation of crystal association and its growth on the electrode surface are very important. The final product can be affected by a series of factors such as concentration of electrolyte, temperature, the type of

substrate and method used for electrodeposition. Furthermore, the nucleation of nanomaterials on the electrode surface depend on the structure of the substrate, free surface energy, adhesion energy, lattice orientation of the electrode surface and crystallographic lattice mismatch at the nucleus/electrode interface [36]. The first step of metallic crystal formation is the nucleation of the metal on the substrate surface, which tends to occur preferentially at the sites of electrode containing defects or others impurities such as inclusions, holes, oxide layers. As illustrated in Fig. 6 A, the nucleation process have several stages: firstly, the hydrated ions diffuse towards the electrolyte/electrode interface (i), at the second stage, ions that reached interface undergo partial desolvation (ii). These desolvated forms are adsorbed at the substrate surface (iii), forming the complete desolvation structures called the local crystal nuclei (iv) [37].

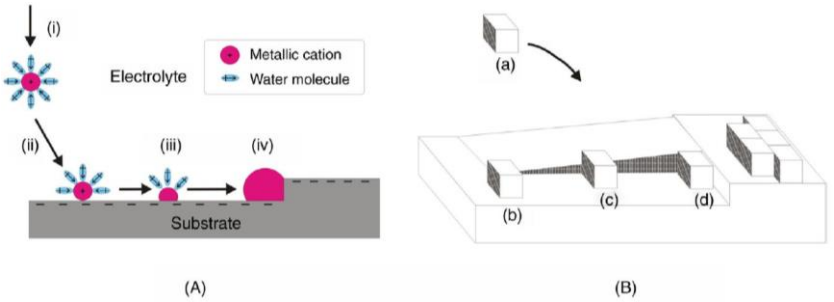

Figure 6. Schematic illustration of the (A) nucleation and crystallization (B) processes on a surface with crystal plane dislocation [34].

Fig. 6 B depicts possible ion attachment places during the crystallization step on electrode surface with crystalline plane dislocation. Accordingly, when the ion at position (a) achieves the electrode surface it can be attached through electron transfer process into the following sites: on the crystal lattice as an adsorbed atom (b) on a step (c) or in a corner (d) [37]. The nanoscale-material nucleation and growth kinetics depend on the method used to formation of electrodeposits. The electrodeposition of metal NPs on the substrate from electrolyte involves nucleation, which depends on diffusion-limited growth. Both cases can affect the particles size and their dispersion [38]. The chemical nature of both metal and substrate determines the type of nucleation (progressive or instantaneous) as well as whether the growth will follow the Frank van der Merve (layer-by-layer), Volmer-Weber (island) or Stranski-Krastanov (mixed layer and island) growth model [39]. It is notable, that electrodeposition reaction might be controlled *via* commonly used mechanisms: charge-transfer, diffusion, chemical reaction and crystallization [40]. The design and composition of electrolyte bath selected for electrodeposition as well as its pH, temperature and presence of additive are

very important and can strongly modulate the structure or electrolyte/electrode interface, the charge or mass transfer kinetics. These factors are crucial for electrodeposition technique. For instance during the reduction of metals such as cobalt, nickel or iron acidic electrolyte containing sulphur and chloride ions are commonly utilized in order to avoid passivation of metals [41]. Recently, Jia et al., have deposited highly dispersed Ag NPs with a size distribution in the range of 5–20 nm from the acidic electrolyte containing 10 mmol L^{-1} $AgNO_3$ and 10 mmol L^{-1} $NaNO_3$ on the ITO surface (Fig. 7 a and b). The final product was assessed by CV analysis, which shows two Ag oxidation peaks at 390 and 780 mV that are attributed to oxidation of Ag(0) to Ag(I) and the second one belongs to oxidation of Ag(I) to Ag(II), respectively [42], as illustrated in Fig 7 c.

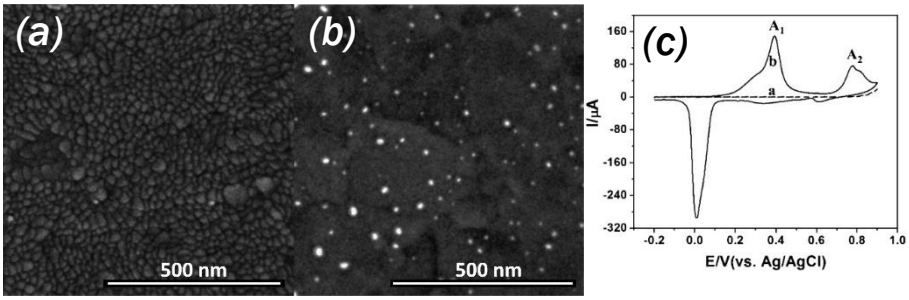

Figure 7. SEM images of bare ITO (a) and electrodecorated with Ag NPs structures (b). In (c) CV curves of bare ITO (a curve) and ITO modified with Ag NPs (b curve), both recorded in 0.1 mol L^{-1} NaOH at a scan rate of 100 mV s^{-1} are shown [43].

Radi et al., highlighted the Cu-Cu_2O core shell NPs of different shapes and size deposited on H-terminated Si(100) substrate by using one-step electrochemical technique. They found that by controlling the concentration of electrolyte the Cu-based products can exhibit cubic, cuboctahedral and octahedral morphology. They also have noted that it is possible to obtain different size and density of NPs by varying the deposition time under even a few seconds (<6 s) [44].

Various nanomaterials, in shape of nanorods, nanobelts, NPs, nanowires, etc., have been successfully synthesised by template-assisted electrodeposition techniques [45]. As templates for fabrication of suitable nanomaterial arrays anodic aluminium oxide (AAO) films, polycarbonate filter membranes, and di-block copolymer matrixes have been widely used [46]. Template synthesis method are cost-effective and may be used for mass production of nanowires with controlled geometry and morphology. For instance, aluminium anodization exhibites two types of Al_2O_3 films: barrier type oxide and porous oxide films. It has been experimentally confirmed that the thickness of barrier-type AAO film is directly proportional to the applied

potential [47]. In order to obtain porous oxide films on alumina surface, the anodization process is performed usually in the acidic electrolytes of phosphoric, sulphuric or oxalic acid [47]. In order to form highly ordered porous structure, the aluminium samples anodization usually is conducted in two stages following the illustration presented in Fig 8 [48].

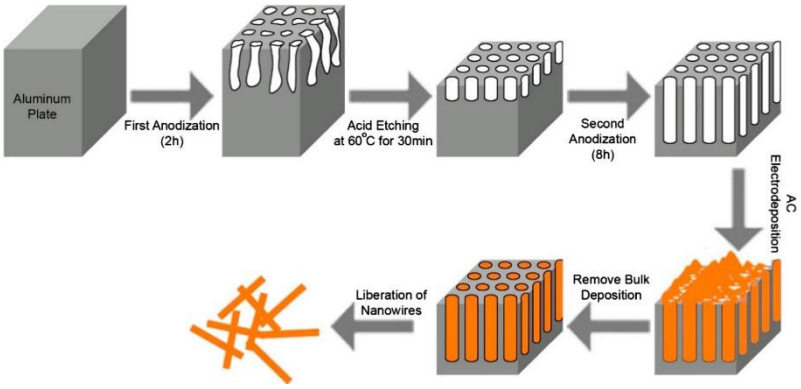

Figure 8. Schematic illustration of the template-assisted electrochemical fabrication route of the Cu nanowires [48].

According to Masuda suggestion [49], high ordered AAO honeycomb-like structure films can be obtained just *via* two steps anodizing of high purity and smooth Al surface under the conditions characteristic for the solution applied. As highlighted by Masuda, after the first prolonged anodizing step under the potentiostatic mode, the oxide layer is removed chemically from the substrate surface. The surface of the metallic aluminium after complete removal of the porous oxide layer is textured with nano-scaled concave features. These concaves act as a pore nucleation sites during the second anodization. After the second anodization under the same bath voltage and temperature, the highly ordered self-organized porous structure on aluminium substrate is achieved. In general, the structure of self-ordered porous AAO is usually defined by several parameters such as pore diameter, interpore distance, porosity, pores density, barrier layer thickness, and pore wall thickness [47]. These structural parameters of porous AAO are known to be dependent on the anodizing conditions: applied voltage value, electrolyte temperature, pH and type of acid [50]. AAO pores can further be filled with various metals, semiconductors and polymers by electroless and electrodeposition methods [46]. Various factors influence the deposition process into the matrix pores: starting from the composition of solution applied, its pH and temperature to the thickness of AAO film and its barrier layer, and the diameter of pores [46]. A typical nanowire production process consist of two main stages: electrochemical reduction of the cation at the bottom of AAO pores and

template removal. Electrodeposition of metal or semiconductor nanowires can be inspired by direct, alternating or pulse current. In order to remove the template of AAO, the phosphoric acid is used. The obtained products exhibit wire-like morphology as illustrated in Fig 9 a, b, c.

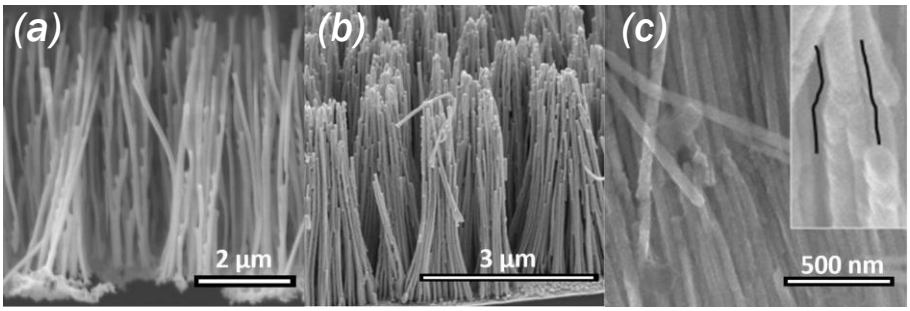

Figure 9. SEM micrographs of Pd (a), Pt (b) and Ni (c) nanowires electrodeposited in the AAO template pores [45, 51, 52].

The major advantage of the above described techniques is the relatively high filling ratio of the AAO pores, the homogeneity of obtained products, and excellent repeatability [53]. There are many papers in scientific area that report a successful fabrication of metal and semiconductor-based nanowire arrays in AAO template through electrochemical deposition route [46]. It has been shown, that electrodeposition can be adapted for fabrication of large variety of nanowired materials including Cu_2O [54], CdS [55], ZnO [56], Ag [57], Ni [58], Fe [59], Co [60], etc.

1.2. Nanomaterials as efficient antimicrobial agents

Microorganism infections are a major cause of chronic infections and humans mortality. In accordance to World Health Organization (WHO) information, the infectious diseases are the second dominating cause of deaths worldwide, resulting in almost 25 % of all global deaths. Furthermore, the situation is even worse in regions like Africa, where the infectious disease are responsible for over 50-52 % of deaths [7]. Besides, it is known that microorganisms such as bacteria are becoming resistant to the common antibiotics and further complicate the problem. From the discovery of Penicillin by A. Fleming in 1928 till the discovery of Ceftalorine in 2015, the resistance of bacteria to antibiotics is widely reported in scientific area. Recently, WHO released the list of 12 antibiotic resistant bacteria that pose the greatest threat to human health and for which new antimicrobial agents are desperately needed [5]. In nowadays, the rising numbers of drug-resistant pathogens is one of the greatest challenges facing the research community. More attention is required to find out a smart solutions or novel antimicrobial agents which could help to solve this problem. One of the promising

alternatives that possess significant antimicrobial activity against a various bacteria or fungi species are the nano-antimicrobials or engineered nanomaterials, including NPs, nanocomposites and nanogels [61]. In the current chapter the antimicrobial behaviour of metal, metal ferrites and metal oxide NPs or their hetero-nanostructures will be described thoroughly.

1.2.1. Ag-based structures as potential antimicrobial agent

A huge number of papers in scientific area revealed that Ag NPs are one of the most popular inorganic NPs used for inhibition of human's pathogen. Since ancient Greece and Egypt, Ag has been known as noble metal that has a promising antiseptic properties. This, probably lead that Ag-based materials have the largest commercialization due to its enhanced biological activity. Nowadays, it is incorporated into numerous of products such as plastics, textile, cosmetics, food packing materials, medicine products as implants, catheters or wound dressings [62]. Furthermore, Ag-based nanomaterials possess some advantages such as the ability to release the Ag ions from solid surface, thus enabling long-term antimicrobial activity, because its ionic form is more active against microorganisms [63]. It is notable, that the antimicrobial efficiency of Ag NPs has been assessed with more than 650 disease-causing microbes and has shown a positive inhibition effect [64]. Besides that Ag-based materials are low toxic or even not toxic to humans. Currently, the scientific community are discovering various other applications of Ag NPs along with its bactericidal characteristics. As highlighted by Ruparelia et al, Ag NPs exhibited the antifungal effect, especially in contact with *Candida albicans* yeast [65]. Furthermore, it was reported that Ag NPs can affect microorganisms *via* synergistic effect when combined with conventional antibiotics. According to Hwang's investigations, spherical-shaped, 3 nm in diameter Ag NPs exhibited the minimal inhibitory concentration (MIC) values of 0.25-2 μg mL^{-1} against Gram-positive (*E. faecium, S. aureus, S. mutans*) and Gram-negative (*E. coli, P. aeruginosa*) bacteria species [66]. In this paper no significant differences between antibacterial activity against Gram-positive or Gram-negative cell were observed, however in general it is widely reported that Ag NPs has more potent against Gram-negative than Gram-positive bacteria [67]. It was also shown, that Ag NPs alone or in combination with commonly used antibiotics as Ampicillin, Chloramphenicol and Kanamycin can inhibit pathogenic bacteria strains. However, in combination with antibiotics, the antimicrobial activity was more effective due to the synergistic effect with the MIC values equaling to 0.375-0.75 μg mL^{-1} (Table 1).

Another important feature of Ag NPs is their ability to prevent and disturb the biofilms based on medically relevant microorganisms. Additionally, a high

number of papers report that Ag NPs or Ag-based structures can successfully affect microbes, but in fact most of these studies, especially the part of antimicrobial assessments have done as killing individual organisms in "planktonic state". Generally, microorganisms can naturally accumulate on a wide variety of solid surfaces, thus forming the self-produced extracellular polymeric matrix of microbial communities that are called biofilms.

Table 1. Antimicrobial activity of Ag NPs and a few commonly used antibiotics alone or in combination with each other against human pathogenic bacteria [66].

Bacteria species	MIC, μg mL^{-1}			
	Ag NPs	Ampicillin	Chloramphenicol	Kanamycin
E. faecium	0.25	$2 \xrightarrow{+Ag} 0.375^{*}$	$4 \xrightarrow{+Ag} 0.375^{*}$	$2 \xrightarrow{+Ag} 0.75^{*}$
S. aureus	0.5	$4 \xrightarrow{+Ag} 0.5^{*}$	$2 \xrightarrow{+Ag} 0.75^{*}$	$4 \xrightarrow{+Ag} 0.375^{*}$
S. mutans	2	$2 \xrightarrow{+Ag} 0.375^{*}$	$4 \xrightarrow{+Ag} 0.5^{*}$	$4 \xrightarrow{+Ag} 0.375^{*}$
E. coli	2	$8 \xrightarrow{+Ag} 0.375^{*}$	$4 \xrightarrow{+Ag} 0.5^{*}$	$4 \xrightarrow{+Ag} 0.375^{*}$
P. aeruginosa	0.5	$2 \xrightarrow{+Ag} 0.5^{*}$	$1 \xrightarrow{+Ag} 0.375^{*}$	$2 \xrightarrow{+Ag} 0.375^{*}$

[*]The Ag NPs additives concentration was equal to 0.1 μg mL^{-1}, whereas the antibiotic concentration was set to be 0.5 μg mL^{-1}, respectively.

These structures are responsible for several disease such as cystic fibrosis, endocarditis or periodontal disease [68]. It is also known that commonly used antibiotics exhibit limited efficiency against biofilms. The NPs combination with antibiotics has shown promising results and has attracted considerable interest of scientific community. Recently Radzig et al., discovered hydrolyzed casein-stabilized Ag NPs (8.3 nm in diameter) that inhibit biofilms formation of *E. coli*, *P. aeruginosa* and *S. proteamaculans* in concentrations ranging between 4 and 20 μg mL^{-1} [69]. As highlighted by Loo et al., the combination of Ag and curcumin NPs (the size of NPs was in the range of 10 - 35 nm) at a concentration of 100 μg mL^{-1} can affect more than 50 % of established bacterial biofilms based on *P. aeruginosa* and *S. aureus* [70]. Ansari's group has showed that gum arabic (GA) capped-Ag NPs (5-10 nm in size) against multi-drug resistant biofilm forming *P. aeruginosa* exhibit the concentration dependent inhibition of biofilms colonizers on the surface of plastic catheters [71]. They also found that treatment of catheters with GA-Ag NPs at 50 μg mL^{-1} leads to 95 % inhibition of bacterial colonization.

It should be noticed, that the properties of Ag NPs such as particle size, surface charge, shape, dispersity or stabilizer are important and have impact on their antimicrobial behaviour. It has been reported that the size of NPs correlate inversely with antimicrobial activity, due to higher active surface

area and the higher activity of smaller NPs [72]. For instance, the dependency of Ag NPs charge to antimicrobial activity was also examined. As highlighted by Badawy et al., positively charged Ag NPs were more effective in comparison with the same size but negatively charged ones against few *Bacillus* species. The effect is attributed to the stronger electrostatic interactions with the cell membrane [73]. With reference to the Ag NPs shape, nanoplates were reported to possess higher bacteria killing efficiency than spherical-shaped, rod-shaped structures or even Ag^+ ions (in the form of $AgNO_3$). These observations were related to their higher exposure area and the more easily ionic dissolution from the lattice facets of truncated triangular Ag NPs crystals [74].

The mechanism of Ag NPs toxicity to microorganisms is still not clearly understood, however several ideas are suggested to be involved as illustrated in Fig. 10. The ionic dissolution of Ag^+ ions from Ag NPs crystals as well as the ability to release chemisorbed ions at the particles surface play a key role in the antibacterial activity of Ag NPs and are recognized by many scientists [75]. As highlighted by Xiu et al., Ag dissolution to Ag^+ did not happened under anaerobic conditions, thus increasing the viability of tested *E. coli* bacteria. They also found that in comparison with MIC of Ag NPs under aerobic conditions, three orders of magnitude higher concentration of Ag NPs did not affect the bacteria in anaerobic environment.

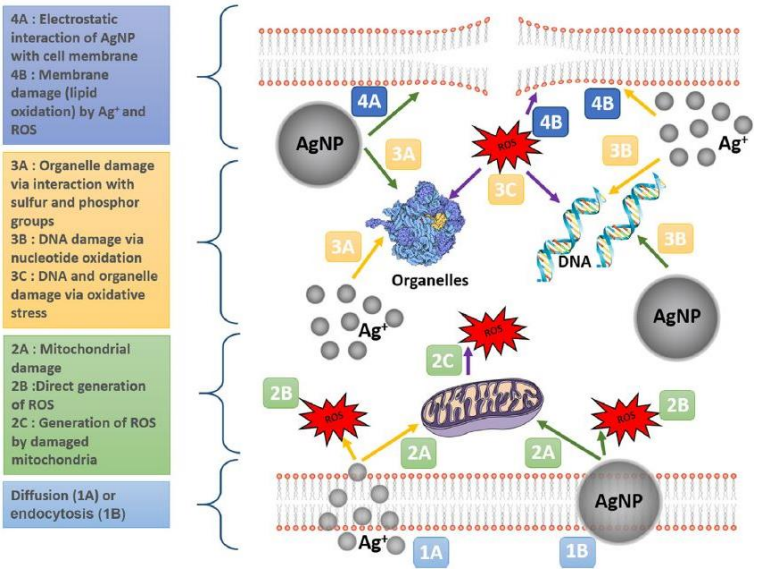

Figure 10. Mechanisms proposed for the interaction of Ag NPs with bacteria cells [68].

Authors also proposed that antibacterial activity could be controlled by modulating Ag^+ release through the oxygen availability, which strongly

modulate the Ag oxidation and Ag^+ release process [76]. For comparison it was shown that Ag ions can attach to the microorganism cell wall and possibly penetrate through the interaction with sulphur-containing proteins resulting in the formation of pits or even large holes within cell membrane [73]. This non-native cell wall structure might be responsible for its collapsed potential, dissipation of proton motive force and depletion of intracellular ATP levels [68]. Besides that, Ag NPs or ionic Ag form can generate high level of reactive oxygen species (ROS) leading to the oxidative damage of bacteria's proteins, lipids or even DNA [77]. These reasons highly influence the impact of bacteria growth and survival. However it should be noticed that the Ag NPs or Ag-based structures affect the multiple cell structures *via* several possible pathways. This is likely one of the main factors that explain such broad-spectrum of antimicrobial activity of these NPs.

1.2.2. Antimicrobial activity of copper, copper oxide and hydroxide nanostructures

Copper has been known as material with biocide properties since the ancient Greeks in the time of Hippocrates (400 BC) when it was used for pulmonary diseases, wounds healing and also for drinking water purification. Recently, copper and its compounds have been used as potential antimicrobial, antifungal and antiviral agent [78]. For instance, $CuSO_4$, copper based complex or Cu-containing polymers are used as antibacterial and antifungal agents. Unfortunately, copper compounds, especially in large amount, may be toxic to humans and other organisms as well as cause environmental hazards. According to literature, the toxicity of Cu based compounds is ranked as Cu^{2+} > nano Cu^0 > nano $Cu(OH)_2$ > nano CuO > micron scale Cu [79]. However, its nanometre-scale form might be replaced to avoid these consequences.

Copper NPs acquired much attention as novel antimicrobial material due to its multitoxicity behaviour against a wide range of microorganisms including pathogens, and virus. According to U.S. Environmental Protection Agency, this material should be capable of killing 99.9 % of most bacteria within 2 h contact [80]. Besides that, copper NPs fabrication as well as bulk material is cheap and cost effective. Furthermore, in ambient conditions these NPs oxidize and form Cu_2O or CuO oxide NPs, which are relatively stable in terms of chemical and physical properties [81]. These copper oxides or hydroxides in particular Cu_2O, CuO or $Cu(OH)_2$ possess antimicrobial effects too [82]. More recently, DeAlba-Montero et al., reported that Cu NPs, Cu-amino acids or EDTA-Cu chelates exhibit antibacterial activity agains *E. coli*, *S aureus* and *E. faecalis* with MIC values of 20-40, 5-10 and 20 mmol L^{-1}, respectively [83]. Authors also found that more effective bactericidal

properties were obtained with Gram-negative bacteria species due to its thinner cell wall structure. Nishino et al., highlighted the antimicrobial activity of extremely high surface area CuO-based coatings produced by different photochemical reactions against *S. aureus* and *E. coli* bacteria. The clear inhibition zones around square-shaped samples were observed after 24 h exposure (Fig. 11 a, b) [84].

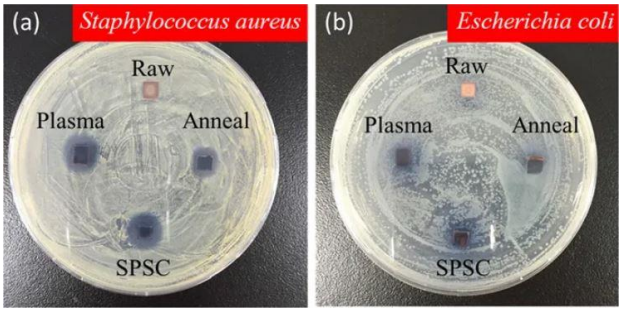

Figure 11. Antimicrobial behaviour of flower like CuO samples fabricated by different photo-induced methods against Gram-positive *S. aureus* and Gram-negative *E. coli* bacteria strains in the agar plates after 24 hours exposure at 37 ℃ [84].

The authors attribute this effect to photo-induced Cu^{2+} generation and its ability to produce ROS such as O_2^-, OH· radical or even H_2O_2. These active species cause disruptions during amino acid biosynthesis and thus leads to the bacterial death [85]. However, it should be noticed that this proposed mechanism of action is not confirmed by real evidence. Other researchers hypothesized that copper based NPs can penetrate inside the cell and inactivate enzymes due to its interaction with –SH groups resulting in the protein denaturation. According to Gopalakrishnan et al., copper oxide NPs interact with cell wall, damaging it and causing its higher permeability [86]. Unfortunately, besides previously mentioned statements, the mechanism of antimicrobial activity of copper or copper oxides NPs are still not clear and new advanced research on this topic are desperately required.

1.2.3. Crystal structure and antimicrobial properties of metal ferrite NPs

Ferrites, d-element metal oxides with spinel structures, are ones of the most important magnetic NPs. Based on the crystal structures and magnetic properties, the ferrites are classified into four main groups including spinel, garnet, hexaferrite, and orthoferrite [87]. Spinel ferrite due to its excellent magnetic properties and potential in various application areas such as catalyst, biomedicine, water, and wastewater treatment have received increasing attention in the past decade and will be further described herein.

Spinel ferrites have general chemical formula of MFe_2O_4 with a face-centered cubic structure, where M is attributed to any divalent metal cations

such as Ni^{2+}, Co^{2+}, Mn^{2+}, Cu^{2+}, Fe^{2+}, Zn^{2+}, Cd^{2+}, etc. This material's unit cell contains of 8 tetrahedral sites and 16 octahedral sites, which are occupied by M^{2+} and Fe^{3+} ions [88] as presented in Fig. 12.

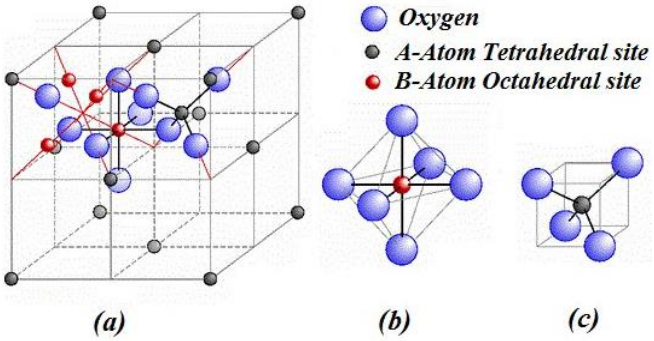

Figure 12. Spinel ferrite unit cell structure (a) and their octahedral interstice (b) or tetrahedral interstice (c).

Depending on the position of M(II) and Fe(III) in the crystal lattice, the known forms of these structures are called normal, inverse and mixed structures [89]. In the case with normal ferrites, the 8 divalent metal ions M(II) occupy tetrahedral sites, whereas 16 trivalent Fe^{3+} ions occupy the octahedral sites. For inverse spinel ferrites (e.g., magnetite or cobalt ferrite) half of the Fe^{3+} ions are distributed between 8 tetrahedral and 8 octahedral sites and all M(II) ions occupy the octahedral sites [88].

Spinel ferrites belong to soft magnetic materials group except the $CoFe_2O_4$, which possess high magneto-crystalline anisotropy, high coercivity at room temperature, and saturation magnetization value equal to 80 emu g^{-1} [90]. It should be highlighted, that the size of cobalt ferrite NPs highly influence the magnetic properties: if the NPs size are less than 10 nm, the superparamagnetic behaviour is observed [91]. However, for ultra-small $CoFe_2O_4$ NPs (diameter less than 2 nm) the paramagnetic properties dominate. Furthermore, doping of $CoFe_2O_4$ NPs with other metals as nickel, manganese, zinc, iron, etc. allows variations in their properties that are frequently required for biomedical applications, for example the usage as antimicrobial agent. It is commonly accepted that cobalt ferrite nano-powder exhibit antimicrobial properties and might be used as a drug delivery system, where the concentration of antibiotic could be minimized due to its synergistic effect with carriers. Inspired by this purpose, many scientists groups tried to fabricate novel cobalt or metal substituted ferrite NPs that shows high killing efficiency to bacteria. As reported by Sanpo et al., 42 nm-sized cobalt ferrite NPs fabricated by sol-gel techniques reduced the viability of *E. coli* bacteria almost 40 %. Furthermore, authors found that the cobalt substitution with

transition metals as Cu, Zn, Mn and Ni with the final formula of $Co_{0.5}X_{0.5}Fe_2O_4$ leads to the improvement of their antimicrobial behaviour. Almost the same size (44-40 nm) $Co_{0.5}Cu_{0.5}Fe_2O_4$ and $Co_{0.5}Zn_{0.5}Fe_2O_4$ NPs inhibit the bacteria survival more than 45 and 50 % respectively [92]. Lopez-Abarrategui et al., highlighted the citric acid coated manganese ferrite NPs (~ 5 nm in size) and it's conjugate with antifungal peptide antimicrobial activity against *Candida albicans* yeast with MIC value of 250 μg mL^{-1}. The antifungal activity of peptide-modified $MnFe_2O_4$ NPs showed higher efficiency with MIC values of 100 μg mL^{-1} [93]. According to Samavati's investigations, the antimicrobial activity depend on the amount of Cu in cobalt ferrite NPs synthesized by co-precipitation method (size of the NPs varying from 20-32 nm), with final formula as $Cu_xCo_{1-x}Fe_2O_4$, where x = 0, 0.3, 0.5, 0.7 and 1.0. They figure out that all tested NPs possess antibacterial activity, however the higher killing efficiency is achieved with $CuFe_2O_4$ NPs [94]. On the one hand the high antimicrobial efficiency is advantage due to opportunity to reduce drug concentration. On the other hand the doping of cobalt ferrite NPs with metals as Zn, Cu or Ni that are known as good antimicrobial agents might result in increased toxicity and would require additional optimization and further investigations. Besides that, the mechanism of spinel ferrites antimicrobial behaviour is still not completely understood, however some possible ideas are already highlighted. One most possible way for antimicrobial activity of these NPs is different oxidation rate, which lead to the generation of cations such as Mn^{2+}, Ni^{2+}, Zn^{2+} or Co^{2+} etc. released from the metal-substituted spinel NPs and can penetrate into the bacteria cell. These cations could interact with negatively charged components as phosphate groups and thus inactivate bacteria or even cause the death of it [95]. Another proposed mechanism state that ions or even whole NPs penetrate trough cell membrane or interact with it and thus promotes the ROS production. These active oxide species (in particular O^{2-}, $\cdot OH^-$, H_2O_2, etc.) are powerful oxidizing agents and readily destroy microbe cell. Summarizing the reported hypothesis it is clear that antimicrobial properties of spinel ferrite NPs antimicrobial properties strongly depend on the chemical composition of NPs, especially on the content of M(II) in the typical spinel structure.

1.2.4. Gold NPs as efficient drug against microorganisms

Gold NPs have attract considerable interest of scientific community due to their properties as convenient surface conjugation, chemical stability, readily size control, easily modifiable and nontoxic to mammalian cells or animals [96]. Furthermore, these NPs can exhibit the antimicrobial activity against some bacteria and fungi strains including species, such as *A. tumefaciens*,

M. oryzae, etc. [97]. However the antimicrobial behaviour of these NPs are weaker in comparison with Ag NPs. Most of the published papers highlighted that the size of Au NP plays a huge role in their antimicrobial potency. In fact, it was reported that only ultra-small gold NPs (size less than 2 nm) could exhibit the antibacterial activity. However there are several studies which confirmed that larger gold NPs also shows antimicrobial or antifungal activity especially if the NPs are functionalized by antimicrobial materials as antifungal peptides, proteins or other drug conjugates. For instance, Mohamed et al., reported that spherical, 25 nm in size gold NPs, possess the MIC values equal to 200 μg mL^{-1} against *C. psudotuberculosis* bacteria. In order to enhance this activity authors combine the action of Au NPs with laser light (520 nm, 20 mW) for exposure time of 5 min, resulting in the decrease in the MIC value at least two times [98]. As highlighted by Payne et al., Au NPs-kanamycin conjugates showed the reduced MIC values against Gram-positive *S. epidermidis* and Gram-negative *E. aerogenes* when comparing them with free kanamycin [99]. Similar observations were obtained by Rattana et al., who evaluated the activity of gallic acid and its mixture with Au NPs against food-borne pathogenic bacteria species *P. shigelloides* and *S. flexneri*. They found that the mixture consist of gallic acid and Au NPs demonstrated significantly lower MIC values than pure gallic acid [100]. The mechanism of antimicrobial activity of gold NPs is still not well understood, however some suggestions are already highlighted. These NPs are capable to attach to the bacteria cell membrane due to electrostatic interactions, thus disrupt its integrity and cause cell death. It was hypothesized that Au NPs can generate the holes in cell wall leading the leakage of cell organelles and bind to the DNA, thus inhibiting transcription process [101]. For the ultra-small NPs is mostly accepted, that it cause bacteria imbalance resulting in an increase of ROS production that culminate in cell death [102].

2. MATERIALS AND METHODS

2.1. Materials and chemicals

2.1.1. Reagents

In this project, all chemicals were of analytical grade and used as received without further purification unless otherwise stated. The main chemicals which were used in this research are given in table 2:

Table 2. The list of chemical reagents used during PhD project and the suppliers where they were purchased.

Reagent	Source
Sulfuric acid (H_2SO_4), 95-98 %	Eurochemicals
Nitric acid (HNO_3), 70 %	
Boric acid (H_3BO_3), 99.5 %	
Sodium hydroxide (NaOH), 98.8 %	
Acetone ($(CH_3)_2CO$), 99.8 %	
Ethylene glycol ($(CH_2OH)_2$), 99 %	
Acetic acid (CH_3COOH), 99.8 %	
Ammonium fluoride (NH_4F), 98 %	Merck
Copper acetate ($Cu(CH_3COO)_2 \cdot H_2O$), 98 %	Sigma-Aldrich
Magnesium acetate ($Mg(CH_3COO)_2 \cdot 4H_2O$), 99 %	
Ammonium heptamolibdate ($(NH_4)_6Mo_7O_{24} \cdot 4H_2O$), 99 %	
Silver nitrate ($AgNO_3$), 99 %	
Magnesium sulfate ($MgSO_4$), 99.99 %	
Triethanolamine ($N(C_2H_4OH)_3$), 98 %	
Cobalt chloride ($CoCl_2 \cdot 6H_2O$), 97 %	
Iron(III) sulfate ($Fe_2(SO_4)_3 \cdot xH_2O$), 97 %	
Citric acid ($HOC(COOH)(CH_2COOH)_2$), 99.5 %	
Iron(II) chloride ($FeCl_2 \cdot 4H_2O$), 99 %	
Iron(III) chloride ($FeCl_3 \cdot 6H_2O$), 99 %	
L-lysine ($H_2N(CH_2)_4CH(NH_2)CO_2H$), 98 %	
Cobalt acetylacetonate ($Co(C_5H_7O_2)_2$), 97 %	
Oleic acid ($CH_3(CH_2)_7CH=CH(CH_2)_7COOH$), 72 %	
Trimethylamine N-oxide ($(CH_3)_3N(O)$), 98 %	
Dibenzyl ether ($C_6H_5CH_2OCH_2C_6H_5$), 98 %	
Iron(III) acetylacetonate ($Fe(C_5H_7O_2)_2$), 97 %	
Tetrachloroauric(III) acid ($HAuCl_4 \cdot 4H_2O$), 99.9 %	
D,L-methionine ($C_6H_{13}NO_2S$), 99 %	
Trisodium citrate ($HOC(COONa)(CH_2COONa)_2$), 99 %	

L-ascorbic acid ($C_6H_8O_6$), 99 %	
Potassium chloride (KCl), 99 %	
Nafion, 5 %	

Milli-Q distilled water (DI, 18.2 MΩ·cm) was used for the preparation of all solutions, synthesis and rinsing of NPs and electrode surfaces.

2.1.2. Materials and microorganisms growth media

All materials as well as the microorganism growth media which were used in this research are listed in Table 3:

Table 3. The list of materials and microorganism growth media used during PhD project and the suppliers where they were purchased.

Material	Source
Aluminium foil (Al), 99.7 % Platinum foil	Russia
Aluminium foil (Al), 99.99 % Titanium foil (Ti), 99.7 % Carbon rod (C), 99.95 %	Sigma-Aldrich
Screen-printed electrodes	Dropsens
Saturated calomel electrode	Gamry
Nutrient agar[a] Nutrient broth[b] Sabouraud CAF agar[c] Yeast extract peptone dextrose agar (YEPD)[d] RPMI-1640[e] M9 5X[f] LB medium[g]	Liofilchem

[a] 2 g L^{-1} yeast extract, 1 g L^{-1} meat extract 5 g L^{-1} peptone, 5 g L^{-1} sodium chloride and 15 g L^{-1} agar;
[b] 1 g L^{-1} glucose, 15 g L^{-1} peptone, 6 g L^{-1} sodium chloride and 3 g L^{-1} yeast extract;
[c] 40 g L^{-1} glucose, 0.5 g L^{-1} chloramphenicol, 15 g L^{-1} agar and 5 g L^{-1} casein peptone;
[d] 20 g L^{-1} peptone, 10 g L^{-1} yeast extract, 20 g L^{-1} glucose and 15 g L^{-1} agar;
[e] 2 g L^{-1} glucose, 1 g L^{-1} amino acids, 5 mg L^{-1} phenol red, 2.1 g L^{-1} salts and 44 mg L^{-1} vitamins;
[f] 33.9 g L^{-1} Na_2HPO_4, 15 g L^{-1} KH_2PO_4, 5 g L^{-1} NH_4Cl and 2.5 g L^{-1} NaCl;
[g] 10 g L^{-1} tryptone, 5 g L^{-1} sodium chloride and 5 g L^{-1} yeast extract.

It is worth noticing that microorganism's growth media as well as containers and biohazardous waste were sterilized *via* autoclaving at 121 °C for 1.5 h before and after usage.

2.1.3. Microorganism's cultures

In this work, antimicrobial activity of NPs and coatings were assessed with eukaryotic and prokaryotic microorganisms, which were obtained from

Nature Research Centre collection of microbial strains. The list of various types of microorganisms are given below:

Yeasts:

- ✓ *Saccharomyces cerevisiae,* (GTC-BTL, M-99)
- ✓ *Candida parapsilosis,* (GTC-BTL, M-16)
- ✓ *Candida krusei,* (GTC-BTL, M-12)
- ✓ *Candida albicans,* (GTC-BTL, M-7)
- ✓ *Geotrichum candidum,* (GTC-BTL, M-40)

Fungi:

- ✓ *Aspergillus versicolor,* (GTC-BTL, B-64)
- ✓ *Aspergillus fumigatus,* (GTC-BTL, G-37)

Bacteria:

Gram-negative strains

- ✓ *Pseudomonas aeruginosa,* (GTC-BTL, B-12)
- ✓ *Escherichia coli,* (GTC-BTL, B-10)
- ✓ *Acinetobacter baumannii,* (ATCC BAA-747)
- ✓ *Salmonella enterica,* (GTC-BTL, B-25)

Gram-positive strains

- ✓ *Micrococcus luteus,* (GTC-BTL, B-30S)
- ✓ *Staphylococcus aureus,* (GTC-BTL, B-26)
- ✓ *Staphylococcus aureus MRSA,* (ATCC 433300)
- ✓ *Streptococcus gordonii,* (GTC-BTL, B-27)

The bacteria strains, were propagated on Nutrient agar, while yeasts or fungi were cultured on Sabouraud CAF agar at 37 ℃ and 27 ℃ for 24 to 48 h before use, respectively.

2.2. Fabrication of Cu_2O, CuO and Ag based antimicrobial coatings

AC and DC deposition techniques as well as a few electrochemical anodization methods were employed in order to achieve well dispersed heterostructures on the materials with high surface area as TiNT or AAO. In this paragraph the formation methods of these nanostructured materials are given briefly.

2.2.1. Thermally and electrochemically inspired Ti oxidation

Decoration of pyramidal-shaped copper (I) oxide (Cu_2O) p-type semiconductor NPs on thermally or anodically oxidized titanium substrate was achieved using AC deposition mode. Commercially pure titanium foil, 0.127 mm thick, were used to prepare ~ 7 mm in radius round-shaped

specimens. Firstly, Ti electrodes (S~1.5 cm^2) were ultrasonically cleaned in ethanol and DI for 6 min in each and dried in air. Titanium oxide nanotube arrays (TiNT) were prepared by anodic oxidation. Anodization experiments were conducted in the thermostated glass cell containing ethylene glycol electrolyte with 0.3 % w/w of ammonium fluoride and 20 mL L^{-1} of water at 20 ± 1 ℃ with gentle magnetic agitation. All anodization experiments were carried out potentiostatically at a constant voltage of 50 V for 40 min. Direct current (DC) power supply platinum sheet cathodes with dimensions of 40 × 70 mm and the Ti electrode (used as a WE) connected to the anode was employed in this process (Fig. 13).

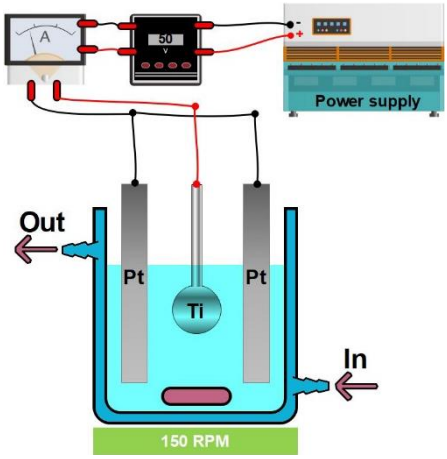

Figure 13. Schematic illustration of titanium anodization used to produce nanotubular TiO_2 films by anodization of Ti.

In order to decrease the thickness of titanium oxide barrier layer, the anodization voltage was step-wise decreased at the end of anodizing from 50 V to 30 V with a 1.0 V min^{-1} rate. Ti surface oxidation was conducted in the organic electrolyte as mentioned above no more than 3 times before replacing with a fresh one. After anodization the Ti electrodes were ultrasonically agitated in ethanol for 5 s. The aim of this procedure was to remove the debris from the TiNT surface. The as-growth products were rinsed with DI and dried in air. The amorphous TiO_2 phase was calcined in air atmosphere at 450 ℃ for 2 hours at 10 ℃ min^{-1} heating rate.

The thermal oxidation of Ti foils was conducted by furnace under ambient atmosphere. Firstly the samples were heated up to 450 ℃, with a heating rate of 10 ℃ min^{-1}. The temperature was kept for 2 h. Subsequently, the furnace was cooled to room temperature with the cooling rate of 10 ℃ min^{-1}.

2.2.2. Decoration with Cu_2O NPs

Electrodeposition of Cu_2O NPs on nanotube walls or compact TiO_2 films was accomplished in the similar deposition bath as represented in Fig. 13, except that several graphite stripes were used instead of platinum electrode. In detail, the prepared electrode was immersed into the deposition electrolyte containing an aqueous solution of 0.1 mol L^{-1} copper acetate, 0.1 mol L^{-1} magnesium acetate and 1.2 mL L^{-1} acetic acid. The pH of the blue solution was adjusted to ~ 5.28. All depositions were performed at room temperature. Mg^{2+} salt was used to prevent the breakdown of the titanium oxide barrier layer during the AC treatment changing the rate of Cu_2O deposition [103]. Owing to the rectifying properties of the titanium barrier layer [104], the depositions were carried out by AC at a constant ($U_{p\text{-}to\text{-}p}$) peak-to-peak voltage mode which varied within the 1.1 – 1.2 V range. The AC frequency was set in the range of 100 Hz for deposition on the thermally oxidized TiO_2 ($t_{deposition}$ = 12 min) and 50 Hz on anodically oxidized TiNT ($t_{deposition}$ = 5 min) using a programmable AC source Chroma AC 61602 (Taiwan). After deposition, each specimen was carefully rinsed with DI and dried under nitrogen.

2.2.3. Formation of CuO/Cu heterostructures by copper anodization

Copper foil disc-shaped samples of ~1.5 cm^2 working area were cut from copper foil. Prior to anodization the specimens were etched for 40 s in 1:1 HNO_3:H_2O solution. Anodic oxidation of copper samples were performed in a hot electrolyte containing 3.75 mol L^{-1} of sodium hydroxide and 0.008 mol L^{-1} $(NH_4)_6Mo_7O_{24}{\cdot}4H_2O$ at 90-95 °C for 15 min. Anodization was carried out in two-electrode cell configuration under galvanostatic mode at 10 mA cm^{-2}, using a Pt sheet as cathode. After oxidation, electrodes were rinsed with DI and dried in an air. The formed black electrodes were annealed in ambient atmosphere at 250 °C for 1 h with a heating rate of 10 °C min^{-1}.

2.2.4. Electrochemical formation of porous AAO

Aluminium electrodes with dimensions of 40 × 40 × 0.05 mm were cut from commercial Al foil (99.7 %). The samples were chemically cleaned by etching in 1.5 mol L^{-1} NaOH at 55-60 °C for 10-12 s and desmutted for 60 s in a 1.5 mol L^{-1} HNO_3 solution. After each procedure the sample was careful rinsed with DI and dried under the nitrogen stream. Electrochemical oxidation of Al electrodes were carried out in a thermostated glass cell and two-electrode configuration whereas the aluminium foil acts as a WE and two platinum sheets were used as a cathode (see Fig. 13). Anodization was performed potentiostatically in 1.2 mol L^{-1} H_2SO_4 electrolyte at 15 °C for 10 min at a constant potential of 10 V. For comparison, some specimens were anodized under the same conditions for 2 h obtaining a porous alumina film with an

average thickness of 9.5 μm. Some electrodes were fabricated from pure aluminium (99.99 %) and polished in a 60 % $HClO_4$ + C_2H_5OH (1:4 w/w) solution at 17 V and 5 °C for 1 min prior oxidation in the same conditions.

2.2.5. Decoration of self-ordered AAO with Ag nanowire arrays

In order to obtain uniform deposition of Ag nanowires into the pores of AAO/Al the galvanostatic and potentiostatic modes were tested. The aim of this experiments was to find out the conditions that required for homogenous AAO pores filling with metallic Ag nanowires thus resulting in uniform colouring of extremely thin AAO film in gold tints. Briefly, the anodized Al sample was immersed into the deposition bath containing an aqueous solution of 10 mmol L^{-1} Ag nitrate and 50 mmol L^{-1} magnesium sulfate. The pH of the colourless solution was adjusted with HNO_3 to ~ 1.45. Due to the rectifying properties of alumina barrier layer [105], the depositions were carried out *via* AC at 50 Hz either at constant current density of 1.5-3 mA cm^{-2} or constant voltage $U_{p\text{-}to\text{-}p}$ ~ 7 V. Anodized and coloured specimens were individually sealed in boiling distilled water for 30 min. After deposition, each specimen was carefully rinsed with DI and dried under the nitrogen stream.

2.3. Synthesis of $CoFe_2O_4$@citrate, $CoFe_2O_4$@Lys, $Co_xFe_{1-x}Fe_2O_4$@Lys, $CoFe_2O_4$@Ole, Fe_3O_4@Au@Met and ultra small Au NPs as a potential antimicrobial material

In this study, the hydrothermal, co-precipitation and thermal decomposition methods were employed to synthesize different in size, shape, lattice composition or environmental cobalt ferrite, magnetite and gold NPs as the new potential drugs against microorganisms. In this chapter the synthesis conditions of NPs applied will be described thoroughly.

2.3.1. Synthesis of citrate stabilized cobalt ferrite NPs

Hydrothermal synthesis as well as co-precipitation method offers many advantages such as inexpensive, one step synthesis procedure and environmental friendliness. Consequently, they have been chosen to produce the citrate stabilized $CoFe_2O_4$ NPs. For this purpose, the 15-nm in size, spherical NPs were synthesized in Teflon-lined stainless steel autoclave from the complex-assisted alkaline solutions containing 45 mmol L^{-1} $CoCl_2$ and $Fe_2(SO_4)_3$ salts and 75 mmol L^{-1} citric acid as a chelating agent. The pH of the brown solution was adjusted with 5 mol L^{-1} of NaOH to ~ 12.35. The prepared mixture was transferred into Teflon-lined autoclave and kept at 130 °C for 10 h with a heating/cooling rate of 10 °C min^{-1}. As-grown black in colour product was washed with DI several times and collected using a permanent

magnet. Small (~ 5 nm in diameter) and ultra-small (~ 2 nm in diameter) NPs were synthesized by co-precipitation method in the thermostated glass reactor at the same conditions. Following Massart's group protocol, the synthesis was carried out at 80 °C for 3 h with the argon gas assisted reaction agitation [20]. Finally, NPs were centrifuged at 7500 G for 15 min and carefully rinsed with DI, repeating the procedure at least 5 times. For collection of ultra-small NPs, the supernatants of last three centrifugations were collected and rinsed further twice in the successional sequence with DI, isopropyl alcohol and DI resulting in brown NPs suspension with pH ~ 7.4.

2.3.2. Synthesis of L-lysine coated Fe-substituted $Co_xFe_{1-x}Fe_2O_4$ NPs

L-lysine coated Fe-substituted magnetic cobalt ferrite NPs with compositions of $Co_xFe_{1-x}Fe_2O_4$ (where x varies from 0.2 to 1.0) were synthesized by hydrothermal method (Fig. 14). Firstly, Co^{2+}, Fe^{2+}, Fe^{3+} salts with molar ratios of 1:4:10 for $Co_{0.2}Fe_{0.8}Fe_2O_4$, 1:1:4 for $Co_{0.5}Fe_{0.5}Fe_2O_4$, 1:2 for $CoFe_2O_4$ and 1:2 for Fe_3O_4 were dissolved in 25 mL DI under magnetic stirring. The total concentration of metal salts was fixed at 75 mM. Secondly, 0.195 mol L^{-1} of L-lysine was dissolved in 12 mL of DI and rapidly added to the mixture. The pH of the brown suspension was adjusted with 5 mol L^{-1} of NaOH to ~ 12.35.

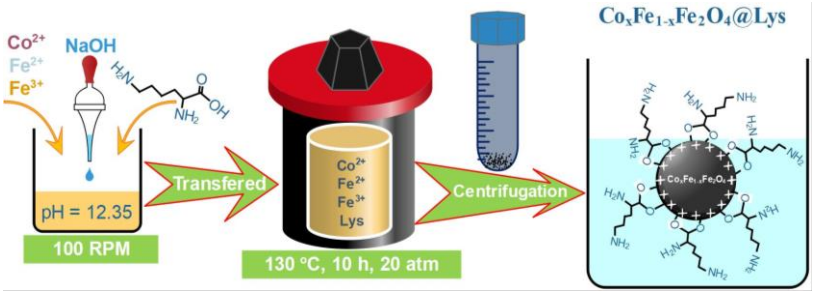

Figure 14. Schematic illustration of the synthesis process of Fe-substituted, L-lysine coated $Co_xFe_{1-x}Fe_2O_4$ NPs.

Finally, the 40 mL of prepared mixture was transferred into a Teflon-lined stainless steel autoclave. The reactor was put to muffle furnace and the reaction was conducted at 130 °C with a heating/cooling rate of 10 °C min^{-1} for 10 h. Prepared black nanopowders were separated magnetically, washed from reaction fluid several times with DI, centrifuged at 7500 G for 15 min and left to dry overnight.

2.3.3. Fabrication of $CoFe_2O_4$@Ole NPs by thermal decomposition approach

Hydrophobic, 7.5 in diameter $CoFe_2O_4$ NPs were synthesized by thermal decomposition method. In more detail, 18 mmol L^{-1} of cobalt acetylacetonate,

36 mmol L^{-1} of iron acetylacetonate, 15 mmol L^{-1} trimethylamine-N-oxide and 41.7 g L^{-1} oleic acid were dissolved in N_2 saturated 45 mL of dibenzyl ether under the magnetic stirring. Oleic acid as well as trimethylamine-N-oxide were used as stabilizing agent. The prepared mixture was heated to 230 ℃ under N_2 gas flow and stirred for 2 h in custom-made glass reactor, followed later by temperature increase to 280 ℃ and processing further under reflux and N_2 bubbling for 1 h. After cooling to room temperature, the crude products were centrifuged, rinsed with acetone/ethanol mixture (2:1) for several times, collected with permanent magnet and dried in air at 60 ℃. For the synthesis of larger cobalt ferrite NPs (mean diameter ~17 nm), the same synthesis protocol was repeated using already synthesized NPs in a double diluted solution, compared to the first one, under the same conditions.

2.3.4. Synthesis of ultra-small gold and Fe_3O_4@Met@Au NPs

In this study, the synthesis of Fe_3O_4@Met NPs was carried out in an alkaline media as described previously (in § 2.3.2 Synthesis of L-lysine coated Fe-substituted $Co_xFe_{1-x}Fe_2O_4$ NPs) except the D,L-methionine amino acid was used instead of L-lysine. The fabrication process of magnetite NPs and the possible interaction of D,L-methionine functional groups supposed through O atom are represented in Fig. 14 and 15.

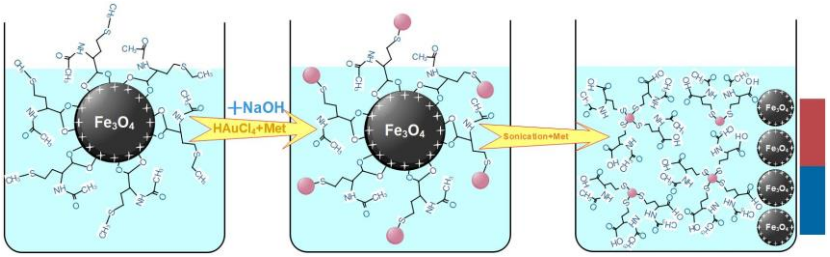

Figure 15. Schematic illustration of ultra-small gold NPs functionalization of methionine shell to achieve Fe_3O_4@Met@Au and Au@Met NPs.

The loading of magnetite surface with ultra-small gold NPs was performed through the methionine-induced [106] chemical reduction of chloroauric acid. Firstly, 3.5 mg of Fe_3O_4@Met NPs were dispersed in 5 mL of distilled water in an ultrasonic bath until the mixture become the bright mustard-coloured solution. Then, 3.5 mL of NPs suspension was transferred into a glass reactor and 5 mL of 10 mmol L^{-1} methionine solution containing 4 mmol L^{-1} of $HAuCl_4$ was added under the ultrasonic agitation. The solution was alkalized to the ~ 12.4 pH value by dropping 5 mol L^{-1} sodium hydroxide. The ultra-small gold NPs crystallization on the Fe_3O_4@Met NPs surface process was performed at 37 ℃ for 4 h under the mild mixing conditions. Immediate formation of gold NPs was observed by change in the dispersion colour and a

notable increase in the NPs density. Finally, the samples were washed several times with DI and re-dispersed in ethanol for further examinations. Resulting NPs were labelled as Fe_3O_4@Met@Au NPs.

In order to detach the Au@Met NPs from the Fe_3O_4@Met@Au surface methionine amino acid has been used as shown in Fig. 15. Following this illustration, the washed precipitates were transferred into the glass beaker containing the solution of 0.3 mol L^{-1} D,L methionine. Then, it was placed in the ultrasonic bath and operate 5-7 minutes until the colour of suspension turns from bright brown to light pink. The products obtained were collected by magnetic separation and stored at 4 ℃ for further experiments.

2.4. Fabrication of concentrated gold and Ag NPs

Gold NPs were synthesized from $HAuCl_4$ *via* modified Turkevich method as described in [107]. Following this protocol, 19.691 mg of tetrachloroauric(III) acid was added to the beaker filled with 50 mL distilled water. Secondly, reaction mixture was transferred on the heat plate preheated to 80-90 ℃ under vigorous stirring. Then, 10 mL of 38.8 mmol L^{-1} trisodium citrate was injected to the solution resulting in the changes in colour from yellow to bluish grey immediately and then to red-wine. After 15 min, the reaction was cooled down to room temperature under stirring. As-synthesized particles were used for size measurements and further concentrated 500 times *via* centrifugation at 7000 G for 20 min. The resulting particles (~1.25×10^{17} NPs L^{-1}) are stabilized with negatively charged citrate ions and were used for screen printed electrode (SPE) modification.

Ag NPs were synthesized using ascorbic acid as reductant and trisodium citrate, which act as a capping agent as reported in [108]. In a hydrothermal synthesis, 2 mL of aqueous solution of sodium citrate (1 wt %), 0.5 mL aqueous solution of silver nitrate (1 wt %) and 1 mL of 8 mmol L^{-1} potassium chloride was consecutively added to the 1.5 mL of distilled water under stirring at room temperature. In parallel, the 100 μL of 0.1 mol L^{-1} ascorbic acid solution was injected to 95 mL of distilled water and were left to heat until 80-85 ℃. After 5 minutes incubation the premixture solution (5 mL) was injected to 95.1 mL of hot water under vigorous stirring resulting in the changes in colour from colourless to yellow. Finally, the reaction mixture was boiled for 1 h under stirring to maximize the production yield of Ag NPs. The products were used for size measurements and further concentrated as described previously. The concentrated Ag NPs (~1.13×10^{16} NPs L^{-1}) are coated with negatively charged citrate ions and were also used for SPE electrodes modification.

2.5. Modification of screen printed electrodes with NPs

Gold-based SPE were partly covered with insulating tape in which empty part between working (WE) and counter (CE) electrode was left open for concentrated NPs suspension (Fig. 16). Care was taken to facilitate and ensure the short-circuiting conductivity, obtained during the dropping of concentrated Ag or Ag and Au containing NPs mixture. In order to deposit particles uniformly and avoid the coffee-ring effect, colloidal suspension droplets on bare SPE were heated to 70-80 ℃ as recommended in [109]. Furthermore, the 1 µL of 5 % of Nafion solution was dropped directly on the NPs to prevent the dissolution of particles as well as enhance the stability of the electrode life time and even biocompatibility [110]. The resistance measured by multimeter between W and C electrode, was less than 10 Ω confirming the good electrical contact.

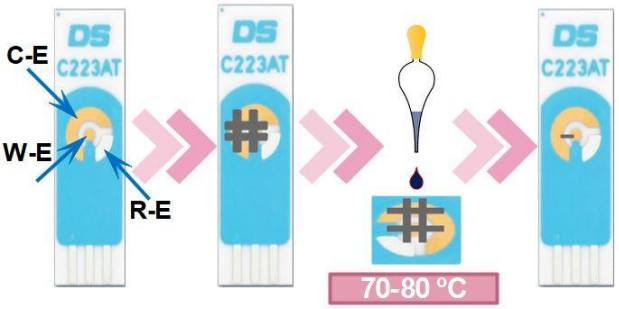

Figure. 16 Schematic illustration of SPE modification with Ag and Au NPs.

The electrochemical conversion $Ag^0 \xrightarrow{oxidation} Ag^+$ was carried out in 140 mmol L^{-1} PBS solution at room temperature. For this, as-prepared Ag or Ag and Au NPs modified SPE and Pt wire were used as working and CE, respectively, in a three-electrode electrochemical cell. A saturated calomel electrode (SCE) was used as a reference. Chronoamperometry was conducted as an electrochemical method for complete and partial Ag NPs oxidation at - 200 mV for 120 s and at -70 mV for 12 s, respectively. After preparation, the SPE were thoroughly washed with DI water and stored dry before being used for measurements.

2.6. Investigation of antimicrobial activity of as-synthesized coatings and NPs

Antimicrobial activity of coatings and NPs, which were synthesized in this study have been studied against several medically relevant eukaryotic and prokaryotic microorganisms, including, *S. cerevisiae*, *C. parapsilosis*, *C. krusei*, *C. albicans*, *G. candidum*, *A. versicolor*, *A. fumigatus*, *P. aeruginosa*, *E. coli*, *A. baumannii*, *S. enterica*, *M. luteus*, *S. aureus* and

S. aureus MRSA. In the following chapter, the techniques for evaluating the *in vitro* antimicrobial susceptibility will be discussed in detail.

2.6.1. Agar-disk diffusion method

The modified agar –disk diffusion method, also known as the Kirby-Bauer method, was used in order to examine the antimicrobial activity of coatings such as thermal and anodically oxidized Ti surface decorated with Cu_2O nanocrystals or alumina foil samples with encapsulated Ag nanowires as well as filter papers loaded with NPs as described previously (Fig. 17) [111].

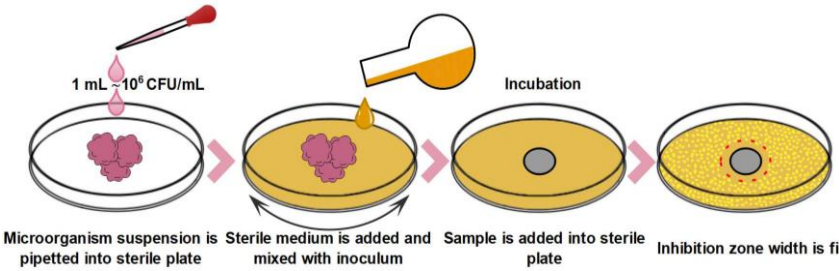

Figure. 17 Schematic illustration of agar-disk diffusion method.

Yeasts and fungi were cultivated on Sabouraud CAF or YEPD agar medium while the bacteria strains were cultivated on Nutrient agar. Briefly, a small piece of microbes was taken from the cell storage bank and inoculated on a growth media. Secondly, in order to prepare suspensions containing approximately $(1\text{-}5)\times10^6$ colony forming units (CFU) per mL^{-1} for yeasts or fungi and $(6.4\text{-}8)\times10^8$ CFU mL^{-1} for bacteria, as measured spectrophotometrically, fresh cell strains were suspended in the 0.9 % NaCl solution. After this, 1 mL of as-prepared suspension was transferred into sterilized Petri dishes. Finally, the microorganism growth media was poured onto prepared dishes, mixed carefully and allowed to solidify in the incubator before applying the loaded coatings or discs. The disc-shaped samples were placed gently on the seeded agar plates. The experiment was carried out in triplicate and the diameters of the inhibition zones were measured after 24 (for bacteria) or 48 h (for fungi) of incubation at 37 ℃ and 28 ℃, respectively. The negative control – inoculated Petri dishes without sample and with filter paper or Ti and AAO electrode were used, while for the positive control – standard antimicrobial agents including fluconazole (100 μg for yeasts), itraconazole (50 μg for fungi) and streptomycin (100 μg for bacteria).

2.6.2. Serial dilution method

Serial dilution method known as broth dilution method was employed to determine the quantitative analysis of antimicrobial behaviour of as-synthesized $Co_xFe_{1-x}Fe_2O_4$, $CoFe_2O_4$@Lys, $CoFe_2O_4$@Ole, Au@Met and

Fe_3O_4@Met@Au NPs (Fig. 18). In this experiments, NPs were cultivated in liquid growth medium under vigorous stirring for 24 or 48 h.

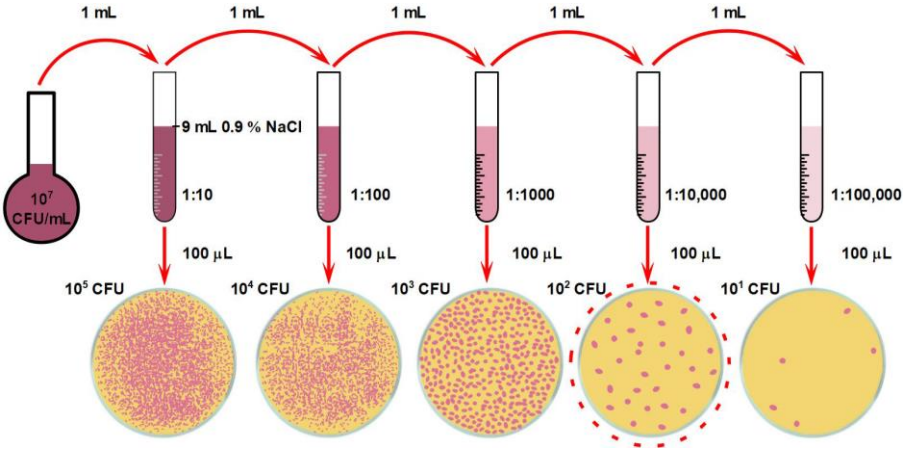

Figure. 18 Schematic illustration of serial dilution method.

Followed by these investigations prokaryotic and eukaryotic microorganisms have been propagated in Nutrient and Sabouraud CAF agar medium. The fresh cultures have been harvested and diluted in sterile nutritional liquid media resulting 0.5 McFarland scale or CFU mL^{-1} inoculum of (1-5) × 10^6 for yeasts or fungi and (6.4 – 8) × 10^8 for bacteria cells. The concentration of microbes was controlled by measuring optical density at 530 nm (OD_{530}) and 600 nm (OD_{600}). The range of OD_{530} and OD_{600} was obtained between 0.12–0.15 and 0.08–0.1, respectively. Then microorganism suspension were collected at the logarithmic stage of growth and transfer into a 50-mL Erlenmeyer flask. Finally the colloidal suspension of NPs was added to the liquid media with inoculum and further incubated at room temperature for 24-72 h with 150 G shaking. During the cultivation, 1 mL of suspension was taken from each reaction mixture, diluted as represented in Fig.18 and seeded on sterile plate using stainless steel spreader. Control – microorganism suspension without NPs addition. Oleic acid, l-lysine, methionine, and magnetite NPs (Fe_3O_4) act as a negative control samples. The counting of microbes colonies as well as their growth were tested after incubation at 37 ℃ and 28 ℃.

2.7. Open circuit potential and chronoamperometry measurements

Open circuit potential (OCP) measurements have been commonly used for description of microbial fuel cells (MFC). It is well known, that microorganisms have ability to form biofilms spontaneously on material surfaces, thus it can subsequently demonstrate electrochemical activity when the biofilm coated electrode is tested electrochemically [112]. In this study, microbial bioanode based on glassy carbon electrode (GCE) was designed and tested under open circuit conditions. The OCP was recorded with digital multimeter (Brandfrd 2286) which was connected to the biofilms hosting electrode (GCE) and Ag/AgCl (3M KCl) RE as represented in Fig. 19. Both electrodes were immersed into a falcon tube (50 mL) filled with 29 mL sterile LB medium. After first OCP measurement, liquid media was inoculated with 1 mL microbes suspension consisted with one or few species such as *Pseudomonas aeruginosa*, *Staphylococcus aureus*, *Escherichia coli*, *Streptococcus gordonii* and *Candida albicans*.

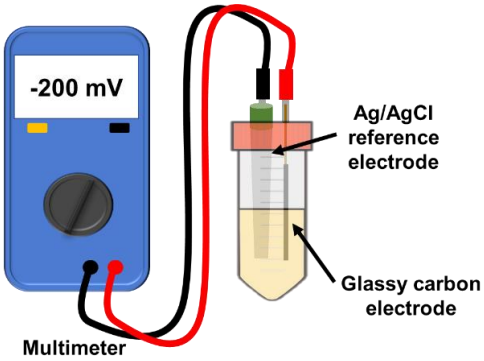

Figure. 19 Schematic illustration of open circuit measurements between biofilm coated GCE and Ag/AgCl (3 mol L^{-1} KCl) RE.

The final concentration of inoculum was adjusted to be 10^6 CFU mL^{-1}. The investigation on negative electrode potential development was performed at various time (*t*) including $t = 0$, $t = 2$, $t = 4$, $t = 6$, $t = 8$, $t = 18$, and $t = 24$ h. Each measurement was done in triplicate. All biological waste such as containers, tubes, plates were autoclaved before recycling or disposal.

In order to investigate the ability of electroactive biofilms to generate electrical current, which is required for reduction of AgCl NPs based sensing layer to metallic Ag, chronoamperometry measurements were performed by applying the constant potential of 5 mV. In this study, two electrode system was used to monitor the electrical current generating by biofilm. The Ag or Ag-Au NPs modified SPE electrode act as a WE, whereas the biofilm coated GC electrode act as a CE. It should be noticed, that before usage, the Ag NPs modified SPE was oxidized electrochemically to have a resistance between 1 and 10 kΩ as described previously. Both electrodes were immersed in a LB

medium and connected to electrochemical analyzer (Ivium technologies). The chronoamperometry was run for 86.400 s.

2.8. Wireless monitoring of electroactive biofilms

A simple radio frequency identification system (RFID) consisted of scanning antenna, passive RFID tag (operating frequency 13.56 MHz, (Smartrac)) and a network analyser (DG8SAQ, VNWA 3). The reader part works as transmitting and receiving unit by consuming an AC to generate a magnetic field to transmit and receive sensor data from the distant sensor. To prepare the NFC-RFID tag for wireless-biofilm monitoring, the passive tag was cut resulting 2 mm gap in the circuit. Furthermore, the NPs modified SPE electrode was connected to the gap. Changes in resistance of NPs modified SPE leads the change in conductivity of the RFID antenna, which can be wirelessly monitored. In addition, the wireless sensor delay time, could be attributed to the time, required to reduce Ag^{+} to Ag^{0}. During the process, electrode resistance changed from 1-10 kΩ to 2-20 Ω leading a small shift between the resonance frequencies from 18 to 13.5 MHz, which corresponded to the reflection coefficient |S11| obtained during the backscattered energy between SPE modified tag and copper coil-based antenna. The frequency range of the antenna was operated in the range of 3 to 30 MHz. The resistance of the NPs modified SPE was measured with a digital multimeter (Extech instruments).

2.9. Characterization techniques

NPs, coatings and other heterostructured materials were characterized using structural and analytical characterization techniques:

- **Scanning electron microscopy** (SEM). The surface morphology, cross-sections and elemental composition of as-synthesized coatings was carried out in a dual beam system of a scanning electron microscope Helios Nanolab 650 (FEI Quanta 200 F) equipped with an EDX spectrometer X-Max (Oxford Instruments), field emission source and imbedded focus ion beam (FIB) system. It should be noticed that before cross-section analysis, a thin (~ 100 nm) platinum layer was deposited on top of the sample.
- **Transmission electron microscopy** (TEM). The morphology, shape and size distributions of NPs were investigated by a transmission electron microscope FEI Tecnai F20 X-TWIN with a field emission gun. For this purpose, NPs were dispersed in ethanol, drop-casted onto carbon-coated nickel grid and dried naturally. TEM images were recorded using a Gatan Orius CCD camera in bright field mode at an acceleration voltage of 200 kV.

In order to measure the mean particle diameter, the ImageJ software was used in this study.

- **Raman spectroscopy**. Raman spectra were recorded using an inVia (Renishaw) spectrometer equipped with a thermoelectrically cooled (- 70 ℃) CCD camera and microscope. The 532 nm solid state diode laser beam was used as an excitation source. The laser power at the sample was restricted to 0.06 mW and 0.6 mW for TiNT/Cu_2O and bare Ti oxide, respectively. Raman spectra were taken using a 50× objective lens. The parameters of bands were determined by fitting the experimental spectra with Gaussian-Lorentzian shape components using GRAMS/A1 8.0 (Thermo Scientific) software.

- **X-ray diffraction** (XRD). Phase analysis of NPs and coatings were carried out using a diffractometer SmartLab (Rigaku) with rotating Cu anode. CuKα radiation (α = 0.154183 nm) was separated by multilayer bent graphite monochromator. The XRD patterns were measured in Bragg-Brentano scan mode with a step 0.02º (in 2θ scale) and counting time 8 s per step. Phase identification was performed using the powder diffraction database PDF4+ (2015). The size of NPs was determined by the Halder-Wagner (H-W) approximation.

- **Fourier-transform infrared spectroscopy** (FTIR). Infrared spectra were recorded in the transmission mode on an ALPHA FTIR spectrometer (Bruker) equipped with a room temperature detector DLATGS. The spectral resolution was set at 2 cm^{-1}. Spectra were acquired from 100 scans. Samples were dispersed in KBr tablets. Parameters of the bands were determined by fitting the experimental spectra with Gaussian-Lorentzian shape components using GRAMS/A1 8.0 (Thermo Scientific) software.

- **X-ray photoelectron spectroscopy** (XPS). XPS experiments were carried out in order to obtain the information about the chemical state of ultra-small gold NPs deposited or detached from Fe_3O_4 NPs surface on the upgraded vacuum generator "VG ESCALAB MK II" (VG Scientific) spectrometer fitted with XR4 twin anode. The non-monochromatised MgKα X-ray source was operated at hν = 1253.6 eV with the 300 W power (20 mA/15 kV). During the spectral acquisition, the pressure in the analysis chamber was lower than 5×10^{-7} Pa. The spectra were acquired with the electron analyser pass energy of 20 eV and resolution of 0.05 eV.

- **Atomic force microscopy** (AFM). The morphology and size distribution of NPs were also investigated with atomic force microscope Veeco AFM diInnova (Veeco Instruments) in a tapping mode. TESPA-2 cantilevers (Veeco Instruments) with a tip curvature of 8 nm were used. Images were acquired at the scan rate of 1 Hz per line with the 512 × 512 pixel

image resolution. Image processing included flattening to remove the background slope caused by the irregularities of the piezoelectric scanner. The analysis was performed using the SpmLabAnalysis software (Veeco Instruments).

- **Mössbauer spectroscopy**. Mössbauer spectra were collected in transmission geometry using $^{57}Co(Rh)$ source. The hyperfine field B distributions and the doublets (singlets) were fitted to the Mössbauer spectra using Win-Normos (Dist) software. Isomer shifts are given relatively to α-Fe.
- **Inductively coupled plasma atomic emission spectroscopy** (ICP-OES). The chemical composition of $Co_xFe_{1-x}Fe_2O_4$, $CoFe_2O_4$@Lys, $CoFe_2O_4$@Ole, Au@Met, Fe_3O_4@Met@Au NPs as well as the amount of encapsulated Ag in AAO pores and electrodeposited Cu_2O on thermal or anodically oxidized Ti substrate were investigated by ICP-OE spectrometer OPTIMA 7000DV (Perken Emler). Firstly, the materials were dissolved in HCl 1:1 (v/v %) or HCl:HNO_3 3:1 (v/v %) solution. Then a calibration curves were drown using a series of calibration standard solutions in the same acidic matrix as the unknown solutions. All measurements were carried out on emission peaks at λ_{Co} = 238.89 nm, λ_{Fe} = 259.94 nm, λ_{Cu} = 327.39 nm, λ_{Ag} = 328.07 nm and λ_{Au} = 367.59 nm.
- **Dynamic light scattering spectroscopy** (DLS) and **Zeta potentional** analysis were used to estimate the size and charge of NPs. These investigations were done using a Nicomp 380 ZLS particle sizing systems (PSS-Nicomp) at a NPs concentration of 0.1 mg mL^{-1}, which were dispersed in 1 mmol L^{-1} NaCl. The pH was adjusted with 0.1 mol L^{-1} HCl or NaOH respectively.
- **Magnetization measurements** were conducted using the vibrating sample magnetometer calibrated by Ni sample of similar dimensions as the studied sample of NPs placed in the plastic tube. The magnetometer was composed of the vibrator, lock-in-amplifier and electromagnet. The magnetic field was measured by the teslameter FH 54 (Magnet-Physics Dr. Steingrover GmbH).
- **Confocal microscopy** was used in order to investigate *C. parapsilosis* cells structure before and after incubation with cobalt ferrite NPs. The photographs were obtained using the confocal scanning laser microscope Nicon eclipse TE2000 C1 Plus (Plan Apo VC, Nikon) equipped with argon laser for 488 nm excitation. Image acquisition was done by utilizing the FV10-ASW1.6 imaging software. Laser scanning was controlled by the Nikon EZ-C1 software. The images were further processed using the EZ-C1 Bronze version 3.80 (Nikon).

3. RESULTS AND DISCUSSION

3.1. Formation, characterization and antimicrobial activity of Cu_2O/TiO_2 Cu_2O/TiNT and CuO/Cu heterostructures

3.1.1. Composition and morphology of heterostructured coatings

In this study, the thermally oxidized Ti surface was decorated with numerous Cu_2O polycrystals *via* AC deposition way from the slightly acidic aqueous Cu (II) acetate solution (pH ~ 5.28) at a constant potential $U_{p\text{-}to\text{-}p}$ = 1.3 V. The morphology of deposited products was assessed by SEM, thus confirming the pyramidal and bi-pyramidal shaped Cu_2O formation on the TiO_2/Ti substrate, as represented in Fig. 20 (a, b, c, d).

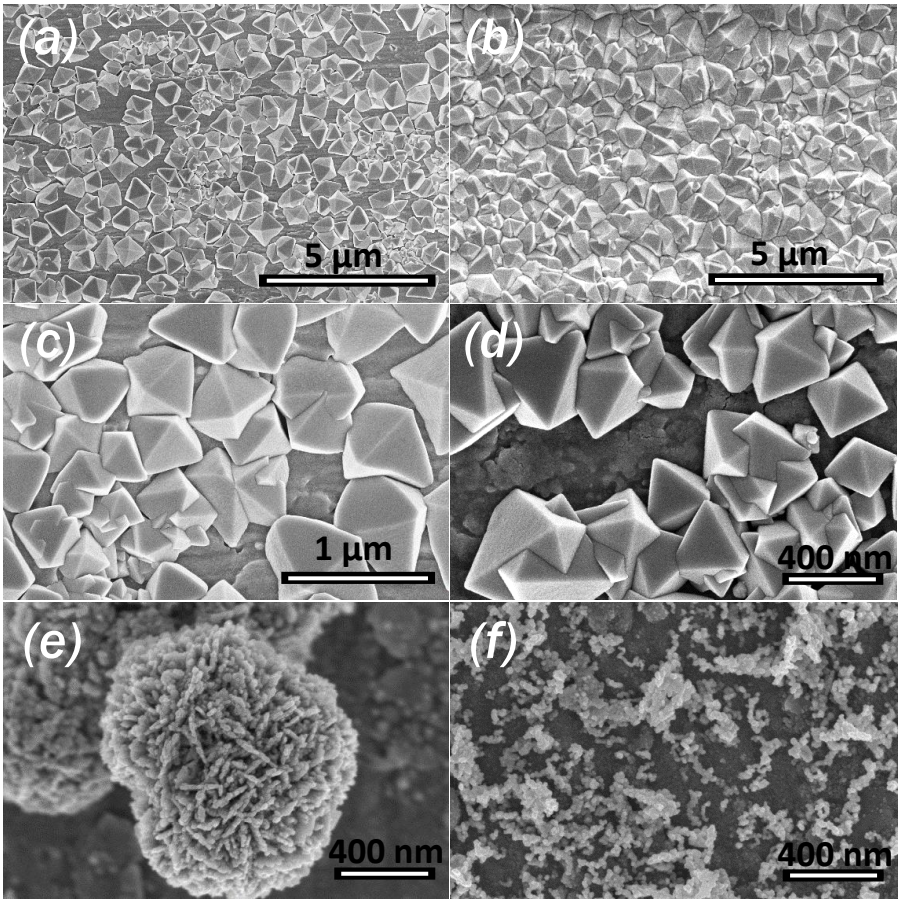

Figure. 20 Top side SEM views of crystallites formed onto thermally oxidized Ti substrate by AC deposition at $U_{p\text{-}to\text{-}p}$ = 1.3 V mode for 10 min in the copper acetate electrolyte kept at the pH: (a, b, c, d) 5.28; (e) 7.0 and (c) 10.0.

The size and shape of deposited Cu_2O species was approximately 200 - 400 nm, which depends on the pH of electrolyte and AC deposition conditions such as $U_{p\text{-}to\text{-}p}$ value, AC frequency or deposition time. Similar trends are observed by varying only a deposition time, resulting in partial (Fig. 20 a, c, d) or complete (Fig. 20 b) coverage of thermally oxidized Ti surface with densely packed pyramidal-shaped Cu_2O crystallites. The most uniform coverage of TiO_2 substrate took place at 100 Hz AC frequency. The planar dimensions of the pyramidal crystals were found to be dependent mainly on the AC treatment time and $U_{p\text{-}to\text{-}p}$ value, attaining sub-micrometre size. It should be noticed, that such structures can be electrodeposited only from the slightly acidic (pH ~ 5.28) copper acetate solutions, whereas the coral-like structures are formed under the same conditions except the pH = 7.0 (Fig. 20 e). These structures consist of small, approximately 20-40 nm in diameter, ellipse shaped crystallites. Moreover, in the alkaline solutions, at pH = 10.0, the nanoparticulate species was found to be dominating after deposition.

Highly ordered, vertically packed TiO_2 nanotube arrays were fabricated *via* cost-efficient Ti anodization in an ethylene glycol electrolyte containing 0.3 % ammonium fluoride and 20 mL L^{-1} H_2O at 50 V for 40 min, as written in paragraph 2.2.1.

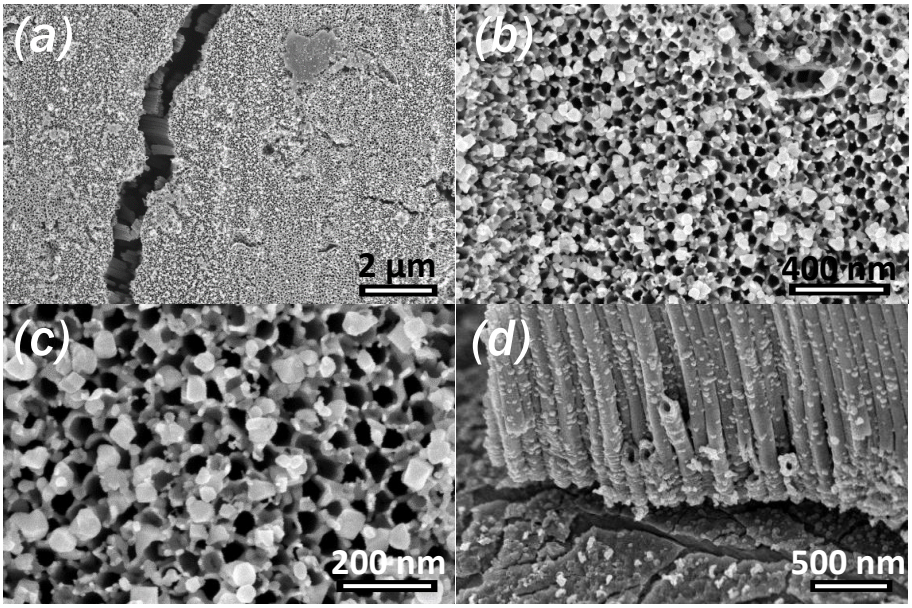

Figure. 21 Top side (a, b, c) and cross-sectional (d) SEM views of crystallites formed onto anodically oxidized Ti substrate by AC deposition regime of j_{ac} ~ 1.5 mA cm^{-2} and f_{ac} ~ 50 Hz for 5 min in the copper acetate electrolyte at pH = 5.28.

The formed TiNT film thickness was found to be from 4 to 6 μm with the inner 45-50 nm diameter of TiO_2 tubes (at the open end). As-grown nanostructured coating were calcined at 450 °C, leading to the polycrystalline anatase phase formation. Then, TiNT walls were decorated with numerous pure Cu_2O species, both inside and outside tubes (Fig. 21 d) under AC deposition at a constant j_{ac} ~ 1.5 mA cm^{-2} and f_{ac} ~ 50 Hz. The same copper acetate solution as for fabrication of Cu_2O/TiO_2 heterostructures was applied. After AC treatment the obtained heterostructures show the deposition of quite uniform, 15-50 nm in size Cu_2O species on the TiNT surface (Fig. 21 b, c). It was also determined that the size and amount of deposited material can be easily controlled by AC treatment duration and processing regime. However, the current density during deposition shouldn't be higher than j_{ac} ~ 3.5 mA cm^{-2}, otherwise TiNT films are destroyed in the corners at some sites of electrode and peeled off from the Ti substrate. As a result, pyramidal shaped Cu_2O crystals are formed in the damaged places, similar as reported in [113]. Unfortunately, the electrochemically fabricated Cu_2O/TiNT coatings have some fissures, caused by surface tension during the processing as clearly seen in Fig. 21 a.

Flake-shaped copper oxide films, possessing extremely high surface roughness, in this study were fabricated by copper anodization in highly alkaline electrolyte containing 8 mmol L^{-1} ammonium molybdate at the constant current density of 10 mA cm^{-2}. The as-prepared black electrodes demonstrated bundle-shaped flake structures with predominant vertical orientation of the flakes (Fig. 22 a, b).

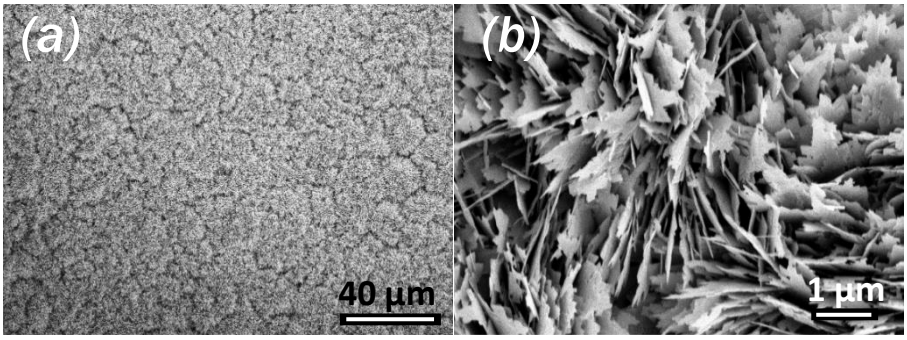

Figure. 22 Top side SEM views of anodically oxidized copper electrode at different magnification.

The planar dimensions of the flakes varied from several tens to several hundreds of nanometres, whereas thickness is just several nanometres. It should be noted, that the CuO coatings consist of two layers: rather compact at base side and more loosely packed at the upper one. The whole CuO layer thickness formed on the Cu substrate varied between 6 and 7 μm resulting in

an extremely high surface area formation, which is 825 ± 20 % higher than reported in [114].

3.1.2. Research on the Cu_2O electrodeposition onto the TiO_2 and TiNT substrates

In order to optimize Cu_2O electrodeposition process on the thermally and anodically oxidized Ti surfaces, the dependences on the amount of reduced Cu during AC treatment were investigated by ICP-OES. Results of this study are shown in Fig 23.

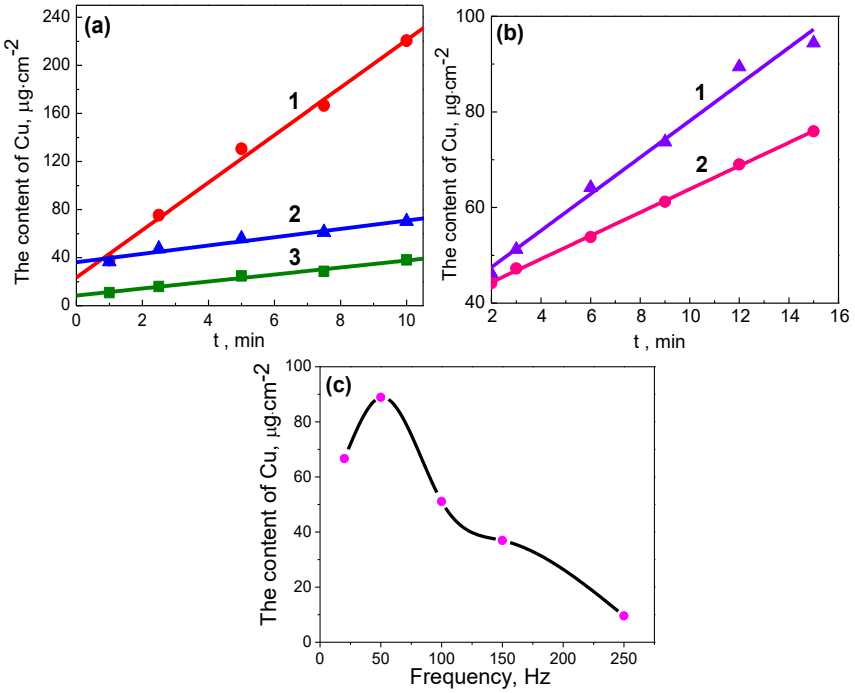

Figure. 23 Linear regressions of the content of deposited cooper suboxide species onto the anodically (a) and thermally (b) oxidized Ti substrates at different AC treatment regime: (a) at f_{ac} ~ 50 Hz and a constant peak-to-peak voltages ($U_{p\text{-}to\text{-}p}$): 1, 2 – 1.8 V; 3 – 1.2 V; (b) 1st at f_{ac} ~ 50 Hz and 1.3 V, whereas 2nd at f_{ac} ~ 100 Hz and 1.3 V. TiNT film was grown in the ethylene glycol and F^- ions containing electrolyte at 50 V for 40 min with (1,3) or without (2) decreasing the voltage down to 30 V at a 1.0 V min^{-1} rate. In (c) the dependency of deposited copper at $U_{p\text{-}to\text{-}p}$ = 1.3 V for 10 min on the AC frequency.

In this way, it was determined that the deposition rate of coper suboxide depends on the $U_{p\text{-}to\text{-}p}$ value allowing us simple control of the amount of deposited material. Note that AC processing at the constant potential of 1.8 V for 10 min leads to more than five times higher amount of deposited Cu_2O on TiNT in comparison with a specimen prepared at 1.2 V. These differences can be attributed to the higher current, which flows during electrodeposition

(i_{ac} ~ 30 mA). It is also clearly seen that the decrease of anodization voltage at the end of TiNT fabrication results in a significant deposition rate increase (Fig. 23 a). Similar results were obtained during the electrodeposition of Cu_2O on the thermally oxidized Ti electrodes (Fig. 23 b). It is notable that in comparison with Cu_2O/TiO_2 electrode, Cu_2O/TiNT exhibited a wider linear regression. In the case of Cu_2O/TiO_2, a linear amount of deposited Cu_2O was observed from 2 to 14 min, thus showing that controllable process started from 2 min, what leads to the uniform growth of crystals over the all electrode surface. The dependency of the amount of Cu_2O electrodeposited on TiO_2 *via* AC treatment frequency was studied too in the same bath under $U_{p\text{-}to\text{-}p}$ ~ 1.3 V for 10 min. It was found, that most uniform deposition was achieved using 100 Hz of AC freaquency (Fig. 23 b, curve 2), whereas some higher deposition rates were observed at 50 Hz frequency as shown in Fig. 23 c. It is notable that randomly dispersed Cu_2O crystals can be formed at up to 250 Hz AC frequency.

3.1.3. Phase analysis of Cu_2O/Ti, Cu_2O/TiNT and CuO/Cu coatings

The phase analysis of synthesized nanostructured Cu_2O/TiO_2, Cu_2O/TiNT and CuO/Cu coatings were assessed by XRD and Raman spectroscopy. XRD investigations (Fig. 24, a) revealed that as-grown and calcined TiNT films are comprised of pure crystalline anatase (PDF: 00-021-1272). As can be seen in Fig. 24 a and b, both XRD patterns contain several obvious diffraction peaks at 2θ positions of 29.58, 36.42, 42.32, 61.46 and 73.60 degrees that, according to PDF card no 01-078-2076, can be attributed to (110), (111), (200), (220) and (311) planes of the cubic phase cuprous oxide, confirming that electroreduced species on the thermally and anodically oxidized Ti surface are polycrystalline Cu_2O.

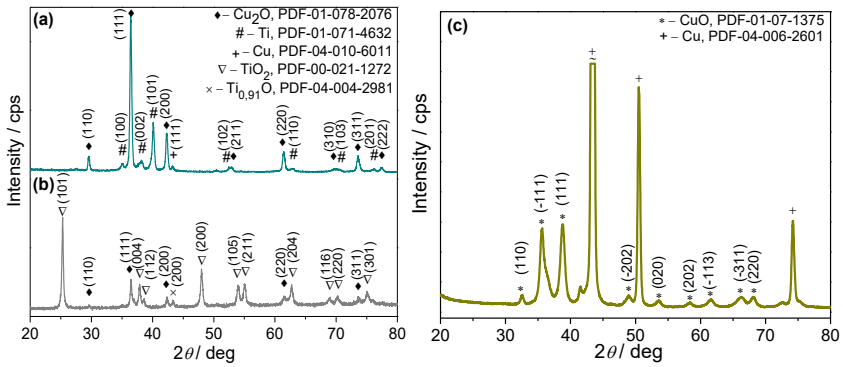

Figure. 24 Typical XRD patterns of Cu_2O/TiNT (a), Cu_2O/TiO_2 (b) and CuO/Cu (c) coatings formed by AC treatment in copper acetate electrolyte (a, b) and Cu anodization (c).

It is also obvious that the preferred orientation of Cu_2O species is (111). The size of Cu_2O crystallites calculated by Halder-Wagner approximation was found to be dependent on the conditions of electrode position varying within 32-45 and 65-85 nm ranges for Cu_2O species deposited inside TiNT and on the TiO_2 substrate, respectively. No significant peaks, that can be indexed as CuO or $Cu(OH)_2$ were detected, although two small diffraction peaks at 2θ positions around 43.3 and 50.4 degree could be linked with the presence of some Cu^0 onto the heat-treated Ti surface.

Anodically oxidized and calcined at 250 ℃ copper specimen was further examined by XRD, which confirmed, that black material are polycrystalline monoclinic tenorite phase – CuO. As can be seen in Fig. 24 c, XRD patterns contain diffraction peaks at 2θ positions of 32.35, 35.56, 38.78, 48.94, 53.63, 58.42, 61.53, 66.13 and 68.24 degree that, according to PDF card no 01-07-1375, can be attributed as (110), (-111), (111), (-202), (020), (202), (-113), (- 311) and (220) planes of the monoclinic phase of copper oxide. It is notable, that diffraction peaks of anodically formed CuO was slightly wider, caused by less crystalline phase of material. No diffraction peaks, that can be attributed to Cu_2O or $Cu(OH)_2$ were detected in this study.

The Raman spectra obtained from the both surfaces looked differently, however, the spectra analysis results are in agreement with those obtained by XRD. Fig. 25 (A) compares the Raman spectra of the Cu_2O/TiNT coatings before and after electrodeposition of Cu_2O species.

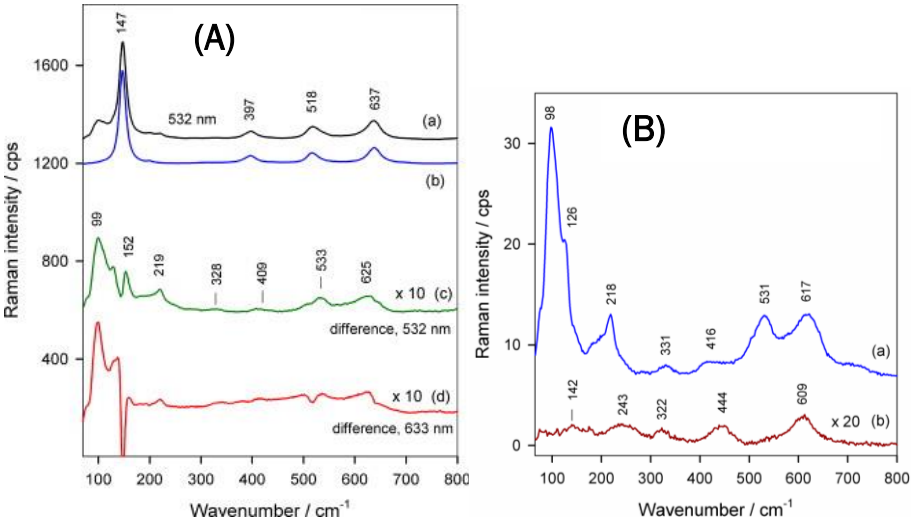

Figure. 25 Raman spectra of Cu_2O/TiNT (A) and Cu_2O/TiO_2 (B) coatings. In (A): the Raman spectra of Cu_2O/TiNT (a), pure TiNT (b) and the difference spectra (c) and (d). In (B): Raman spectra of Cu_2O/TiO_2 (a) and pure heat-treated Ti (b). Spectra were recorded using laser beam with an excitation wavelengths equal to 532 nm (a, b, c) and 633 nm (d).

Strong Raman bands at 147, 397, 518 and 637 cm^{-1} are characteristic of crystalline anatase TiO_2 structure [115]. The dominant band at 147 cm^{-1} are attributed to $E_g(1)$ Raman-active mode, while the peaks at 397 and 637 cm^{-1} belong to $B_{1g}(1)$ and $E_g(3)$ eigenmodes, respectively [116]. The peak near 518 cm^{-1} is composed of two eigenmodes, $B_{1g}(2)$ and A_{1g}, which can be distinguished at lower temperatures. The difference spectrum (Fig. 25 A: c and d) clearly demonstrated several peaks associated with copper oxygenous compounds. In detail, the bands at 219, 533 and 625 cm^{-1} evidenced the presence of Cu_2O phase [117]. The comparison of Raman spectra obtained with 532 and 633 nm excitations showed some enhancement of Cu_2O bands with lower wavelength excitation. The Raman spectrum of pure thermally oxidized Ti substrate corresponds to the rutile TiO_2 phase with characteristic E_g and A_{1g} modes at 444 and 609 cm^{-1}, respectively. Bands at 98, 215, 531 and 617 cm^{-1} according to [117] evidenced the presence of Cu_2O. No evidence for the presence of CuO phase was observed by Raman spectroscopy. Usually, the most intense Raman band of CuO appears near 296 cm^{-1} [118]. No such peak was obtained during this analysis.

3.1.4. Antimicrobial activity of Cu_2O/TiO_2, Cu_2O/TiNT and CuO/Cu coatings

Antimicrobial assessment of the fabricated Cu_2O/TiO_2, Cu_2O/TiNT and CuO/Cu heterostructures were tested against prokaryotic (*E. coli*, *P. aeruginosa*, *M. luteus*) and eukaryotic (*S. cerevisiae*, *A. versicolor*, *P. chrysogenum*, *C. cladosporioides*, *C. parapsilosis*, *C. krusei*) microorganisms using zone inhibition method. Briefly, disc-shaped electrodes were placed gently on a lawn of microbes in sterile Sabouraud and Nutrient agar plates. Antimicrobial characteristics were evaluated by determination of clear zone around the specimens after 48 hours as described previously. All assays were carried out in triplicate. The obtained results are presented in Table 4. The antimicrobial activity results revealed that the pyramidal-shaped Cu_2O crystals electrodeposited on TiO_2 and TiNT substrates acted as the excellent antimicrobial agents against almost all tested fungi and bacteria species. Furthermore, these coatings provide the inhibitory effect, which was indicated mostly as fungicidal or bactericidal. However, it should be noticed, that in the case of Cu_2O/TiO_2 a fungistatic effect was observed for *A. versicolor* and *C. parapsilosis* fungi, whereas in the case of Cu_2O/TiNT the fungistatic effect was obtained in the Petri dishes with *A. versicolor*, *C. parapsilosis* and *C. krusei* lawns (Fig. 26 c and d). Both coatings exhibited no antimicrobial behaviour on *P. chrysogenum* and *C. cladosporioides* microbes. However, CuO/Cu based coatings demonstrate surprisingly stronger antimicrobial activity against all tested microbes, except

P. chrysogenum fungi. Enhanced antimicrobial potency of flake-shaped CuO can be attributed to significantly higher surface area, thus leading the higher amount of ion dissolved from the surface. Moreover, this coating effected *A. versicolor* and *C. cladosporioides* cells two times more than 50 μg itraconazole – commercial antimicrobial drug, which exhibit fungicidal zone approximately 5-4 mm (Fig. 27 A).

Table 4. Qualitative analysis of Cu_2O/TiO_2, Cu_2O/TiNT and CuO/Cu coatings

Microorganism	Specimens	Disc potency, μg	Diameter of disc (d), mm	Diameter of zone (z), mm	z/d
S. cerevisiae[a]	Cu_2O/TiNT	33	14	25	1.8±0.1
	Cu_2O/TiO_2	114	14	27	1.9±0.1
	CuO/Cu	∞	14	32	2.3±0.1
	Cu	∞	14	27	1.9±0.2
	Fluconazole	100	6	17	2.8±0.1
A. versicolor[b]	Cu_2O/TiNT	33	14	19	1.3±0.2
	Cu_2O/TiO_2	114	14	24	1.7±0.2
	CuO/Cu	∞	14	26	1.9±0.2
	Cu	∞	14	-	-
	Itraconazole	50	6	11	1.8±0.1
P. chrysogenum[c]	Cu_2O/TiNT	33	14	-	-
	Cu_2O/TiO_2	114	14	-	-
	CuO/Cu	∞	14	-	-
	Cu	∞	14	-	-
	Itraconazole	50	6	10	1.7±0.1
C. cladosporioides[d]	Cu_2O/TiNT	33	14	-	-
	Cu_2O/TiO_2	114	14	-	-
	CuO/Cu	∞	14	24	1.7±0.2
	Cu	∞	14	-	-
	Itraconazole	50	6	10	1.3±0.1
C. parapsilosis[e]	Cu_2O/TiNT	33	14	17	1.2±0.1
	Cu_2O/TiO_2	114	14	18	1.3±0.1
	CuO/Cu	∞	14	24	1.7±0.2
	Cu	∞	14	-	-
	Fluconazole	100	6	25	4.2±0.2
C. krusei[f]	Cu_2O/TiNT	33	14	18	1.3±0.1
	Cu_2O/TiO_2	114	14	-	-
	CuO/Cu	∞	14	20	1.4±0.1
	Cu	∞	14	-	-
	Fluconazole	100	6	14	2.3±0.1
P. aeruginosa[g]	Cu_2O/TiNT	33	14	25	1.8±0.2
	Cu_2O/TiO_2	114	14	24	1.7±0.1

	CuO/Cu	∞	14	24	1.7±0.1
	Cu	∞	14	20	1.4±0.1
	Streptomycin	100	6	18	3±0.1
	Cu_2O/TiNT	33	14	15.5	1.1±0.1
	Cu_2O/TiO_2	114	14	15.5	1.1±0.1
E. coli[h]	CuO/Cu	∞	14	18	1.3±0.1
	Cu	∞	14	-	-
	Streptomycin	100	6	17	2.8±0.1
	Cu_2O/TiNT	33	14	16	1.1±0.1
	Cu_2O/TiO_2	114	14	17	1.2±0.1
M. luteus[i]	CuO/Cu	∞	14	19	1.3±0.2
	Cu	∞	14	17	1.2±0.1
	Streptomycin	100	6	17	2.8±0.1

a-f cultivated in Sabouraud CAF agar at 27 °C;

g-i cultivated in Nutrient agar at 36 °C.

It is worth mentioning, that all coatings and even a pure copper foil inhibited *S. cerevisiae* microbes fungicidally, with clear zone as long as 10 - 18 mm (Fig. 26 b). If compare the antimicrobial activity of Cu_2O/TiO_2 with Cu_2O/TiNT coating, some slightly stronger fungicidal effect are characteristic for Cu_2O on the rutile electrodes. This effect might be related to almost 3.5 times higher amount of Cu_2O on the titanium oxide surface.

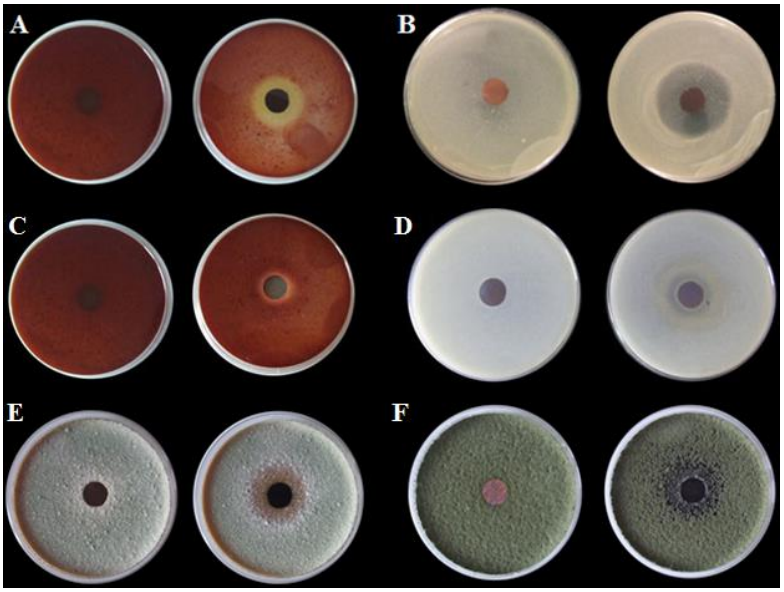

Figure. 26 Inhibition zone produced by copper oxide-based coatings 1st row – Cu_2O/TiO_2, 2nd row – Cu_2O/TiNT, 3rd row – CuO/Cu against eukaryotic microbes: A, C, E – *A. versicolor*, B – *S. cerevisiae*, D – *C. krusei* and F – *C. cladosporioides*. In the left side – control specimen.

The antimicrobial efficiencies of copper oxides based coatings on various substrate were also assessed against typical gram-negative (*E. coli* and *P. aeruginosa*) and gram-positive (*M. luteus*) bacteria. The obtained results are presented in Table 4. Note that *P. aeruginosa* was found to be more sensitive for all proposed coatings: the average inhibition zone in this bacteria lawn was 1.5 to 1.6 times wider than in the *E. coli* or *M. luteus* bacteria lawns (Fig. 28 b, c and f).

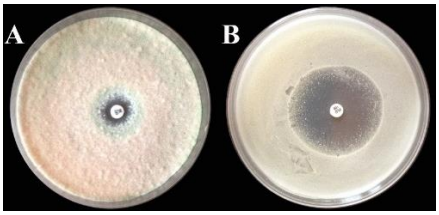

Figure. 27 Inhibitory activity of itraconozole (a) and flucanozole (b) against *A. versicolor* (a) and *C. parapsilosis* (b) microbes.

It is notable, that pure copper electrode also exhibit antimicrobial activity against *P. aeruginosa* and *M. luteus* microbes. However, this effect is 2 times weaker in comparison with Cu_2O inspired by microorganism inactivation. Moreover, in the way with prokaryotic organisms CuO/Cu coatings demonstrate similar antibacterial activity as Cu_2O-based coatings. Besides that, all proposed coatings exhibit 2 times lower bactericidal effect in comparison with streptomycin – commercial antibiotic used as a positive control in this study.

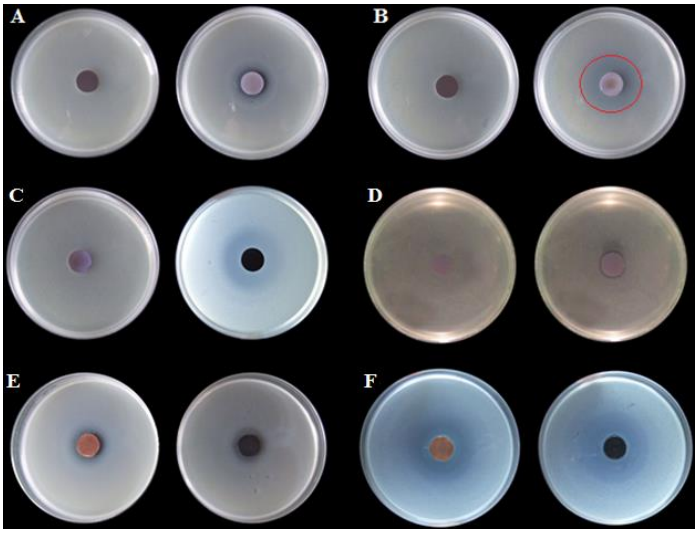

Figure. 28 Inhibition zone produced by copper oxide-based coatings 1st row – Cu_2O/TiO_2, 2nd row – Cu_2O/TiNT, 3rd row – CuO/Cu against prokaryotic microbes: A, E – *M. luteus*, B, C, F – *P. aeruginosa* and D – *E. coli*. In the left side – control specimen.

Recently, Li et al., reported, that spherical and cubic shaped Cu_2O NPs does not affect *E. coli* bacteria strains [119]. On the other hand, as published by Ren et al., [120] Cu_2O octahedral single crystals bounded as facets, as in this study, exhibited higher *E. coli* killing efficiency than cubic ones. It was hypothesized, that efficient antimicrobial activity of the Cu_2O species attached on TiO_2 or TiNT substrate could be linked to the semiconducting properties of cuprous oxide capable of absorbing visible light and through synergetic coupling with titanium oxides, which resulting the production of ROS such as OH^- or H_2O_2 [121].

3.2. Fabrication of extremely thin and flexible food packaging aluminium foil with enhanced antimicrobial behaviour

3.2.1. Morphology of AAO encapsulated with Ag nanowires coatings

In order to provide a decorative and protective finish of aluminium or aluminium alloys, they are usually anodized in an aqueous 180-200 g L^{-1} sulphuric acid electrolyte at a constant potential of ~ 17-18 V, resulting in AAO growth rate approximately equal to 0.4 μm min^{-1}. However, in case of the food packing, this layer should be no more than 1 μm, while retaining the AAO elasticity, which is particularly crucial for packaging materials.

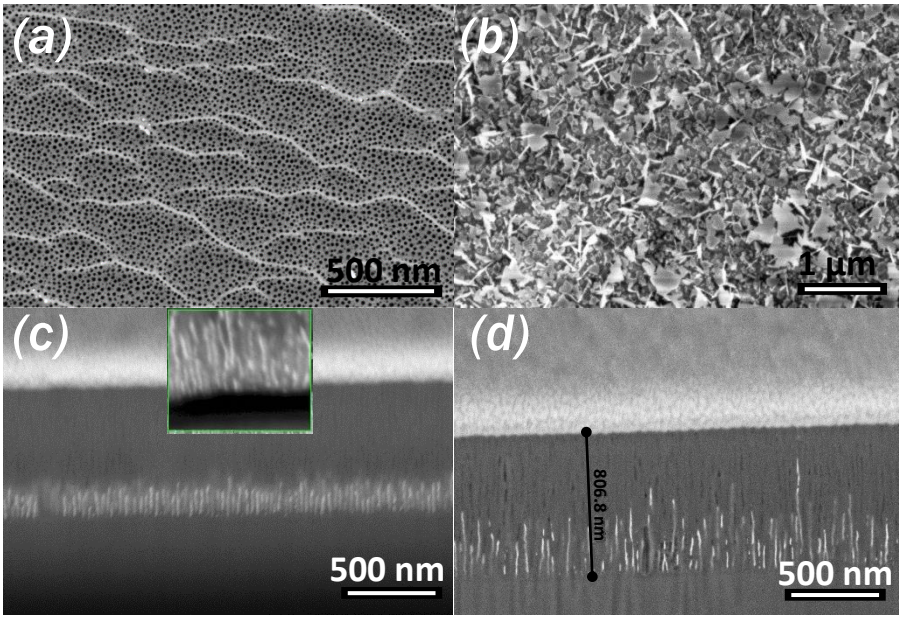

Figure. 29 Top side (a, b) and cross-sectional (c, d) SEM views of 0.8 μm thick porous alumina film before (a) and after AC deposition of Ag at a constant $U_{p\text{-}to\text{-}p}$ potential of 7 V mode for 40 (c), 150 (d) and 600 s (b).

To achieve a good flexibility of fabricated coatings, in this study short-time Al anodizing at the lower bath concentrations and voltages, namely at 1.2 mol L^{-1} of H_2SO_4 and 10 V, respectively, have been chosen. Such porous AAO films consist of approximately (1.5-1.7) × 10^{11} pores cm^{-2}, which are densely packed and oriented perpendicularly to the surface, as represented in Fig. 29 a. The prepared AAO/Al coatings were assessed *via* SEM, which confirms formation of porous anodic oxide with an average pore diameter of 10 ± 0.5 nm and a pore length of ~ 0.8 μm ± 10 nm (Fig. 29 a, d). Fig. 29 c and d depicts Ag nanowire encapsulated in AAO matrix using AC deposition method. The mean size of the Ag crystallites was found to be 8-10 nm – similar to those of aluminium pores. The deposition of Ag nanowires at the bottom of AAO pores was started from ~ 1.5 mA cm^{-2} current density. The cross-sectioned SEM observations indicated that at the range of 1.5 to 3.0 mA cm^{-2} AC current density the most alumina pores were filled to a height of ~ 200-250 nm. If the deposition further continue, an uneven growth of Ag nanowires prevailed (Fig. 29 d). Further AC treatments lead the deposition of Ag onto the film surface, covering it with different in size and shape Ag^0 crystals (Fig. 29 b).

3.2.2. The amount of deposited Ag in the porous AAO and their phase investigations

The phase analysis of synthesized Ag/AAO/Al coatings were assessed by XRD (Fig. 30, a), which revealed that fabricated coatings are comprised of Ag nanowires within the alumina pores and exhibit a polycrystalline structure (PDF: 00-021-1272) with the prevailing orientation along (110) direction. It should be noticed, that XRD patterns looked noisy, due to amorphous phase of aluminium oxide matrix.

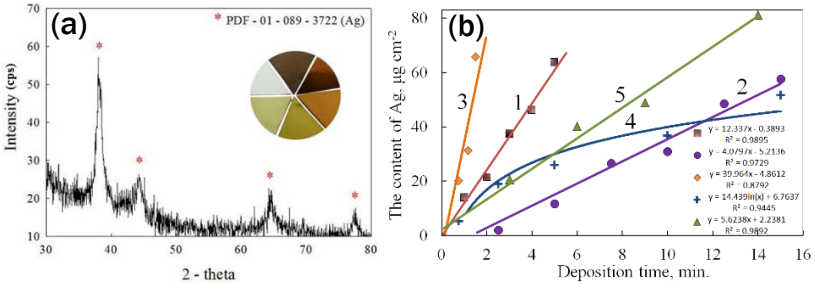

Figure. 30 Typical XRD patterns (a) of porous alumina films decorated with Ag nanowire arrays from the solution containing 10 mmol L^{-1} $AgNO_3$ and 50 mmol L^{-1} $MgSO_4$. In (b) the linear and exponential regressions of the content of deposited Ag species into anodically oxidized alumina at AC current densities (mA cm^{-2}): 1.5 (2), 2.0 (1, 5), 3.0 (3) and at the constant potential of $U_{p\text{-}to\text{-}p}$ ~ 7 V ± 0.3 V (4). *Insets:* Diagram of the alumina colours obtained by Ag electrodeposition.

In order to optimize the deposition of metallic Ag nanowires into AAO matrix with a thickness of ≤ 1.0 μm and their Ag-amount dependent multi-coloured properties, the dependence of the amount of reduced Ag *versus* AC treatment time was investigated by ICP-OES. The results of this study are shown in Fig. 30 b. It was found, that at a constant AC current density j_{ac} within the range from 1.5 to 3.0 mA cm^{-2}, the electrodeposition of Ag nanowires inside the alumina pores proceeds at a constant rate strongly depending on the j_{ac} value, while increasing of the j_{ac} resulted in an increase of Ag deposition rate. It is notable, that no Ag deposition was obtained at the lower than 1.5 mA cm^{-2} current density. Furthermore, at the current densities lower than 2.0 mA cm^{-2}, the deposition started after some time (0.5-2.5 min) possibly required to re-organize the high-resistant barrier layer of AAO at the film oxide interface [122]. One unanticipated finding was that deposition of Ag inside the pores with small thickness (0.8 μm) at a constant current density, ca. j_{ac} ~ 2.0 mA cm^{-2}, proceeds at a significantly higher rate (Fig. 30 1st curve) than in the thicker pores of the same diameter Ø ~ 10 nm (Fig. 30 5th curve).

An increase in the amount of deposited Ag inside the pores of an extremely thin AAO film results in the changes of the film colour from light gold to bright brown as shown in Fig. 30 insets. It was observed, that at the lower AC current densities, the obtained coatings demonstrated more uniform colour distribution around all electrode surface. Besides that, at the potentiostatic regime and a constant AC voltage of $U_{p\text{-}to\text{-}p}$ ~ 7 V the filling of alumina pores proceeds at a decreasing deposition rate (Fig. 30 4th curve), indicating that the longer AC treatment times than at a constant j_{ac} are required for deposition of the same amount of Ag. These results suggested that the potentiostatic regime is more suitable for achieving uniform colouring of alumina films in the same tint.

3.2.3. Antimicrobial activity of flexible aluminum foil decorated with Ag nanowires

Antimicrobial assessment of fabricated Ag/AAO/Al coatings were further tested against prokaryotic (*E. coli*, *M. luteus*) and eukaryotic (*S. cerevisiae*, *A. fumigatus*, *G. candidum*, *C. parapsilosis*) microorganisms using zone inhibition and quantitative methods. Firstly, antimicrobial activity of Ag nanowires encapsulated inside AAO pores was carried out with *S. cerevisiae* colonization in the liquid YEPD media in the presence and absence of Ag-in-alumina pellets. Some samples containing defined amount of Ag, namely 5.22, 19.00 and 33.33 μg cm^{-2} were sealed in the boiling water, thus comparing them with unsealed ones. Similar tests were performed by incubation of *S. cerevisiae* cells in the solutions containing 1.0, 2.5 and 5.0 ppm of Ag^{+} ions, Ag coated alumina film pellets and pure alumina films, which act as a negative

control. It should be noticed, that after exposure with the tested materials, the percentage of viable yeast cells were estimated by quick staining with the methylene blue dye method [123]. The alive yeast cells contain an enzyme, which capable easily decolourise methylene blue, contrariwise as the dead cells, which are stained blue as represented in Fig. 31.

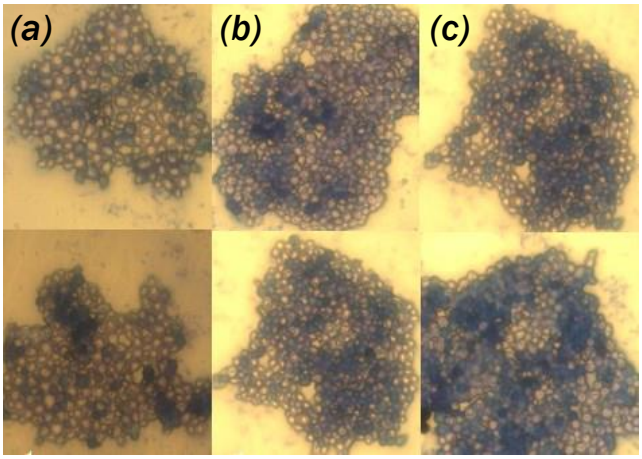

Figure. 31 Optical microscopy images of *S. cerevisiae* cells after 1 (a), 5 (b) and 25 h incubation with Ag modified AAO electrodes (Ag loading of 19 μg cm^{-2}) in liquid YEPD media after exposure with methylene blue dye.

The quantitative analysis results obtained from antimicrobial activity assays against *S. cerevisiae* are represented in Fig. 32. It was found that if Ag was fully encapsulated into the pores of AAO film (sealed) antimicrobial activity was insignificant and independently of the content of encased Ag (Fig 32 A). These observations could be explained by the slow or complicated Ag^+ ions diffusion through the surface layer of the sealed alumina film.

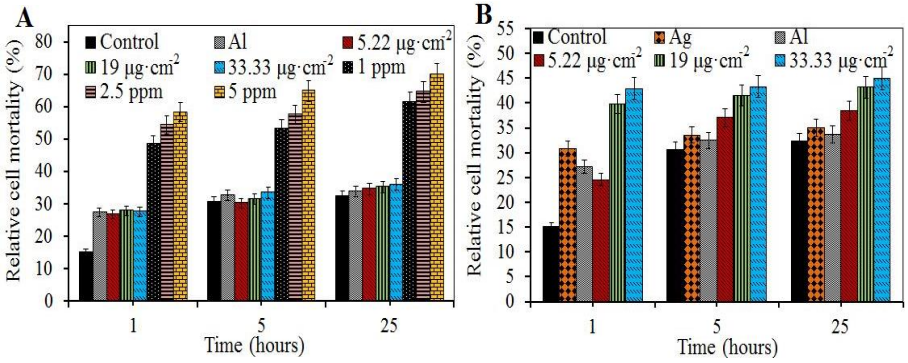

Figure. 32 Antimicrobial activities of the various as-grown (B) and sealed (A) Ag in alumina specimens after 1, 5 and 25 h incubation in YEPD medium with *S. cerevisiae* yeasts. Error bars represent the standard deviation.

Meanwhile, unsealed Ag/AAO/Al coatings exhibited antimicrobial efficiency, which dependent on the content of deposited Ag nanowires. It is

notable, that metallic Ag decorated AAO species demonstrate higher inhibitory activity towards *S. cerevisiae* than Ag coated AAO film with the same geometric area. These results match well those obtained by other studies, which indicate that antimicrobial activity of nanostructured particles, such as Fe_3O_4 [124], ZnO [125], MgO [126] or Ag^0 [127] increased with decreasing the particle size. As can be seen in Fig. 32 A, even the lowest concentration of Ag ions (~ 1 ppm) shows a strong antimicrobial activity by killing a half of yeast cells during the *in vitro* assay. However, this effect was expected and well known. Besides that Ag^+ ions-based solutions have been long used in healthcare as wider described in paragraph 1.2.1.

The comparable results were obtained using the inhibition zone tests against such bacteria, yeasts and fungi cells that are prevailing in the human's environmental, especially on a wide variety of food products. The obtained results are presented in Table 5.

Table 5. The results of qualitative antimicrobial behaviour of as deposited Ag nanowire arrays in alumina pores and Ag^+ ions.

Microorganism	Specimens	The content of Ag^0, μg cm^{-2} or $[Ag^+]$	Effect	Inhibition zone, mm
A. fumigatus[a]	Ag/AAO/Al	5.22	-	-
		19	Fungistatic	19-24
		33.33	Fungistatic	21-24
	Ag/AAO/Al*	5.22	-	-
		19	-	-
		33.33	-	-
	$AgNO_3$	1-5 mg L^{-1}	Fungicidic	1.5
C. parapsilosis[b]	Ag/AAO/Al	5.22	-	-
		19	-	-
		33.33	-	1.5
	Ag/AAO/Al*	5.22	-	-
		19	-	-
		33.33	-	-
	$AgNO_3$	1-5 mg L^{-1}	-	-
G. candidum[c]	Ag/AAO/Al	5.22	-	-
		19	Fungistatic	15-36
		33.33	Fungistatic	21-25
	Ag/AAO/Al*	5.22	-	-
		19	-	-
		33.33	-	-
	$AgNO_3$	1-5 mg L^{-1}	-	-
E. coli[d]	Ag/AAO/Al	5.22	-	-

		19	Bactericidal	3
		33.33	Bactericidal	2-4
		5.22	-	-
	Ag/AAO/Al*	19	-	-
		33.33	-	-
	$AgNO_3$	1-5 mg L^{-1}	-	-
		5.22	Bactericidal	1.7
	Ag/AAO/Al	19	Bactericidal	2.1
		33.33	Bactericidal	2.5
M. luteus[e]		5.22	-	-
	Ag/AAO/Al*	19	-	-
		33.33	-	-
	$AgNO_3$	1-5 mg L^{-1}	-	-

a-c cultivated in Sabouraud CAF agar at 27 °C;

d-f cultivated in Nutrient agar at 36 °C;

*- sealed Ag/AAO/Al samples.

It was found that all Ag^+ solutions exhibited a fungicidal effect against *A. fumigatus* lawns, whereas in the *C. parapsilosis*, *G. candidum*, *E. coli* and *M. luteus* lawns no inhibition zones were detected. Meanwhile, as-deposited Ag in the AAO samples demonstrated a wide zone of inhibition against *A. fumigatus* micromycetes (Fig. 33 b), if the films contained 33.33 μg cm^{-2} of Ag, thus suggesting the fungistatic activity for the Ag nanowires encased inside the thin AAO pores. Similar results has been obtained with *G. candidum* fungi and *M. luteus*, *E. coli* bacteria strains except the main difference of inhibitory effect (see Table 5), whereas *C. parapsilosis* yeast showed the resistance against all tested materials.

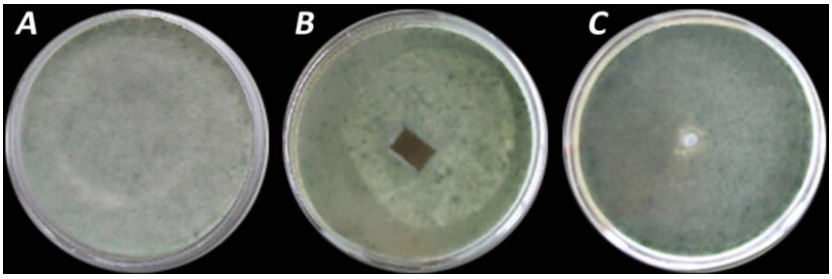

Figure. 33 Antimicrobial activities of Ag modified AAO electrodes and Ag^+ ions against *A. fumigatus* fungi: (a) – control, (b) Ag in alumina coating (with 33.33 μg cm^{-2} loading) and (c) 5 mg L^{-1} $AgNO_3$.

However, as expected, no inhibition of microorganism growth was seen for sealed (boiled electrodes in water for 30 min) Ag in AAO coatings against all tested bacteria and fungi species. This effect can be attributed to the lack of direct contact between microorganism and Ag phase, as well as the decreased content of the Ag ions diffusing through the compact alumina

surface layer. It is notable, that in the case with gram-negative *E. coli* bacteria strains the antimicrobial activity of as-proposed Ag in alumina coatings were approximately 1.4 – 1.6 times higher in comparison with those obtained with gram-positive *M. luteus* bacteria. These results are in accord with recent studies indicating that gram-negative bacteria species are more sensitive to Ag-based nanocomposite due to different cell wall structure [128].

3.3. Synthesis, characterization and antimicrobial activity of various $CoFe_2O_4$ NPs

In this study, the hydrothermal, co-precipitation and thermal decomposition methods were employed to synthesize different in size, shape, lattice composition or surface chemistry cobalt ferrite NPs as a new potential drug against microorganisms. In this chapter, the cobalt ferrite NPs morphology, surface chemistry, phase analysis magnetic properties and antimicrobial activity against a wide range of microbes such as *S. cerevisiae*, *C. parapsilosis*, *C. krusei*, *C. albicans*, *S. aureus*, and *E. coli* will be presented and compared thoroughly.

3.3.1. Morphology assessment of different in size, chemical composition and surface chemistry of $CoFe_2O_4$ NPs

Citrate stabilized, different in size cobalt ferrite NPs were synthesized by co-precipitation and hydrothermal methods as described previously (see paragraph 2.3.1.). Varying the synthesis conditions and separations 2, 5 and 15 nm of $CoFe_2O_4$@citrate NPs were synthesized from the complex-assisted alkaline solutions containing 45 mmol L^{-1} Co^{2+} and Fe^{3+} salts and 75 mmol L^{-1} citric acid, which was used as a chelating agent. The obtained products morphology were assessed by TEM and AFM techniques, thus confirming spherical shape of fabricated $CoFe_2O_4$@citrate NPs as shown in Fig. 34 c, f, i. The size distribution histograms of synthesized products were calculated from the AFM images, revealing their average diameter approximately equal to 1.65 (1^{st} row), 5.0 (2^{nd} row) and 15 nm (3^{rd} row). For more precise characterization, TEM analysis has been performed in this study. As can be seen in Fig. 34, the AFM analysis data match well the results obtained from the TEM observations, which shows quit narrow size distribution of $CoFe_2O_4$@citrate NPs with an average diameter similar to AFM established ones. Furthermore, the HR-TEM observations and EDX spectra of 15 nm-sized in diameter $CoFe_2O_4$ NPs, synthesized by hydrothermal way at 130 °C for 10 h, also confirmed formation of polycrystalline structure with atomic Co-Fe percentage ratio of 1:2 (Fig. 35).

In order to develop biocompatible magnetic cobalt ferrite NPs, possessing a narrow size distribution, L-lysine amino acid was applied as NPs growth and stabilizing agent in the hydrothermal synthesis conducted by a co-precipitation approach [129].

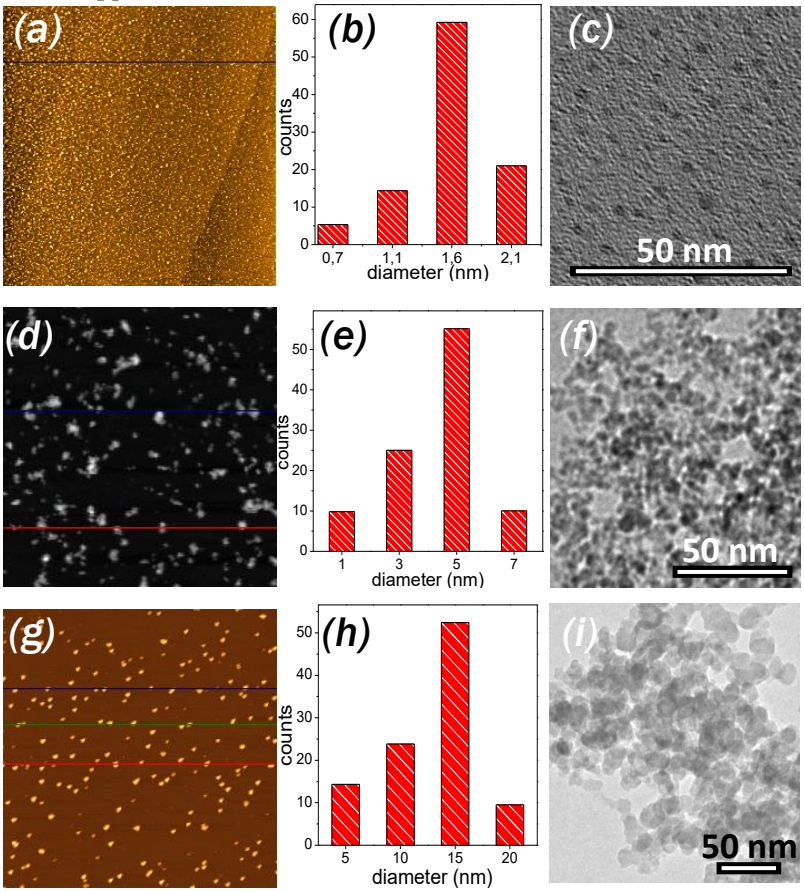

Figure. 34 Size distribution histograms (b, e, h) calculated from the presented AFM (a, d, g) and TEM (c, f, i) images of the synthesized $CoFe_2O_4$@citrate NPs in an average diameter of 1.65 (a), 5.0 (d) and 15.0 nm (g).

The aim of this synthesis, was to obtain similar size ~ 5-7 nm iron-substituted cobalt ferrite NPs labelled as $Co_xFe_{1-x}Fe_2O_4$@Lys, where x varies from 0.2 to 1.0. At this stage, attention was focused on determination the influence of cobalt content in the magnetic cobalt ferrite NPs on their antimicrobial efficiency against the eukaryotic and prokaryotic microbes. For comparison, similarly sized magnetite NPs were also formed under the same hydrothermal synthesis conditions from Fe^{2+}, Fe^{3+} and L-lysine precursors at 1:2 molar ratio. TEM observations of as-synthesized NPs demonstrated that Fe_3O_4@Lys, $CoFe_2O_4$@Lys and Fe-substituted cobalt ferrite NPs exhibit

mainly spherical shape with an average diameter 5.0-6.4 nm and quite narrow size distribution (Fig. 36 a, b, c).

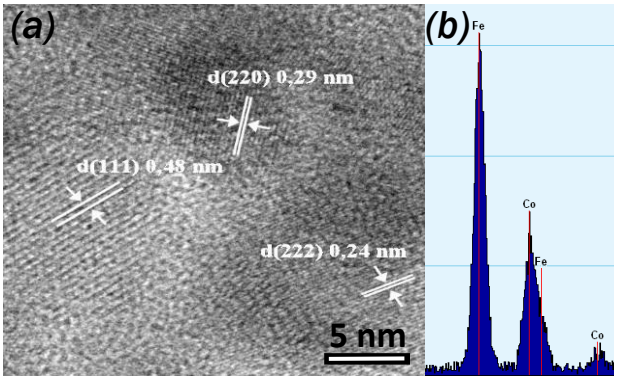

Figure. 35 HR-TEM image (a) and EDX spectra (b) of 15 nm sized $CoFe_2O_4$@citrate NPs synthesized by hydrothermal approach at 130 °C for 10 h.

High resolution TEM images clearly prove that the NPs grow with a lattice interatomic distance of 0.25 nm (Fig. 36 *Insets*). It is noteworthy, that according to analysis of numerous TEM images, the decrease in the cobalt content results in the formation of smaller NPs.

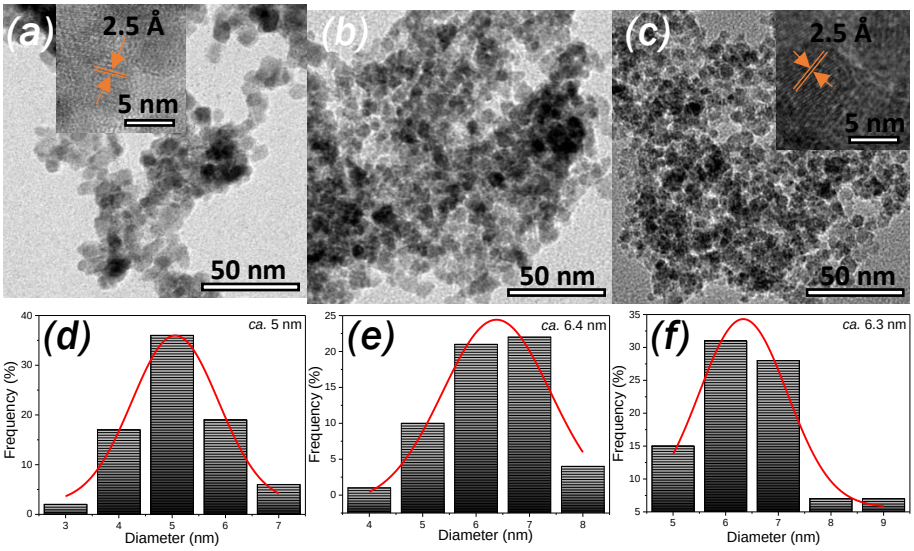

Figure. 36 TEM, HRTEM (*Insets*) images of fabricated transition metal-substituted cobalt ferrite NPs: (a) $Co_{0.2}Fe_{0.8}Fe_2O_4$@Lys, (b) $Co_{0.5}Fe_{0.5}Fe_2O_4$@Lys and (c) $CoFe_2O_4$@Lys and their size distribution histograms with the average diameter of (d) 5 nm, (e) 6.4 nm and (f) 6.3 nm.

Utilization of magnetic NPs in nanomedicine depends largely on their properties such as size, structure, shape, composition and nature of

stabilization shell. It is well known, that NPs usually are covered by organic or inorganic shell, thus increasing their stability and preventing agglomeration. However the NPs shell affect their antimicrobial properties, as reported by many scientists. For example, it has been reported recently that $CoFe_2O_4$ NPs capped with the folic acid and hematoporphyrin fragments are effective anticancer agent [130]. Inspired by such observations, in this work $CoFe_2O_4$ NPs with oleic acid shell were successfully synthesized by the thermal decomposition method and the effect of shell on their antimicrobial activity was studied. Furthermore, the size dependence of $CoFe_2O_4$@Ole NPs on their antimicrobial efficacy was also investigated and compared with $CoFe_2O_4$@Lys NPs. In comparison with $CoFe_2O_4$@Lys NPs, the uniformity and spacing of $CoFe_2O_4$@Ole NPs are individually more isolated as expected and can be seen in Fig. 37 a and d.

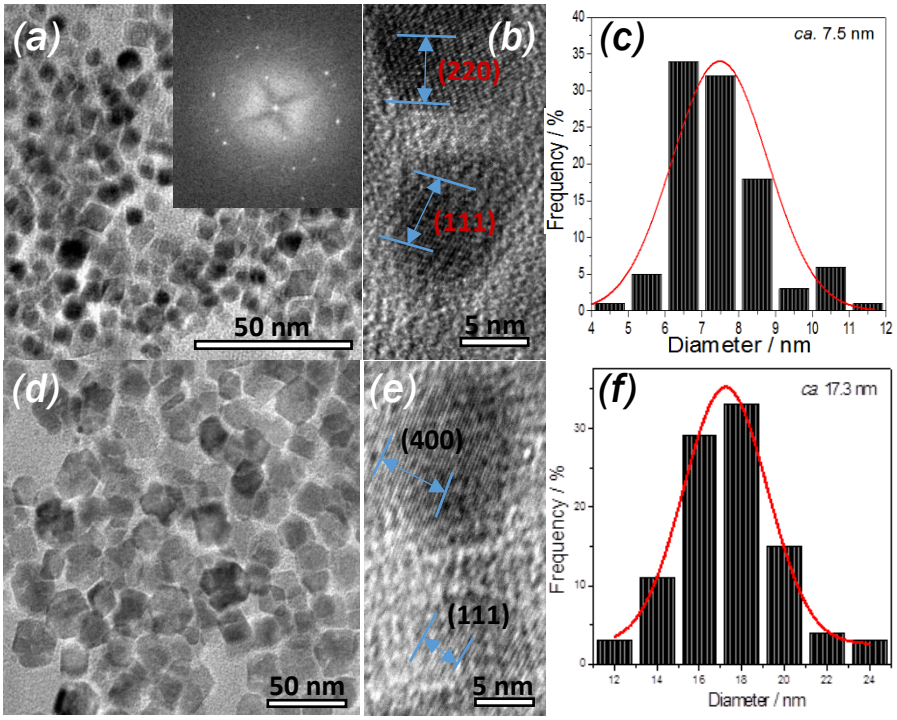

Figure. 37 TEM (a, d) and HRTEM (b, e) images of small (~ 7 nm) $CoFe_2O_4$@Ole (1st row) and larger (~ 17 nm) $CoFe_2O_4$@Ole (2nd row) NPs and their size distribution histograms. *Insets*: typical SAED pattern of cobalt ferrite NPS formed by the thermal decomposition.

In this study, the most uniform and well grained $CoFe_2O_4$@Ole NPs with a mean diameter of 7.5 nm have been formed by thermal decomposition of organometallic Co^{2+} and Fe^{3+} precursors in the presence of oleic acid and trimethylamine-N-oxide. In order to obtain larger NPs, the repeated

decomposition of $Co(acac)_2$ and $Fe(acac)_3$ were performed onto the as-growth $CoFe_2O_4$@Ole NPs in the same conditions as at the first time. In this way, significantly larger cobalt ferrite NPs with a mean diameter of ~ 17 nm have been formed (Fig. 37 d). HR-TEM as well as SAED patterns revealed a well-expressed crystalline structure of $CoFe_2O_4$@Ole NPs (Fig. 37 b, e, *Insets*).

3.3.2. Characterization of $CoFe_2O_4$@citrate, $CoFe_2O_4$@Lys, $Co_xFe_{1-x}Fe_2O_4$@Lys and $CoFe_2O_4$@Ole NPs

The phase and composition analysis of various synthesized citrate stabilized $CoFe_2O_4$@citrate NPs were performed by XRD and ICP-OES. The representative XRD patterns of ultra-small ($\varnothing_{mean}$ ~ 1.65 nm) and small ($\varnothing_{mean}$ ~ 5.0 nm) NPs are shown in Fig. 38 a. A well crystallized single phase cobalt ferrite with a face-centered cubic (fcc) spinel structure was detected.

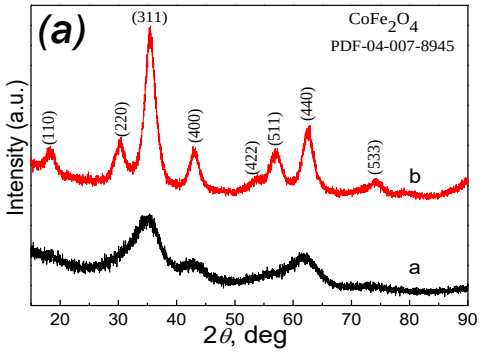

(b)

NPs size, nm	Fe:Co ratio, %	
	By EDX	By ICP-OES
~ 2	1.99	1.97
~ 5	2.01	2.05
~ 15	1.97	1.96

Figure. 38 Typical XRD patterns of ultra-small, ca. $\varnothing_{mean}$ ~ 1.65 nm (a) and $\varnothing_{mean}$ ~ 5.0 nm (b) citrate-stabilized cobalt ferrite NPs. In (b), a table displaying an average proportion of iron and cobalt amounts in the synthesized NPs, determined by the EDX and ICP-OES analysis, is presented.

As can be seen in Fig. 38 a and b, both XRD patterns contain several obvious diffraction peaks at 2θ positions of 18.31, 30.29, 35.52, 43.14, 53.68, 57.01, 62.54 and 74.24 degrees, which according to PDF card no 04-007-8945, can be attributed to (110), (220), (311), (400), (422), (511), (440), and (533) planes. These results confirm that hydrothermally synthesized powder is composed of polycrystalline $CoFe_2O_4$. The broadening of diffraction peaks indicate the nanometer size of NPs as confirmed by HRTEM. The chemical composition of 1.65, 5 and 15 nm-sized $CoFe_2O_4$@citrate NPs, evaluated by EDX and ICP-OES also shows the stoichiometric structure with Co:Fe atomic ratio equal approximately to 1:2 (Fig. 38 b). In order to determine the stability and surface charge of as-synthesized NPs, ζ-potential analysis was performed in this work. The average ζ-potential of the negatively charged citrate-stabilized 15 nm $CoFe_2O_4$@citrate NPs was found to be -43.78 mV allowing

us to conclude their partial stability without aggregation. In order to determine the magnetic properties of 1.65, 5, and 15 nm-sized $CoFe_2O_4$@citrate NPs, their hysteresis loops were determined at room temperature. The obtained magnetization curves are presented in Fig. 39.

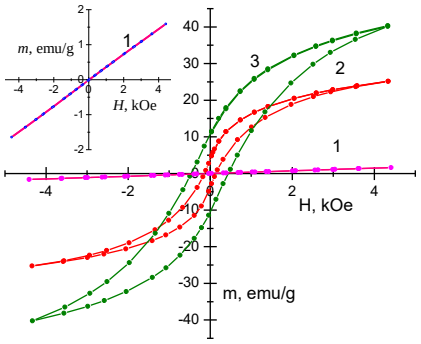

Figure. 39 Magnetization curves of $CoFe_2O_4$@citrate NPs in average diameter of 1.65 (1), 5.0 (2) and 15 nm (3).

The main parameters extracted from the loops were the coercive field (H_c) and saturation magnetization (M_s), which are shown in Fig 39. All curves exhibited the characteristic features typical for ferromagnetic materials (H_c is non zero dimension). The saturation magnetization M_s value calculated for 15 nm-sized $CoFe_2O_4$@citrate NPs was found to be 40 emu g^{-1}, whereas 5 and 1.65 nm-sized NPs exhibited approximately 25 and 1.5 emu g^{-1}, respectively. It was reported by Millan et al., that saturation magnetization of NPs decreases with decrease of their size, approaching zero for 3 nm and smaller NPs [131]. For ultra-small NPs, the domain core disappears and the disordered part becomes prevailing, thus changing the chemical and binding properties of NPs. As a result of this effect, the significantly low M_s was observed (Fig. 39 Insets).

Phase and crystallinity of hydrophobic (stabilized with oleic acid) and hydrophilic (stabilized with L-lysine) cobalt ferrite NPs, synthesized by the thermal decomposition and hydrothermal approaches, respectively, were determined by XRD (Fig 40 b). The XRD patterns of the both tested spinels proved their highly crystalline nature because of the strong intensities ascribed to the peaks of (311), (440), (511), (220), (400), and (422) crystal planes. The size of NPs, estimated from the corresponding XRD patterns using Halder-Wagner approximation, equaled to 4.0 nm whereas for the larger ones – to 14.0 nm. It is notable, that observed diffraction peaks and their relative intensities for both $CoFe_2O_4$@Ole and $CoFe_2O_4$@Lys samples matched well to the standard $CoFe_2O_4$ data, reported in the PDF card No. 00-022-1086. Due to the diffraction peaks broadening, some wider diffraction peaks of the small NPs have been observed. However, the size of NPs, determined from XRD

patterns, were significantly smaller in comparison with the TEM images (Fig. 37 a, d). This contrast mostly should be due to NPs sub-grains structure, which is inseparable by XRD as recently reported for the Fe_3O_4 NPs [132].

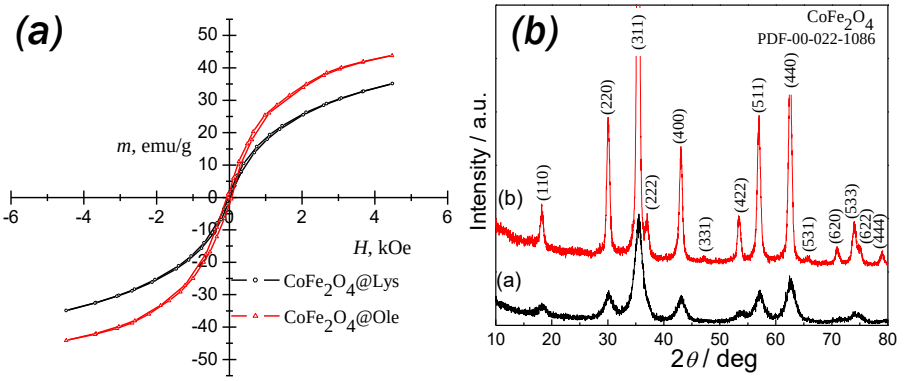

Figure. 40 Magnetization curves (a) of 5-7 nm-sized $CoFe_2O_4$@Ole, $CoFe_2O_4$@Lys NPs and XRD patterns of ~7 nm (a) and 17 nm (b) of oleic acid stabilized cobalt ferrite NPs.

The hysteresis loops of 7 and 17 nm $CoFe_2O_4$@Ole NPs demonstrate the superparamagnetic behaviour obtained by the vibrating sample magnetometer measurements with a magnetic field of ± 10 kOe at room temperature. It was observed, that smaller cobalt ferrite NPs capped with oleic acid exhibited higher saturation magnetization value e.g. 52 emu g^{-1}, than the larger ones (46 emu g^{-1}). This result might be explained by the surface spin canting and other size-related effects. Moreover, in most cases of magnetic NPs, the saturation magnetization has tendency to increase with the particle size for the same composition material [133]. It is claimed, that the larger magnetic NPs generally have higher saturation magnetization value [134]. Besides that, the similar tendency was observed with the citrate stabilized $CoFe_2O_4$@citrate NPs, as shown in Fig. 39. However, oleic acid capped magnetic particles exhibited a stronger magnetic properties and different type of magnetism.

In order to prove the oleic acid and L-lysine adsorption on $CoFe_2O_4$ NPs, FTIR spectra were recorded in this work. The FTIR absorbance spectrum of oleic acid capped cobalt ferrite NPs (Fig. 41 A-a) shows the broad bands around 401 and 591 cm^{-1}, which belong to Fe-O and/or Co-O bond stretching vibration, respectively. It is claimed, that in a ferrite the metal ions are situated in two separate sub-lattices, namely tetrahedral and octahedral, according to geometrical configuration of the oxygen nearest neighbours [135]. The higher energy absorption band is associated with metal-oxygen bond vibration of tetrahedral complexes and the lower energy – to octahedral complexes. These results confirmed the cubic spinel structure of cobalt ferrite NPs. Furthermore,

the vibration bands at the high frequency around 1562 and 1603 cm^{-1} are attributable to asymmetric stretching vibration of COO^- carboxylate anion. Moreover, the broad band near 1406 cm^{-1} can be indexed as a symmetric stretching vibration of carboxylate group, thus proving the hypothesis that, oleate anions are absorbed on the surface of $CoFe_2O_4$ NPs. The FTIR spectra of bulk oleic acid (Fig. 41 A-b) indicated the vibration band at 1710 cm^{-1}, which is attributable to carboxyl group C=O bond, whereas in the $CoFe_2O_4$@Ole absorbance spectra no spectroscopic evidence for the presence of oleic acid around $CoFe_2O_4$ NPs was observed.

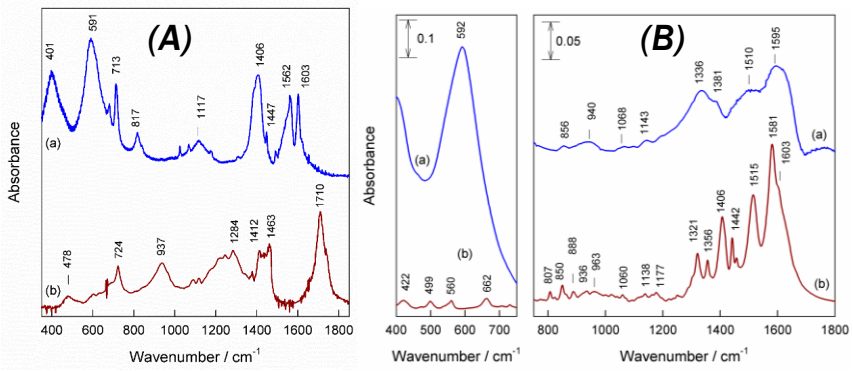

Figure. 41 (A): FTIR absorbance spectra of (a) oleic acid capped ~7 nm $CoFe_2O_4$@Ole NPs and (b) pure oleic acid in the spectral region of 350-1850 cm^{-1}. In (B): L-lysine modified 5-7 nm $CoFe_2O_4$@Lys NPs (a) and (b) pure L-lysine powder in the spectral regions of 400-700 (left panel) and 750-1800 cm^{-1} (right panel).

The FTIR absorbance spectrum of L-lysine capped 5-7 nm $CoFe_2O_4$ NPs as well as L-lysine powder are represented in Fig. 41 B. Similar as in the way with $CoFe_2O_4$@Ole NPs the broad band around 592 cm^{-1} was observed, thus corresponding to the stretching vibration of Fe-O and/or Co-O bonds. It could be clearly seen a several broad bands with the lower intensity at a lower energy range, which might be associated with the vibrations of carboxylate and/or amino groups of adsorbed L-lysine amino acid used for stabilization of Fe-substituted $Co_xFe_{1-x}Fe_2O_4$@Lys or $CoFe_2O_4$@Lys NPs. The higher intense band in the IR spectrum of L-lysine was detected around 1581 cm^{-1} (Fig 41 B- b). These observations were assigned to the antisymmetric carboxylate anion COO^- vibration [136]. The IR mode seen at 1603 cm^{-1} belongs to the antisymmetric deformation vibration of proximal and distal NH_3^+ groups, whereas the vibration modes at 1515 and 1406 cm^{-1} should be attributed to the NH_3^+ symmetric deformation and symmetric stretching vibration of COO^- groups. IR modes in the spectral region between 1321 and 1356 cm^{-1} are due to the coupled vibrations of $-CH_2-$ antisymmetric deformation and CH deformation modes [137]. The downshifts from 1406 to

1381 cm^{-1} was obtained with L-lysine capped cobalt ferrite NPs, thus demonstrating that carboxylate groups are bind to the surface. Recently, SERS studies indicated that this significant shifting is the main sign of the direct binding of carboxylate group with metal surface [138]. These findings suggest that L-lysine amino acid binds to cobalt ferrite NPs surface through the carboxylate group probably *via* electrostatic interaction, whereas the amino groups remain protonated. These results match well with those obtained by ζ - potential analysis, which was carried out in order to determine the surface charge of oleic and L-lysine amino acid stabilized cobalt ferrite NPs. The dependency of zeta potential on pH of the solution containing dispersed $CoFe_2O_4$@Ole and $CoFe_2O_4$@Lys NPs with the final concentration of 0.25 g L^{-1} in 10 mmol L^{-1} sodium saline aqueous solution is depicted in Fig. 42.

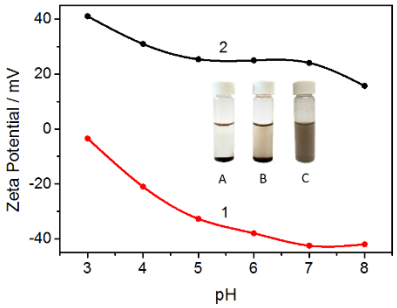

Figure. 42 Variables of the ζ-potential values *versus* pH for an aquenous suspension of $CoFe_2O_4$@Ole (1) and $CoFe_2O_4$@Lys (2) NPs at a constant concentration of 0.25 g L^{-1}. In the inset: 17 nm in size $CoFe_2O_4$@Ole dispersed in water without (a) and with ultrasonic agitation for 3 h (b) and 6 h (c) products view.

It is clearly seen, that L-lysine stabilized $CoFe_2O_4$ NPs in the pH range from 3 to 8 are positively charged due to the exposed protonated amino groups of amino acid molecules (Fig. 42 curve 2). The increase in pH resulted in the decrease of ζ-potential value from ~41 mV at a pH = 3 to ~23 mV at a pH = 8. However, variations of zeta potential value are insignificant in the pH range of 5-7.2; such conditions are similar to the cultivation media of microorganisms and approximately equal to 23 ± 1 mV. In the way with oleic acid stabilized $CoFe_2O_4$ NPs, surface charge of NPs are negative, mainly due to oleate anions attached around the particles. The dependency of zeta potential on pH of the colloidal suspension exhibit comparable curve profile. However differently than in the case with $CoFe_2O_4$@Lys NPs, an increase in the pH leads to the increase in zeta potential value form -4 to -44 mV. It should be emphasized, that $CoFe_2O_4$@Ole NPs generally possess the hydrophobic behaviour as can be seen in the samples presented in Fig. 42 *Insets* (A). In

order to transform this behaviour and provide better solubility in water, the prolonged ultrasonic agitation of these NPs was used at this stage. By this processing way, after 4-6 h of agitation quite stable, black-coloured colloidal solution has been produced and further used for characterization and antimicrobial assessments.

Phase analyses of 5-7 nm-sized Fe-substituted $CoFe_2O_4$@Lys NPs synthesized by the hydrothermal approach were assessed by XRD. These investigations (Fig. 43, A) revealed that as-growth $Co_{0.2}Fe_{0.8}Fe_2O_4$@Lys, $Co_{0.5}Fe_{0.5}Fe_2O_4$@Lys, and $CoFe_2O_4$@Lys NPs exhibit a face-centred, cubic symmetry spinel structure (PDF: 04-016-1272, space group *Fd-3m*, $a = b = c$ = 8.385 Å). As can be seen in Fig. 43 a, b and c diffractograms all positions and relative intensities of diffraction peaks meet well each other, thus corresponding to standard diffraction data. On the one hand, such XRD patterns suggested a good crystallinity of prepared products and insignificant amount of impurities in the NPs powder. On the other hand, this analysis do not explain the main task about the chemical composition of $Co_xFe_{1-x}Fe_2O_4$@Lys NPs. However, using Halder-Wagner approximation for analysis of XRD patterns, the size of proposed Fe-doped cobalt ferrite was estimated confirming a quit uniform size of $Co_{0.2}Fe_{0.8}Fe_2O_4$@Lys (3.6 nm), $Co_{0.5}Fe_{0.5}Fe_2O_4$@Lys (3.1 nm), and $CoFe_2O_4$@Lys NPs (3.8 nm), respectively.

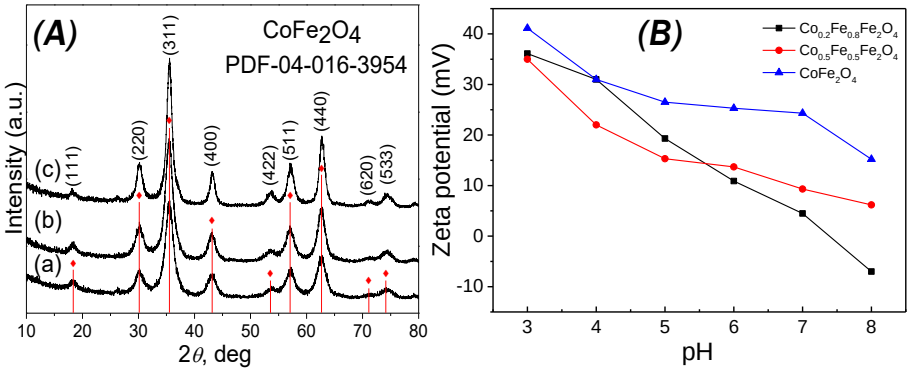

Figure. 43 Typical XRD patterns (A) of Fe-substituted cobalt ferrite NPs: (a) $Co_{0.2}Fe_{0.8}Fe_2O_4$@Lys, (b) $Co_{0.5}Fe_{0.5}Fe_2O_4$@Lys, and (c) $CoFe_2O_4$@Lys. In (B) ζ - potential *versus* pH dependency for an aqueous suspension of $Co_xFe_{1-x}Fe_2O_4$@Lys NPs.

ζ - potential measurements of Fe-substituted cobalt ferrite NPs stabilized with L-lysine amino acid indicated that all particles are positively charged in the pH range from 3 to 7; similar to those described previously. It was observed, that $CoFe_2O_4$@Lys NPs show higher zeta potential than that $Co_{0.2}Fe_{0.8}Fe_2O_4$@Lys and $Co_{0.5}Fe_{0.5}Fe_2O_4$@Lys, emphasizing the role of Co^{2+}

substitution with Fe^{2+}. This effect might be attributed to the higher amount of L-lysine adsorbed on the NPs surface, exposing amino groups in the protonated form [139].

In order to determine the composition of Fe-substituted cobalt ferrite NPs, the Mössbauer spectra were collected under the transmission mode at an ambient temperature. The obtained 6-line magnetic hyperfine patterns were found to be different due to the variations in the composition and possibly in the particle size (Fig. 44 a, b, c).

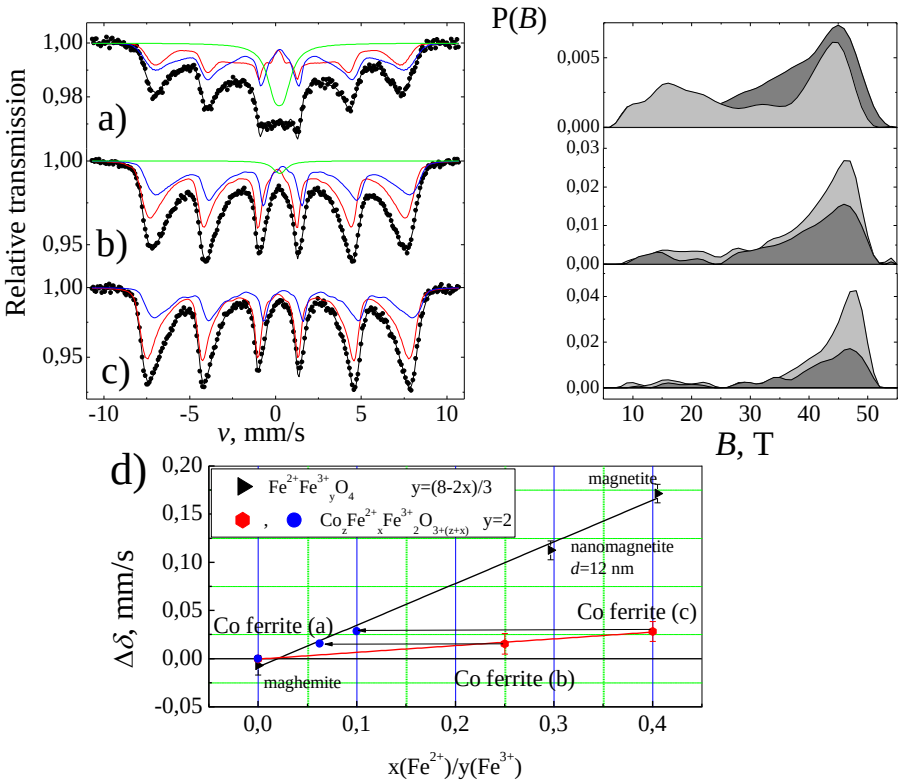

Figure. 44 Mössbauer spectra of $CoFe_2O_4$@Lys (a) and iron substituted cobalt ferrite NPs in particular $Co_{0.5}Fe_{0.5}Fe_2O_4$@Lys (b) and $Co_{0.2}Fe_{0.8}Fe_2O_4$@Lys (c), whereas the hyperfine distributions are placed on the right. In (d) variations of the Mössbauer spectra centrum shifts of tested NPs relatively to pure $CoFe_2O_4$@Lys NPs.

The evaluation of Fe^{2+} amount in the $Co_xFe_{1-x}Fe_2O_4$@Lys powder was done using two methods. The collected spectra were fitted using two hyperfine field distribution and different isomer shift values, e.g. 0.23-0.26 and 0.53-0.58 mm s^{-1}. Through the assignment of the area covered by hyperfine distribution with the larger isomer shift to [Fe^{2+}] (tetrahedral) and [Fe^{3+}] (octahedral) iron sites, as in the magnetite NPs, it was obtained that approximately 17-20 % of all Fe cations are divalent. However, it is notably

that isomer shift of B sublattice (octahedral site) of magnetite is larger reaching around ~0.67 mm s^{-1}, while subspectra strongly overlap due to superparamagnetic relaxation and Co^{2+} ions shifting in the cobalt ferrite lattice. Noteworthly that if the isomeric shift values of Fe-substituted NPs are compared with the corresponding values of the similar sized Fe_3O_4 and Fe_2O_3 NPs, some misunderstandings, associated with the fitting mode of Mössbauer spectra, can be avoided. According to these results, the content of Fe^{2+} might be about four times lower than the expected for $Co_{0.5}Fe_{0.5}^{2+}Fe_2^{3+}O_4$@Lys and $Co_{0.2}Fe_{0.8}^{2+}Fe_2^{3+}O_4$@Lys composites (blue points in Fig. 44 d). It was attempted to collect the Mössbauer spectra of synthesized NPs at cryogenic temperature approximately equal to 10 K; however the spectra obtained was not informative probably due to the charge redistribution below a Verway temperature. It should be noticed that Mössbauer spectra taken at the enhanced temperatures differ because of further NPs oxidation. As a control, the composition of Fe-substituted cobalt ferrite NPs were investigated by ICP - OES analytical method. The calculation performed on the basis of obtained results are shown in Table 6.

Table 6. ICP-OES analysis results of Fe-substituted cobalt ferrite NPs and calculated composition of the synthesized NPs.

Specimen	$[Co^{2+}]$, mg L^{-1}	$[Fe^{3+}]$, mg L^{-1}	Fe^{2+}/Co^{2+} ratio	Calculated formula
$CoFe_2O_4$	45.7	91.17	1.95	$CoFe_2O_4$
$Co_{0.5}Fe_{0.5}Fe_2O_4$	17.8	79.56	1.23	$Co_{0.45}Fe_{0.55}Fe_2O_4$
$Co_{0.2}Fe_{0.8}Fe_2O_4$	5.64	70.53	3.50	$Co_{0.16}Fe_{0.84}Fe_2O_4$

In order to obtain the content of Co^{2+} and Fe^{3+} in $Co_xFe_{1-x}Fe_2O_4$@Lys NPs, the probe of NPs was dissolved in the diluted HCl solution and examined by a ICP-OE spectrometer. It is claimed, that this chemical analysis do not separate the Fe^{2+} and Fe^{3+} ions. However, assuming the formula of $M_{Fe(II)} + M_{Co(II)} = 0.5\ M_{Fe(III)}$ the chemical composition of Fe-doped ferrites was determined as $Co_{0.45}Fe_{0.55}Fe_2O_4$ and $Co_{0.16}Fe_{0.84}Fe_2O_4$. Following that rule (keeping the goal of simplicity) these stoichiometric coefficients have been rounded up and labelled as $Co_{0.5}Fe_{0.5}Fe_2O_4$ and $Co_{0.2}Fe_{0.8}Fe_2O_4$.

3.3.3. Antimicrobial properties of $CoFe_2O_4$@citrate, $CoFe_2O_4$@Lys, $Co_xFe_{1-x}Fe_2O_4$@Lys and $CoFe_2O_4$@Ole NPs

The antimicrobial activity of different in size citrate stabilized $CoFe_2O_4$@citrate NPs were investigated against *S. cerevisiae*, *C. parapsilosis*, *C. krusei* and *C. albicans* microorganisms using the zone inhibition and broth

dilution methods. Briefly, disc-shaped filter papers with NPs loading of 0.67 mg cm^{-2} for 15 nm in diameter $CoFe_2O_4$@citrate NPs and 0.33 mg cm^{-2} for 2 and 5 nm in size $CoFe_2O_4$@citrate NPs were placed gently on a lawn of microbes in sterile Sabouraud agar plates. For quantitative analysis, 1 g L^{-1} of suggested NPs were injected into the inoculated media at room temperature for 48 h. Finally, antimicrobial characteristics were evaluated by determination of clear zone around the specimens as well as counting the CFU in the Petri dishes after 48 h as described previously. All assays were carried out in triplicate. The obtained results are presented in Table 7.

Table 7. The antimicrobial behaviour of 2, 5 and 15 nm-sized $CoFe_2O_4$@citrate NPs against *S. cerevisiae* and three different *Candida* species.

Microorganism	Size of $CoFe_2O_4$ NPs, nm	Diameter of disc (d), mm	Diameter of zone (z), mm	z/d
S. cerevisiae	15	11	22	2.0±0.2
	5	11	24	2.4±0.1
	2	11	24	2.4±0.1
C. parapsilosis	15	11	13	1.2±0.05
	5	11	15	1.4±0.1
	2	11	16	1.4±0.1
C. krusei	15	11	13	1.3±0.05
	5	11	15	1.4±0.1
	2	11	16	1.4±0.1
C. albicans	15	11	13	1.2±0.05
	5	11	14	1.3±0.1
	2	11	16	1.4±0.1

It is easy to see that 2, 5 and 15 nm in diameter $CoFe_2O_4$@citrate NPs exhibited the highest antimicrobial activity against *S. cerevisiae* yeast. The clear inhibition zone with approximately 11-13 mm length (Fig. 45-47 B) prove the fungicidal effect, whereas the lysis zone around commercial antimicrobial agent – fluconazole, used in this experiments as a positive control, showed ~30 % smaller effect in the *S. cerevisiae* lawns. Furthermore, the ability to inactivate several *Candida* species in particular *C. krusei*, *C. parapsilosis* and *C. albicans* were approximately fourfold weaker (Fig. 45 - 47 A, C, D) in comparison with *S. cerevisiae*, reaching only 2-5 mm of their lysis zones in an agar diffusion assay. Moreover, only in the case with 5 nm $CoFe_2O_4$@citrate NPs, the fungistatic effect has been observed around the partially covered filter papers (Fig. 46 C). Besides that, small (2-5 nm) $CoFe_2O_4$@citrate NPs demonstrated higher killing efficiency in comparison

with larger ones, thus creating the narrower inhibition zones in the microorganisms lawns. These results match those, obtained by previous researches, which also prove the idea of size dependent antimicrobial activity of other metal oxide NPs such as ZnO [140], MgO [126] or CuO [141].

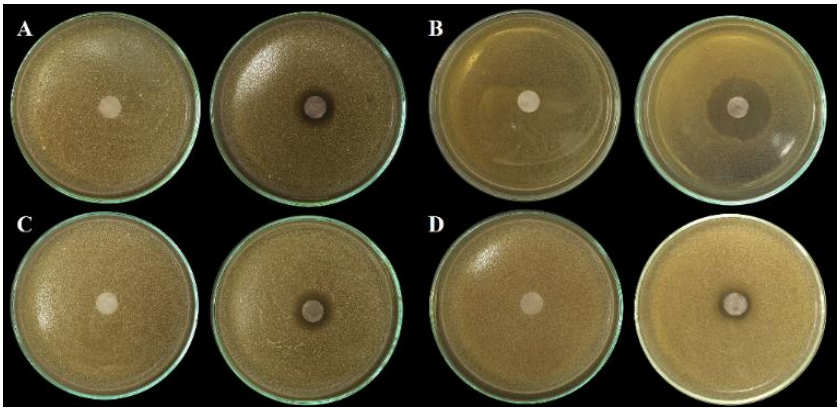

Figure. 45 Inhibition zone produced by 2 nm $CoFe_2O_4$@citrate NPs loaded filter paper specimens against the lawns of *C. krusei* (A), *S. cerevisiae* (B), *C. parapsilosis* (C) and *C. albicans* (D). In the left side – the control specimens.

Significant difference exist between the inhibition zones, established with the samples containing the same amount of 2 and 5 nm-sized cobalt ferrite NPs.

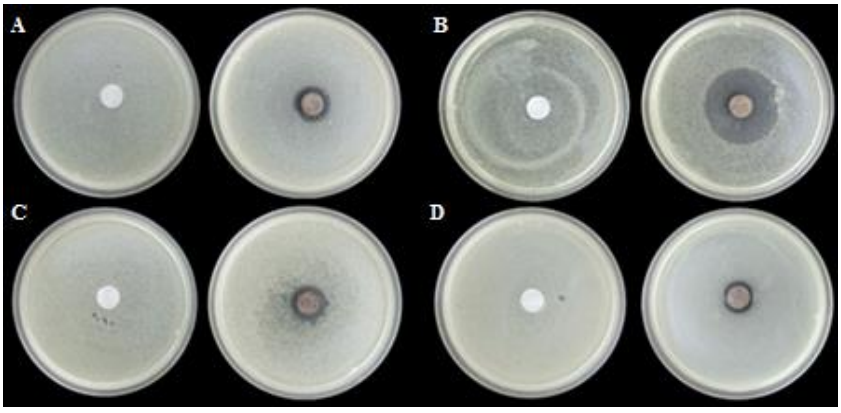

Figure. 46 Inhibition zone produced by 5 nm $CoFe_2O_4$@citrate NPs loaded filter paper specimens against the lawns of *C. krusei* (A), *S. cerevisiae* (B), *C. parapsilosis* (C) and *C. albicans* (D). In the left side – control specimen.

In the cases of *C. parapsilosis*, *C. krusei* and *C albicans*, the fungicidal zone caused by smaller NPs was found to be approximately 20-40 % higher in comparison with those, caused by 5 nm-sized NPs.

In order to evaluate the quantitative analysis of different in size $CoFe_2O_4$@citrate NPs *in vitro* tests were carried out further with two different

yeast species. The results obtained in this examination against *S. cerevisiae* and *C. parapsilosis* are shown in Fig. 48.

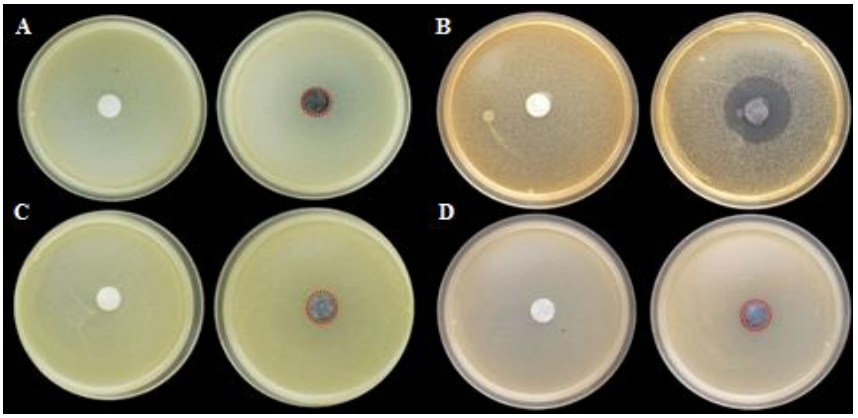

Figure. 47 Inhibition zone produced by 15 nm-sized $CoFe_2O_4$@citrate NPs loaded filter paper specimens against the lawns of *C. krusei* (A), *S. cerevisiae* (B), *C. parapsilosis* (C) and *C. albicans* (D). In the left side – control specimens.

It was demonstrated, that the results obtained by modified Kirby Bauer technique match well those obtained *via* serial dilution analysis, implying much more effective antimicrobial action of 2 and 5 nm-sized cobalt ferrite NPs in comparison with 15 nm-sized ones. However, the 15 nm-sized cobalt ferrite NPs also reduced the count of CFU, determined after their growth on the Sabauraud agar media, as seen in the histogram of Fig 48. Comparing of pure *S. cerevisiae* and *C. parapsilosis* inoculum with those, exposed with 2 nm-sized in diameter NPs, it was found that antimicrobial efficiency of these NPs is approximately in 12 % higher than in the case of 5 nm-sized and almost in 25 % higher than using a 15 nm-sized ones.

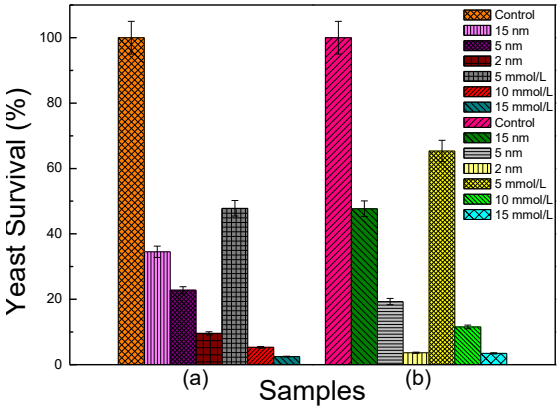

Figure. 48 Antimicrobial activity of 2, 5 and 15 nm $CoFe_2O_4$@citrate NPs and Co^{2+} ions against *S cerevisiae* (a) and *C. parapsilosis* (b) yeasts. Error bars represent the standard deviation.

Comparable results were obtained with *C. parapsilosis*. For this microbe, 2 nm-sized NPs exhibited 15 % higher killing rate than 5 nm-sized as well as approximately 44 % higher killing rate than 15 nm-sized $CoFe_2O_4$@citrate NPs. Furthermore, half volume of the smallest NPs provided the same antimicrobial efficiency against *S. cerevisiae* as 5 nm-sized ones whereas in the case of *C. parapsilosis* just in 10 % higher killing efficiency was observed. Summarizing results obtained in this study, it was concluded that antimicrobial activity of citrate stabilized cobalt ferrite NPs is size-dependent in the range between ~2 and 15 nm. As a result, the content of CFU decreased while decreasing these particle size as shown in Fig 49. The mechanism of antimicrobial action was not studied herein, however, some possible suggestions can be discussed. According to previous research, the antimicrobial action of $CoFe_2O_4$ was initiated due to NPs diffusion inside the cell, interacting with the cell membrane or producing ROS, which cause an oxidative stress and finally the DNR damage [131]. Another hypothesis cited in this work was attributed to Co^{2+} ions distribution in the NPs shell, which significantly depends on the size of NPs.

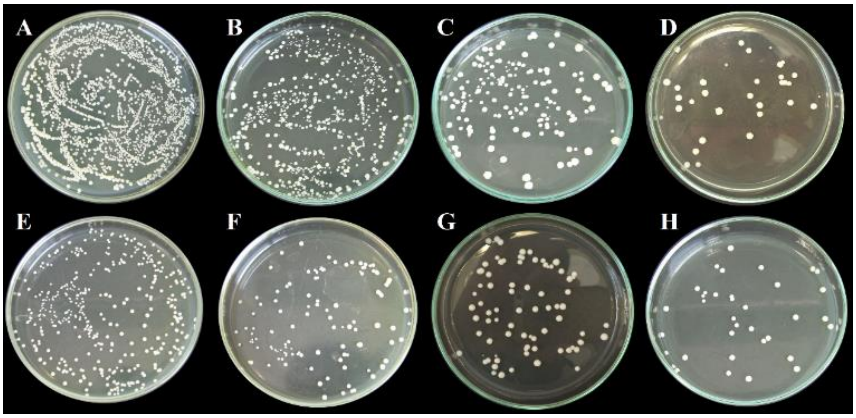

Figure. 49 The amount of CFU in the Petri dishes grown on the Sabouraud agar media after incubation with different in size $CoFe_2O_4$@citrate NPs against *C. parapsilosis* (top row) and *S. cerevisiae* (bottom row). All yeasts were incubated in liquid media without (a, e) and with 2 nm-sized (d, h), 5 nm-sized (c, g) or 15 nm-sized (b, f) NPs for 48 h.

In general, it can be expected that the continuous increase in the amount of Co^{2+} ions dissolved from the inner part of cobalt ferrite NPs are associated with the particles size decrease and could be the main reason of higher antimicrobial activity of small (~5 nm) and ultra-small (~2 nm) NPs. In order to test this assumption, the Co^{2+} antimicrobial activity as well as minimal inhibitory concentrations (MICs) were determined using *S. cerevisiae* and *C. parapsilosis* yeasts. These two microorganisms had MIC of 21 and

25 mmol L^{-1}, respectively. It was also observed, that the killing efficiency of cobalt ions are significantly higher with *S. cerevisiae*, whereas *C. parapsilosis* showed a higher Co^{2+} resistance after 25 h cultivation. However, all tested Co^{2+} solutions, in particular 5, 10, and 15 mM, exhibited a clear antimicrobial activity dependency on the [Co^{2+}] as shown in Fig. 48. These results are in accordance with those reported by Wan's group [142], which indicated that the Co^{2+} ions released from the NPs caused eventually an oxidative stress resulting in the DNA damage. However, it is worth mentioning that the ratio of NPs surface to volume ($S_{surface}/V_{NP}$) increases significantly with NP size decrease from 15 to 5 and 2 nm and are equal to 4.8, 10.8, and 33.4, respectively. These calculations allow to predict the higher toxicity of smaller NPs due to increase in their surface size and a higher contacting area with microorganisms.

In the next stage, the influence of Co^{2+} content in the spinel NPs on antimicrobial activity was tested against well-known typical pathogens, which usually cause skin, tissue, blood and respiratory infections. To achieve this goal, the similar in size (~5-7 nm), Fe-substituted NPs with chemical formula of $CoFe_2O_4$@Lys, $Co_{0.5}Fe_{0.5}Fe_2O_4$@Lys and $Co_{0.2}Fe_{0.8}Fe_2O_4$@Lys were investigated as potential microbial inhibitors against some prokaryotic and eukaryotic microorganisms. Firstly, the antimicrobial activity was investigated by a modified Kirby-Bauer protocol against *C. albicans*. In this way, the widest inhibition zone around the disc-shaped filter paper, loaded with NPs, was achieved with $CoFe_2O_4$ NPs, as shown in Fig 50 d.

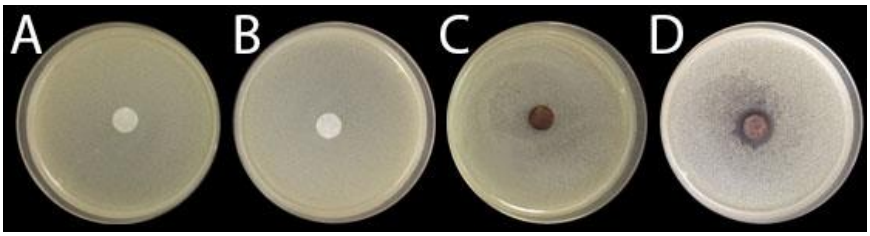

Figure. 50 Antimicrobial activity of L-lysine functionalized cobalt ferrite NPs dispersed on the disc-shaped filter papers against *C. albicans* strains: A – pure filter paper, B – L-lysine, C – Fe_3O_4@Lys and D – $CoFe_2O_4$@Lys NPs.

Note, that by this examination no inhibition zone was observed around Fe_3O_4@Lys NPs impregnated filter paper confirming that magnetite NPs are microorganism friendly material. Furthermore, it can be assumed, that the absence of Co^{2+} in the spinel structure leads to non toxicity for microorganisms and probably for human cells. These results differ from ones published in [143], in which the antimicrobial activity has been evidenced for Fe_3O_4 NPs against *B. cereus* and *K. pneumoniae*.

In accordance with Wang's group findings [92], reported that zinc and cobalt doping of cobalt ferrite NPs significantly increase their antimicrobial efficiency against several bacteria strains it was expected to determine the lower antimicrobial activity of Fe^{2+} enriched cobalt ferrite NPs. Following this assumption quantitative analysis was carried out against multi-drug resistant clinical pathogens such as *S. aureus*, *E. coli*, *C. parapsilosis* and *C. albicans* by assessing the CFU. In order to quantify the bactericidal and fungicidal potencies, 1 g L^{-1} of $CoFe_2O_4$@Lys or Fe-doped NPs were suspended in the liquid media with microorganism's inoculum and incubated for 24 and 72 h, respectively. L-lysine amino acid (100 mg L^{-1}), used as a stabilization agent for NPs synthesis and Fe_3O_4@Lys (1 g L^{-1}) were examined too and act as a negative control samples. The results obtained from these inspections are shown in Fig. 51.

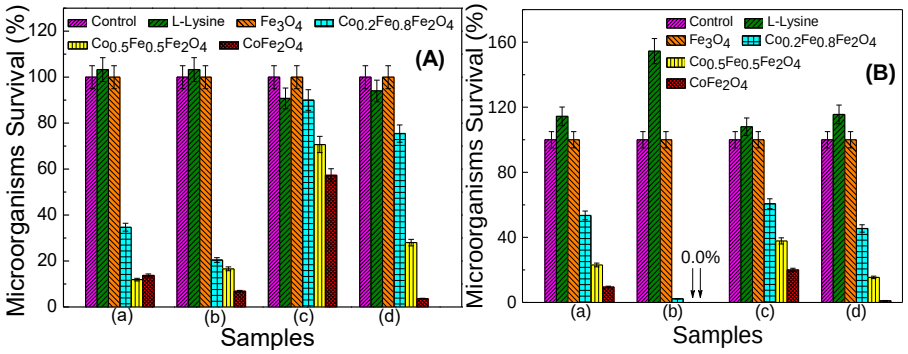

Figure. 51 Antimicrobial activities of 5-7 nm-sized $CoFe_2O_4$@Lys and Fe-substituted cobalt ferrite NPs after 24 h (A) and 72 h (B) incubation with *C. albicans* (a), *C. parapsilosis* (b), *E. coli* (c) and *S. aureus* (d). Pure L-lysine and magnetite NPs were investigated as a negative control. Error bars represented the standard deviations.

These results match well with those obtained with qualitative analysis, showing that Fe-substituted cobalt ferrite NPs also possess antimicrobial activity against all tested microbes. At this stage, a good correlation was obtained between the total amount of Co^{2+} in cobalt ferrite NPs and the microorganism survival. The highest killing efficiency belonged to $CoFe_2O_4$@Lys NPs as expected, while comparing to control samples these NPs exhibited the antimicrobial potency of 93.1-86.3 % for eukaryotic and 96.4-42.7 % for prokaryotic organism species. Meanwhile, both Fe-substituted cobalt ferrites, labelled as $Co_{0.5}Fe_{0.5}Fe_2O_4$ and $Co_{0.2}Fe_{0.8}Fe_2O_4$ show 11-24 % and 21-70 % powerless killing efficiency in comparison with $CoFe_2O_4$ NPs, respectively. The most striking effect obtained from the data was that the same content of both $CoFe_2O_4$ NPs and $Co_{0.5}Fe_{0.5}Fe_2O_4$ destroyed a huge part of *C. parapsilosis* yeast cells after 72 h incubation, as presented in

Fig. 51 B. Furthermore, some surprising results were obtained in case with L-lysine amino acid, which possess bactericidal potency against *E. coli* and *S. aureus* bacteria after 24 h incubation. However this effect is negligible, since the percentage of bacteria survival reached approximately 91 % and 94 %, respectively. It is known, that L-lysine is a biocompatible amino acid and deserves further investigation, as a control sample because of their possibility to be implemented in medicine. However, the number of all tested microorganism increased after 72 h incubation with L-lysine amino acid. It was hypothesized that such increase is caused by increased nutritions in cultivation media, because the yeasts and bacteria probably use L-Lysine as a one of food component. It should be noticed that Fe_3O_4@Lys NPs exhibited no antimicrobial activity against all tested microorganisms, as expected. Summarizing obtained results, the photographs of eukaryotic and prokaryotic microorganism's CFU grown on Sabouraud and Nutrient agar plates were taken in order to show the dependency of Co^{2+} content in the spinel NPs as a function on microorganism survival (Fig. 52).

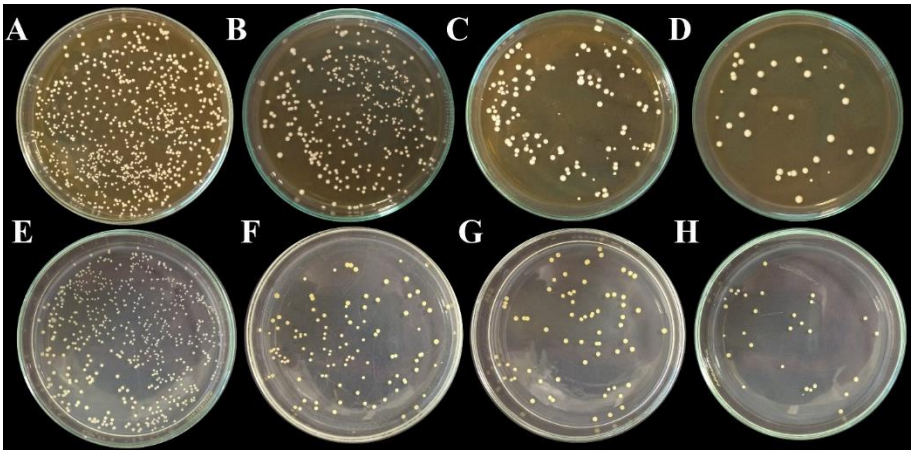

Figure. 52 The amount of CFU in Petri dishes grown on Sabouraud and Nutrient agar media after incubation with 5-7 nm $CoFe_2O_4$@Lys (D, H), $Co_{0.5}Fe_{0.5}Fe_2O_4$@Lys (C, G) and $Co_{0.2}Fe_{0.8}Fe_2O_4$@Lys (B, F) NPs against *C. albicans* (top row) and *S. aureus* (bottom row). All microorganism were incubated in liquid media without (a, e) and with NPs for 24 h.

It was shown that the count of CFU significantly reduces with an increase in the content of Co^{2+} in the Fe-doped cobalt ferrite NPs. As can be seen in Fig. 52 D, H, only a few dozen instead of hundreds of CFU remains alive after incubation with 10 μg mL^{-1} $CoFe_2O_4$ NPs.

In order to observe more information about interaction between cobalt ferrite NPs and microorganism, the SEM investigations were conducted. It is notable, that yeast cell was chosen due to its suitable size, because bacteria are

usually 2-3 times smaller, thus complicating their morphological investigation with SEM. Considerable alterations of *C. parapsilosis* cells were observed during this study as presented in Fig. 53. The native morphology of intact cells was attributed to ellipse-shaped ones as seen in Fig. 53 a. Following the incubation with $CoFe_2O_4$@Lys NPs cell lose its native structure and become erythrocyte – like structure (Fig. 53 b).

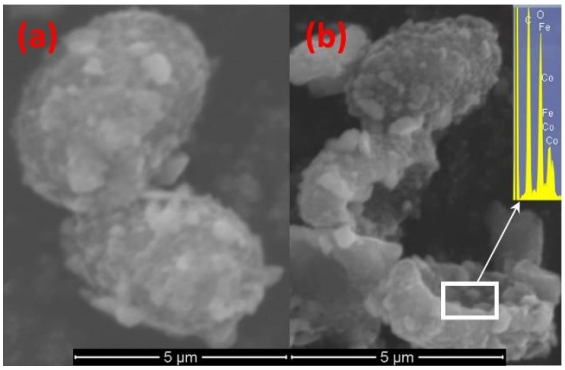

Figure. 53 Scanning electron micrographs of *C. parapsilosis* cells in the absence (a) and in the presence of L-lysine coated $CoFe_2O_4$ NPs (b). Represented images show the cell biomass fixed on the carbon tape destruction due to interactions with cobalt ferrite NPs. *Inset*: EDX spectra of *C. parapsilosis* surface after incubation with cobalt ferrite NPs.

The interaction between $CoFe_2O_4$@Lys and yeast cell was confirmed using EDX. The EDX spectrum of cobalt ferrite treated *C. parapsilosis* surface shows the presence of Fe and Co in the damaged cell sites, confirming the interaction of NPs with yeast cell. However the antimicrobial mechanism of L-lysine capped cobalt ferrite or Fe-substituted spinel NPs is not clear and demands further investigation. Nevertheless, some possible reason of such antimicrobial potency can be discussed. Firstly, as confirmed by zeta potential measurements, the positively charged NPs due to L-lysine amino acid, which adsorbed on the NPs surface could rapidly interact electrostatically with the negative charged bacteria cell wall and damage it. In accordance with previous research [139], this effect can be assigned to L-lysine induced generation of negative curvature at the surface of membrane due to a selective interaction. The NH_4^+ group induces negative curvature wrapping of anionic membranes leading to micellization/vesiculation and disrupt of membrane integrity causing the thinning of membranes. Secondly, as mentioned previously, on the surface of Fe-doped cobalt ferrite NPs, the L-lysine molecules bind harder in comparison with $CoFe_2O_4$ surface, thus decreasing the content of amino acid and resulting in weaker antimicrobial behaviour. The less Co^{2+} is encased,

the less amount of amino acid are attached on the NPs, thus a lower zeta potential is created.

In the final stage the influence of cobalt ferrite shell on antimicrobial activity was tested against several kind of pathogenic microorganism in particular *S. aureus*, *E. coli*, *C. parapsilosis*, *C. albicans*. Following this purpose, oleic acid stabilized 7 and 17 nm-sized, spherically-shaped $CoFe_2O_4$@Ole NPs were used for antimicrobial tests. As a comparison, ~5 - 7 nm L-lysine stabilized $CoFe_2O_4$@Lys NPs were also examined. It is worth mentioning, that a small probe of L-lysine and oleic acid in concentrations of 0.1 mg mL^{-1} and 5 v/v %, respectively, acted as a negative control. Firstly, the modified Kirby-Bauer technique was applied in order to determine the differences between antimicrobial potency of the same size $CoFe_2O_4$@Lys and $CoFe_2O_4$@Ole NPs. The results obtained from these examinations are shown in Fig. 54.

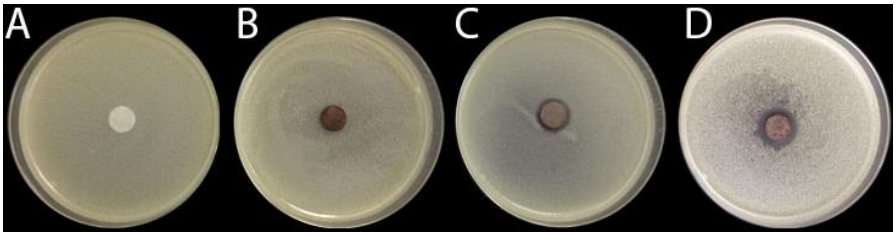

Figure. 54 Antimicrobial activity of L-lysine and oleic acid functionalized cobalt ferrite NPs dispersed on disc-shaped filter papers against *C. albicans* strains: A – pure filter paper, B – Fe_3O_4@Lys, C – $CoFe_2O_4$@Lys and D – $CoFe_2O_4$@Ole NPs.

The largest inhibition zone was obtained around the filter paper impregnated with oleic acid stabilized cobalt ferrite NPs as presented in Fig. 54 D. The clear lysis zone was approximately 2.5 times longer in comparison with the L-lysine modified NPs induced one (Fig. 54 C), which reached only 1-2 mm. In order to examine the influence of environment of NPs to the antimicrobial activity, the more precise quantitative analysis was carried out in this work. For this purpose, 1 g L^{-1} NPs were inoculated with microorganisms and were incubated for 24 and 72 h. The obtained results are presented by histograms (Fig. 55) and further support the findings obtained by the zone inhibition method. After exposure with oleic acid the bacteria as well as yeast cells propagated their numbers, thus proving non-toxically behaviour of this stabilization agent. In the case with *S. aureus* and *E coli*, the content of CFU increased approximately to 33 and 43 %, respectively, after 24 h cultivation and remains stable after 72 h. Meanwhile, in the case with *C. parapsilosis* and *C. albicans* microorganism the colony counts stay close to control after 24 h incubation, whereas after 72 h, the numbers of cell

increased significantly approximating 65 and 33 % higher count than control sample, respectively. The difference between the times, required for the growing number of bacteria in comparison with yeasts was obtained probably due to their rapid metabolism process and faster cell proliferation. It is notable, that L-lysine modified Fe_3O_4 NPs did not show any antimicrobial efficiency, thus echoing our findings as described previously. Furthermore, 7 nm and 17 nm-sized oleic acid stabilized $CoFe_2O_4$@Ole NPs possess surprisingly high killing efficiency for all tested microorganism. In comparison with L- Lysine stabilized $CoFe_2O_4$@Lys NPs the same size $CoFe_2O_4$@Ole NPs shows higher antimicrobial activity. The largest difference has been obtained in the case with *E. coli*, where the bacteria survival varied more than 55 %.

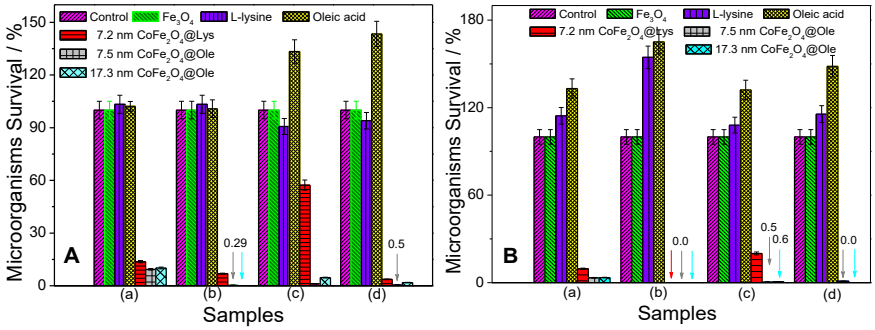

Figure. 55 Antimicrobial activities of 5-7 nm-sized $CoFe_2O_4$@Lys and oleic acid stabilized 7 and 17 nm-sized $CoFe_2O_4$@Ole after 24 h (A) and 72 h (B) incubation with *C. albicans* (a), *C. parapsilosis* (b), *E. coli* (c), and *S. aureus* (d). Pure L-lysine and magnetite NPs were investigated as a negative control. Error bars represent the standard deviations.

Consequently, in the cases with ~7 and ~17 nm-sized $CoFe_2O_4$@Ole NPs, the viability of microorganism were only 0.1 – 3.3 % after 72 h cultivation. The most striking result obtained in this examination was the absence of significant difference between 7 nm and 17 nm-sized cobalt ferrite NPs on the antimicrobial activity; contrary with results described previously, whereas the size dependant antimicrobial activity was observed. In order to evaluate the damages of microorganism cells caused by $CoFe_2O_4$@Ole NPs the confocal microscopy images were acquired after exposure with Co^{2+} ions and with *C. parapsilosis* cells. It was clearly seen that owing to auto-fluorescence of microorganism untreated, oval shaped *C. parapsilosis* cells (Fig. 56 a) display intact cell walls. However, after incubation with MIC content of Co^{2+} ions it was easy to observe the considerable alternations on cell walls (Fig. 56 b). In comparison with damaged yeast cells (Fig. 56 b) after 24 h treatment with $CoFe_2O_4$@Ole NPs, similar damaged cells were observed. Furthermore, the

aglomeration of NPs on the surface of microorganism, became visible, thus confirming the direct interaction of $CoFe_2O_4$ with the yeast cell.

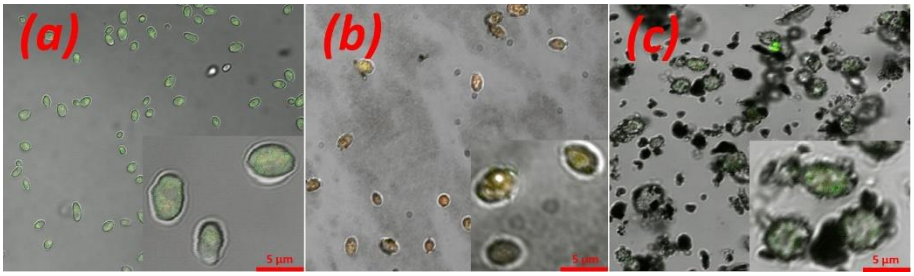

Figure. 56 Laser confocal microscopy images of *C. parapsilosis* strains before (a) and after incubation with MIC of Co^{2+} ions (b) and $CoFe_2O_4$@Ole NPs (c).

The possible explanations of significantly higher antimicrobial activity of $CoFe_2O_4$@Ole NPs might be related with their greater stability in liquid media. In general, the toxicity of solid material as NPs are associated with their size and probably with their active surface area [144]. As confirmed by TEM analysis, $CoFe_2O_4$@Ole NPs exhibit finely grained structure thus increasing the surface area of contacting material. On the other hand, negative charge of oleine acid stabilized NPs, perhaps can affect proteins and their positively charged groups in cell wall, due to electrostatic interactions, thus increasing the synthesized NPs toxicity. However, the mechanism of inactivation of microbes of such NPs are still not clear and additional experiments need to be performed.

3.4. Ultra-small gold NPs for inactivation of most dangerous bacteria strains

In this chapter, fabrication of ultra-small gold and gold-coated magnetite NPs *via* hydrothermal pathway and the subsequent gold ions reduction on the magnetite surface by methionine amino acid will be presented thoroughly. The surface chemistry, phase analysis, and antimicrobial activity of these NPs, were examined against three of 12 the worst bacteria families released by the WHO, in particular *A. baumannii*, *S. enterica*, *S. aureus* (MRSA) and *M. luteus* will be also presented and discussed as well.

3.4.1. Morphology and phase characterization of Fe_3O_4@Met NPs

In an attempt to develop biocompatible magnetic NPs the D,L-methionine amino acid was applied as NPs growth, gold ion reducing and stabilizing agent in the hydrothermal synthesis that employ both Fe^{2+} and Fe^{3+} salts at 2:1 molar ratio as precursors. The morphology of D,L-Met capped magnetite NPs synthesized *via* hydrothermal approach was investigated by high-resolution

TEM. It can be seen that magnetite NPs are mainly spherical (Fig. 57 a) with an average diameter of 11 nm and have quite narrow size distribution. Fig 57 a shows that Fe_3O_4@Met NPs are composed of single crystalline domain, as indicated clearly by atomic lattice fringes. Overall, these results indicated that NPs grow with a lattice spacing of 0.252 nm.

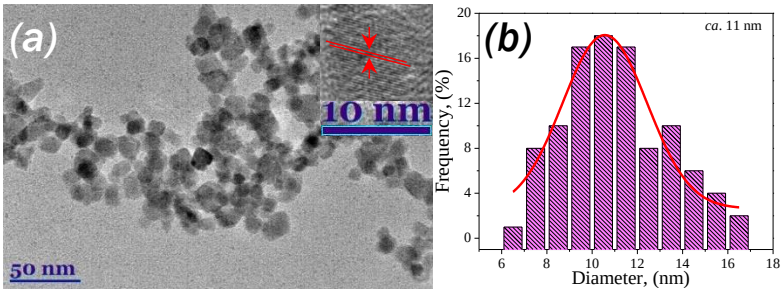

Figure. 57 TEM image (a) and size distribution histogram (b) of magnetite NPs synthesized hydrothermally in the solution containing 15 mmol L^{-1} $FeSO_4$, 30 mmol L^{-1} $FeCl_3$ and 0.195 mol L^{-1} methionine and NaOH to pH=12.4 at 130 °C for 10 h. The *Inset* illustrates atomic lattice fringes of a single Fe_3O_4@Met NP.

TEM observations are consistent with the data obtained in XRD (Fig. 58 a) confirming a face-centered cubic (fcc) crystal structure (space group *Fd-3m*, $a = b = c = 8.396$ Å).

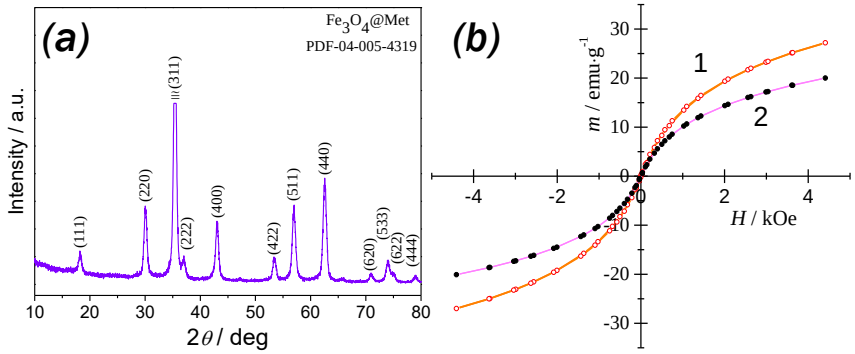

Figure. 58 XRD patterns (a) of Fe_3O_4@Met NPs and the magnetic responses (b) of Fe_3O_4@Met NPs before (1) and after sonication in a 10 mmol·L^{-1} $HAuCl_4$ solution, kept at a pH 12.2 and 37 °C for 4 h (2) are presented.

The XRD pattern of magnetite NPs (Fig. 58 a) implied the formation of pure, inverse spinel structure as all diffraction peaks at 2Θ positions: 18.28 (111), 30.08 (220), 35.43 (311), 43.06 (400), 53.42 (422), 56.94 (511), 62.53 (440), 70.94 (620), 73.97 (533), 74.97 (622) and 78.93 (444) match well with the standard polycrystalline Fe_3O_4 diffraction data summarized in the PDF Card No. 04-005-4319. The size of Fe_3O_4@Met NPs estimated from the corresponding XRD patterns using Halder-Wagner approximation equaled to

11.90±0.15 nm complementing the fact, that synthesized NPs are quite uniformly-sized.

3.4.2. Fabrication of gold decorated Fe_3O_4@Met@Au NPs *via* methionine induced Au^{3+} reduction

The gold-magnetite NPs hybrid was fabricated by methionine amino acid induced Au^{3+} reduction on Fe_3O_4@Met NPs surface. The process was carried out in the thermostatic bath containing well dispersed Fe_3O_4@Met NPs, methionine and $HAuCl_4$ solutions under the adapted conditions, as described previously. Figure 59 a and b shows the formation of numerous gold seeds at the surface of methionine-stabilized Fe_3O_4@Met NPs.

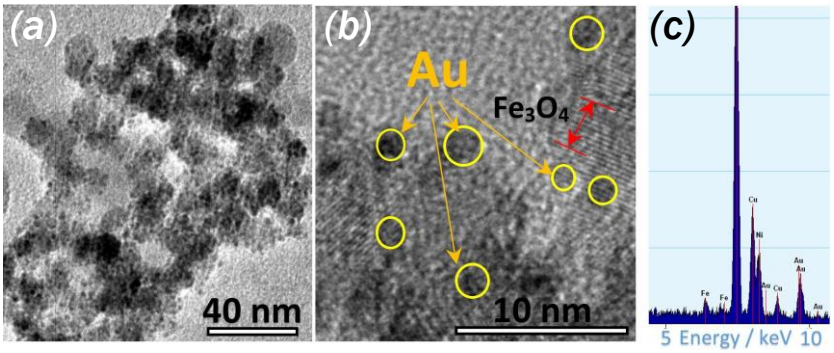

Figure. 59 TEM (a) and HRTEM (b) image of magnetite NPs after functionalization with gold nanocrystals *via* methionine-induced $HAuCl_4$ reduction under sonication and their EDX spectrum (c).

From TEM analysis, probably it was complicated to determine the size of deposited gold species, however, most of them seem to be in the range of 2-3 nm. According to previous research, the functionalization of magnetic particles with gold species usually decreased their saturation magnetization value [145]. Inspired by this idea, in this work the magnetic properties of pure magnetite and gold-magnetite hybrid NPs were assessed too. As can be seen in Fig. 58 b, both samples have magnetic saturation value approximately equal to 27 and 21 emu g^{-1} (at H_{max}= 4.4 kOe) thus confirming that magnetic NPs are surrounded by deposited small gold species. Furthermore, this data suggest that even after functionalization with gold seeds, the Fe_3O_4@Met@Au NPs have superparamagnetic behaviour, because the saturation magnetization value decrease by only 6 emu g^{-1}. Moreover, the formation of gold-magnetite hybrid was also verified by EDX spectrum as presented in Fig. 59 c.

3.4.3. Methionine induced detachment of ultra-small Au@Met NPs

To detach ultra-small gold NPs from the surface of magnetic NPs methionine amino acid was used. This process was linked to the stronger methionine-Au interaction comparing with Fe_3O_4@Met-Au bond. In order to obtain the particles size distribution as-formed, light-pink in colour solution with ultra-small gold NPs was further investigated by TEM. The images and size distribution histogram of NPs are presented in Fig. 60.

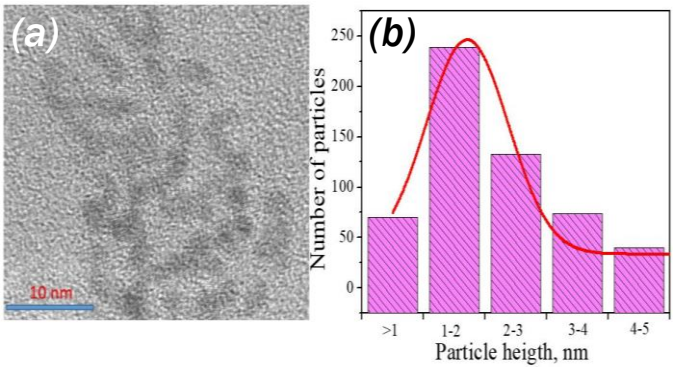

Figure. 60 TEM image (a), and size distribution histogram (b) of gold NPs detached from magnetite NPs.

As could be seen in the TEM views, ultra-small gold NPs exhibit spherical morphology with an average diameter of ~2.0 nm and have a quite narrow size distribution. Furthermore, these particles seem not to aggregate.

3.4.4. Antimicrobial activity of Fe_3O_4@Met, Fe_3O_4@Met@Au and Au@Met NPs against clinically isolated pathogens

For these studies, three of 12 the worst bacterial families as listed by WHO, of the drug-resistant bacteria that pose the greatest threat to human health and for which new antibiotics are desperately needed [5], have been chosen herein. Therefore, antimicrobial activity of ultra-small gold and Fe_3O_4@Met@Au NPs was investigated against gram-negative *A. baumannii*, *S. enterica*, and gram-positive *S. aureus* MRSA and *M. luteus* by assessing the CFU. In accordance with this investigation, Au@Met and Fe_3O_4@Met@Au NP probes containing 70 and 30 mg L^{-1} of these species were incubated in the M9 liquid media with the tested microorganisms under shaking for 24 hours. The histograms showing the percentage ratio of bacteria survival obtained from these assays are shown in Fig. 61. Besides that, 100 mg $L^{-1}$of D,L-methionine amino acid and 1 g L^{-1} of Fe_3O_4@Met NPs probes were also investigated as the negative control samples. It was observed that Au and Fe_3O_4@Met@Au NPs show the highest killing efficiency against *M. luteus* bacteria strains. This results further support the hypothesis, that human pathogenic microorganism

are more virulent and resistant than antibiotic-susceptible microbes such as *M. luteus* [146].

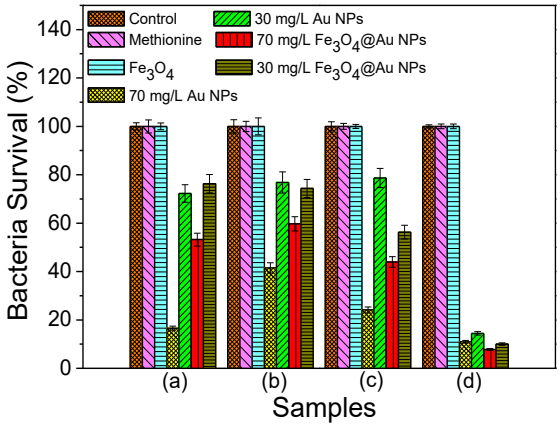

Figure. 61 Antimicrobial activities of synthesized ultra-small gold and Fe_3O_4@Met@Au NPs after 24 h incubation with gram-negative *A. baumannii* (a), *S. enterica* (b) and gram-positive *S. aureus* (MRSA) (c), *M. luteus* (d). For comparison, the behaviour of pure D,L-methionine and magnetite NPs is presented.

A positive correlation was obtained between the concentration of Au in NPs and bacteria survival. In comparison with the control sample, 70 mg L^{-1} of Au NPs exhibit the killing efficiency of 84.4-58.5 % against gram-negative and 89.1-75.7 % against gram-positive bacteria. In addition, Fig. 62 shows the quantity of gram-negative and gram-positive microorganisms grown on the Nutrient agar plates demonstrating a significant reduction of colonies count.

One unanticipated finding was that decreasing in the concentration of gold NPs approximately 2.3 times leads to bacteria assessment become by 3.05, 2.52, 1.35, and 1.04 fold weaker against *A. baumannii*, *S. enterica*, *S. aureus* (MRSA), and *M. luteus* bacteria, respectively. These results seem to be consistent with other researches which found that AuNPs of 5 nm showed no concentration dependent antibacterial effect against *B. subtilis* and *E. coli* microorganisms [102]. It should be noted that *S. enterica* demonstrated the strongest resistance against ultra-small gold and Fe_3O_4@Met@Au NPs. In the case of D,L-methionine coated magnetite NPs, as well as for the D,L- methionine amino acid, the same amount of CFU, as for the control sample, was obtained. However, the antimicrobial mechanism of D,L- methionine amino acid capped gold or gold-magnetite hybrid NPs is not clear and required further investigation. Nevertheless, some possible explanations of such antimicrobial behaviour might be related to the composition and structure of ultra-small gold NPs, because methionine shell are non-toxic. In order to clarify the reasons of such antimicrobial efficiency,

Au@Met and Fe_3O_4@Met@Au NPs were investigated by XPS. The obtained results are illustrated in Fig. 63 a and b.

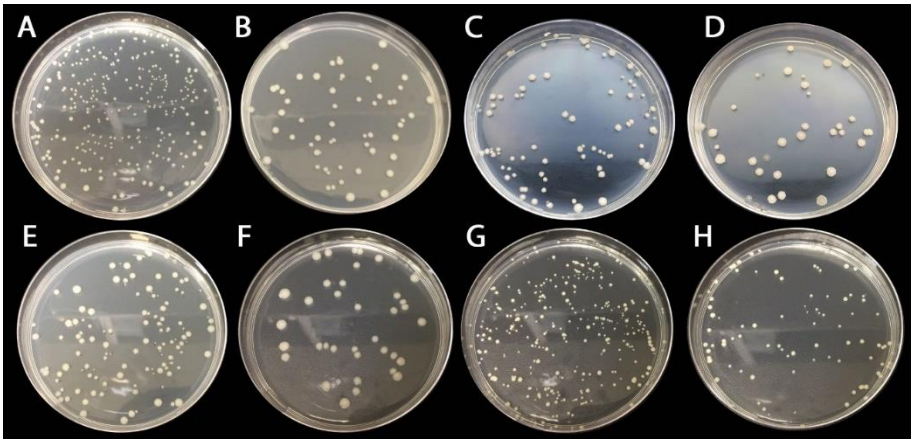

Figure. 62 Photographs showing the antimicrobial activity of Au NPs for growth inhibition of gram-negative (a-b) *A. baumannii*, (c-d) *S. enterica* (top row) and gram- positive (e-f) *S. aureus* MRSA, (g-h) *M. luteus* (bottom row) microorganisms incubated in the Nutrient agar plates. All microorganisms were cultivated in liquid M9 medium without (a, c, e, g) and with (b, d, f, h) 70 mg L^{-1} Au NPs for 24 h.

The XPS survey spectrum (Fig. 63 a) confirmed that our synthesis product consist of Fe, O, C, S and Au elements. Furthermore, carbon and sulphur peaks can be attributed to methionine molecules attached to the Fe_3O_4 or Au NPs surface. The main Au 4 $f_{7/2}$ photoelectron peak in the deconvoluted Au 4f spectrum (Fig. 63 b) is located at a binding energy (BE) of 83.94 eV, indicating the presence of pure metallic Au^0 [147].

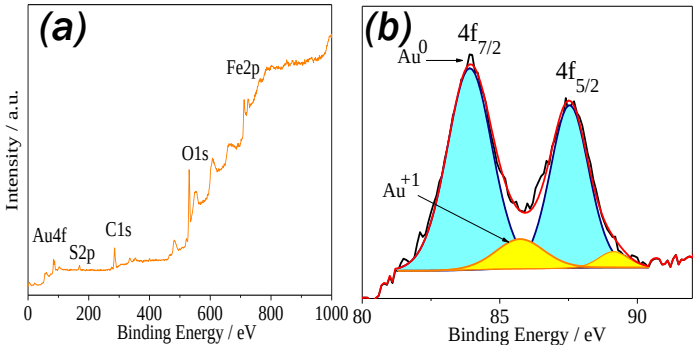

Figure. 63 XPS survey spectrum (a) of gold-magnetite hybrid NPs and deconvoluted spectrum of Au 4f (b).

The fitting of this spectrum was further performed by two spin-orbit split Au 4 $f_{7/2}$ and Au 4 $f_{5/2}$ components, separated by 3.56 eV. During this calculations additional peak was obtained at 85.74 eV indicating the presence

of Au^+ [148]. In accordance with the relative contents of elements, measured by XPS, the average content of the deposited gold was estimated roughly to be 1.67 % of the total NPs weight. We suspect that even insignificant amount of Au^+ ions attached to the surface of Au^0 NPs might be a reason of antimicrobial behaviour of tested NPs. Therefore, it was hypothesized, that bactericidal effect of Au@Met and Fe_3O_4@Met@Au NPs is due to Au^+ capable interact with bacteria membranes or proteins, thus leading to the microorganism death.

3.5. Wireless monitoring of biofilms of medically relevant bacteria and fungus

In this chapter, the innovative wireless sensing platform based on Ag/Ag^+ NPs redox couple for monitoring of medically relevant microbes such as *P. aeruginosa*, *E. coli*, *S. aureus*, *C. albicans* and *S. gordonii* will be described thoroughly. The biofilms, were grown on the carbon electrode, thus generating the electrons, which were used to reduce the poor conducting AgCl NPs to Ag^0 NPs. During this process, the resistance of Ag-Au NPs mixture modified SPE have changed significantly from 2-3 kΩ to 2-20 Ω. The response of electroactive biofilms was detected using RFID technology. The custom-made RFID antenna tag was connected to Ag-Au NPs decorated SPE, which act as a part of passive RFID tag and modulate the changes in conductivity of RFID antenna.

3.5.1. OCP measurements

In order to develop the battery-less sensing platform for monitoring of biofilms, the OCP measurement was determined firstly at various time periods. Following this procedure, glassy carbon rode was employed as an electron acceptor electrode, which was immersed in a fresh LB medium. The initial potential, measured by multimeter, was in the range of 35 – 160 mV *vs* Ag/AgCl reference potential (Fig. 64 t = 0). Then the experiment media was inoculated with microorganisms such as *P. aeruginosa*, *E. coli*, *S. aureus*, *C. albicans*, *S. gordonii* or their mixture with the final concentration of cells approximately equal to 10^6 CFU mL^{-1}. This content is relevant to the bacteria concentration in wounds normally reaching the numbers below 10^5 CFU g^{-1} tissue [149]. After inoculation, the potential gradually shifted to the negative direction and achieved the values varying in the range of -70 to -300 mV. The potential reduction rate slightly depended on the nature of microorganism culture and their growth characteristics. It was found that an OCP of GC electrode becomes negative after 4 h incubation with *E.coli* and *S. aureus*,

whereas *P.aeruginosa*, *S. gordonii* and *C. albicans* based biofilms generate negative potential just after 8 and 18 hours, respectively (Fig. 64 c, d, e).

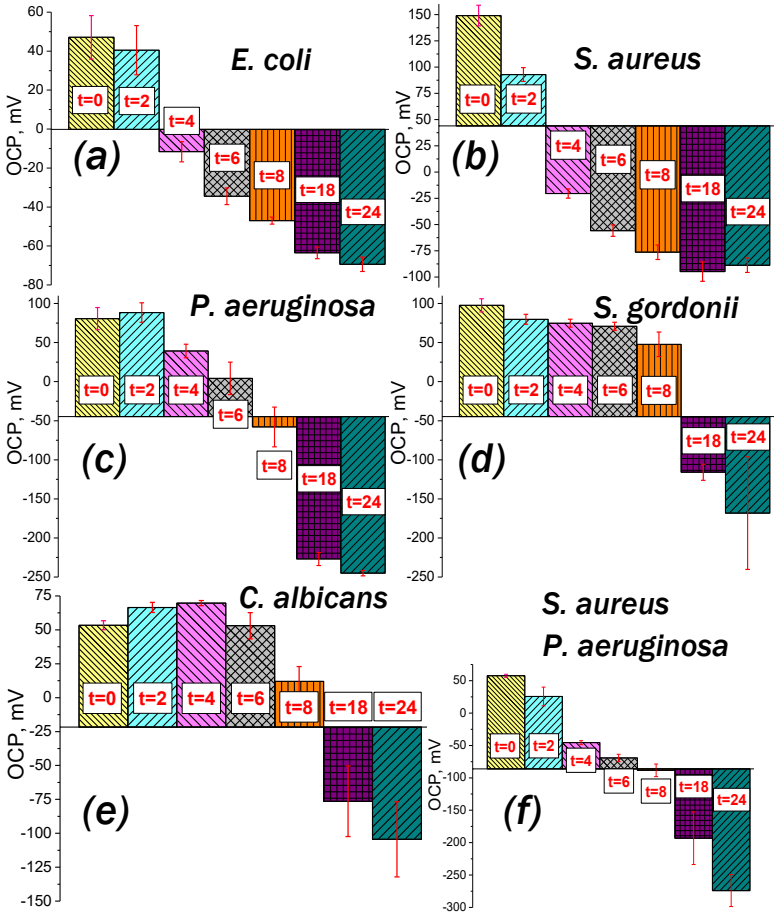

Figure. 64 OCP of bioanode immersed in LB media before (t=0) and after (t=2-24) inoculation with 10^6 CFU mL^{-1} of (a) *E. coli*, (b) *S. aureus*, (c) *P. aeruginosa*, (d) *S. gordonii*, (e) *C. albicans*, (f) co-culture of *S. aureus* and *P. aeruginosa*.

Furthermore, the potential developed by *P. aeruginosa* was more negative in comparison with other single species and reached around -250 mV. However, this microbe is well known as electroactive bacteria, which produce a soluble redox mediators as pyocyanin, phenazines or flavins that helps transfer an electrons [150]. Moreover, the co-culture conditions of *S. aureus* and *P. aeruginosa* were adapted since they are mainly responsible for chronic wound infections. According to the findings of Carolyn B. Ibberson's group, 10 fold less of *P. aeruginosa* than *S. aureus* were inoculated in order to prevent the predomination of *P. aeruginosa* after cultivation [151]. It was shown, that after 24 hours cultivation of co-culture, the potential developed by biofilms

achieved approximately -275 mV, thus facilitating the design of bioanode and improve its characteristics.

3.5.2. Design of sensing platform for wireless detection of biofilms

For construction of wireless biofilm detection platform, Ag and Au NPs modified screen printed electrodes were used as a sensing layer. As reported previously, the counter and working electrodes were short-circuited with layer formed by 1:5 (v/v) concentrated, 20-30 nm in diameter Ag and Au NPs mixture. The resistance measured between these electrodes after drop-casted deposition of NPs varied in the range of 2-30 Ω. In the next stage, fabricated electrodes were electrochemically oxidized into the chlorine containing electrolyte solutions. Note that this process has caused an increase in resistance to at least 2-3 kΩ due to $Ag^0 \rightarrow Ag^+$ conversion. The proof of concept was demonstrated using chronoamperometry, whereas the biofilms hosted electrode was coupled with Au-Ag modified SPE under a 5 mV negligible constant potential between them (Fig 65 a). The initial current approaching to zero μA due to poor conductivity of AgCl NPs, however it started to increase slowly at the first 2 hours. At this stage the co-culture of *S. aureus* and *P. aeruginosa* microbes require a time period to attach and form biofilm on the electrode surface, therefore generate a low amount of electrons. The reduction current increased rapidly at the time period of 2-7 hours with exponential regression until it reached complete reduction stage as illustrated in Fig. 65 a. The maximal reduction current value was around 170 μA. At this point, the resistance of SPE electrode dramatically dropped to ~ 25 Ω confirming the biofilms inspired completed reduction process of $Ag^+ \rightarrow Ag^0$ NPs.

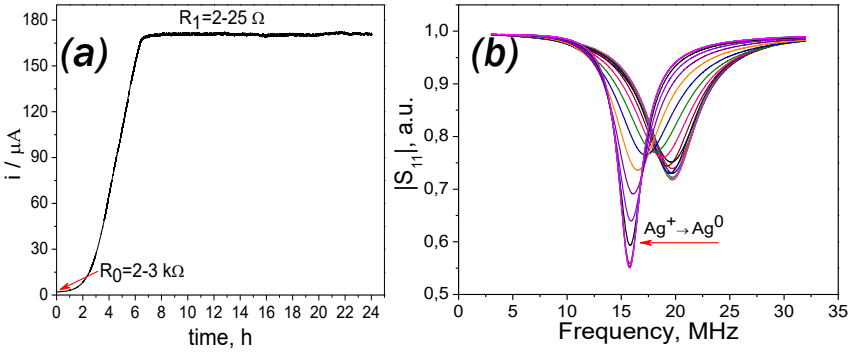

Figure. 65 *I-t* curve (a) obtained in two electrode cell, whereas the Ag-Au modified SPE was coupled to biofilms hosting electrode operated at a constant potential of 5 mV for 24 hours. In (b) the reflection coefficient |S11| as a function of frequency response of biofilms sensing platform immersed in *S. aureus* and *P. aeruginosa* containing LB media for 24 h.

The possibility of wireless biofilms monitoring *via* detection platform based on GCE, which act as a biofilm hosting electrode and Ag-Au NPs modified SPE was tested herein too. For this purpose, GCE was connected with SPE, which act as a part of passive RFID tag and modulate the changes in conductivity of RFID antenna. The electroactive biofilms formation on the bioanode inspired the reduction of AgCl NPs formed layer between C-W electrodes, resulting the higher backscattered energy to antenna. This process cause the resonance frequency shift from 18.0-20.0 MHz to 14-16.0 MHz as well as magnitude |S11|, which comes down from 0.7 to 0.55 a.u. as can be observed in Fig. 65 b. It was shown, that Ag-Au NPs employment as a short-circuit load between C-W electrodes on SPE determined a higher number of shifts in the range from higher to lower frequency, meaning that the changes in resistance of tag occurs gradually (Fig. 65 b). This alteration provides important advantages due to possibility read-out the signal at different frequency, resulting the shorter response time. These characteristics might allow a possibility to adapt such sensor designs for non-invasive monitoring of biofilms, especially in chronic wound infections. Furthermore, it might be transferred into medical hygiene products, particularly those used for elderly or incontinent. Besides that, wireless monitoring *via* proposed biofilms sensing platform could be easily integrated into the internet of things (IoT).

CONCLUSIONS

1. Black copper anodic oxide films exhibit the higher antimicrobial activity in comparison with the Cu_2O/TiO_2 and Cu_2O/TiNT heterostructures against *S. cerevisiae*, *A. versicolor*, *C. cladasporioides*, *C. parapsilosis* and *C. krusei* microorganisms.

2. Extremely thin porous anodic AAO films (≤ 1 μm) decorated with Ag nanowires array demonstrate bactericidal effect against *E. coli* and *M. luteus* bacteria. These coatings also inhibit the growth of *A. fumigatus* and *G. candidum* fungi and possess the fungicidal effect against *S. cerevisiae* yeast.

3. Cobalt ferrite NPs in the diameter of 2, 5 and 15 nm possess size-dependant antimicrobial activity against *S. cerevisiae* and several *Candida* species, in particular, *C. parapsilosis*, *C. krusei* and *C. albicans*.

4. L-lysine coated, similar in size (5-6 nm), iron substituted cobalt ferrite NPs demonstrate the high, Co^{2+} content-dependent antimicrobial efficiency against gram-negative *E. coli* and gram-positive *S. aureus* bacteria and several *Candida* species.

5. Antimicrobial activity strongly depends on the nature of ligands capped on the surface of NPs. Oleic acid stabilized $CoFe_2O_4$@Ole NPs demonstrate enhanced antimicrobial behaviour against *E. coli*, *S. aureus*, *C. parapsilosis* and *C. albicans* in respect to similar in size $CoFe_2O_4$@Lys ones.

6. Ultra-small gold (≤ 2 nm) and gold-magnetite NPs hybrid with the concentration of 70 mg L^{-1} shows the killing efficiency of 84.4-58.5 % against gram-negative *A. baumannii*, *S. enterica* bacteria and 89.1-75.7 % against gram-positive *S. aureus* MRSA, *M. luteus* bacteria strains.

SANTRAUKA

Įvadas

Infekcinių ligų sukėlėjai yra įvairių rūšių mikroorganizmai, plačiąja prasme – tai mikroskopiniai grybai, bakterijos ir virusai. Antibiotikams atsparūs mikroorganizmai (AAM), kurie inicijuoja infekcijas šiandieniniame pasaulyje sukelia apie 700000 mirčių per metus. Prognozuojama, jog iki 2050 metų šis skaičius išaugs iki 10 milijonų per metus [1]. Preliminariai apskaičiuota, kad AAM sukeltų infekcijų daroma žala pasaulyje sieks iki 100 trilijonų JAV dolerių [2]. Paminėtina, kad ekonomiškai silpnesniuose regionuose, kaip antai Afrika, Rusija ir Azija įskaitant Kiniją, AAM sukeltų infekcijų gydymas auga eksponentiškai. Žinoma, kad AAM sukeltos infekcijos šiais laikais Europoje pražudo beveik po 25 tūkstančius pacientų kasmet, kas Europos sąjungai kainuoja apie 1,5 milijonų eurų per metus [3]. Jei nieko nebus imtasi iki 2050 metų šis skaičius išaugs tokiu būdu sumažindamas bendrąjį Europos sąjungos BVP nuo 1 % iki 4,5 %. Taigi, naujų potencialių antimikrobinių preparatų sukūrimas ir tobulinimas yra būtinas siekiant apsisaugoti nuo AAM sukeltų infekcijų.

Augantis antibiotikams atsparių patogeninių mikroorganizmų skaičius yra vienas iš didžiausių iššūkių su kuriais susiduria šių laikų mokslo bendruomenė. Anot Römling ir jos bendraautorių, iki 80 % žmogaus infekcijų, kurių kaltininkės yra bakterijos, sietinos su bioplėveles formuojančiomis padermėmis. Šios bioplėveles sudarančios bakterijos sukelia įvairias audinių infekcijas; pagrindinės iš jų: lėtinės žaizdos, vidurinės ausies uždegimas, infekcinis endokarditas, cistinė fibrozė ar su ja susijusios plaučių infekcijos [4]. Visai neseniai, pasaulio sveikatos organizacija (PSO) paskelbė sąrašą dvylikos pačių pavojingiausių antibiotikams atsparių bakterijų. Tarpe jų yra ir tokios rūšys, kaip antai *Acinetobacter baumannii, Pseudomonas aeruginosa* ar *Staphylococcus aureus* MRSA ir kt. Jos kelia didžiausią pavojų žmogaus sveikatai o efektyviam gydymui reikalingi nauji antimikrobiniai preparatai [5]. Dėl šios priežasties yra būtina sutelkti mokslininkų pastangas, efektyvesnių antimikrobinių agentų paieškai ir inovatyvių sprendimo idėjų plėtotei kas padėtų spręsti mikrobinės taršos problemas. Vienas iš tokių būdų yra sumanių nanodalelių (ND), galinčių padėti kovoje su antibiotikams atspariomis bakterijomis, panaudojimas. Šios nanometrų dydžio medžiagos dažnai pasižymi unikaliomis savybėmis kurios nėra būdingos iš daug tų pačių atomų sudarytoms medžiagoms. Teigiama, kad dėka didelio jų paviršiaus ploto/tūrio santykio ir universalumo, nanodalelės galėtų padidinti gydymo efektyvumą ir sumažinti vaistų šalutinį poveikį [6]. Yra žinoma, kad ZnO, Cu,

CuO, Cu_2O, Ag, Au, MgO nanodalelelės pasižymi ne tik antimikrobinėmis savybėmis bet ir galimybe sumažinti mikroorganizmų gyvybingumą ant skirtingų paviršių bei neleidžia pastariesiems formuoti bioplėvelių [7]. Naujausi tyrimai rodo, kad kobalto feritas ar kitu metalu legiruotos jo formos taip pat pasižymi antimikrobinėmis savybėmis prieš įvairias mikrobų rūšis ir galbūt gali būti naudojamas kaip perspektyvus antimikrobinis preparatas. Deja, tikslesnis jų poveikis prieš plataus spektro bakterijas ir mikroskopinius grybus, ypač tuos, kurie yra atsparūs antibiotikams, kol kas yra nežinomas. Siekiant išplėsti ir praturtinti turimas žinias bei inicijuoti tolimesnius darbus susijusius su metalinių ir puslaidininkių ND pritaikymo galimybėmis antimikrobinių medžiagų srityje, pastarosios šiame darbe buvo aktyviai tyrinėjamos, o gauti rezultatai yra teikiami šiame darbe.

Darbo tikslas

Susintetinti metalines ir puslaidininkines nanodaleles ir ištirti jų antimikrobines savybes plataus spektro bakterijų, mielių ir mikroskopinių grybų aplinkose.

Darbo uždaviniai

- ✓ Padengti titano oksidų paviršių vario suboksido nanodariniais ir palyginti jų antimikrobines savybes su dvivalenčio vario oksido anodinėmis dangomis suformuotomis ant Cu padėklo.
- ✓ Sukurti elastines, sidabro nanodariniais dekoruotas anodines oksidines dangas maistinių aliuminio folijų paviršiuje, suteikiant joms antikorozines, dekoratyvines ir antimikrobines savybes.
- ✓ Susintetinti skirtingo dydžio kobalto ferito ND ir įrodyti jų antimikrobinio efektyvumo priklausomybę nuo dydžio.
- ✓ Suformuoti L-lizino amino rūgštimi stabilizuotas kobalto ferito ND su skirtingu Fe kiekiu ir nustatyti gautų darinių antimikrobinių savybių priklausomybę nuo kobalto.
- ✓ Ištirti superparamagnetinių kobalto ferito ND stabilizuojančios apsupties įtaką antimikrobiniam jų aktyvumui įvairių bakterijų ir mikroskopinių grybų terpėse.
- ✓ Susintetinti ultra-smulkių aukso ir magnetito-aukso ND, stabilizuojant jas D,L-metionino amino rūgštimi ir įvertinti jų antimikrobinę elgseną prieš

antibiotikams atsparias bakterijų padermes, kaip antai *S. enterica*, *S. aureus* MRSA ir *A. baumannii*.

Darbo naujumas

- ✓ Pirmą kartą ištirtos dangų Cu_2O/TiO_2, Cu_2O/TiNT ir CuO/Cu antimikrobinės savybės. Išsiaiškinta, kad anodiškai oksiduotas varis pasižymi didesniu antimikrobiniu aktyvumu prieš visas tirtas mielių ir mikroskopinių grybų padermes.
- ✓ Pirmą kartą parodyta, kad itin ploni poringi anodinio aliuminio oksido sluoksniai (≤ 1 μm) užauginti ant aliuminio folijų paviršiaus ir elektrochemiškai dekoruoti aukso atspalvį suteikiančiomis sidabro nanovielomis pasižymi antimikrobiniu aktyvumu ir gali rasti naujų taikymų greitai gendančių produktų pakavimui.
- ✓ Pirmą kartą parodyta kobalto ferito ND antimikrobinės elgsenos priklausomybė nuo jų dydžio, cheminės sudėties ir aplinkos.
- ✓ Pirmą kartą pademonstruotos ultra-smulkių aukso ir magnetito-aukso hibridinių ND antimikrobinės savybės prieš antibiotikams atsparias bakterijų *S. enterica*, *S. aureus* MRSA ir *A. baumannii* padermes.

Ginamieji teiginiai

- ✓ Juodos spalvos dvivalenčio vario oksido nanostruktūrizuotos dangos pasižymi stipresniu antimikrobiniu aktyvumu prieš mielių ir mikroskopinių grybų rūšis nei vienvalenčio vario oksido dangos.
- ✓ Itin plonų (≤ 1.0 μm) anodinio aliuminio oksido plėvelių dekoravimas metalinio sidabro nanovielomis suteikia maistinio aliuminio folijai antimikrobines, dekoratyvines ir antikorozines savybes.
- ✓ Kobalto ferito ND yra perspektyvus antimikrobinis preparatas, o jo antimikrobinė elgsena bakterijų ir mikroskopinių grybų aplinkose ženkliai priklauso nuo ND dydžio, cheminės sudėties ir aplinkos.
- ✓ Ultra-smulkios aukso (~2 nm) ir magnetito-aukso hibridinės ND, kurių koncentracija – 30 mg L^{-1} ir daugiau slopina antibiotikams atsparių bakterijų *Salmonella enterica*, *Staphylococcus aureus* MRSA ir *Acinetobacter baumannii* augimą.

Autoriaus indėlis

Disertacijos autorius pats sintetino, formavo ir surinkinėjo disertaciniame darbe minėtas dangas bei nanodaleles. Taip pat pats atliko antimikrobinius tyrimus, ND minimalios inhibuojančios koncentracijos nustatymus, paruošė bandinius SEM, PEM ir konfokalinės mikroskopijos analizėms. Be to, autorius svariai prisidėjo analizuojant gautus eksperimentinius duomenis, kūrė grafines iliustracijas bei rengė mokslines publikacijas. Žodinius ir stendinius pranešimus tarptautinėse konferencijose pristatinėjo pats. Visi neorginalūs paveikslai teikiami šiame darbe yra cituojami.

4. LITERATŪROS APŽVALGA

Mikroorganizmų sukeltos infekcijos yra viena iš pagrindinių lėtinių infekcijų ir žmonių mirtingumo priežastis. Remiantis Pasaulio sveikatos organizacijos (PSO) paskelbtais duomenimis užkrečiamos ligos yra antra labiausiai paplitusi žmonių mirtingumo priežastis, apimanti beveik 25 % žmonių mirčių visame pasaulyje. Be to, ši situacija yra kur kas blogesnė regionuose, tokiuose kaip Afrika, kur užkrečiamos ligos sukelia apie 50-52 % visų mirčių [7]. Negana to, yra žinoma, kad mikroorganizmai, kaip antai bakterijos, mutuoja ir tampa vis atsparesnės antibiotikų poveikiui; tokiu būdu dar labiau komplikuodamos padėtį. Nuo 1928 metų, kai A. Flemingas atrado peniciliną iki 2015 metų, kai buvo atrastas ceftarolinas, bakterijų atsparumo antibiotikams problema buvo ir yra dažnai pabrėžiama mokslinėje spaudoje. Didėjantis vaistams atsparių patogeninių mikroorganizmų skaičius yra vienas iš svarbiausių šių laikų iššūkių su kuriais susiduria mokslo visuomenė. Dėl šios priežasties yra būtina atkreipti platesnį mokslininkų dėmesį, kurti inovatyvias sprendimo idėjas ir antimikrobinius agentus, kurie išspręstų ar bent padėtų spręsti kylančią problemą. Vienas iš tokių būdų – sumanių nanodalelių (ND), nanokompozitinių medžiagų ar nanogelių, galinčių padėti kovoje su antibiotikams atspariomis bakterijomis panaudojimas [61].

Nanodalelės dažnai pasižymi unikaliomis fizikinėmis ir cheminėmis savybėmis. Šias savybes, kurios nėra būdingos iš daug tų pačių atomų sudarytoms medžiagoms, lemia didelis jų paviršiuje esančių nekoordinuotų atomų su koordinuotais santykis ir kvantinės savybės [152]. Dėka šitų savybių sidabro, vario, cinko, magnio, titano oksidų ir kt. ND baktericidinis poveikis dažnai yra efektyvesnis, nei antibiotikų [3]. Tad pastaraisiais metais sparčiai tyrinėjamos įvairios medžiagos nano-dydžių skalėje. Šioje disertacijoje pagrindinis dėmesys skiriamas kobalto ferito ND jų aplinkos ir cheminės sudėties bei dydžio įtakos antimikrobinio poveikio efektyvumui. Taip pat aprašomos vario bei sidabro pagrindu suformuotos antimikrobinės dangos, bei ultra-smulkios aukso ND, kurios slopina antibiotikams atsparių bakterijų gyvybingumą. Disertacijos literatūrinėje dalyje plačiau aptariamos darbe naudotos ND sintezės metodikos, taip pat apžvelgtos sidabro, vario, vario oksidų, kobalto ferito ir aukso ND antimikrobinės savybės, bei naujausi atradimai šioje srityje.

5. EKSPERMENTO METODIKA

Šio darbo metu kintamos ir nuolatinės srovės nusodinimo, bei elektrocheminio anodavimo metodikos buvo panaudotos siekiant gauti heterostruktūrizuotas Cu_2O/TiO_2, Cu_2O/TiNT, CuO/Cu ir Ag/AAO dangas. Hidroterminis, ko-nusodinimo ir terminio skaldymo metodai buvo naudojami siekiant suformuoti skirtingo dydžio, cheminės aplinkos ir cheminės sudėties kobalto ferito ND. Ultra-smulkios aukso ir magnetito-aukso hibridinės ND buvo formuojamos dėka metionino (MET) amino rūgšties inicijuotos aukso rūgšties redukcijos ant magnetinių ND paviršiaus. Pasinaudojant stipresne Au-MET sąveika, Au ND buvo „atkabinamos“ nuo Fe_3O_4 ND paviršiaus. Disertaciniame darbe sintetintos dangos ir ND buvo tirtos įvairiais fizikiniais ir cheminiais metodais. Pagrindiniai iš jų trumpai aprašyti šioje dalyje:

Dangų paviršiaus ir lūžio morfologijos bei jų storis buvo tirtas skenuojančiu elektroniniu mikroskopu Helios Nanolab 650 (FEI Quanta 200 F, Olandija). Nanodalelių dydis, forma bei kristališkumas buvo įvertinti peršvietimo elektroniniu mikroskopu Tecnai F20 X-TWIN (FEI, Olandija). Elementinė nanodalelių sudėtis buvo tiriama energijos dispersijos spektrometru (EDAX, JAV), integruotu tiek prie PEM tiek prie SEM mikroskopų. Dalelių fazinė sudėtis bei jų aplinkos chemija buvo nustatyta Ramano spektrometru In Via (Renishaw, Didžioji Britanija). Suformuotų dangų bei miltelių fazinė analizė atlikta rentgeno spindulių difraktometru SmartLab (Rigaku, Japonija). ND stabilizuojančių L-Lys, D,L-Met ir oleino rūgšties adsorbcija ant ND paviršiaus tirta Furjė transformacijos infraraudonųjų spindulių spektrometru ALPHA FTIR (Bruker, Vokietija). Magnetito-aukso ir Au ND elementinė sudėtis bei jų valentingumas tirti rentgeno fotoelektronų spektroskopu VG ESCALAB MK II (VG Scientific, Didžioji Britanija). Aukso ir kobalto ferito ND dydis bei dispersiškumas tirti atominės jėgos mikroskopu Veeco AFM diInnova (Veeco Instruments, JAV). Geležimi pakeistų kobalto ferito ND cheminė sudėtis tirta Mesbauerio spektroskopu Wissel (Wissenschaftliche Elektronik GmBH, Vokietija) bei indukuotos plazmos optinės emisijos spektrofotometru OPTIMA 7000DV (Perkin Elmer, JAV). ND zeta potencialas išmatuotas Nicomp 380 ZLS matavimo sistema. ND magnetinės savybės tirtos panaudojant FH 54 teslametrą (Magnet-Physics, GmBH, Vokietija). Mielių ląstelių mikroskopavimas ir ląstelės struktūros pokyčiai po tiesioginės sąveikos su ND fiksuoti konfokaliniu mikroskopu Nicon eclipse TE2000 C1 Plus (Plan Apo VC, Japonija).

Detalesnė tyrimų metodika ir ND bei dangų sintezės sąlygos plačiau aprašytos disertacijos metodinėje dalyje.

6. TYRIMO REZULTATAI IR JŲ APTARIMAS

6.1. Heterostruktūrizuotų Cu_2O/TiO_2, Cu_2O/TiNT ir CuO/Cu dangų sintezė, charakterizavimas ir antimikrobinių savybių tyrimas

6.1.1. Heterostruktūrizuotų dangų paviršiaus morfologija

Vienvalenčio vario kristalais dekoruoto, termiškai oksiduoto Ti paviršiaus SEM nuotraukos (1 pav. a ir b dalis) iliustruoja, kad silpnai rūgščiuose (pH ~ 5,28) vario acetato tirpaluose kintančiosios srovės lauke nusodinami kristalai yra oktaedrinės struktūros Cu_2O, kurie pasižymi gana taisyklinga forma. Jų dydis – 200-400 nm.

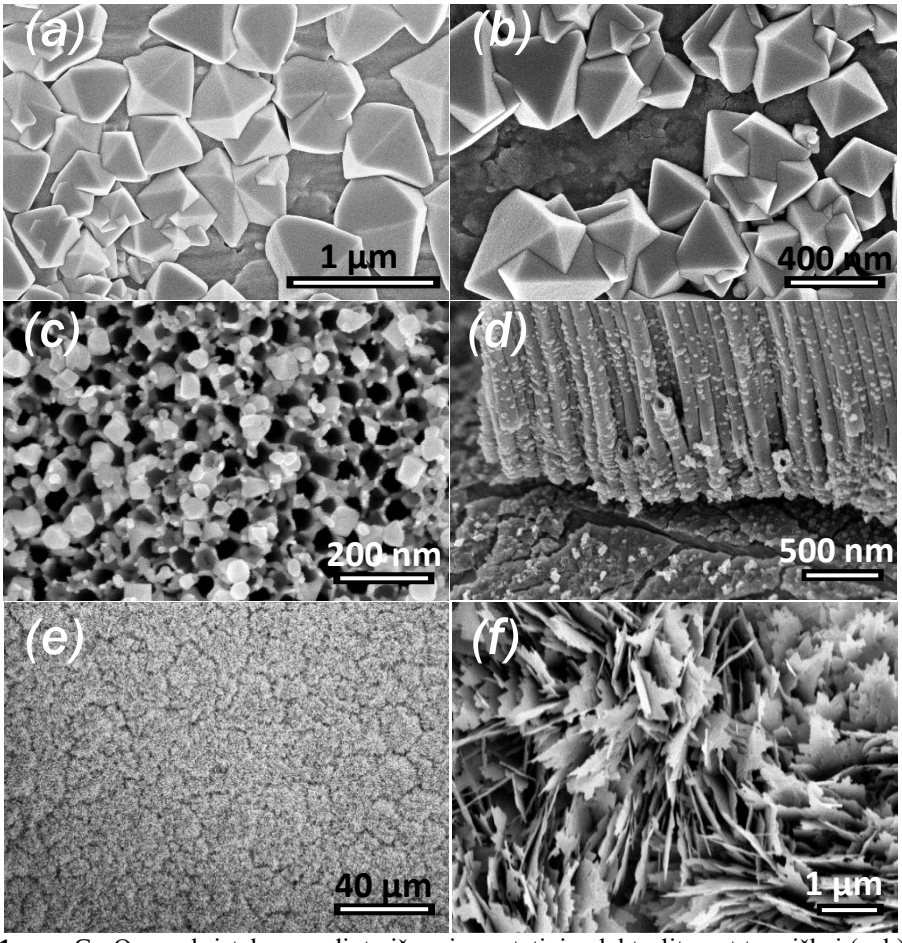

1 pav. Cu_2O nanokristalų nusodintų iš vario acetatinio elektrolito ant termiškai (a, b) ir elektrochemiškai oksiduoto Ti paviršiaus (c) ir lūžio (d) SEM vaizdai. Elektrochemiškai anoduoto vario paviršiaus SEM vaizdai pateikti (e, f).

Ilgėjant nusodinimo trukmei, „augančios“ struktūros uždengia vis didesnį paviršiaus plotą kol ilgainiui padengia jį pilnai. Tęsiant sodinimą ilgiau, susidaro įvairios formos aglomeratai. Pastabėta, kad elektronusodinimo metu palaikant 100 Hz kintančios srovės dažnį, oktaedrinės formos Cu_2O kristalai „auga“ šiek tiek mažesni, be to jų sėdimas yra kur kas tolygesnis.

Korinės struktūros titano paviršius gaunamas anoduojant Ti etilenglikolio-vandens-amonio fluorido elektrolite (1 pav. c ir d dalis). Šių tyrimų sąlygomis gautų vamzdelių, orientuotų statmenai paviršiui, ilgis buvo 4-6 μm o diametras – 45-50 nm. Susiformavusi amorfinė danga buvo rekristalizuota oro atmosferoje prie 450 °C temperatūros. Taip buvo gaunama gryna anatazo kristalinė fazė. Tokios dangos kintančiąja srove „dekoruotos“ Cu_2O nanokristalais naudojant tą pačią elektrolito sudėtį. Esant optimaliomis nusodinimo sąlygomis, nanokristalai paviršių padengia gana tolygiai. Dalis Cu_2O nusėda išilgai nanovamzdelių (1 pav. d), dalis ant paviršiaus (1 pav. c). Suformuotų kristalitų dydis vyrauja nuo 15 iki 50 nm. Nustatyta, jog nusodintų darinių kiekį TiO_2 matricoje ir dalelių dydį galima kontroliuoti varijuojant nusodinimo trukme ir režimu. Be to, pastarasis neturėtų viršyti $j_{ks} \sim 3{,}5$ mA cm^{-2}, nes esant tokiam srovės tankiui, bandinių kampuose prasideda TiO_2 plėvelės destrukcija.

Pluoštinės struktūros CuO dangos buvo gautos anoduojant vario elektrodus karštame natrio šarmo ir amonio molibdato elektrolite. Gauti produktai buvo rekristalizuojami oro atmosferoje, 250 °C temperatūroje. Nustatyta, kad susidariusi juodos spalvos anodinio oksido danga yra dvisluoksnė. Apatinė jos dalis susideda iš gana kompaktiško ir vientiso sluoksnio. Paviršiuje didžioji dalis anodinės oksidacijos metu gautų “lapelių” yra orientuoti vertikaliai (1 pav. f). Jų plotis vyrauja nuo keleto dešimčių iki šimtų nanometrų, tuo tarpu lapelio storis – vos keletas nanometrų. Tokiu būdu suformuotų dangų storis buvo 6-7 μm, o jos paviršiaus plotas, lyginant su geometriniu, išaugo net 825 kartus [114].

6.1.2. Cu_2O nusodinimo ant termiškai ir anodiškai oksiduoto Ti kinetika

Siekiant optimizuoti Cu_2O nusodinimo ant termiškai ir anodiškai oksiduoto Ti paviršiaus tolygumą, buvo tiriamos nusodinto vario kiekio priklausomybės nuo elektrocheminio sodinimo sąlygų. Vykdant nusodinimą ant anodiškai oksiduoto Ti paviršiaus Cu_2O kiekis tiesiškai priklauso nuo proceso trukmės, taip pat priklauso nuo lauko stiprio ir dažnio (2 pav. a). Kai U_{pik}=1,8 V, Cu_2O nusėda žymiai daugiau nei prie U_{pik}=1,2 V. Tai sietina su ženkliai didesniais srovės kiekiais (j_{ks}=30 mA), pratekančiais per elektrodą. Nustatyta, kad didelę įtaką Cu_2O elektrocheminio nusodinimo kinetikai Ti vamzdelių matricoje turi TiO_2 barjerinis sluoksnis. Siekiant jį suploninti,

anodavimo proceso pabaigoje buvo mažinama įtampa iki 30 V kas 1 V min^{-1}. Šiuo keliu TiO_2 barjeras patirpinamas ir Cu_2O išsikrovimas vėliau vyksta kur kas sparčiau ir tolygiau visame TiO_2 paviršiaus plote (1 ir 3 kreivės).

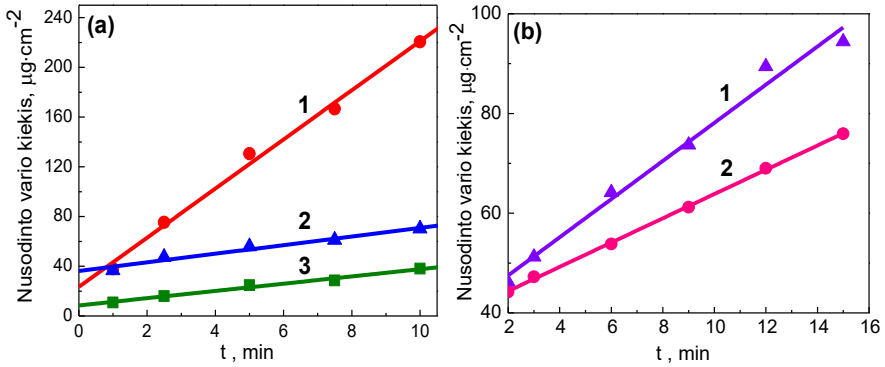

2 pav. Vario kiekio priklausomybės nuo sodinimo laiko ant anoduoto (a) ir termiškai oksiduoto (b) Ti. (a): 1 ir 2 kreivė žymi Cu_2O nusodinimą esant U_{pik}=1,8 V ir 3 – esant 1,2 V, o kintančiosios srovės dažnis 50 Hz. (b) kai U_{pik}=1,3 V o dažnis 50 (1) arba 100 (2) Hz.

Tiesinė vario priklausomybė nuo sodinimo trukmės buvo gauta nusodinant Cu_2O ant termiškai oksiduoto Ti (2 pav b dalis). Šių tyrimų metu buvo tiriama kintančiosios srovės dažnio ir lauko stiprio įtaka. Nustatyta, kad nusodinamo Cu_2O kiekis priklauso ir nuo srovės dažnio (2 pav. 1 ir 2 kreivės). Būtina paminėti, jog tiesinės $m_{Cu_2O}(t)$ ryšys yra charakteringas tik nuo antros sodinimo minutės, kai procesas visame paviršiuje vyksta tolygiai. Nustatyta, kad esant 50 Hz kintančiosios srovės dažniui, sėdimas vyksta greičiau (2 pav. 1), tačiau esant 100 Hz dažniui – kur kas tolygiau.

6.1.3. Cu_2O/Ti, Cu_2O/TiNT ir CuO/Cu dangų fazinė analizė

Suformuotų korinės struktūros dangų rentgenofazinė analizė rodo, kad atkaitinus oro atmosferoje anoduotą Ti dangą prie 450 °C, ši tapo kristaline anatazo faze su jai būdinga tetragonine kristaline struktūra (3 pav b). Pažymėtina, jog rekristalizacijos metu, TiO_2|Ti fazių sąlyčio riboje susidaro šiek tiek priemaišinės nestechiometrinės, kubinės gardelės $Ti_{0,91}O$ fazės. Priešingai nei anoduoto Ti atveju, termiškai inicijuotos TiO_2 fazės susidarymo įrodymų net užrašant rentgenogramą slystančio kampo metodu gauta nebuvo. Tai galima aiškinti tuo, kad terminės oksidacijos metu, susidariusios TiO_2 kiekis yra per mažas, dėl to TiO_2 charakteringų smailių gauta nebuvo. Remiantis literatūra, anatazo kristalinė fazė formuojasi jau esant 400 °C temperatūrai [153]. Atkaitinus aukštesnėje temperatūroje ($t \geq 500$ °C), būtų gaunamas rutilas – termodinamiškai stabiliausia TiO_2 fazė, tačiau dėl jam būdingos greitos elektrono-skylės rekombinacijos, kas labai sumažintų tokių

sluoksnių fotokatalitinį aktyvumą [154] rutilo dangos nebuvo formuojamos ir tiriamos.

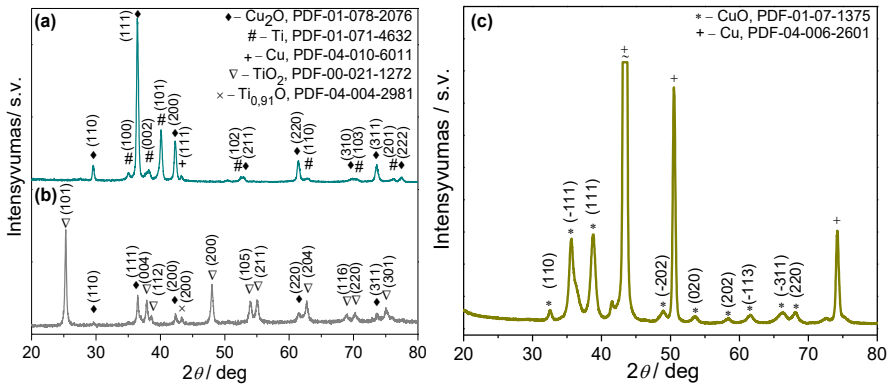

3 pav. Vienvalenčio vario oksidais dekoruoto termiškai (a) ir anodiškai (b) oksiduoto Ti dangų difraktogramos. (c) anoduoto vario, atkaitinto 250 °C temperatūros oro atmosferoje, rentgenograma.

Rentgenogramose (3 pav. a ir b dalis) aiškiai matomos intensyviausios smailės 2θ kampų intervale 29,58, 36,42, 42,32, 61,46 ir 73,60. Jų Milerio indeksai atitinkamai yra (110), (111), (220) ir (311), ir liudija polikristalinę kubinės struktūros kuprito (Cu_2O) fazę. Taip pat, ant termiškai oksiduoto Ti, dekoruoto Cu_2O kristalais, yra stebima ir metaliniam variui būdinga smailė (3 pav. a), tačiau jokių pašalinių CuO ar $Cu(OH)_2$ fazių nebuvo identifikuota. Anoduoto vario rekristalizuoto oro atmosferoje prie 250 °C temperatūros rentgenograma įrodo, kad šarminiuose amonio molibdato elektrolituose gautos juodos spalvos dangos yra monoklininės kristalinės struktūros tenoritas – CuO (3 pav. c). Kadangi vario oksido storis nėra didelis (6-7 μm), difraktogramoje yra Cu pagrindui charakteringos smailės. Verta pažymėti, kad jokių pašalinių Cu_2O ar $Cu(OH)_2$ fazių gauta nebuvo.

6.1.4. Elektrochemiškai suformuotų Cu_2O/Ti, Cu_2O/TiNT ir CuO/Cu dangų antimikrobinės savybės

Gautų dangų antimikrobinės savybės buvo tirtos lizės zonų metodu prokariotinių (*E. coli, P. aeruginosa, M. luteus*) ir eukariotinių (*S. cerevisiae, A. versicolor, P. chrysogenum, C. cladosporioides, C. parapsilosis, C. krusei*) mikroorganizmų aplinkose. Apie disko formos bandinius susidariusios inhibicinės zonos (4 pav.) įrodo, jog elektrochemiškai suformuotos dangos pasižymi antimikrobinėmis savybėmis. Šios dangos didžiąja dalimi demonstruoja fungicidinį ir bakteriocidinį poveikio mechanizmą prieš testuotas mikrobų rūšis. Tačiau yra ir išimčių: Cu_2O/TiO_2 dangos atveju fungistatinis efektas užfiksuotas prieš *A. versicolor* ir *C. parapsilosis*

mikroskopinius grybus, o Cu_2O/TiNT dangos atveju šis efektas pasireiškė prieš *A. versicolor*, *C. parapsilosis* ir *C. krusei* mikromicetus. Be to abu heterostruktūrizuoti paviršiai nerodė jokio antimikrobinio aktyvumo prieš *P. chrysogenum* ir *C. cladosporioides* mikroskopinius grybus.

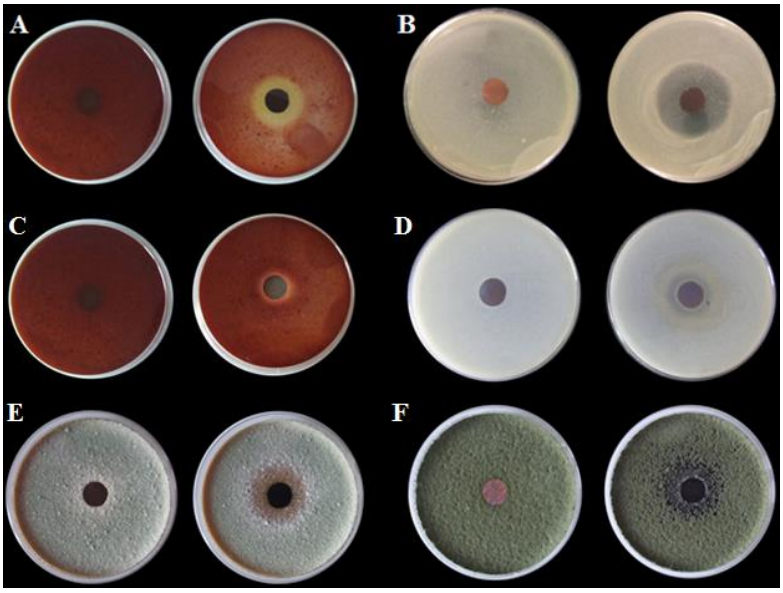

4 pav. Kokybinės analizės rezultatai panaudojant eukariotinius mikroorganizmus: pirma eilutė – Cu_2O/TiO_2, antra – Cu_2O/TiNT ir trečia – CuO/Cu dangos prieš A, C, E – *A. versicolor*, B – *S. cerevisiae*, D – *C. krusei* ir F – *C. cladosporioides*. Kairėje pusėje – ląstelių kultūros kontrolė, dešinėje pusėje – fungistatinė/cidinė zona.

Būtina paminėti, jog CuO/Cu dangos demonstravo pastebimai didesnį antimikrobinį aktyvumą prieš visas minėtas kultūras, išskyrus *P. chrysogenum* mikroskopinius grybus. Toks efektyvumas siejamas su itin dideliu dangų paviršiaus plotu, kas lemia padidintą potencialią vario jonų „atsipalaidavimo“ galimybę nuo nanostruktūrizuoto CuO paviršiaus. Panašūs rezultatai buvo gauti su prokariotiniais mikroorganizmais. Gana plačios baktericidinės zonos *P. aeruginosa* bakterijų gazonuose sufleruoja, jog Cu_2O ir CuO heterostruktūrizuoti paviršiai yra stiprūs baktericidai.

6.2. Itin plonos ir lanksčios antimikrobinės dangos ant maistinės aliuminio folijos formavimo ir savybių tyrimai

6.2.1. Anoduoto aliuminio dangų su įkapsuliuotais sidabro nanosiūleliais paviršiaus morfologija

Siekiant gauti lanksčias anodinio aliuminio oksido (AAO) dangas šiame darbe buvo pasirinkti mažesnės koncentracijos (120 g L^{-1}) ir šaltesni (15 °C) H_2SO_4 tirpalai bei švelnesnis anodavimo režimas (10 V). Tokiomis sąlygomis

„užaugintos“ AAO matricos primena korinę struktūrą, kurioje tankiai supakuotų, statmenai bandinio paviršiui esančių porų tankis apytiksliai lygus (1,5-1,7) × 10^{11} porų cm^{-2}. Nustatyta, kad tokių AAO storis yra apie 0,8 μm, o akučių skersmuo – 10-11 nm (5 pav. a ir d).

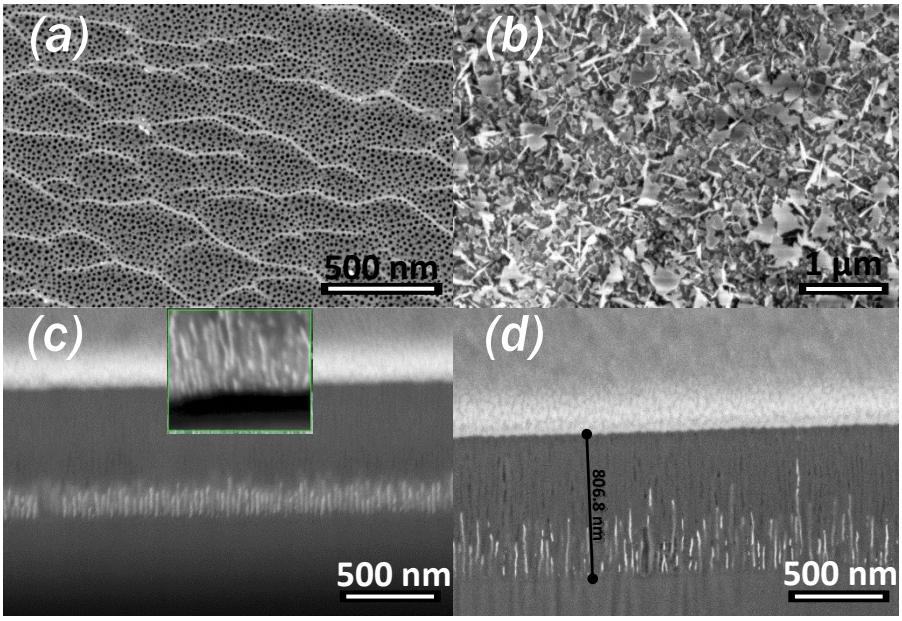

5 pav. AAO plėvelių paviršiaus (a, b) ir lūžių (c, d) SEM vaizdai prieš (a) ir po (b-d) sidabro nusodinimo kintamąja srove iš vandeninio $AgNO_3$ ir $MgSO_4$ tirpalo (pH=1,45), esant pastoviai U_{pik} įtampai 7 V ir nusodinimo trukmei (s): 40 (c), 150 (d) ir 600 (b).

Iš SEM nuotraukų matosi, kad sidabras gana tolygiai sėda didžiojoje daugumoje AAO porų (5 pav. c) tiek pastovaus srovės tankio (2,5 - 4,5 mA cm^{-2}) tiek kintamosios srovės pastovaus elektrinio lauko stiprio sąlygomis. Nusodintų Ag nanosiūlelių diametras yra artimas AAO poroms ir siekia apie 8-10 nm o jų ilgis – 200-250 nm. Tęsiant nusodinimą toliau, dangos paviršiuje pradeda formuotis atsitiktinio dydžio ir formos metalinis sidabras (5 pav. b).

6.2.2. Sidabro nusodinimo AAO matricoje priklausomybė nuo pasirinkto režimo bei gautų darinių fazinė analizė

Suformuotų Ag/AAO/Al dangų rentgenofazinė analizė parodė, kad gautas produktas yra polikristalinės struktūros metalinis sidabras su vyraujančia orientacija išilgai (110) plokštumos (PDF: 00-021-1272). Būtina paminėti, kad difraktogramoje matomas triukšmas yra gautas dėka amorfinės AAO fazės (6 pav. a). Siekiant optimizuoti sidabro nusodinimo AAO porose tolygumą ir nuspalvinimą, buvo tiriamas nusodinto sidabro kiekio

priklausomybės nuo elektrocheminio nusodinimo sąlygų bei plėvelių nuspalvinimo kokybė. Nustatyta, kad nusodinto Ag kiekis tiesiškai priklauso nuo proceso trukmės (6 pav. b), jei nusodinimo metu palaikomas pastovus kintamos srovės stipris j_{ks}.

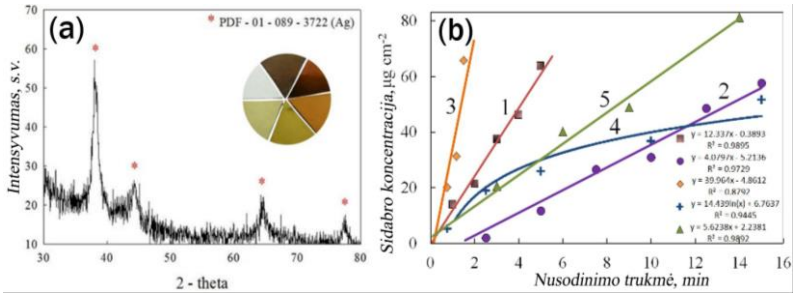

6 pav. Metalinio Ag nanosiūleliais dekoruotos AAO matricos rentgenofazinė analizė (a) bei nusodinto Ag kiekio priklausomybė nuo sodinimo laiko, kai vidutinis kintančiosios srovės tankis: (1, 5) 2,0; (2) 1,5; (3) 3,0 mA cm^{-2}. (4) kai nusodinimo metu palaikoma pastovi U_{pik} = 7±0,3 V kintančiosios srovės įtampa. Intarpe: AAO spalvų gama didėjant nusodinto Ag kiekiui.

Sidabro sėdimo greitis ženkliai išauga didėjant j_{ks} nuo 2,0 iki 4,0 mA cm^{-2}. Kai srovės tankis yra žemesnis už 1,5 mA cm^{-2}, sidabras į poras nebesėda. Be to, kai j_{ks} < 2,0 mA cm^{-2}, sidabro sėdimas pastoviu greičiu prasideda tik po tam tikro laiko (0,5-2,5 min.) priklausomai nuo j_{ks} vertės. Spėjama, kad tai sietina su oksidinės plėvelės barjerinio sluoksnio persitvarkymu [122]. Kuo mažesnė j_{ks}, tuo daugiau laiko reikia barjero persitvarkymui.

6.2.3. AAO plėvelių, elektrochemiškai dekoruotų Ag nanosiūleliais antimikrobinis aktyvumas

Fungicidinės plonų plėvelių su sidabro užpildu savybės tirtos stebint mielių ląstelių *S. cerevisiae* gyvybingumą jas dažant bei lizės zonų metodu mikromicetų ir bakterijų aplinkose.

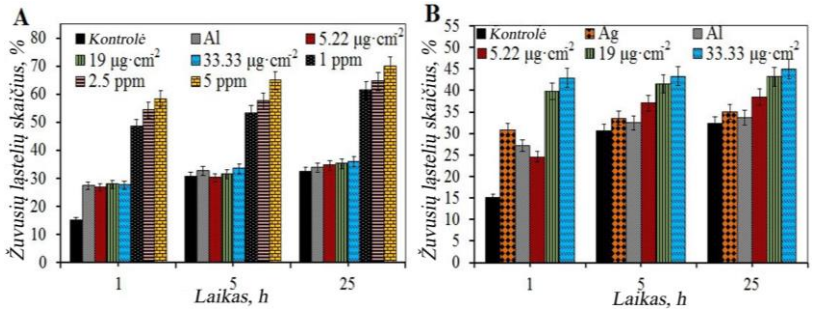

7 pav. Mielių ląstelių gyvybingumas jas kultivuojant su sidabro, Ag/AAO/Al dangomis bei skirtingos koncentracijos Ag^+ jonų priedais, kai sidabras pilnai įkapsuliuotas AAO matricoje jas „uždarant“ (A), bei atvirkščiai (B).

Gauti rezultatai rodo, kad AAO dekoruoto Ag nanosiūleliais dangoms būdingos antimikrobinės savybės (7 pav. a ir b). Didėjant nusodinto sidabro kiekiui, žuvusių tomis pačiomis sąlygomis mielių ląstelių daugėja. Tuo tarpu, mėginių su įkapsuliuotu sidabru poveikis kur kas silpnesnis. Šie rezultatai puikiai dera su lizės zonų metodų gautais duomenimis. Nustatyta, kad sidabru dekoruotos AAO plėvelės pasižymi fungistatinėmis savybėmis jas kultivuojant su eukariotiniais *G. candidum* ir *A. fumigatus* mikromicetais ir tik tada, kai nusodinto sidabro kiekis yra 33,33 μg cm^{-2}. Manoma, kad tai priklauso nuo sidabro kiekio, kuris sąlyčio su terpe taške minimaliai difunduoja į ją, taip paveikdamas mikroorganizmų kultūrų augimą. Rezultatai gauti dangas kultivuojant su *E. coli* ir *M. luteus* bakterijomis patvirtina, kad šioms dangoms būdingos ir baktericidinės savybės. Pastebėta, kad dangos su didesniu sidabro kiekiu žudo bakterijas efektyviau, nei esant mažesniam jo kiekiui.

6.3. Skirtingo dydžio, cheminės sudėties bei aplinkos kobalto ferito nanodalelių sintezė, charakterizavimas ir antimikrobinių savybių tyrimas

Šiame darbe skirtingo dydžio, cheminės sudėties bei aplinkos kobalto ferito ND šiame darbe buvo sintetinamos hidroterminiu, ko-nusodinimo ir terminio skaldymo metodais. Šiame skyriuje bus apžvelgta šių ND morfologija, paviršiaus chemija, fazinė analizė, magnetinės savybės bei antimikrobinis aktyvumas kultivuojant jas *S. cerevisiae, C. parapsilosis, C. krusei, C. albicans, S. aureus,* ir *E. coli* mikroorganizmų aplinkoje.

6.3.1. Skirtingo dydžio, sudėties bei cheminės aplinkos $CoFe_2O_4$ ND morfologija

Citratu stabilizuotos, skirtingo dydžio kobalto ferito ND ($CoFe_2O_4$@cit) buvo sintetinamos ko-nusodinimo ir hidroterminiu metodu iš stipriai šarminių (pH~12,5) vandeninių tirpalų. Šių sintezių metu citrinos rūgštis buvo naudota kaip kompleksus sudarantis bei ND stabilizuojantis agentas. Gautų produktų morfologija buvo tirta peršviečiamąja elektronine mikroskopija (PEM) ir atomine jėgos mikroskopija (AJM). 8 paveiksle pavaizduotos ND dydžio pasiskirstymo diagramos, gautos apdorojus AJM duomenis rodo, kad $CoFe_2O_4$@cit ND diametras apytiksliai lygus 1,65 (1 eilutė), 5,0 (2 eilutė) ir 15 nm (3 eilutė). Šios analizės metu gauti rezultatai sutampa su PEM analizės rezultatais, kuri patvirtina, jog dalelės yra sferinės formos ir joms būdingas gana siauras dydžio pasiskirstymo intervalas (8 pav. c, f ir i dalis). PEM analizės metu nustatyti tarpplokštuminiai atstumai iliustruoja, kad hidroterminiu būdu suformuoti dariniai yra polikristalinės struktūros. 15 nm kobalto ferito ND rentgeno spindulių energijos dispersijos spektroskopijos

(EDS) analizės metu aptiktas atominis Co ir Fe elementų santykis yra lygus 1:2 ir atitinka teoriškai paskaičiuotą kiekį.

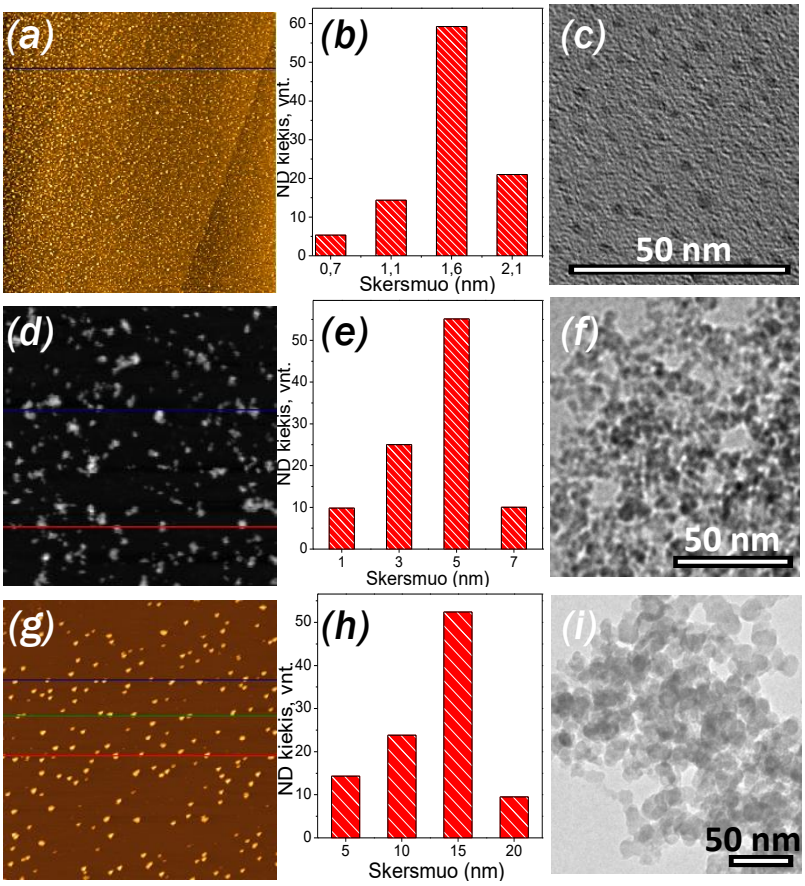

8 pav. $CoFe_2O_4$@cit ND dydžio pasiskirstymo diagramos (b, e, h) apskaičiuotos iš AJM (a, d, g) nuotraukų bei jų PEM (c, f, i) vaizdai.

Siekdami susintetinti panašaus dydžio, biologiškai „draugiškesnes“ kobalto ferito ND su skirtinga chemine sudėtimi, L-lizino amino rūgštis buvo panaudota kaip augimą reguliuojantis bei stabilizuojantis agentas hidroterminės sintezės metu. Gautų ND dydis ir forma tirta PEM analize, o charakteringos nuotraukos pateiktos 9 pav. a, b, c dalyse. Pagrindinis šio darbo tikslas – suformuoti panašaus dydžio, bet skirtingos cheminės sudėties, kaip antai $Co_xFe_{1-x}Fe_2O_4$@Lys ND, kur x kinta nuo 0,2 iki 1,0 ir ištirti suformuotų darinių antimikrobinio efektyvumo priklausomybę nuo Co^{2+} kiekio kristalinėje gardelėje. Iš PEM fotografijų, pateiktų 9 pav. a, b ir c dalyse, matoma, kad susintetintos kobalto ferito bei geležimi-pakeisto kobalto ferito ND yra sferinės formos; jų dydis 5,0-6,4 nm. Intarpuose stebimi tarpplokštuminiai atstumai įrodo, jog susintetintos ND yra kristalinės fazės, jų augimas vyksta išilgai (311) plokštumai su 0,25 nm atstumu.

Yra žinoma, kad magnetinių ND panaudojimas medicinoje stipriai priklauso nuo jų savybių, tokių kaip dydis, struktūra, forma ar sudėtis. Nemenką įtaką turi ir ND stabilizuojančio apvalkalo, kuris naudojamas siekiant padidinti ND stabilumą bei išvengti jų aglomeracijos, prigimtis.

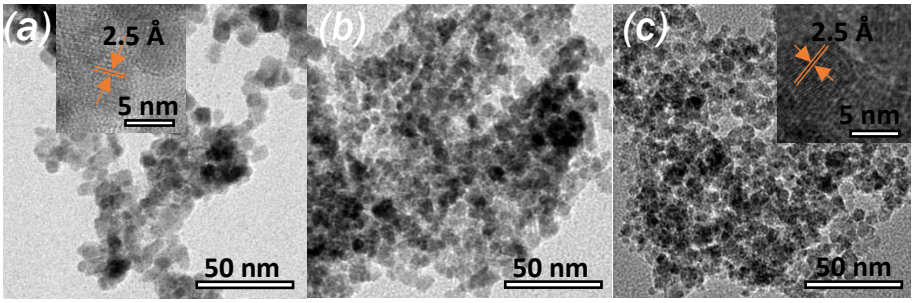

9 pav. $Co_{0,2}Fe_{0,8}Fe_2O_4$@Lys (a), $Co_{0,5}Fe_{0,5}Fe_2O_4$@Lys (b) ir $CoFe_2O_4$@Lys (c) ND PEM vaizdai. Intarpe: aukštos skyros PEM vaizdai.

Nustatyta, kad ND stabilizuojantis apvalkalas ir jo elgsena gali turėti įtakos gautų produktų antimikrobiniam efektyvumui. Pavyzdžiui, visai nesenai buvo pastebėta, kad $CoFe_2O_4$ ND padengtos folio rūgštimi bei hematoporfirino fragmentais gali būti naudojamas kaip efektyvus antivėžinis preparatas [130]. Siekiant palyginti panašaus dydžio kobalto ferito ND su skirtinga apsuptimi antimikrobines savybes, šiame darbe terminio skaldymo metodu buvo susintetintos oleino rūgštimi stabilizuotos 7 ir 17 nm dydžio ND (10 pav. a, b).

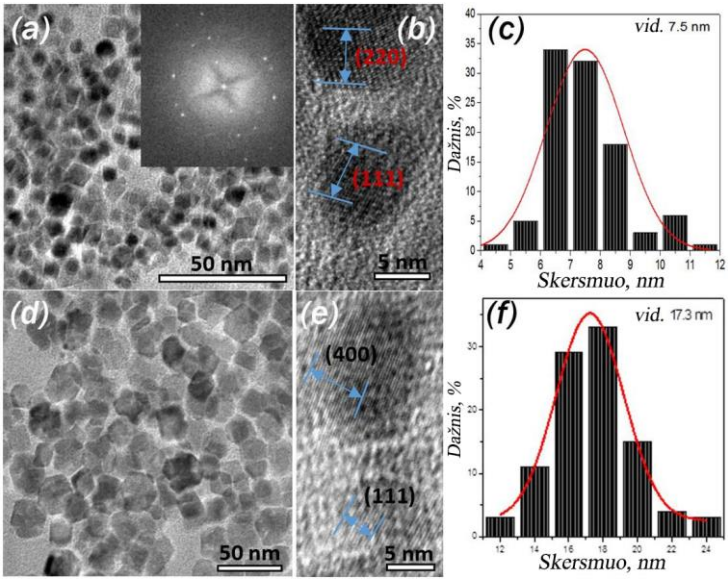

10 pav. Oleino rūgštimi stabilizuotų (~ 7 nm) $CoFe_2O_4$@Ole (a, b) ir (~ 17 nm) $CoFe_2O_4$@Ole ND (d, e) PEM bei aukštos skyros PEM vaizdai bei jų dydžių pasiskirstymo diagramos (c, f).

Gautų ND PEM analizė sufleruoja, kad oleinu stabilizuotos ND yra kristalinės struktūros kobalto feritas. Jos ženkliai mažiau aglomeruotos. Paveiksle pateiktos dydžio pasiskirstymo diagramos patvirtina, kad vidutinis ND dydis yra 7 ir 17 nm.

6.3.2. $CoFe_2O_4$@cit, $CoFe_2O_4$@Lys, $Co_xFe_{1-x}Fe_2O_4$@Lys ir $CoFe_2O_4$@Ole nanodalelių charakterizavimas

Siekiant įvertinti suformuotų ND fazinę analizę buvo atlikta citratu stabilizuotų, skirtingo dydžio kobalto ferito ND rentgenofazinė analizė (RSD). 11 pav. pateiktos rentgenogramos buvo gautos analizuojant itin smulkias (~ 1,65 nm, a kreivė) ir mažas (~5 nm, b kreivė) ND. Šios analizės metu nustatyta, kad suformuotas produktas yra vienalytis, kristalinės fazės kobalto feritas, kuriam būdinga špinelinė, paviršiuje centruotos kubinės gardelės struktūra. Remiantis PDF kortele Nr. 04-007-8945, difrakcinės analizės metu gauti smailių intensyvumai 2θ kampų intervale 18,31, 30,29, 35,52, 43,14, 53,68, 57,01, 62,54 ir 74,24 sutinka su PDF kortelėje nurodytais dydžiais; jų Milerio indeksai atitinkamai (110), (220), (311), (400), (422), (511), (440) ir (533) iliustruoja polikristalinę $CoFe_2O_4$ fazę. Itin-smulkių ND atveju stebimas difrakcinių smailių išplatėjimas susijęs su nano-metrinio dydžio efektu.

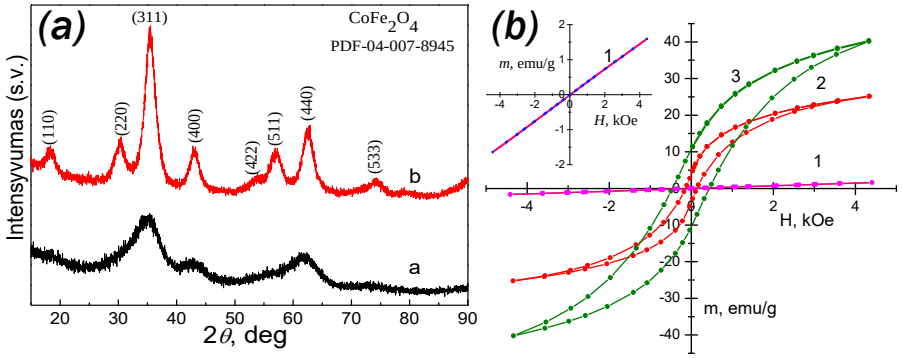

11 pav. Citratu stabilizuotų, itin smulkių ~ 1,65 nm (A) ir mažų ~ 5,0 nm (B) kobalto ferito ND rentgenofazinė analizė (a) bei magnetinės susintetintų ND, kurių vidutinis skersmuo 1,65 (1), 5,0 (2) ir 15 nm (3) kreivės (b).

Magnetinės susintetintų 1,65, 5,0 ir 15,0 nm skersmens ND savybės buvo tirtos kambario temperatūroje veikiant jas išoriniu magnetiniu lauku. Gautos histerezės kreivės demonstruoja feromagnetikams būdingus profilius, kaip antai nenulinis koercinio lauko stipris H_c. Pastebėta, kad mažėjant ND dydžiui soties įmagnetėjimo vertės M_s mažėja ir yra lygios atitinkamai 40, 25 ir 1,5 emu g^{-1}. Remiantis Millan ir jo kolegų darbu [131] galima teigti, jog šis dėsningumas buvo pastebėtas jau kur kas anksčiau. Autoriai pabrėžė, kad itin

smulkių magnetinių Fe_2O_3 ND (≤ 3 nm) M_s reikšmė artėja į nulį. Tai sietina su itin mažų ND domeno šerdies „pradingimu“, todėl netvarkingai orientuotos jų dalys tampa vyraujančios, tokiu būdu pakeisdamos chemines ND savybes. Magnetinės analizės metu gauti duomenys (11 pav. b dalies 1 kreivė ir intarpas) įrodo, kad itin smulkioms (~ 1,65 nm skersmens) ND būdingas magnetinės histerezės profilis su pastebimai sumažėjusia soties įmagnetėjimo verte ir koreliuoja su anksčiau pastebėtais dėsningumais.

Terminio skaldymo ir hidrotermiškai suformuotų, oleino rūgštimi ir L- lizinu stabilizuotų kobalto ferito ND kristališkumas bei fazinė analizė tirta RSD metodu. Gautos difraktogramos įrodo, kad darbe sintetintiems nano-dariniams būdingas kristališkumas, kas atsispindi stipriai išreikštose rentgenogramos smailėse (12 pav. b dalis).

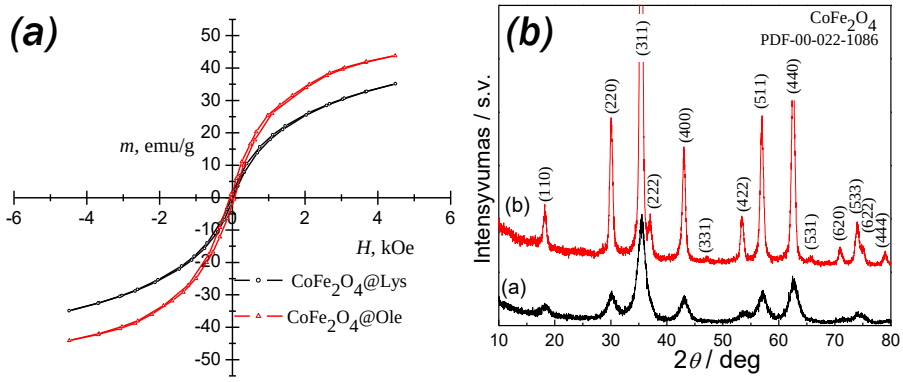

12 pav. Oleino rūgštimi ir L-lizino amino rūgštimi stabilizuotų, ~5-7 nm skersmens kobalto ferito ND magnetinės histerezės kilpos (a). (b) dalyje pavaizduotos ~7 nm (a) ir ~17 nm (b) $CoFe_2O_4$@Ole ND rentgenogramos.

Susintetintų ND dydis, papildomai, buvo nustatytas iš gautų rentgenogramų naudojant Halder-Wagner matematinį modelį ir atitinkamai siekė 4,0 bei 14,0 nm. Lyginant su dydžiais gautais PEM analizės metu, nesunku pastebėti, kad RSD tyrimo metu gautos vertės yra šiek tiek mažesnės. Tai sietina su ND sudarančių domenų struktūra, kurios įprastai negalima atskirti RSD analizės metu. Panašūs pastebėjimai buvo neseniai publikuoti tyrinėjant magnetito (Fe_3O_4) ND [132].

Histerezės kilpų profiliai (12 pav. a dalis), gauti tyrinėjant ~5-7 nm skersmens $CoFe_2O_4$@Ole ir $CoFe_2O_4$@Lys ND iliustruoja, jog suformuotoms kobalto ferito ND būdinga superparamagnetinė elgsena veikiant jas išoriniu magnetiniu lauku. Pastebėta, kad ~7 nm skersmens dydžio $CoFe_2O_4$@Ole ND pasižymėjo šiek tiek didesniu soties įmagnetėjimu, kurio vertė 52 emu g^{-1}, tuo tarpu mažesnės (~5 nm) $CoFe_2O_4$@Lys ND demonstravo šiek tiek mažesnius M_s dydžius – 46 emu g^{-1}. Manoma, jog tai sietina su nanometrinio dydžio bei

paviršinių sukinių pakrypimo reiškiniais. Panašios tendencijos gautos ir analizuojant citratu stabilizuotas kobalto ferito ND, kurios aprašytos ankstesniame skyriuje.

Siekiant įrodyti oleino rūšties ir L-lizino amino rūgšties molekulių adsorbciją ant magnetinės ND paviršiaus buvo atlikta Furjė transformacijos infraraudonųjų spindulių spektroskopinė (FTIR) analizė. Oleino rūgštimi stabilizuotų kobalto ferito ND FTIR sugerties spektras (13 pav. A dalies a kreivė) rodo aiškiai išreikštas plačias smailes prie 401 ir 591 cm^{-1}, kurios yra charakteringos Fe-O ir/ar Co-O ryšių vibracijai. Analogiški rezultatai gauti ir su L-lizino amino rūgštimi stabilizuotomis $CoFe_2O_4$@Lys ND (13 pav. B dalies a kreivė).Virpesiai gauti ties 1562 ir 1603 cm^{-1} yra priskirtini asimetriniams karboksilo jonų (COO^-) virpesiams.

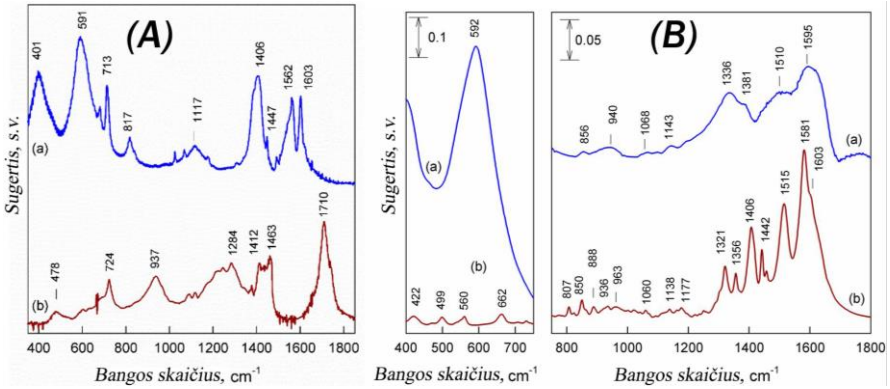

13 pav. Oleino rūgštimi stabilizuotų (A) $CoFe_2O_4$@Ole ir L-lizinu stabilizuotų $CoFe_2O_4$@Lys ND (B) FTIR sugerties spektrai: (a) kreivės gautos analizuojant $CoFe_2O_4$@Ole/Lys ND, (b) kreivės žymi oleino rūgšties bei L-lizino aminorūgšties IR sugertį.

Švarios oleino rūgšties FTIR spektras (13 pav. A dalies b kreivė) demonstruoja sugerties piką ties 1710 cm^{-1}. Jis priskirtinas karboksilo grupių (C=O) virpesiams. Tuo tarpu $CoFe_2O_4$@Ole ND atveju, tame pačiame energijos diapazone, jokių sugerties pikų gauta nebuvo, kas reiškia, jog dalelių apsuptyje nėra laisvos oleino rūgšties pėdsakų.

$CoFe_2O_4$@Lys ND FTIR analizės metu gautos kelios platesnės, mažesnio intensyvumo smailės esančios didesnių energijų srityje galimai yra priskirtinos karboksilato anijonų ir/ar amino grupių virpesiams, kurie fiksuojami dėka ant ND paviršiaus adsorbuotų L-lizino molekulių. Didesnio intensyvumo virpesių piko dubletas, atitinkamai gautas ties 1581 ir 1603 cm^{-1} (13 pav. B dalies b kreivė), yra priskirtinas COO^- bei NH_3^+ grupių antisimetrinės deformacijos virpesiams. Tuo tarpu 1515 ir 1406 cm^{-1} gauti virpesiai priskirtini NH_3^+ ir COO^- grupių simetrinei vibracijai. FTIR smailės

gautos spektro dalyje nuo 1321 iki 1356 cm^{-1} priklauso vibracijoms kurias sukelia $–CH_2$- bei CH grupių antisimetriniai virpesiai [137]. Švarios L-lizino amino rūgšties atveju virpesių pikas gautas ties 1406 cm^{-2} pasislenka link 1381 cm^{-2} COO^- grupėms elektrostatiškai prisijungiant prie ND paviršiaus. Visai nesenai šis pastebėjimas buvo įvardintas kaip vienas iš karboksilato anijono sąveikos su ND įrodymų [138]. Remiantis šiais pastebėjimais buvo manoma, kad susintetintos $CoFe_2O_4$@Lys ND yra stabilizuotos L-lizino molekulėmis, kurios, tikėtina, elektrostatiškai prisijungia prie ND paviršiaus.

Siekiant nustatyti geležimi pakeistų kobalto ferito ND apsuptį bei kompoziciją, susintetintos medžiagos buvo tiriamos Mesbauerio bei induktyviai susietos plazmos optinės emisijos (ISP-OES) spektrofotometrais. Mesbauerio spektrai užrašyti esant kambario temperatūrai bei pralaidumo režimui (14 pav.).

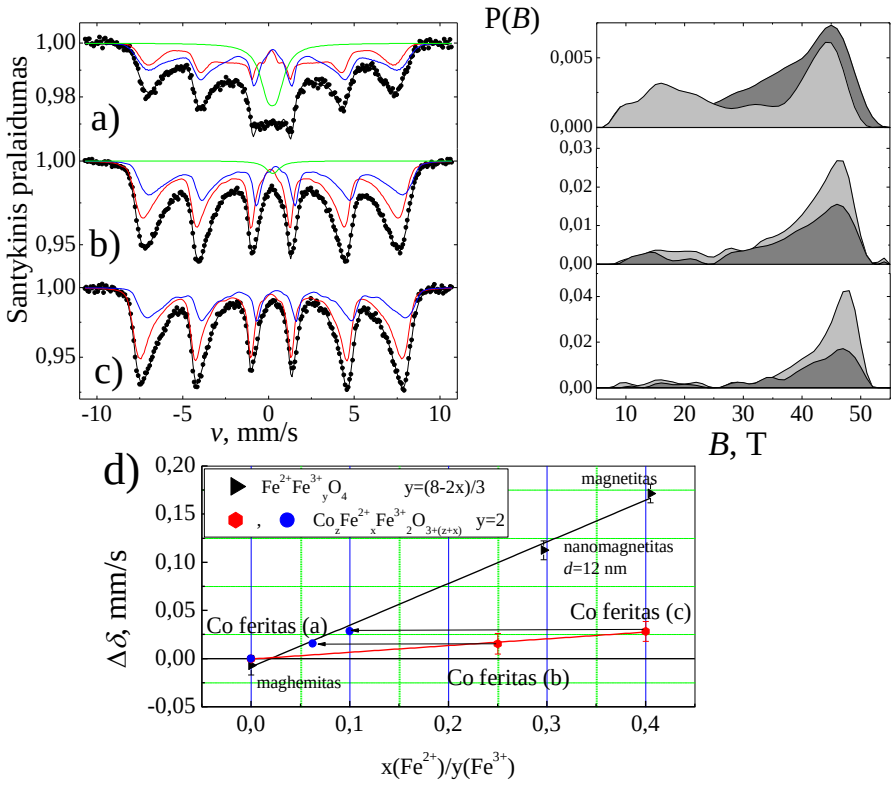

14 pav. Kobalto ferito $CoFe_2O_4$@Lys (a) ir geležimi pakeistų feritų $Co_{0.5}Fe_{0.5}Fe_2O_4$@Lys (b) ir $Co_{0.2}Fe_{0.8}Fe_2O_4$@Lys (c) Mesbauerio spektrai bei jų hipersmulkaus lauko pasiskirstymai (dešinėje). Mesbauerio spektro centrinės kreivės vidutiniai poslinkiai lyginant juos su švarioms $CoFe_2O_4$@Lys ND būdinga pozicija.

Kaip matyti iš 14 pav. keičiantis ND kristalinės gardelės kompozicijai pastebėti hipersmulkaus sekstetų profilio skirtumai, kurie galimai susiję su

ND sudėtimi bei dydžiu. Siekiant nustatyti Fe^{2+} kiekį $Co_xFe_{1-x}Fe_2O_4$@Lys ND buvo taikyti du skirtingi metodai. Pirmiausia užrašytas spektras buvo normalizuotas naudojant hipersmulkaus lauko pasiskirstymo bei skirtingų izomerų poslinkių vertes, kaip antai 0,23-0,26 ir 0,53-0,58 mm s^{-1}. Priskiriant hipersmulkaus lauko pasiskirstymo apibrėžtą plotą prie Fe^{2+} poslinkio tetraedrinėje bei Fe^{3+} oktaedrinėse padėtyse buvo nustatyta, kad 17-20 % visų geležies katijonų yra dvivalenčiai. Palyginus izomerinių geležimi pakeistų feritų ND poslinkių vertes su vertėmis gautomis analizuojant tokio pat dydžio magnetito Fe_3O_4 ir maghemito Fe_2O_3 ND buvo gauta, kad nustatyta Fe^{2+} koncentracija bandiniuose beveik keturis kartus yra mažesnė nei tikėtasi (mėlyni taškai 14 pav. d dalyje). Siekiant tiksliau įvertinti bandinių cheminę sudėtį, jie buvo analizuojami ISP-OES metodu. Dalelių kompozicija apskaičiuota remiantis gautais rezultatais; jie pateikiami 1 lentelėje.

1 lentelė. ISP-OES analizės rezultatai bei apskaičiuotos geležimi pakeistų feritų formulės.

Bandinys	$[Co^{2+}]$, mg L^{-1}	$[Fe^{3+}]$, mg L^{-1}	Fe^{2+}/Co^{2+} santykis	Apskaičiuota formulė
$CoFe_2O_4$	45.7	91.17	1.95	$CoFe_2O_4$
$Co_{0.5}Fe_{0.5}Fe_2O_4$	17.8	79.56	1.23	$Co_{0.45}Fe_{0.55}Fe_2O_4$
$Co_{0.2}Fe_{0.8}Fe_2O_4$	5.64	70.53	3.50	$Co_{0.16}Fe_{0.84}Fe_2O_4$

Būtina paminėti, kad šios analizės metu negalima atskirti Fe^{2+} ir Fe^{3+} jonų, tačiau pasinaudojus formule $M_{Fe(II)} + M_{Co(II)} = 0,5\ M_{Fe(III)}$ buvo apskaičiuotos preliminarios ND kompozicijos, jų formulės atitinkamai yra $Co_{0.45}Fe_{0.55}Fe_2O_4$@Lys ir $Co_{0.16}Fe_{0.84}Fe_2O_4$@Lys. Siekiant supaprastinti šias formules, gauti stechiometriniai koeficientai buvo suapvalinti ir pažymėti, kaip antai $Co_{0.5}Fe_{0.5}Fe_2O_4$@Lys ir $Co_{0.2}Fe_{0.8}Fe_2O_4$@Lys.

6.3.3. $CoFe_2O_4$@cit, $CoFe_2O_4$@Lys, $Co_xFe_{1-x}Fe_2O_4$@Lys ir $CoFe_2O_4$@Ole nanodalelių antimikrobinės savybės

Skirtingo dydžio, citratu stabilizuotų $CoFe_2O_4$@cit ND antimikrobinės savybės tirtos zonų inhibicijos bei serijinio skiedimo metodais *S. cerevisiae*, *C. parapsilosis*, *C. krusei* ir *C. albicans* mieliagrybių aplinkose. Tuo tikslu ant standžios mikroorganizmų mitybinės terpės su pasėliais buvo uždedami filtrinio popieriaus diskeliai su tiriamomis ND. Antimikrobinis ND aktyvumas buvo nustatytas išmatuojant gautas inhibicijos zonas gautas po 48 h kultivavimo. Gauti rezultatai rodo, kad 2, 5 ir 15 nm dydžio $CoFe_2O_4$@cit ND fungicidinis efektas stipriausiai pasireiškė prieš *S. cerevisiae* kultūrą – aplink tiriamus bandinius susiformavusios inhibicijos zonos plotis siekė 11-13 mm

(15 pav. B). Toks antimikrobinis aktyvumas buvo stebėtinai didelis lyginant jį su flukanozoliu, – komerciniu antimikrobiniu preparatu, kuris buvo naudojamas darbe kaip teigiama kontrolė ir demonstravo beveik 30 % silpnesnį poveikį prieš *S. cerevisiae* mieles (2 lentelė).

2 lentelė. Skirtingo dydžio $CoFe_2O_4$@cit ND antimikrobinės elgsenos prieš *S. cerevisiae* ir tris skirtingas *Candida* rūšis rezultatai.

Mikrobų kultūra	$CoFe_2O_4$ ND dydis, nm	Disko skersmuo (d), mm	Zonos skersmuo (z), mm	z/d
S. cerevisiae	15	11	22	2.0±0.2
	5	11	24	2.4±0.1
	2	11	24	2.4±0.1
C. parapsilosis	15	11	13	1.2±0.05
	5	11	15	1.4±0.1
	2	11	16	1.4±0.1
C. krusei	15	11	13	1.3±0.05
	5	11	15	1.4±0.1
	2	11	16	1.4±0.1
C. albicans	15	11	13	1.2±0.05
	5	11	14	1.3±0.1
	2	11	16	1.4±0.1

Nepaisant to, skirtingo dydžio $CoFe_2O_4$@cit ND poveikis *Candida* rūšies mieliagrybiams, kaip antai *C. krusei*, *C. parapsilosis* ir *C. albicans* buvo apytiksliai keturis kartus mažesnis lyginant jį su poveikiu gautu *S. cerevisiae* ląstelių aplinkose.

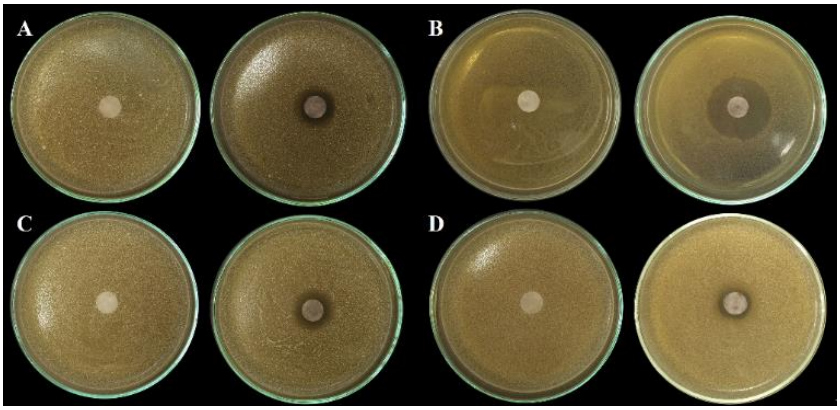

15 pav. Kobalto ferito $CoFe_2O_4$@cit ND (2 nm) antimikrobinio aktyvumo tyrimo rezultatai: stebimos inhibicijos zonos apie tiriamus bandinius *C. krusei* (A), *S. cerevisiae* (B), *C. parapsilosis* (C) ir *C. albicans* (D) kultūrų gazonose. Kairėje – mikroorganizmų kultūros kontrolė.

Šiuo atveju inhibicijos zonų plotis siekė 2-5 mm. Be to, pastebėta, kad mažos $CoFe_2O_4$@cit ND (2-5 nm) demonstruoja platesnes inhibicijos zonas nei 15 nm $CoFe_2O_4$@cit ND, kas sufleruoja, jog gautiems produktams yra būdingos nuo dydžio priklausančios antimikrobinės savybės. Šie rezultatai įrodo ankstesnių tyrėjų paskelbtas idėjas apie metalų oksidų, kaip antai ZnO [140], MgO [126] ar CuO [141] ND antimikrobinio efektyvumo priklausomybę nuo ND dydžio.

Siekiant nustatyti skirtingo dydžio kobalto ferito ND antimikrobinį efektyvumą kiekybiškai, susintetintos ND buvo kultivuojamos kartu su *S. cerevisiae* ir *C. parapsilosis* mikroorganizmais. Gauti rezultatai sutampa su anksčiau aprašytais: smulkesnės ND (2-5 nm) pasižymi kur kas efektyvesniu poveikiu pasirinktoms kultūroms nei didesnių ND (15 nm) atveju (16 pav.).

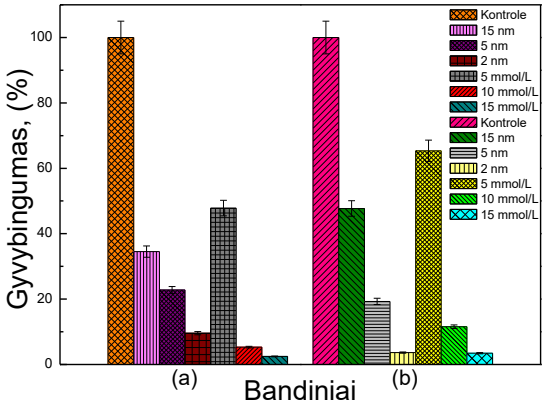

16 pav. 2, 5 ir 15 nm skersmens kobalto ferito $CoFe_2O_4$@cit ND bei skirtingos koncentracijos Co^{2+} jonų poveikio skystoje terpėje prieš *S cerevisiae* (a) ir *C. parapsilosis* (b) mieliagrybius rezultatai.

Nepaisant to, kultivuojant 15 nm skersmens kobalto ferito ND mikroorganizmų kultūrų aplinkoje, pastarosios taip pat ženkliai sumažina kolonijas sudarančių vienetų skaičių. Lyginant gautus rezultatus su *S. cerevisiae* ir *C. parapsilosis* mikroorganizmų kultūros kontrole pastebėta, kad 2 nm skersmens ND antimikrobinis efektyvumas yra apytiksliai 12 % didesnis nei 5 nm ND bei net 25 % didesnis už 15 nm dydžio ND sukeltą poveikį. Tokia antimikrobinė elgsena galimai sietina su Co^{2+} jonų kiekiu, disocijavusiu nuo ND paviršiaus. Kaip pastebėta Wan grupės, Co^{2+} jonų atsipalaidavimas nuo ND paviršiaus gali sukelti oksidacinį stresą kuris galiausiai lemia DNR pažeidimus ir ląstelės žūtį [142]. Manoma, kad stipresnis mažesnių ND poveikis turėtų būti siejamas su didesniu jų paviršiaus plotu, nuo kurio galimas ir didesnis Co^{2+} jonų atsipalaidavimas.

Siekiant nustatyti antimikrobinio efektyvumo priklausomybę nuo kobalto kiekio špinelinėje gardelėje šiame darbe buvo susintetintos geležimi pakeistos kobalto ferito ND. Gautų darinių antimikrobinės savybės buvo tirtos panaudojant patogeninius mikrobus, sukeliančius odos, audinių, kraujo ir kvėpavimo takų infekcijas. Pirmiausia ši ND elgsena tirta modifikuotu Kirby-Bauer metodu *C. albicans* mikroorganizmų aplinkoje. Gauti rezultatai rodo, kad $CoFe_2O_4$@Lys ND pasižymi mikroorganizmų inhibicija. Gautų lizės zonų plotis *C. albicans* ląstelių kultūros gazone siekė 3-4 mm. Norėdami įvertinti antimikrobines savybės kiekybiškai, susintetintos ND (1 g L^{-1}) buvo kultivuojamos skystoje terpėje su mikrobais. Po 24 ir 72 h kultivavimo suskaičiavus kolonijas sudarančius vienetus (KSV) pastebėta, kad L-lizinu stabilizuotos kobalto ferito bei geležimi pakeistos jo formos pasižymi antimikrobiniu aktyvumu prieš visas testuotas padermes (17 pav. A ir B).

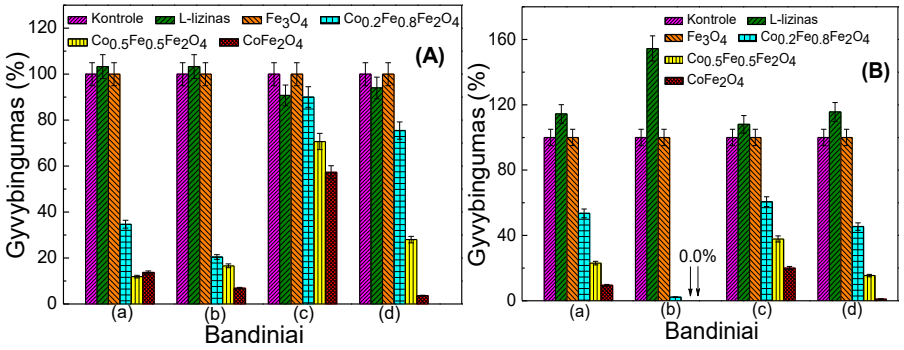

17 pav. 5-7 nm dydžio kobalto ferito bei geležimi dopuotų feritų, kultivuotų skystoje terpėje su *C. albicans* (a), *C. parapsilosis* (b), *E. coli* (c) ir *S. aureus* (d) mikroorganizmais, antimikrobinis efektyvumas po 24 (A) ir 72 h (B). Švarus L-lizinas ir magnetito ND buvo naudotos kaip neigiama kontrolė.

Analizuojant gautus rezultatus pastebėta, kad kobalto ferito ND toksiškumas mikrobams priklauso nuo Co^{2+} kiekio ND. Kaip ir tikėtasi, didžiausiu antimikrobiniu efektyvumu pasižymėjo $CoFe_2O_4$@Lys ND: eukariotinių mikroorganizmų inhibicija siekė 93,1-86,3 %, o prokariotinių – 96,4-42,7 %. Lyginant šiuos duomenis su geležimi pakeistomis kobalto ferito $Co_{0.5}Fe_{0.5}Fe_2O_4$@Lys ir $Co_{0.2}Fe_{0.8}Fe_2O_4$@Lys ND, pastarosios demonstravo apytiksliai 11-24 % ir 21-70 % silpnesnį mikrobų žudymo efektyvumą. Pastebėta, kad tiek $CoFe_2O_4$@Lys, tiek $Co_{0.5}Fe_{0.5}Fe_2O_4$@Lys ND inhibuoja didžiąją dalį *C. parapsilosis* mieliagrybių po 72 h kultivavimo (17 pav. B). Be to, tyrinėjant L-lizino įtaką mikroorganizmų gyvybingumui, buvo nustatyta, jog šiai amino rūgščiai yra būdingas antimikrobinis efektas, tačiau poveikis yra labai mažas: tirtų *E. coli* ir *S. aureus* bakterijų gyvybingumas atitinkamai siekė 91 ir 94 %. Kaip matoma iš pateiktų diagramų, šis efektas išnyksta

stebint KSV skaičiaus kaitą po 72 h kultivavimo. Priešingai, bakterijų skaičius išauga, kas galimai yra dėl to, jog L-lizino amino rūgštis veikia kaip maisto papildomos medžiagos, kurias savo augimui ir dauginimuisi naudoja mikroorganizmų ląstelės. Kaip ir tikėtasi tyrinėjant Fe_3O_4@Lys ND jokio antimikrobinio efekto gauta nebuvo. Apibendrinant gautus rezultatus KSV skaičiaus kaita (18 pav.) gana žymiai priklauso nuo Co^{2+} kiekio špinelinės struktūros ND.

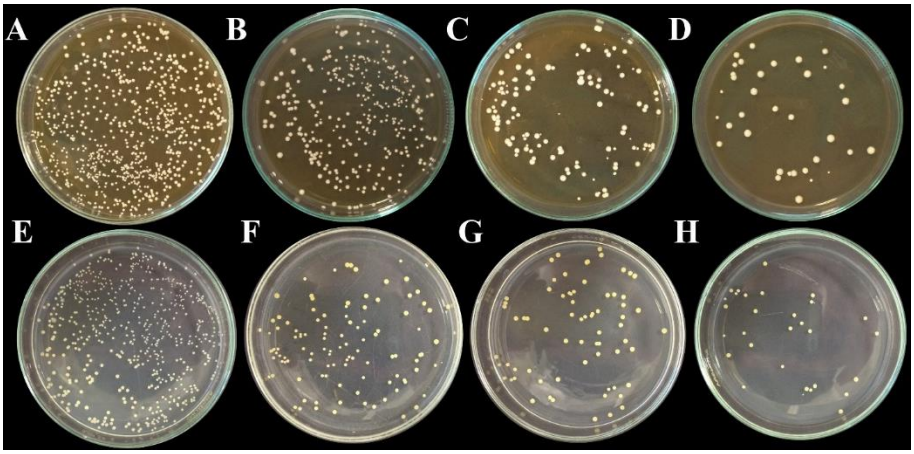

18 pav. KSV skaičiaus pokytis Petri lėkštelėse su standžia Saburo terpe po inkubacijos su 5-7 nm $CoFe_2O_4$@Lys (D, H), $Co_{0.5}Fe_{0.5}Fe_2O_4$@Lys (C, G) ir $Co_{0.2}Fe_{0.8}Fe_2O_4$@Lys (B, F) ND bei *C. albicans* (viršutinė eilutė) ir *S. aureus* (apatinė eilutė) mikrobais. Visi mikroorganizmai buvo auginti 24 h skystoje mitybinėje terpėje be (a, e) ir su tiriamomis ND.

18 pav. aiškiai stebimos KSV skaičiaus sumažėjimas, didėjant Co^{2+} koncentracijai geležimi pakeistose kobalto ferito ND. Gautos nuotraukos (18 pav. D ir H) rodo, kad palyginus su kontrole $CoFe_2O_4$@Lys ND apsuptyje kultivuotų *C. albicans* ir *S. aureus* mikroorganizmų skaičius kinta nuo keleto šimtų iki dešimčių, kas patvirtina, jog šioms ND yra būdinga gana stipri antimikrobinė elgsena.

Siekiant nustatyti ląstelių morfologijos pokyčius po sąveikos su tirtomis kobalto ferito ND buvo atlikta ląstelių SEM analizė (19 pav.). Sveikų ląstelių SEM nuotraukos patvirtina, kad *C. parapsilosis* mieliagrybiams būdinga elipsės formos struktūra, ląstelių dydis – 4-6 μm. Kaip matome iš 19 pav. B fotografijos, po kultivavimo su ND *C. parapsilosis* morfologija pakinta ir tampa panaši į eritrocitams būdinga struktūrą, atsiranda įdubimas, kuris sietinas su ląstelės žūtimi. Ląstelių sąveika su ND buvo patvirtinta energijos dispersijos spektrometru (EDS), kurio spektras pateiktas 19 pav. intarpe. Kaip matyti iš šio EDS spektro, ant pažeistos *C. parapsilosis* ląstelės yra aptinkami Co ir Fe elementai, kas patvirtina kad ND yra aplipusios ir/ar galimai

difundavusios į ląsteles. Kobalto ferito bei geležimi dopuotų feritų, stabilizuotų L-lizino amino rūgštimi, antimikrobinio veikimo mechanizmas nebuvo tirtas. Manoma, jog mikroorganizmų žūčiai didelę įtaką turi Co^{2+} jonų disocijacija nuo ND paviršiaus. Be to, hipotezuojama, kad ND paviršiuje adsorbuotas L-lizinas gali elektrostatiškai sąveikauti su neigiamai įkrautomis bakterijų sienelėmis taip sutrikdydamas jos funkciją ir pažeisdamas ją.

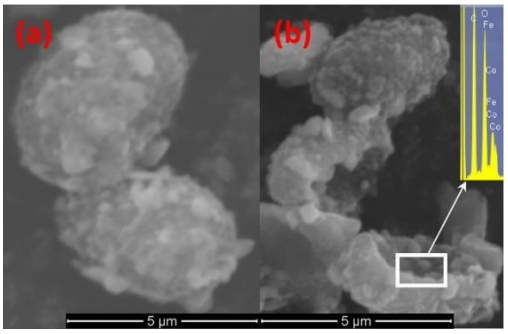

19 pav. *C. parapsilosis* ląstelių SEM vaizdai gauti kultivuojant jas be (a) ir su kobalto ferito ND (b). Intarpe: *C. parapsilosis* ląstelės paviršiaus EDS spektras po kultivavimo su $CoFe_2O_4$@Lys ND.

Trečiuoju etapu norėta išsiaiškinti kobalto ferito ND apsupties poveikį antimikrobiniam efektyvumui. Šiam tikslui pasiekti buvo susintetintos oleino bei L-lizino amino rūgštimi stabilizuotos 7 ir 17 nm $CoFe_2O_4$@Ole ND bei 5 - 7 nm dydžio $CoFe_2O_4$@Lys ND. Suformuotų ND antimikrobinės savybės buvo ištirtos mediciniškai svarbių mikroorganizmų, kaip antai *S. aureus*, *E. coli*, *C. parapsilosis* ir *C. albicans* aplinkose. Gauti rezultatai rodo, kad oleino rūgštimi stabilizuotos 7 ir 17 nm dydžio kobalto ferito ND pasižymi stipresniu antimikrobiniu efektu, lyginant jį su L-lizino amino rūgštimi stabilizuotomis $CoFe_2O_4$@Lys ND (20 pav. A ir B).

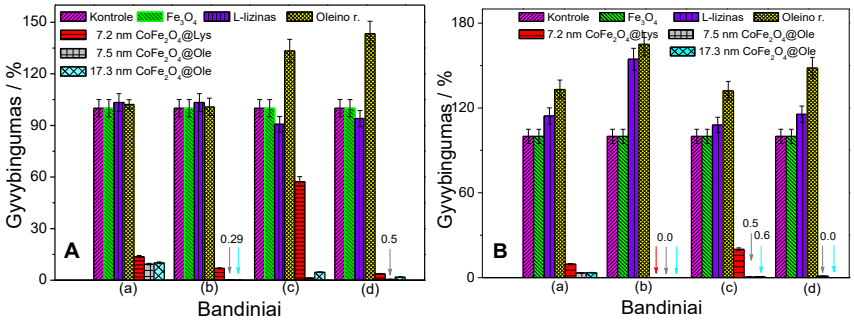

20 pav. L-lizino amino rūgštimi stabilizuotų 5-7 nm dydžio $CoFe_2O_4$@Lys bei oleino rūgštimi stabilizuotų 7 ir 17 nm dydžio $CoFe_2O_4$@Ole ND antimikrobinių savybių tyrimo rezultatai kultivuojant juos 24 h (A) ir 72 h (B) su *C. albicans* (a), *C. parapsilosis* (b), *E. coli* (c), ir *S. aureus* (d) mikroorganizmais. Švari L-lizino amino rūgštis bei magnetito ND čia naudotos kaip neigiama kontrolė.

Didžiausias skirtumas buvo nustatytas *E. coli* bakterijomis kur antimikrobinis efektyvumas tarp $CoFe_2O_4$@Lys ir $CoFe_2O_4$@Ole ND varijavo daugiau nei 55 %. Tuo tarpu, mikroorganizmų gyvybingumas po 72 h kultivavimo su 7 ir 17 nm $CoFe_2O_4$@Ole ND siekė vos 0,1-3,3 %. Be to, skirtingai nei su citratu stabilizuotomis ND, jokio ryškesnio antimikrobinio efektyvumo skirtumo tarp 7 ir 17 nm oleino rūgštimi stabilizuotų kobalto ferito ND gauta nebuvo. Būtina paminėti, kad oleino rūgštis naudota darbe kaip ND stabilizuojantis agentas bei neigiama kontrolė jokių antimikrobinių aktyvumo požymių nerodė. Priešingai, – kultivuojant mikroorganizmus su oleino rūgštimi jų kiekis išauga, kas reiškia, kad ši medžiaga nėra toksiška mikroorganizmams. Analogiški rezultatai gauti ir su magnetito ND.

Siekiant parodyti $CoFe_2O_4$@Ole ND poveikio pažeidimus mikrobų ląstelėms, šiame darbe buvo naudota konfokalinė mikroskopija. Nuotraukose matomos žalios spalvos taškai gauti dėka savaiminės baltymų autofluorescencijos (21 pav.).

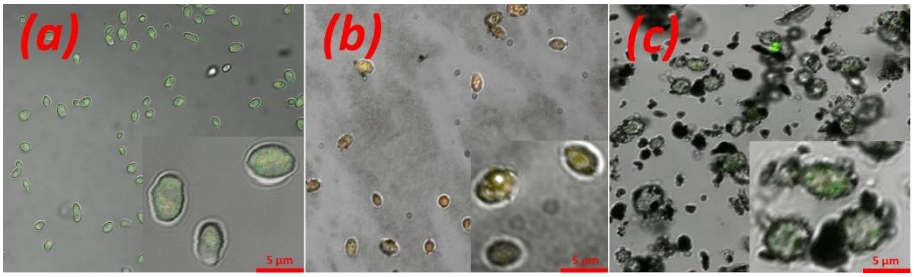

21 pav. Konfokalinės mikroskopijos nuotraukos stebint *C. parapsilosis* ląsteles prieš (a) ir po kultivavimo su Co^{2+} jonais (b) ir $CoFe_2O_4$@Ole ND (c).

21 pav. A dalyje parodyta „švarios“ *C. parapsilosis* ląstelės būdinga elipsės formos morfologija. Geriau įsižiūrėjus matosi nepažeista, vientisa ląstelių sienelė. Tuo tarpu mikroskopuojant mikrobus, kurie auginti Co^{2+} jonų aplinkose yra aiškiai matomi pažeidimai, kurie, kaip manome, ir lemia ląstelių žūtį. Palyginus fotografijas, gautas kultivuojant ląsteles su Co^{2+} jonais bei $CoFe_2O_4$@Ole ND, matosi, jog pažeidimai iš esmės sutampa. Negana to, yra stebima ND aglomeracija aplink mikroorganizmų ląsteles, kas patvirtina tiesioginę dalelių bei ląstelės sąveiką.

6.4. Pavojingiausių bakterijų inaktyvacija ultra-smulkiomis aukso nanodalelelėmis

Šiame skyriuje pristatomos ultra-smulkios aukso ND, susintetintos magnetinių ND paviršiuje metionino amino rūgšties inicijuota aukso rūgšties redukcija magnetinių ND paviršiuje. Nustatyta gautų dalelių fazinė sudėtis, paviršiaus chemija bei ištirtos antimikrobinės savybės. Šiems tyrimams atlikti

buvo pasirinktos trys padermės, kaip antai *A. baumannii*, *S. enterica*, ir *S. aureus* (MRSA), – jos visos patenka į pasaulio sveikatos organizacijos paskelbtų 12-os pačių pavojingiausių bakterijų sąrašą.

6.4.1. Fe_3O_4@Met ND morfologija ir charakterizavimas

Siekiant susintetinti biologiškai draugiškas magnetito ND, D,L-metionino amino rūgštis buvo panaudota kaip ND augimo reguliatorius, aukso jonų reduktorius bei stabilizuojantis agentas. Magnetito Fe_3O_4@Met ND buvo suformuotos hidroterminiu metodu. Gautos dalelės yra kristalinės būsenos, joms būdinga sferinė forma bei gana siaura ND dispersija, jų vidutinis dydis – 11 nm (22 pav.).

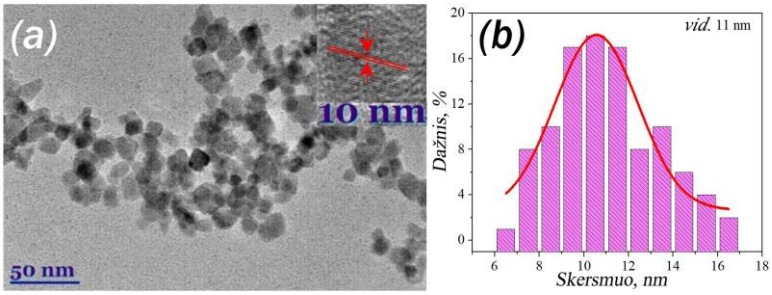

22 pav. Magnetito ND PEM nuotrauka (a) bei dydžių pasiskirstymo diagrama (b). Intarpe: vienos Fe_3O_4@Met ND AR-PEM nuotrauka rodanti matomus gardelės tarpplokštuminius atstumus.

Nanodalelių PEM analizės rezultatai sutampa su rezultatai gautais RSD metodu, kuris patvirtina paviršiuje centruotos kubinės gardelės kristalo struktūrą. Iš difraktogramos matoma, jog gauti produktai yra kristalinės struktūros magnetitas (23 pav. (a)). Būtina paminėti, jog jokių priemaišinių fazių šia analize gauta nebuvo.

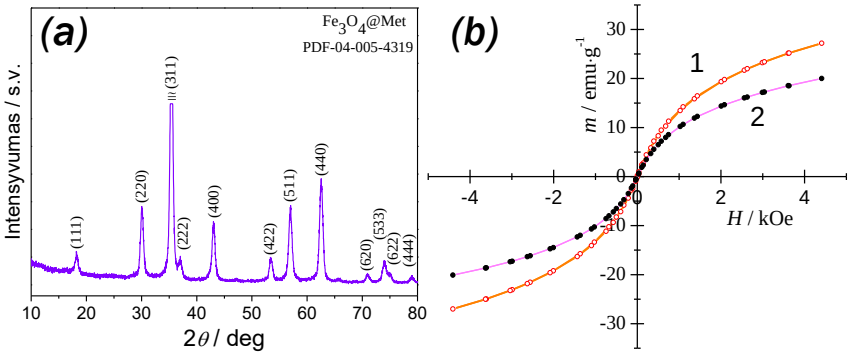

23 pav. Fe_3O_4@Met ND rentgenograma (a) ir magnetinės histerezės kreivės (b) užrašytos prieš (1) ir po (2) funkcionalizavimo aukso ND.

Be to, naudojant Halder-Wagner matematinį modelį išmatuotas ND dydis siekia 11,90±0,15 nm, kas įrodo, jog ND būdingas gan siauras dydžio pasiskirstymas. Gautų dalelių magnetinės histerezės profilis (23 pav. (b) dalies 1 kreivė) pagrindžia, kad magnetiniam lauke ND būdinga superparamagnetinė elgsena. Tokioms medžiagoms būdingas neryškus koercinis laukas, o jų likutinis įmagnetėjimas artėja į nulį, ką ir rodo histerezės kreivė. Pastebėta, kad ~11 nm skersmens dydžio Fe_3O_4@Met ND pasižymėjo soties įmagnetėjimu, kurio vertė 27 emu g^{-1}.

6.4.2. Metionino inicijuotas Fe_3O_4@Met ND funkcionalizavimas auksu

Magnetito Fe_3O_4@Met ND funkcionalizavimas auksu buvo vykdomas panaudojant reduktorių – metionino aminorūgštį. Gautos Fe_3O_4@Met@Au ND charakterizuotos PEM metodu (24 pav. a ir b).

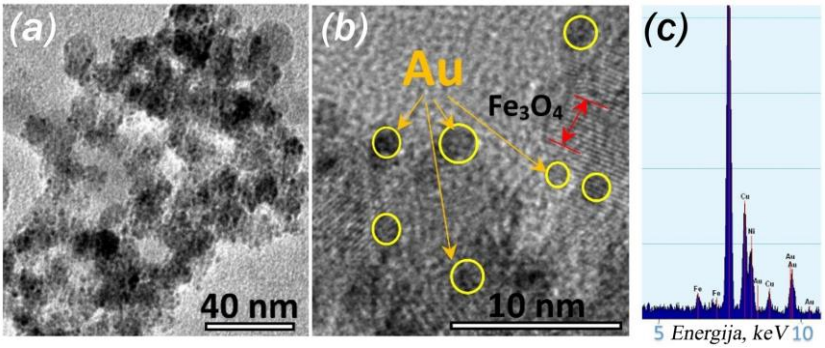

24 pav. Auksuotų magnetinių Fe_3O_4@Met@Au ND AR-PEM vaizdai esant skirtingiems didinimams (a, b) bei jų EDS spektras (c).

PEM nuotraukose rodyklėmis pavaizduotos prikibusios aukso ND, patvirtina sėkmingą, metioninu inicijuotą, aukso rūgšties redukciją magnetinės dalelės paviršiuje. Gautos aukso ND yra sferinės formos, apytiksliai 2 nm dydžio. Kaip minėta anksčiau, nuotraukoje aiškiai matomi magnetito ND tarpplokštuminiai atstumai lygūs 2,5 Å patvirtina kristalinę Fe_3O_4 ND struktūrą. Siekiant įrodyti, jog gautos smulkios dalelės, kuriomis nusėtas magnetinių ND paviršius yra Au, buvo atlikta EDS analizė (24 pav. c). Gauti rezultatai patvirtina, jog tiriama medžiaga yra sudaryta iš geležies, deguonies ir aukso. Be to, stebint auksuotų magnetito ND elgseną išoriniame magnetiniame lauke yra fiksuojamas ~22 % soties įmagnetėjimo sumažėjimas (23 pav. (b) dalies 2 kreivė). Remiantis literatūra, buvo patvirtinta, kad toks sumažėjimas yra gautas dėka smulkių aukso ND nusodinimo ant magnetito ND paviršiaus [145]. Būtina paminėti, jog pavienių aukso nanodalelių PEM analizės metu pastebėta nebuvo, nepaisant to, kad ruošiant bandinį PEM,

mėginys buvo veikiamas ultragarsu. Daroma prielaida, jog gautos paauksuotos ND yra stabilios ir tinkamos tolimesniems tyrimams.

6.4.3. Metionino inicijuotas ultra-smulkių Au@Met Nd „atkabinimas“

Siekiant gauti ultra–smulkias aukso ND, šiame darbe buvo panaudota metionino aminorūgštis Au „atkabinimui“ nuo Fe_3O_4@Met ND paviršiaus. Šis procesas yra siejamas su stipresne aukso ND sąveika su metionino molekulėmis. Ultra–smulkios aukso ND charakterizuotos PEM metodu. PEM analizės vaizdų pagalba nustatyta, jog nuo magnetito paviršiaus atskirtos aukso ND yra sferinės formos, vidutiniškai ~2,0 nm dydžio (25 pav.).

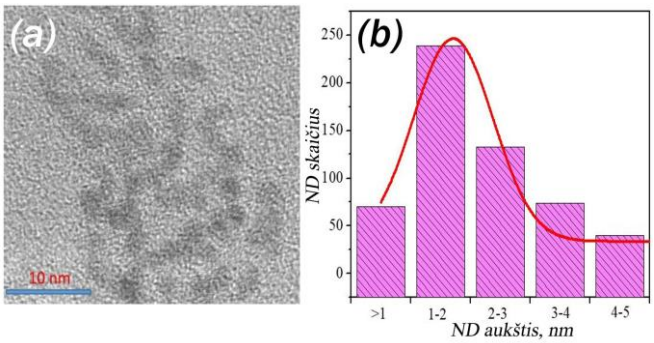

25 pav. Aukso ND PEM vaizdas (a) ir ND dydžių pasiskirstymo histograma (b).

Iš PEM nuotraukų buvo apskaičiuotas ND pasiskirstymas, atvaizduotas histogramoje (25 pav. b) rodo, jog ND būdingas siauras dispersiškumas.

6.4.4. Fe_3O_4@Met, Fe_3O_4@Met@Au ir Au@Met ND antimikrobinis aktyvumas prieš mediciniškai svarbias padermes

Antimikrobinis ultra–smulkių aukso ir Fe_3O_4@Au ND aktyvumas tirtas Gram-neigiamų *A. baumannii, S. enterica* ir Gram-teigiamų *M. luteus* bei meticilinui atsparių *S. aureus* bakterijų aplinkose, įvertinant kolonijas formuojančių vienetų skaičių (CFU). Kiekybinės analizės rezultatai pateikti bakterijų gyvybingumo procentinė išraiška (26 pav.). Nesunku pastebėti, kad Au@Met ir Fe_3O_4@Met@Au ND pasižymi didžiausiu antibakteriniu efektyvumu *M. luteus* mikroorganizmams, jų išgyvenamumas siekia tik 7,76 – 14,43 %. Šie rezultatai patvirtina, kad žmogaus patogeniški mikroorganizmai yra atsparesni ir virulentiškesni už antibiotikams neatsparias bakterijas, tokias kaip *M. luteus* [155]. Pastebėta teigiama koreliacija tarp Au kiekio mėginyje ir bakterijų gyvybingumo. Palyginus su kontroliniais mėginiais, didesnės koncentracijos 70 mg mL^{-1} Au@Met ND koloidiniai tirpalai demonstravo 84,4–58,5% žudymo efektyvumą Gram-neigiamoms ir 89,1–75,7% Gram-teigiamoms bakterijoms. Be to, aiškiai matoma, jog ultra–smulkios Au nanodalelės kur kas efektyviau veikia mikroorganizmų

gyvybingumą, nei tos pačios koncentracijos pagal auksą Fe_3O_4@Met@Au dalelės.

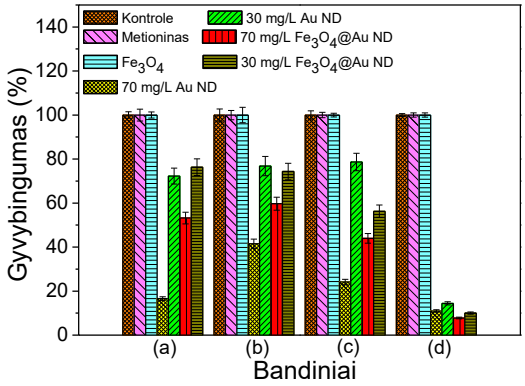

26 pav. Ultra-smulkių aukso ir Fe_3O_4@Met@Au ND antimikrobinio aktyvumo tirto mediciniškai svarbių Gram-neigiamų *A. baumannii* (a), *S. enterica* (b) ir Gram- teigiamų *S. aureus* (MRSA) (c), *M. luteus* (d) bakterijų aplinkose, diagrama. Švari D,L-metionino amino rūgštis bei magnetito ND buvo naudotos kaip neigiama kontrolė.

Reikėtų paminėti, kad *S. enterica* bakterijos demonstravo stipriausią atsparumą ultra–smulkioms Au@Met ir Fe_3O_4@Met@Au ND. Palyginus su kontroliniais mėginiais, *S. enterica* bakterijų išgyvenamumas buvo apytiksliai lygus 67,14%.

6.5. Belaidis bioplėvelių sudarytų iš mediciniškai svarbių bakterijų ir grybų detektavimas

Šiame skyriuje pristatytas belaidžio, mediciniškai svarbių mikroorganizmų, kaip antai *P. aeruginosa, E. coli, S. aureus, C. albicans* ir *S. gordonii* jutiklio, paremto Ag/Ag^+ redokso pora veikimo principas ir pagrindinės charakteristikos. Savaiminis bioplėvelių susidarymas ant darbinio elektrodo paviršiaus bei jas formuojančių mikroorganizmų metabolitiniai procesai lemia elektronų generaciją, kurie yra panaudojami nelaidžių AgCl ND redukcijai iki metalinio Ag^0. Šio proceso metu, ant paviršiaus spausdintų elektrodų (PSE) suformuotas metalinių ND kontaktas keičia savo varžą, kurios pokytis fiksuotas radijo dažnių indentifikavimo sistema (RDIS).

6.5.1. Atviros grandinės potencialo matavimai

Siekiant sukonstruoti belaidį bioplėvelių augimo kontrolės jutiklį, kuris nenaudotų jokios išorinės energijos šaltinio, pirmiausia buvo atlikti atviros grandinės potencialo matavimai (27 pav.). Tuo tikslu stiklo grafito strypelis buvo įmerkiamas į švarią LB terpę. Atviros grandinės potencialas išmatuotas

standartinio Ag/AgCl elektrodo atžvilgiu. Pradiniu laiko momentu jis svyravo tarp 35-160 mV (27 pav. t = 0). Nustatyta, kad po mikroorganizmų įnešimo, šis potencialas pradeda žemėti ir galiausiai įgauna neigiamą vertę, kuri varijuoja nuo -70 iki -300 mV. Pastebėta, kad šių verčių kitimo greitis priklauso nuo mikroorganizmų kultūros ir jai būdingo augimo charakteristikų.

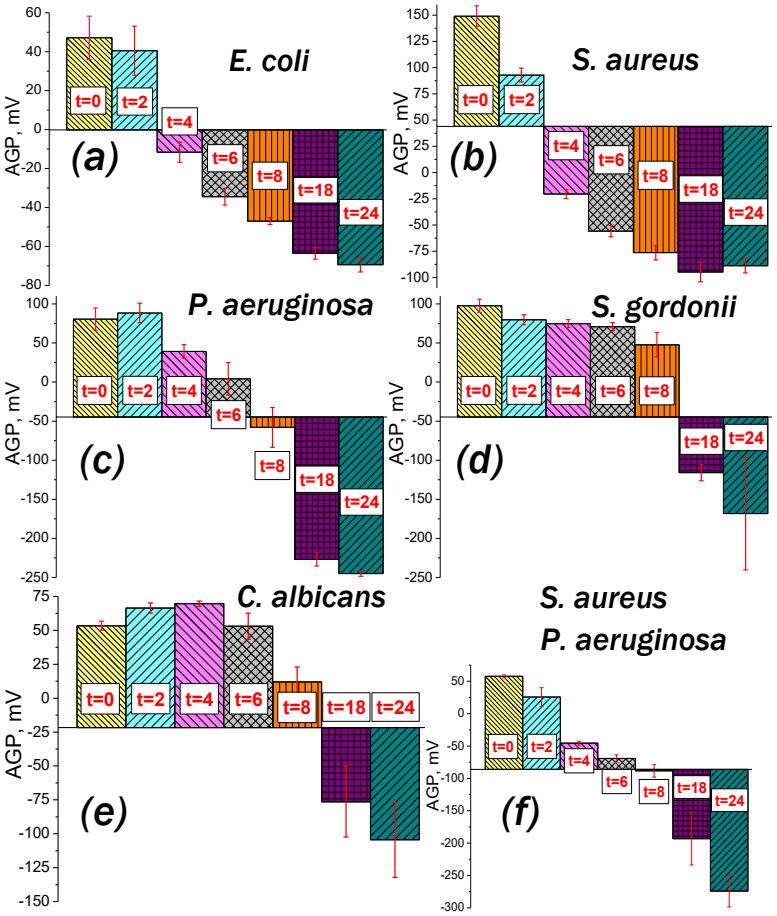

27 pav. Bioanodo atviros grandinės potencialo matavimų rezultatai gauti panardinus darbinį elektrodą į LB terpę prieš (t=0) ir po (a) *E. coli*, (b) *S. aureus*, (c) *P. aeruginosa*, (d) *S. gordonii*, (e) *C. albicans*, (f) *S. aureus* ir *P. aeruginosa* mikroorganizmų, kurių koncentracija 10^6 KSV mL^{-1} įnešimo (t=2-24).

Stiklo grafito atviros grandinės potencialas tampa neigiamas po 4 valandų inkubacijos su *E.coli* ir *S. aureus*, tuo tarpu bioplėvelės sudarytos iš *P .aeruginosa, S gordonii* ir *C. albicans* mikrobų generuoja neigiamą potencialą po 8 ir 18 valandų (27 pav. c, d, e). Didžiausias neigiamas potencialas buvo gautas su *P. aeruginosa* bakterijomis ir siekė -250 mV. Remiantis literatūra, toks aktyvumas yra aiškinamas dėka bakterijų ląstelių

gaminamų tirpių redokso mediatorinių, kaip antai piocianinas, fenazinai ir flavinai, kurie palengvina elektronų transportą [150].

6.5.2. Belaidžio jutiklio, skirto bioplėvelių detektavimui, konstravimas

Siekiant sukonstruoti belaidžio jutiklio detektavimo platformą šiame darbe buvo naudojami sidabro ir aukso ND mišiniais modifikuoti paviršiaus spausdinti elektrodai. Darbinis ir pagalbinis PSE elektrodai buvo sujungiami siauru ND kontaktu. Matuojant varžą tarp darbinio ir pagalbinio elektrodo gautos vertės svyruodavo nuo 2-30 Ω. Sekančiu etapu šis ND paviršius buvo elektrochemiškai oksiduojamas, tokiu būdu padidinant varžą iki 2-3 kΩ. Paruoštas PSE elektrodas buvo sujungiamas su bioanodu – stiklografito elektrodu, ant kurio "auga" ir formuojasi bioplėvelės. Idėjos koncepcija pavaizduota naudojant chronoamperometriją (28 pav. a).

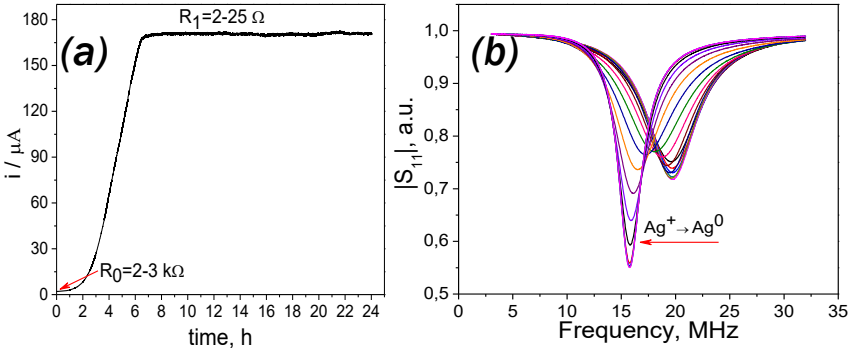

28 pav. Chronoamperometrinės biojutiklio veikimo charakteristikos (a) bei atspindžio koeficiento |S11| priklausomybė nuo sistemos dažnio (b), kuris veikia kaip atsakas ir kinta detektuojant biopleveles LB terpėje su *S. aureus* ir *P. aeruginosa* bakterijomis.

Kaip matome proseso pradžioje srovė yra labai nežymi, dėka prasto AgCl ND laidumo. Po 2 h ji pradeda didėti ir proporcingai auga 2-7 h intervale, kol pasiekia įsisotinimą, kuris žymi AgCl ND redukciją iki laidaus metalinio sidabro. Šios reakcijos kitimus patogu registruoti belaide RDIS sistema. Kuo daugiau elektronų gaunama iš bioplėvelių, tuo greičiau AgCl ND yra redukuojamos, todėl gaunamas atspindžio koeficiento rezonanso poslinkis dažnių skalėje kaip pavaizduota 28 pav. b dalyje. Šis pokytis ir yra konstruojamo jutiklio atsakas.

IŠVADOS

1. Palyginus su Cu_2O/TiO_2 ir Cu_2O/TiNT heterostruktūrizuotomis dangomis, nanolapelinės struktūros juodos anodinio vario oksido dangos pasižymi didžiausiu antimikrobiniu efektyvumu prieš *S. cerevisiae*, *A. versicolor*, *C. cladasporioides*, *C. parapsilosis* ir *C. krusei* mikroorganizmus.

2. Itin ploni porėto AAO paviršiai, dekoruoti sidabro nanosiūleliais demonstruoja baktericidinį poveikį prieš *E. coli* ir *M. luteus* bakterijas. Šios dangos taip pat slopina *A. fumigatus* ir *G. candidum* mikroskopinių grybų augimą bei visiškai pražudo *S. cerevisiae* ląsteles.

3. 2, 5 ir 15 nm dydžio kobalto ferito ND būdingos nuo dydžio priklausančios antimikrobinės savybės prieš *S. cerevisiae* ir keletą *Candida* rūšių, kaip antai, *C. parapsilosis*, *C. krusei* ir *C. albicans*.

4. L-lizino amino rūgštimi apvilktos, panašaus dydžio (5-6 nm), kobalto ferito ND pasižymi aukštu, nuo Co^{2+} kiekio priklausančiu antimikrobiniu efektyvumu prieš Gram-neigiamas *E. coli* ir Gram-teigiamas *S. aureus* bakterijas bei keletą *Candida* genties rūšių.

5. Antimikrobinis ND aktyvumas smarkiai priklauso nuo daleles supančių medžiagų prigimties. Oleino rūgštimi stabilizuotų $CoFe_2O_4$@Ole ND fiksuotas antimikrobinis efektyvumas yra ženkliai didesnis prieš *E. coli*, *S. aureus*, *C. parapsilosis* ir *C. albicans* padermes nei to paties dydžio $CoFe_2O_4$@Lys ND.

6. Ultra-smulkios aukso ($\leq$ 2 nm) bei aukso-magnetito hibridinės ND, kurių koncentracija 70 mg L^{-1}, pasižymi aukštu mikroorganizmų žudymo efektyvumu; jis atitinkamai lygus 84.4-58.5 % prieš Gram-neigiamas *A. baumannii*, *S. enterica* bakterijas ir 89.1-75.7 % prieš Gram-teigiamas *S. aureus* MRSA, *M. luteus* bakterijų padermes.

REFERENCES

1. Machowska, A. and C. Stalsby Lundborg, *Drivers of irrational use of antibiotics in europe.* International journal of environmental research and public health, 2018. **16**(1): p. 27.
2. Chandler, C.I.R., *Current accounts of antimicrobial resistance: stabilisation, individualisation and antibiotics as infrastructure.* Palgrave communications, 2019. **5**: p. 1-13.
3. Paladini, F., et al., *Metal-based antibacterial substrates for biomedical applications.* Biomacromolecules, 2015. **16**(7): p. 1873-1885.
4. Römling, U. and C. Balsalobre, *Biofilm infections, their resilience to therapy and innovative treatment strategies.* Journal of Internal Medicine, 2012. **272**(6): p. 541-561.
5. Willyard, C., *The drug-resistant bacteria that pose the greatest health threats.* Nature, 2017. **543**(7643): p. 15.
6. Vallet-Regí, M., B. González, and I. Izquierdo-Barba, *Nanomaterials as promising alternative in the infection treatment.* International journal of molecular sciences, 2019. **20**(15): p. 3806.
7. Khan, S.T. and A.A. Al-Khedhairy, *Chapter 8 - Metals and metal oxides: important nanomaterials with antimicrobial activity*, in *Antimicrobial Nanoarchitectonics*, A.M. Grumezescu, Editor. 2017, Elsevier. p. 195-222.
8. Heiligtag, F.J. and M. Niederberger, *The fascinating world of nanoparticle research.* Materials Today, 2013. **16**(7): p. 262-271.
9. Walter, P., et al., *Early use of PbS nanotechnology for an ancient hair dyeing formula.* Nano Letters, 2006. **6**(10): p. 2215-2219.
10. Tulinski, M. and M. Jurczyk, *Nanomaterials synthesis methods.* Metrology and Standardization of Nanotechnology, 2017: p. 75-98.
11. Yu, H.-D., et al., *Chemical routes to top-down nanofabrication.* Chemical Society Reviews, 2013. **42**(14): p. 6006-6018.
12. Scheu, M., et al., *Mapping nanotechnology patents: The EPO approach.* World Patent Information, 2006. **28**(3): p. 204-211.
13. Odularu, A.T., *Metal nanoparticles: thermal decomposition, biomedicinal applications to cancer treatment, and future perspectives.* Bioinorganic Chemistry and Applications, 2018. **2018**: p. 6.
14. Cruz, I.F., et al., *Chapter 3 - Multifunctional ferrite nanoparticles: from current trends toward the future*, in *Magnetic Nanostructured Materials*, A.A. El-Gendy, J.M. Barandiarán, and R.L. Hadimani, Editors. 2018, Elsevier. p. 59-116.
15. Byrappa, K. and M. Yoshimura, *Hydrothermal technology: principles and applications*, in *Handbook of Hydrothermal Technology (Second Edition)*, K. Byrappa and M. Yoshimura, Editors. 2013, William Andrew Publishing: Oxford. p. 1-49.

16. Roy, R., *Accelerating the kinetics of low-temperature inorganic syntheses.* Journal of Solid State Chemistry, 1994. **111**(1): p. 11-17.
17. Namratha, K., M.B. Nayan, and K. Byrappa, *Hydrothermal synthesis and photocatalytic properties of modified and unmodified zinc oxide nanoparticles.* Materials Research Innovations, 2011. **15**(1): p. 36-42.
18. Yoshimura, M. and K. Byrappa, *Hydrothermal processing of materials: past, present and future.* Journal of Materials Science, 2008. **43**(7): p. 2085-2103.
19. Tsang, M.-K., G. Bai, and J. Hao, *Stimuli responsive upconversion luminescence nanomaterials and films for various applications.* Chemical Society Reviews, 2015. **44**(6): p. 1585-1607.
20. Massart, R., *Preparation of aqueous magnetic liquids in alkaline and acidic media.* IEEE Transactions on Magnetics, 1981. **17**(2): p. 1247-1248.
21. Wu, W., C.Z. Jiang, and V.A.L. Roy, *Designed synthesis and surface engineering strategies of magnetic iron oxide nanoparticles for biomedical applications.* Nanoscale, 2016. **8**(47): p. 19421-19474.
22. Ait Kerroum, M.A., et al., *The effect of basic pH on the elaboration of $ZnFe_2O_4$ nanoparticles by co-precipitation method: Structural, magnetic and hyperthermia characterization.* Journal of Magnetism and Magnetic Materials, 2019. **478**: p. 239-246.
23. Pereira, C., et al., *Superparamagnetic MFe_2O_4 (M = Fe, Co, Mn) nanoparticles: tuning the particle size and magnetic properties through a novel one-step coprecipitation route.* Chemistry of Materials, 2012. **24**(8): p. 1496-1504.
24. Vikram, S., et al., *Investigations of suspension stability of iron oxide nanoparticles using time-resolved UV–visible spectroscopy.* Journal of Nanoparticle Research, 2016. **18**(9): p. 272.
25. Li, L., et al., *Superparamagnetic iron oxide nanoparticles as MRI contrast agents for non-invasive stem cell labeling and tracking.* Theranostics, 2013. **3**(8): p. 595-615.
26. Woo, K., et al., *Easy synthesis and magnetic properties of iron oxide nanoparticles.* Chemistry of Materials, 2004. **16**(14): p. 2814-2818.
27. Ramanavičius, S., et al., *Shell-dependent antimicrobial efficiency of cobalt ferrite nanoparticles.* Nano-Structures & Nano-Objects, 2018. **15**: p. 40-47.
28. Yu, W.W., et al., *Synthesis of monodisperse iron oxide nanocrystals by thermal decomposition of iron carboxylate salts.* Chemical Communications, 2004(20): p. 2306-2307.
29. Bhattacharjee, A., et al., *Solventless synthesis of hematite nanoparticles using ferrocene.* Journal of Materials Science, 2013. **48**(7): p. 2961-2968.
30. Lu, A.-H., E.L. Salabas, and F. Schüth, *Magnetic nanoparticles: synthesis, protection, functionalization, and application.* Angewandte Chemie International Edition, 2007. **46**(8): p. 1222-1244.

31. Chen, H., et al., *Highly crystallized iron oxide nanoparticles as effective and biodegradable mediators for photothermal cancer therapy.* Journal of Materials Chemistry B, 2014. **2**(7): p. 757-765.
32. Charles, R.G. and M.A. Pawlikowski, *Comparative heat stabilities of some metal acetylacetonate chelates.* The Journal of Physical Chemistry, 1958. **62**(4): p. 440-444.
33. Lu, L.T., et al., *Synthesis of magnetic cobalt ferrite nanoparticles with controlled morphology, monodispersity and composition: the influence of solvent, surfactant, reductant and synthetic conditions.* Nanoscale, 2015. **7**(46): p. 19596-19610.
34. Trivinho-Strixino, F., J.S. Santos, and M. Souza Sikora, *Electrochemical synthesis of nanostructured materials*, in *Nanostructures*, A.L. Da Róz, et al., Editors. 2017, William Andrew Publishing. p. 53-103.
35. Grgur, K.I.P.S.D.N., *Surface morphology of metal electrodeposits*, in *Fundamental Aspects of Electrometallurgy*. 2002, Springer US: Boston, MA. p. 29-100.
36. Gurrappa, I. and L. Binder, *Electrodeposition of nanostructured coatings and their characterization: A review.* Science and Technology of Advanced Materials, 2008. **9**(4): p. 043001.
37. Despić, A.R., *Deposition and dissolution of metals and alloys. Part B: Mechanisms, kinetics, texture, and morphology*, in *Comprehensive Treatise of Electrochemistry: Volume 7 Kinetics and Mechanisms of Electrode Processes*, B.E. Conway, et al., Editors. 1983, Springer US: Boston, MA. p. 451-528.
38. Oskam, G., et al., *Electrochemical deposition of metals onto silicon.* Journal of Physics D: Applied Physics, 1998. **31**(16): p. 1927-1949.
39. Ji, C., G. Oskam, and P.C. Searson, *Electrochemical nucleation and growth of copper on Si(111).* Surface Science, 2001. **492**(1): p. 115-124.
40. Allen J. Bard, L.R.F., *Electrochemical methods: fundamentals and applications, 2nd Edition*. John Wiley & Sons. 1980, New York. 51-52.
41. Matsushima, J.T., F. Trivinho-Strixino, and E.C. Pereira, *Investigation of cobalt deposition using the electrochemical quartz crystal microbalance.* Electrochimica Acta, 2006. **51**(10): p. 1960-1966.
42. Quan, H., S.-U. Park, and J. Park, *Electrochemical oxidation of glucose on silver nanoparticle-modified composite electrodes.* Electrochimica Acta, 2010. **55**(7): p. 2232-2237.
43. Jia, M., et al., *A novel process for the fabrication of a silver-nanoparticle-modified electrode and its application in nonenzymatic glucose sensing.* Electroanalysis, 2012. **24**(9): p. 1864-1868.
44. Radi, A., et al., *Nanoscale shape and size control of cubic, cuboctahedral, and octahedral Cu−Cu_2O core−shell nanoparticles*

on Si(100) by one-step, templateless, capping-agent-free electrodeposition. ACS Nano, 2010. **4**(3): p. 1553-1560.
45. Holubowitch, N., L.C. Nagle, and J.F. Rohan, *Porous alumina thin films on conductive substrates for templated 1-dimensional nanostructuring.* Solid State Ionics, 2012. **216**: p. 110-113.
46. Huczko, A., *Template-based synthesis of nanomaterials.* Applied Physics A, 2000. **70**(4): p. 365-376.
47. Lee, W. and S.-J. Park, *Porous anodic aluminum oxide: anodization and templated synthesis of functional nanostructures.* Chemical Reviews, 2014. **114**(15): p. 7487-7556.
48. Santos, J.P.F., et al., *Nanofibers of poly(vinylidene fluoride)/copper nanowire: Microstructural analysis and dielectric behavior.* European Polymer Journal, 2018. **101**: p. 46-55.
49. Masuda, H. and K. Fukuda, *Ordered metal nanohole arrays made by a two-step replication of honeycomb structures of anodic alumina.* Science, 1995. **268**(5216): p. 1466-1468.
50. Sulka, G.D., *Highly Ordered Anodic Porous Alumina Formation by Self-Organized Anodizing*, in *Nanostructured Materials in Electrochemistry*. p. 1-116.
51. Gymama, S. and A. Kweku, - *Vertically aligned Pd nanowires for glucose oxidase bioanode.* 2012.
52. Guo, Q., et al., *Structural analysis and angle-dependent magnetic properties of Y-branched Ni nanowires.* Physica E: Low-dimensional Systems and Nanostructures, 2012. **44**(10): p. 1988-1991.
53. Stępniowski, W.J. and a.M. Salerno, *Manufacturing nanostructures*. 2014, United Kingdom: One Central Press.
54. Ko, E., et al., *Cu_2O Nanowires in an alumina template: electrochemical conditions for the synthesis and photoluminescence characteristics.* ChemPhysChem, 2006. **7**(7): p. 1505-1509.
55. Aguilera, A., et al., *Porous alumina templates and nanostructured CdS for thin film solar cell applications.* Solar Energy Materials and Solar Cells, 2006. **90**(6): p. 713-726.
56. Gomez, H., et al., *Growth and characterization of ZnO nanowire arrays electrodeposited into anodic alumina templates in DMSO solution.* Journal of Solid State Electrochemistry, 2012. **16**(1): p. 197-204.
57. Keilbach, A., et al., *Electrodeposition of copper and silver nanowires in hierarchical mesoporous silica/anodic alumina nanostructures.* Chemistry of Materials, 2010. **22**(19): p. 5430-5436.
58. Lin, S.W., et al., *Fabrication and magnetic properties of nickel nanowires.* Journal of Magnetism and Magnetic Materials, 2004. **282**: p. 28-31.
59. Haehnel, V., et al., *Towards smooth and pure iron nanowires grown by electrodeposition in self-organized alumina membranes.* Acta Materialia, 2010. **58**(7): p. 2330-2337.

60. Bao, J., et al., *Fabrication of cobalt nanostructures with different shapes in alumina template.* Scripta Materialia, 2004. **50**(1): p. 19-23.
61. Sahu, P., et al., *Chapter 5 - Nanogels: a new dawn in antimicrobial chemotherapy*, in *Antimicrobial Nanoarchitectonics*, A.M. Grumezescu, Editor. 2017, Elsevier. p. 101-137.
62. Ge, L., et al., *Nanosilver particles in medical applications: synthesis, performance, and toxicity.* International journal of nanomedicine, 2014. **9**: p. 2399-2407.
63. Lok, C.N., et al., *Silver nanoparticles: partial oxidation and antibacterial activities.* J Biol Inorg Chem, 2007. **12**(4): p. 527-34.
64. Parham, S., et al., *Antimicrobial treatment of different metal oxide nanoparticles: a critical review.* Journal of the Chinese Chemical Society, 2016. **63**(4): p. 385-393.
65. Ruparelia, J.P., et al., *Strain specificity in antimicrobial activity of silver and copper nanoparticles.* Acta Biomater, 2008. **4**(3): p. 707-16.
66. Hwang, I.S., et al., *Synergistic effects between silver nanoparticles and antibiotics and the mechanisms involved.* J Med Microbiol, 2012. **61**(Pt 12): p. 1719-26.
67. Shrivastava, S., et al., *Characterization of enhanced antibacterial effects of novel silver nanoparticles.* Nanotechnology, 2007. **18**(22): p. 225103.
68. Pinto, R.J.B., et al., *Chapter 9 - Antimicrobial properties and therapeutic applications of silver nanoparticles and nanocomposites*, in *Antimicrobial Nanoarchitectonics*, A.M. Grumezescu, Editor. 2017, Elsevier. p. 223-259.
69. Radzig, M.A., et al., *Antibacterial effects of silver nanoparticles on gram-negative bacteria: influence on the growth and biofilms formation, mechanisms of action.* Colloids Surf B Biointerfaces, 2013. **102**: p. 300-6.
70. Loo, C.Y., et al., *Combination of silver nanoparticles and curcumin nanoparticles for enhanced anti-biofilm activities.* J Agric Food Chem, 2016. **64**(12): p. 2513-22.
71. Ansari, M.A., et al., *Gum arabic capped-silver nanoparticles inhibit biofilm formation by multi-drug resistant strains of Pseudomonas aeruginosa.* J Basic Microbiol, 2014. **54**(7): p. 688-99.
72. Choi, O. and Z. Hu, *Size dependent and reactive oxygen species related nanosilver toxicity to nitrifying bacteria.* Environmental Science & Technology, 2008. **42**(12): p. 4583-4588.
73. El Badawy, A.M., et al., *Surface charge-dependent toxicity of silver nanoparticles.* Environmental Science & Technology, 2011. **45**(1): p. 283-287.
74. Pal, S., Y.K. Tak, and J.M. Song, *Does the antibacterial activity of silver nanoparticles depend on the shape of the nanoparticle? A study*

of the Gram-negative bacterium Escherichia coli. Applied and environmental microbiology, 2007. **73**(6): p. 1712-1720.
75. Rizzello, L. and P.P. Pompa, *Nanosilver-based antibacterial drugs and devices: mechanisms, methodological drawbacks, and guidelines.* Chem Soc Rev, 2014. **43**(5): p. 1501-18.
76. Xiu, Z.-m., et al., *Negligible particle-specific antibacterial activity of silver nanoparticles.* Nano Letters, 2012. **12**(8): p. 4271-4275.
77. Xu, H., et al., *Role of reactive oxygen species in the antibacterial mechanism of silver nanoparticles on Escherichia coli O157:H7.* Biometals, 2012. **25**(1): p. 45-53.
78. Ingle, A.P., N. Duran, and M. Rai, *Bioactivity, mechanism of action, and cytotoxicity of copper-based nanoparticles: A review.* Applied Microbiology and Biotechnology, 2014. **98**(3): p. 1001-1009.
79. Edis, Z., et al. *Copper-based nanoparticles, their chemistry and antibacterial properties: A Review*. 2019. Cham: Springer International Publishing.
80. Hans, M., et al., *Role of copper oxides in contact killing of bacteria.* Langmuir, 2013. **29**(52): p. 16160-16166.
81. Usman, M.S., et al., *Copper nanoparticles mediated by chitosan: synthesis and characterization via chemical methods.* Molecules, 2012. **17**(12): p. 14928-14936.
82. Christy, A.J., L.C. Nehru, and M. Umadevi, *A novel combustion method to prepare CuO nanorods and its antimicrobial and photocatalytic activities.* Powder Technology, 2013. **235**: p. 783-786.
83. DeAlba-Montero, I., et al., *Antimicrobial properties of copper nanoparticles and amino acid chelated copper nanoparticles produced by using a soya extract.* Bioinorganic chemistry and applications, 2017. **2017**: p. 1064918-1064918.
84. Nishino, F., et al., *Formation of CuO nano-flowered surfaces via submerged photo-synthesis of crystallites and their antimicrobial activity.* Scientific Reports, 2017. **7**(1): p. 1063.
85. Ekthammathat, N., T. Thongtem, and S. Thongtem, *Antimicrobial activities of CuO films deposited on Cu foils by solution chemistry.* Applied Surface Science, 2013. **277**: p. 211-217.
86. K. Gopalakrishnan, C.R., V. Ragunathan, M. Thamilselvan, M. Thamilselvan, *Antibacterial activity of Cu_2O nanoparticles on E. coli synthesized from Tridax Procumbens leaf extract and surface coating with polyaniline.* Digest Journal of Nanomaterials and Biostructures, 2012. **7**(2): p. 833-839.
87. Amiri, M., M. Salavati-Niasari, and A. Akbari, *Magnetic nanocarriers: Evolution of spinel ferrites for medical applications.* Advances in Colloid and Interface Science, 2019. **265**: p. 29-44.
88. Srinivasan, S.Y., et al., *Applications of cobalt ferrite nanoparticles in biomedical nanotechnology.* Nanomedicine (Lond), 2018. **13**(10): p. 1221-1238.

89. Kefeni, K.K., B.B. Mamba, and T.A.M. Msagati, *Application of spinel ferrite nanoparticles in water and wastewater treatment: A review.* Separation and Purification Technology, 2017. **188**: p. 399-422.
90. Amiri, S. and H. Shokrollahi, *The role of cobalt ferrite magnetic nanoparticles in medical science.* Materials Science and Engineering: C, 2013. **33**(1): p. 1-8.
91. Yáñez-Vilar, S., et al., *A simple solvothermal synthesis of MFe_2O_4 (M=Mn, Co and Ni) nanoparticles.* Journal of Solid State Chemistry, 2009. **182**(10): p. 2685-2690.
92. Sanpo, N., et al., *Transition metal-substituted cobalt ferrite nanoparticles for biomedical applications.* Acta Biomaterialia, 2013. **9**(3): p. 5830-5837.
93. Lopez-Abarrategui, C., et al., *The intrinsic antimicrobial activity of citric acid-coated manganese ferrite nanoparticles is enhanced after conjugation with the antifungal peptide Cm-p5.* Int J Nanomedicine, 2016. **11**: p. 3849-57.
94. Samavati, A. and A. F. Ismail, *Antibacterial properties of copper-substituted cobalt ferrite nanoparticles synthesized by co-precipitation method.* Particuology, 2017. **30**: p. 158-163.
95. Jesudoss, S.K., et al., *Studies on the efficient dual performance of $Mn_{1-x}Ni_xFe_2O_4$ spinel nanoparticles in photodegradation and antibacterial activity.* Journal of Photochemistry and Photobiology B: Biology, 2016. **165**: p. 121-132.
96. Badwaik, V.D., et al., *Size-dependent antimicrobial properties of sugar-encapsulated gold nanoparticles synthesized by a green method.* Nanoscale Research Letters, 2012. **7**(1): p. 623.
97. Basu, A., et al., *Evaluating the antimicrobial, apoptotic, and cancer cell gene delivery properties of protein-capped gold nanoparticles synthesized from the edible mycorrhizal fungus Tricholoma crassum.* Nanoscale Res Lett, 2018. **13**(1): p. 154.
98. Mohamed, M.M., et al., *Antibacterial effect of gold nanoparticles against Corynebacterium pseudotuberculosis.* International Journal of Veterinary Science and Medicine, 2017. **5**(1): p. 23-29.
99. Payne, J.N., et al., *Novel synthesis of kanamycin conjugated gold nanoparticles with potent antibacterial activity.* Frontiers in Microbiology, 2016. **7**(607).
100. Rattanata, N., et al., *Gallic acid conjugated with gold nanoparticles: antibacterial activity and mechanism of action on foodborne pathogens.* International journal of nanomedicine, 2016. **11**: p. 3347-3356.
101. Rai, A., A. Prabhune, and C.C. Perry, *Antibiotic mediated synthesis of gold nanoparticles with potent antimicrobial activity and their application in antimicrobial coatings.* Journal of Materials Chemistry, 2010. **20**(32): p. 6789-6798.

102. Zheng, K., et al., *Antimicrobial gold nanoclusters.* ACS Nano, 2017. **11**(7): p. 6904-6910.
103. Jagminas, A., *Influence of magnesium and aluminium ions on the copper a.c. deposition into aluminium anodic oxide film nanotubes.* Journal of Applied Electrochemistry, 2002. **32**(11): p. 1201-1209.
104. Huber, F., *On the rectification of anodic oxide films of titanium.* Journal of The Electrochemical Society, 1968. **115**(2): p. 203-208.
105. Nielsch, K., et al., *Uniform nickel deposition into ordered alumina pores by pulsed electrodeposition.* Advanced Materials, 2000. **12**(8): p. 582-586.
106. Jagminas, A., et al., *Methionine-mediated synthesis of magnetic nanoparticles and functionalization with gold quantum dots for theranostic applications.* Beilstein J Nanotechnol, 2017. **8**: p. 1734-1741.
107. Turkevich, J., P.C. Stevenson, and J. Hillier, *A study of the nucleation and growth processes in the synthesis of colloidal gold.* Discussions of the Faraday Society, 1951. **11**(0): p. 55-75.
108. Li, H., et al., *Simple synthesis of monodisperse, quasi-spherical, citrate-stabilized silver nanocrystals in water.* Langmuir, 2013. **29**(16): p. 5074-5079.
109. Li, Y., et al., *Rate-dependent interface capture beyond the coffee-ring effect.* Scientific Reports, 2016. **6**: p. 24628.
110. Turner, R.F.B., D.J. Harrison, and R.V. Rojotte, *Preliminary in vivo biocompatibility studies on perfluorosulphonic acid polymer membranes for biosensor applications.* Biomaterials, 1991. **12**(4): p. 361-368.
111. Andrews, J.M. and f.t. BSAC Working Party on Susceptibility Testing, *BSAC standardized disc susceptibility testing method.* Journal of Antimicrobial Chemotherapy, 2001. **48**: p. 43-57.
112. Xu, F., J. Duan, and B. Hou, *Electron transfer process from marine biofilms to graphite electrodes in seawater.* Bioelectrochemistry, 2010. **78**(1): p. 92-95.
113. Jagminas, A., et al., *Decoration of the TiO_2 nanotube arays with copper suboxide by AC treatment.* Electrochimica Acta, 2014. **125**: p. 516-523.
114. Juodkazytė, J., et al., *Evaluation of electrochemically active surface area of photosensitive copper oxide nanostructures with extremely high surface roughness.* Electrochimica Acta, 2013. **98**: p. 109-115.
115. Mikami, M., et al., *Lattice dynamics and dielectric properties of TiO_2 anatase: A first-principles study.* Physical Review B, 2002. **66**(15): p. 155213.
116. Ohsaka, T., F. Izumi, and Y. Fujiki, *Raman spectrum of anatase, TiO_2.* Journal of Raman Spectroscopy, 1978. **7**(6): p. 321-324.
117. Carabatos, C. and B. Prevot, *Rigid ion model lattice dynamics of cuprite (Cu_2O).* physica status solidi (b), 1971. **44**(2): p. 701-712.

118. Debbichi, L., et al., *Vibrational properties of CuO and Cu_4O_3 from first-principles calculations, and raman and infrared spectroscopy.* The Journal of Physical Chemistry C, 2012. **116**(18): p. 10232-10237.
119. Li, B., et al., *Shape-controlled synthesis of Cu_2O nano/microcrystals and their antibacterial activity.* Journal of Physics and Chemistry of Solids, 2013. **74**(12): p. 1842-1847.
120. Ren, J., et al., *Crystallography facet-dependent antibacterial activity: the case of Cu_2O.* Industrial & Engineering Chemistry Research, 2011. **50**(17): p. 10366-10369.
121. Hou, Y., et al., *Fabrication of Cu_2O/TiO_2 nanotube heterojunction arrays and investigation of its photoelectrochemical behavior.* Applied Physics Letters, 2009. **95**(9): p. 093108.
122. Jagminienė, A., et al., *The influence of the alumina barrier-layer thickness on the subsequent AC growth of copper nanowires.* Journal of Crystal Growth, 2005. **274**(3): p. 622-631.
123. Painting, K. and B. Kirsop, *A quick method for estimating the percentage of viable cells in a yeast population, using methylene blue staining.* World J Microbiol Biotechnol, 1990. **6**(3): p. 346-7.
124. Tran, N., et al., *Bactericidal effect of iron oxide nanoparticles on Staphylococcus aureus.* International journal of nanomedicine, 2010. **5**: p. 277-283.
125. Yamamoto, O., et al., *Adsorption and growth inhibition of bacteria on carbon materials containing zinc oxide.* Carbon, 2001. **39**(11): p. 1643-1651.
126. Makhluf, S., et al., *Microwave-assisted synthesis of nanocrystalline MgO and its use as a bacteriocide.* Advanced Functional Materials, 2005. **15**(10): p. 1708-1715.
127. Baker, C., et al., *Synthesis and antibacterial properties of silver nanoparticles.* J Nanosci Nanotechnol, 2005. **5**(2): p. 244-9.
128. Egger, S., et al., *Antimicrobial properties of a novel silver-silica nanocomposite material.* Appl Environ Microbiol, 2009. **75**(9): p. 2973-6.
129. Laurent, S., et al., *Magnetic iron oxide nanoparticles: synthesis, stabilization, vectorization, physicochemical characterizations, and biological applications.* Chemical Reviews, 2008. **108**(6): p. 2064-2110.
130. Choi, K.-H., et al., *Optimized photodynamic therapy with multifunctional cobalt magnetic nanoparticles.* Nanomaterials, 2017. **7**(6): p. 144.
131. Millan, A., et al., *Surface effects in maghemite nanoparticles.* Journal of Magnetism and Magnetic Materials, 2007. **312**(1): p. L5-L9.
132. Belachew, N., D.R. Devi, and K. Basavaiah, *Facile green synthesis of l-methionine capped magnetite nanoparticles for adsorption of pollutant Rhodamine B.* Journal of Molecular Liquids, 2016. **224**: p. 713-720.

133. Tiano, A.L., et al., *Correlating size and composition-dependent effects with magnetic, Mössbauer, and pair distribution function measurements in a family of catalytically active ferrite nanoparticles.* Chemistry of Materials, 2015. **27**(10): p. 3572-3592.
134. Tan, Y., et al., *Room-temperature soft magnetic iron oxide nanocrystals: synthesis, characterization, and size-dependent magnetic properties.* Chemistry of Materials, 2008. **20**(15): p. 5029-5034.
135. Selvan, R.K., et al., *Combustion synthesis of $CuFe_2O_4$.* Materials Research Bulletin, 2003. **38**(1): p. 41-54.
136. Paiva, F.M., et al., *Infrared and Raman spectroscopy and DFT calculations of DL amino acids: Valine and lysine hydrochloride.* Journal of Molecular Structure, 2017. **1127**: p. 419-426.
137. Martusevičius, S., et al., *Adsorption of l-histidine on copper surface as evidenced by surface-enhanced Raman scattering spectroscopy.* Vibrational Spectroscopy, 1996. **10**(2): p. 271-280.
138. Roddick-Lanzilotta, A.D., P.A. Connor, and A.J. McQuillan, *An in situ infrared spectroscopic study of the adsorption of lysine to TiO_2 from an aqueous solution.* Langmuir, 1998. **14**(22): p. 6479-6484.
139. Hyldgaard, M., et al., *The antimicrobial mechanism of action of epsilon-poly-l-lysine.* Applied and Environmental Microbiology, 2014. **80**(24): p. 7758-7770.
140. Yamamoto, O., *Influence of particle size on the antibacterial activity of zinc oxide.* International Journal of Inorganic Materials, 2001. **3**(7): p. 643-646.
141. Azam, A., et al., *Size-dependent antimicrobial properties of CuO nanoparticles against Gram-positive and -negative bacterial strains.* International journal of nanomedicine, 2012. **7**: p. 3527-3535.
142. Wan, R., et al., *DNA damage caused by metal nanoparticles: involvement of oxidative stress and activation of ATM.* Chemical research in toxicology, 2012. **25**(7): p. 1402-1411.
143. Shakeel Ahmed Ansari, M.O., Rukhsana Satar, Anish Khan, Syed Ismail Ahmad, Mohammad Alam Jafri, Syed Kashli Zaidi, Mohammad Husein Alqahtani, *Antibacterial activity of iron oxide nanoparticles synthesized by co-precipitation technology against Bacillus cereus and Klebsiella pneumoniae.* Polish Journal of Chemical Technology, 2017. **19**(4): p. 110-115.
144. Kvítek, L., et al., *Effect of surfactants and polymers on stability and antibacterial activity of silver nanoparticles (NPs).* The Journal of Physical Chemistry C, 2008. **112**(15): p. 5825-5834.
145. Karamipour, S., M.S. Sadjadi, and N. Farhadyar, *Fabrication and spectroscopic studies of folic acid-conjugated Fe_3O_4@Au core–shell for targeted drug delivery application.* Spectrochimica Acta Part A: Molecular and Biomolecular Spectroscopy, 2015. **148**: p. 146-155.

146. Rozgonyi, F., et al., *Is MRSA more virulent than MSSA?* Clinical Microbiology and Infection, 2007. **13**(9): p. 843-845.
147. Moulder, J.F., Sticker, W.F., Sobol, P.E., Bomben, K.D., King R.C., *Handbook of X-ray photoelectrons spectroscopy.* Physical Electronics, 1995.
148. Venezia, A.M., et al., *Relationship between structure and CO oxidation activity of ceria-supported gold catalysts.* The Journal of Physical Chemistry B, 2005. **109**(7): p. 2821-2827.
149. Kallstrom, G., *Are quantitative bacterial wound cultures useful?* Journal of clinical microbiology, 2014. **52**(8): p. 2753-2756.
150. Robb, A.J., et al., *Electrochemical detection of small molecule induced Pseudomonas aeruginosa biofilm dispersion.* Electrochimica acta, 2018. **268**: p. 276-282.
151. Ibberson, C.B., et al., *Co-infecting microorganisms dramatically alter pathogen gene essentiality during polymicrobial infection.* Nature microbiology, 2017. **2**: p. 17079-17079.
152. Seil, J.T. and T.J. Webster, *Antimicrobial applications of nanotechnology: methods and literature.* Int J Nanomedicine, 2012. **7**: p. 2767-81.
153. Zhou, B., et al., *Preparation and characterization of TiO_2 thin film by thermal oxidation of sputtered Ti film.* Materials Science in Semiconductor Processing, 2013. **16**(2): p. 513-519.
154. Katoh, R., M. Murai, and A. Furube, *Electron–hole recombination in the bulk of a rutile TiO_2 single crystal studied by sub-nanosecond transient absorption spectroscopy.* Chemical Physics Letters, 2008. **461**(4): p. 238-241.
155. Rozgonyi, F., et al., *Is MRSA more virulent than MSSA?* Clin Microbiol Infect, 2007. **13**(9): p. 843-5.

PUBLICATIONS

The main results of the doctoral thesis were published in 6 scientific publications (P: 1-6).

P1. **Žalnėravičius R**., Paškevičius A., Kovger J., Jagminas A. Fabrication by AC Deposition and Antimicrobial Properties of Pyramidal-Shaped Cu_2O-TiO_2 Heterostructures. *Nanomaterials and Nanotechnology*, 2014, DOI: 10.5772/59997, (**IF** = 1.6).

P2. Jagminas A., **Žalnėravičius R**., Rėza A., Paškevičius A., Selskienė A. Design, optical and antimicrobial properties of extremely thin alumina films colored with silver nanospecies. *Dalton Transactions*, 2015, 44, 4512-4519 DOI: 10.1039/c4dt03644a, (**IF** = 4.052).

P3. **Žalnėravičius R**., Paškevičius A., Kurtinaitienė M., Jagminas A. Size-dependent antimicrobial properties of the cobalt ferrite nanoparticles. *Journal of Nanoparticle Research*, 2016, 18, 300-310. DOI: 10.1007/s11051-016-3612-x, (**IF** = 2.009).

P4. **Žalnėravičius R**., Paškevičius A., Mažeika K., Jagminas A. Fe(II)-substituted cobalt ferrite nanoparticles against multidrug resistant microorganisms. *Applied Surface Science*, 2018, 435, 141-148. DOI: 10.1016/j.apsusc.2017.11.028, (**IF** = 5.155).

P5. Ramanavičius S., **Žalnėravičius R**., Drabavičius A., Jagminas A. Shell-Dependent Antimicrobial Efficiency of Cobalt Ferrite Nanoparticles. *Nano-Structures & Nano-Objects*, 2018, 15, 40–47, DOI: 10.1016/j.nanoso.2018.03.007, (**IF** = -).

P6. **Žalnėravičius R**., Mikalauskaite A., Niaura G., Paškevičius A., Jagminas A. Ultra-small methionine-capped Au^0/Au^+ nanoparticles as efficient drug against the antibiotic-resistant bacteria, *Materials Science and Engineering C-Materials for Biological Applications*, 2019, 102, 646-652. DOI: 10.1016/j.msec.2019.04.062, (**IF** = 4.959).

The reprinted articles could be find in the following pages.

1st publication / 1 publikacija

Fabrication by ac deposition and antimicrobial properties of pyramidal-shaped Cu_2O-TiO_2 heterostructures

Žalnėravičius R., Paškevičius A., Kovger J., Jagminas A.
Nanomaterials and Nanotechnology, 4 (2014)
DOI: 10.5772/59997

The article could be find online at https://doi.org/10.5772/59997

Nanomaterials and Nanotechnology

OPEN ACCESS
ARTICLE

Fabrication by AC Deposition and Antimicrobial Properties of Pyramidal-Shaped Cu_2O-TiO_2 Heterostructures

Regular Paper

Rokas Žalnėravičius[1], Algimantas Paškevičius[1], Jelena Kovger[1] and Arūnas Jagminas[1]*

1 Centre for Physical Sciences and Technology, Institute of Chemistry, Vilnius, Lithuania
Institute of Botany of Nature Research Centre, Vilnius, Lithuania
* Corresponding author(s) E-mail: jagmin@ktl.mii.lt

Received 03 July 2014; Accepted 27 Oct 2014

DOI: 10.5772/59997

Abstract

Nanoparticulate surfaces possessing antimicrobial and fungicidal properties under visible light illumination have found wide applications in a number of fields. In this study, titania nanotubes, as well as titania compact films were designed with pure Cu_2O crystals in a mildly acidic copper acetate solution using a simple alternating current (AC) deposition approach. In this way, the thermally oxidized Ti substrate was coated by densely packed pyramidal and bi-pyramidal shaped Cu_2O crystals with dominant (111) planes and investigated against several types of fungi and bacteria. For comparison, TiO_2 nanotube (TiNT) films were also decorated with similar crystals and tested. The results showed that, compared to bare TiO_2 films, both Cu_2O-in-TiNT and Cu_2O-on-TiO_2 heterostructures exhibited remarkably enhanced activity against tested fungi and bacteria. We also demonstrated that the high photoactivity of these crystals remained even after 50 h stability tests under bright light illumination. The results obtained from in vitro tests indicated that Cu_2O-in/on-TiO_2 heterostructures show promise as visible light driven antimicrobial materials.

Keywords nanocomposite, titania nanotube films, cuprous oxide, antimicrobial

1. Introduction

Titanium (Ti), due to its high mechanical hardness, low density, elevated chemical stability, relatively low cost, environmentally-friendly characteristics and photocatalytic activity under UV irradiation, belongs to the category of metals suitable for the production of orthopaedic and dental implants, chirurgical instruments and self-cleaning surfaces. In air, this metal is always covered by a thin TiO_2 film, the thickness of which can be increased simply by thermal and chemical oxidation or anodization high up in the sub-μm scale. TiO_2 films produced by anodizing/

annealing may vary in terms of electronic and phase structure (anatase, brookite, rutile) porosity and activity [1]. Due to a large band gap energy (~3.2 eV) and a more positive conduction band potential than the potential required for water reduction (1.23 V *vs*. NHE at pH = 0), pure TiO_2 films effectively absorb light, split water and demonstrate self-cleaning properties under UV light illumination [2, 3]. The antibacterial behaviour of UV illuminated TiO_2 powders were first reported three decades ago [4]. Recent reports on the bactericidal properties of various TiO_2 nanoparticles and films are frequently based on pure TiO_2 photocatalytic behaviour under UV irradiation [5]. Many studies have also been devoted to the formation of TiO_2-based bactericide particles under visible-light illumination [6-9]. For example, the solvothermal approach has been proposed for the synthesis of various Cu_2O crystals, indicating that the obtained Cu_2O crystals show good antibacterial effects and that with the morphology of the Cu_2O crystals changing from cubic to octahedral, their antibacterial properties change from general bacteriostasis to high selectivity [10]. Dispersed in the tested solutions, these photocatalysts have shown promising bactericidal effects under visible light irradiation. However, in all of these applications, the post-separation of doped TiO_2 species from the disinfected solutions are required. This procedure is tedious and cost-intensive, rendering it unsuitable for the cleaning of drinking water.

In the past decade, to avoid the cleaning of tested solutions, immobilization of the TiO_2-based photocatalyst species onto various substrates have been proposed [11-14]. For example, CNT-doped TiNT on glass by dip-coating [11], Ag/TiO_2 composite films [12], CdS/Pt-TiNT [13] and high-efficient CdS/TiNT films [14] on the Ti substrate have been reported. However, most of these surfaces showed either low-effectiveness under illumination by bright light or were toxic due to the application of CdS.

Currently, several routes have been also reported for TiO_2 conduction and valence band re-design, for example, via attachment of non-toxic lower band gap semiconducting nanoparticles, such as Cu_2O [14, 15] and CuO [16, 17].

Cuprous oxide (Cu_2O) is typically a *p*-type semiconductor possessing a direct band gap of 2.0-2.2 eV [18]. Owing to visible light absorption, chemical and physical stability, and its low cost, nanostructured Cu_2O particle arrays have recently drawn significant interest in terms of the photo conversion of bright light into electrical or chemical energy [15, 19, 20]. Note that solar conversion efficiency is equal to 11% from the theoretically possible [21]. In addition, recent studies have implied that Cu_2O crystallites demonstrated distinctive antimicrobial activity against some types of bacteria [22,23]. According to Lu et al. [10], the antimicrobial activity of Cu_2O crystallites, including cubic, octahedral, hexa-spindel, polyhedral, etc., depended on their morphology. All of these crystallites demonstrated antibactericidal activity, but only octahedral-shaped ones possessed high selectivity. Furthermore, it has recently been reported that polycrystalline Cu_2O with four-sided pyramidal shape species that electrodeposited onto the ITO glass substrate, in contrast to single-crystal *p*-Cu_2O ones [24, 25], were quite stable in aqueous solutions under visible light illumination [26, 27]. This stability was linked to the predominant Cu^+-termination of (111) planes of electrodeposited *p*-Cu_2O, at which the reduction of Cu_2O to Cu^0 by reaction $Cu_2O + H_2O + 4e \rightarrow 2Cu^0 + 2OH^-$ did not take place [27]. It was therefore suspected that if well-attached to the titanium oxide substrate, numerous pyramidal Cu_2O crystallites with (111) planes could provide stable fungicidal and antimicrobial activity under visible light illumination.

The aim of this study was to design TiO_2/Cu_2O heterostructured films onto the titanium substrate possessing high stability and effective antimicrobial properties against several types of fungi and bacteria under solar light illumination. To achieve this result, an aqueous solution comprising Cu(II) acetate, Mg acetate and acetic acid at a pH = 5.3, as well as an alternating current approach, are proposed in this study. For comparison, polyhedral- and pyramidal-shaped Cu_2O crystals with (111) prevailing surfaces were organized both inside the TiO_2 nanotube (TiNT) film and onto the TiO_2 substrate. The stability of Cu_2O species tethered to the thermally oxidized Ti surface was investigated in a 0.5 mol L^{-1} Na_2SO_4 aqueous solution at -0.35 V (*vs*. Ag/AgCl, sat.) and 100 W tungsten lamp illumination for 50 h. The antimicrobial properties of the obtained Cu_2O/TiO_2 heterostructures were tested against several types of fungi and bacteria.

2. Experimental

2.1 Reagents

A 98% purity copper acetate, $Cu(CH_3COO)_2 \bullet H_2O$, 99% purity magnesium acetate, $Mg(CH_3COO)_2 \bullet 4H_2O$ and 99% purity ammonium hepta molibdate, $(NH_4)_6Mo_7O_{24} \bullet 4H_2O$, were purchased from Sigma Aldrich. NaOH (98.8%), aceton (99.8%), ethylene glycol (99%) and acetic acid, CH_3COOH (99.8%) were obtained from Eurochemicals, Slovakia. Ammonium fluoride (98% purity) was obtained from Merck.

Saccharomyces cerevisiae, *Aspergillus versicolor*, *Candida parapsilosis* and *Candida krusei* fungi and *Pseudomonas aeruginosa, Escherichia coli*, and *Micrococcus luteus* bacteria were obtained from the Liofilchem (Italy).

2.2 Electrochemical formation of TiNT films

Ti foil at 99.7% purity and 0.127 mm thick and purchased from Aldrich was used to prepare disc-shaped specimens 13.8 mm in diameter. The surface of samples was ultrasonically cleaned in acetone, ethanol and water, for 6 min in each, air dried and anodized in the thermostated glass cell containing ethylene glycol (Etg) with 0.3% wt. NH_4F and 20 mL L^{-1} H_2O at 20±1ºC and 50 V using a DC power supply

for 40 min. To decrease the thickness of the titania barrier-layer, the anodizing voltage was decreased at the end of anodizing at a 1.0 V min^{-1} rate down to 30 V. Two platinum plates were maintained at a distance of 13 mm from the Ti specimen as cathodes. Each sample was anodized in a fresh solution. Resulting films were calcined in air at 450ºC for 2 hrs using a 10ºC min^{-1} ramp and were also subjected to alternating current (AC) treatment. TiO_2 compact films were obtained via thermal oxidation of Ti specimens in air at 450ºC for 2 hrs using a 10ºC min^{-1} ramp.

2.3 Electrodeposition of Cu_2O species

Electrodepositions of Cu_2O on TiO_2 nanotube walls and TiO_2 surface were accomplished in a two-electrode glass cell, in a 200 mL volume and containing an aqueous solution of 0.1 mol L^{-1} copper acetate, $Cu(CH_3COO)_2$ H_2O, 0.1 mol L^{-1} magnesium acetate, $Mg(CH_3COO)_2$ $4H_2O$ and acetic acid. Based on previous investigations [28], Mg(II) salt was used to prevent the breakdown of the titania barrier layer during AC treatment. Several graphite stripes connected and positioned around the working specimen were used as a counter electrode. All depositions were carried out in a room temperature solution. Milli-Q water (18 MΩ) was used for the preparation of the Cu_2O deposition solution. Analytical grade $Mg(OOCCH_3)_2$, $Cu(OOCCH_3)_2$ and acetic acid were purchased from Eurochemicals Ltd. Owing to the rectifying properties of the titania barrier layer [29], the depositions were carried out by AC at a constant peak-to-peak voltage ($U_{p\text{-}to\text{-}p}$) mode using a programmable alternating current source Chroma AC (model 61602, Taiwan). The frequency of AC was varied within the 25 to 500 Hz range. All solutions were prepared with deionized water and reagent grade chemicals. After deposition, each sample was thoroughly rinsed with pure water and air dried.

2.4 Characterization

To ascertain the purity of Cu_2O species tethered to the TiNT walls, voltammetric measurements were performed using a potentiostat/galvanostat AUTOLAB 302 and a three-electrode electrochemical cell, in which Pt wire and a hydrogen electrode were used in the working solution (RHE) as a counter and reference electrodes, respectively. Prior to measurements, a working solution composed of 0.1 mol L^{-1} KOH was de-aerated by Ar gas bubbling for at least 0.5 h.

The stability tests of Cu_2O crystals tethered to the TiO_2 surface was carried out in 0.5 mol L^{-1} Na_2SO_4 solution under ~10 mW cm^{-2} irradiation provided by 100 W tungsten arc lamp illumination potentiostatically at -0.35 V (*vs.* Ag/AgCl, sat.) for up to 50 hrs. The content of Cu_2O and Cu deposited (and dissolved during stability tests) was determined by the analysis of solutions, obtained via etching the specimens in a hot HNO_3:H_2O (1:1) solution followed by careful rinsing and sonication in Milli-Q water. The inductively coupled plasma emission spectrometer OPTIMA 7000DV (Perkin Elmer, USA) was employed for analysis. Measurements were made on emission peaks at 327.393 and 324.752 nm for Cu, at least five times for the same solution.

To examine the morphology of films on the surface and in cross-sections, a scanning electron microscope, model FEI Quatra 200F and a Cross Beam Workstation Auriga, equipped with a field emission gun and EDX spectrometer were used.

Phase composition of the obtained heterostructures was studied by X-ray powder diffraction (XRD) using a D8 diffractometer (Bruker AXS, Germany), equipped with a Göbel mirror as a primary beam monochromator for CuK_α radiation. A step-scan mode was used in the 2Θ range from 18 to 77° with a step-length of 0.02° and a counting time of 8 s per step. The size of crystallites was determined from the broadening of all diffraction peaks using PDXL software and Halder-Wagner (H-W) approximation.

Raman spectra were recorded using an inVia (Renishaw) spectrometer equipped with a thermoelectrically cooled (-70°C) CCD camera and microscope. The 532 nm solid state diode laser beam was used as an excitation source. The laser power at the sample was restricted to 0.06 mW and 0.6 mW for samples Ti oxide/Cu_2O and bare Ti oxide, respectively. The Raman scattering wavenumber axis was calibrated by the silicon peak at 520.7 nm. The spectral slit width near 500 cm^{-1} was 6.7 cm^{-1}. The 50x objective was used during all measurements. The laser line was focused to a ~ 2 μm diameter spot on the sample. The parameters of bands were determined by fitting the experimental spectra with Gaussian-Lorentzian shape components using GRAMS/A1 8.0 (Thermo Scientific) software.

The antibacterial effects of the fabricated films were assessed using the *Saccharomyces cerevisiae*, *Aspergillus versicolor*, *Clodosporium cladosporioides*, *Candida parapsilosis* and *Candida krusei* fungi, cultured in Sabouraud CAF agar at 27°C, and *Pseudomonas aeruginosa*, *Escherichia coli* and *Micrococcus luteus* bacteria cultured in Nutrient agar at 27°C, and the effects on colony-forming units were analysed.

The antimicrobial activity of Cu_2O-in/on-TiNT samples against *Micrococcus luteus* (*M. luteus*), *Escherichia coli* (*E. coli*), *Aspergilus fumigatus* (*A. fumigatus*), *Geotrichum candidum* (*G. candidum*) and *Candida parapsilosis* (*C. parapsilosis*) was investigated using the zone inhibition method. Following this method, the pieces of alumina films were pressed gently onto Sabouraud CAF agar or Nutrient-agar ("Liofilchem", Italy) plates inoculated with ≅10^6 CFU mL^{-1} microorganisms and analysed after 48 h incubation at 27±1 ºC.

It should be noted that unless otherwise indicated, all the above-mentioned experiments were repeated three times and the obtained results were statistically analysed by

calculating averages and standard deviations. The resulting data were applied for building corresponding diagrams.

3. Results and discussion

3.1 Composition and structure of heterostructured films

We have reported recently that TiNT walls can be decorated with numerous pure Cu_2O species both inside and outside tubes *via* alternating current deposition from a slightly acidic Cu(II) acetate solution (Fig.1 A, B) [29]. The size of crystallites increased with the deposition bath voltage and AC treatment time attaining 60 nm. In this study, we demonstrate that the same solution can be successfully explored for the formation of densely packed pyramidal- and bi-pyramidal-shaped (octahedral) Cu_2O crystals onto the thermally oxidized Ti substrate (Figures 1C and D). The shape of crystallites was found to be dependent on the pH of solution and AC deposition conditions, similar to the case of potentiostatic depositions from the alkaline cupric lactate solution onto the ITO substrate [27]. The pH of solution kept at a pH within 5.2 to 5.35 range was found to be an optimal. In this solution, by variables in the AC treatment conditions ($U_{p\text{-}to\text{-}p}$ value, AC frequency and deposition time) the surface of the thermally oxidized Ti substrate can be predictably covered with densely packed pyramidal-shaped crystallites (Fig. 1C). The planar dimensions of the pyramidal and bi-pyramidal crystals were found to be dependent mainly on the AC treatment time and $U_{p\text{-}to\text{-}p}$ value, attaining sub-micrometre size. Most uniform covering of TiO_2 surface took place at 100 Hz frequency although some higher deposition rates were observed at 50 Hz frequency (Figure 2). Please note that randomly dispersed crystals can be formed at up to 250 Hz frequency. The shape of the deposited species depends on the pH of the solution although the pyramidal-shaped species can be deposited only from slightly acidic acetate solutions (Figure 3A). In the neutral solutions, e.g. at around pH = 7.0, the coral-shaped species (Figure 3B) were formed, whereas in the alkaline solutions, e.g. at pH = 10.0 (Figure 3C) the nano-particulate species dominated.

XRD and Raman investigations were used to characterize the phase structures of the deposited species. Figure 4 shows the XRD patterns of the Cu_2O/TiNT heterostructure (A) and Cu_2O octahedra obtained by AC deposition from a slightly acidic Cu(II) acetate solution on the thermally oxidized Ti substrate (B). As can be seen, both XRD patterns contain several obvious diffraction peaks at 2Θ positions 29.58, 36.42, 42.32, 61.46 and 73.60 that, according to PDF card no 01-078-2076, can be indexed as (110), (111), (200), (220), and (311) planes of the cubic phase cuprous oxide, allowing us to deduce that the deposited species are polycrystalline Cu_2O. It is also obvious that the preferred orientation of Cu_2O grains is (111). The size of Cu_2O grains calculated from the main diffraction line (111) broadening

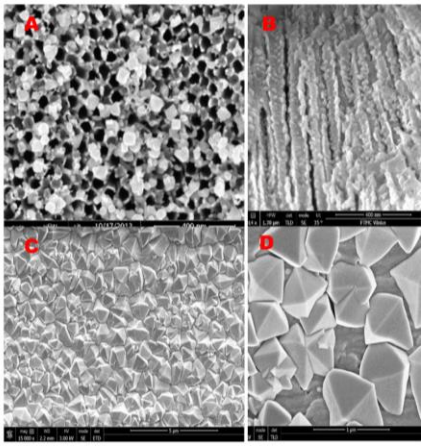

Figure 1. Top-side (A) and cross-sectional (B) SEM views of TiNT film fabricated by Ti anodizing in ethylene glycol solution, then annealed at 450 °C for 2 h and AC treated in Cu(II) acetate electrolyte at $U_{p\text{-}to\text{-}p}$ = 1.1 V for 5 min. In (C) and (D): typical top-side SEM views of crystallites formed onto the thermally oxidized Ti substrate by AC deposition in the same solution at $U_{p\text{-}to\text{-}p}$ 1.3 V for 10 min

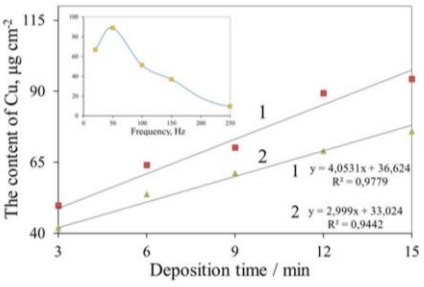

Figure 2. Variations of the content of deposited copper suboxide species onto the thermaly oxidized Ti substrate in the solution comprising 0.1 mol L^{-1} $Cu(OOCCH_3)_2$ + 0.1 mol L^{-1} $Mg(OOCCH_3)_2$ + CH_3COOH (pH = 5.3) at $U_{p\text{-}to\text{-}p}$ = 1.3 V and AC frequency: (1) 50, (2) 100 Hz on the deposition time. In the *Inset*: the dependency of deposited copper at $U_{p\text{-}to\text{-}p}$ = 1.3 V for 10 min on the AC frequency

was found to be dependent on the conditions of electrodeposition varying within 32-45 and 65-85 nm ranges for Cu_2O species deposited inside the TiNT and onto the TiO_2 substrate, respectively. No peaks that can be ascribed to CuO or $Cu(OH)_2$ were detected, although two small peaks at 2Θ positions around 43.3° and 50.4° (Figure 4B) could be linked with the presence of some Cu^0 onto the heat-treated Ti surface. It is also obvious that the pattern of TiNT film demonstrating a set of 10 reflections as shown in Figure 4A by the blue stars, according to PDF card no 00-021-1272,

indicated the presence of TiNT in the anatase-TiO_2 phase, whereas these peaks are absent in the heat-treated specimen.

Figure 5A compares the Raman spectra of the TiNT film before and after deposition of copper containing species. Strong Raman bands at 147, 397, 518, and 637 cm^{-1} are characteristic of crystalline anatase TiO_2 structure [30, 31] whereas difference spectrum (c) clearly shows several peaks associated with copper oxygenous compounds. In brief, bands at 219, 533, and 625 cm^{-1} evidence the presence of Cu_2O [32-34]. The Raman spectrum of pure thermally oxidized Ti substrate corresponds to the rutile TiO_2 phase with characteristic E_g and A_{1g} modes at 444 and 609 cm^{-1}, respectively (Figure 5B) [31], whereas bands at 98, 215, 531, and 617 cm^{-1} according to [33-35] evidence the presence of Cu_2O.

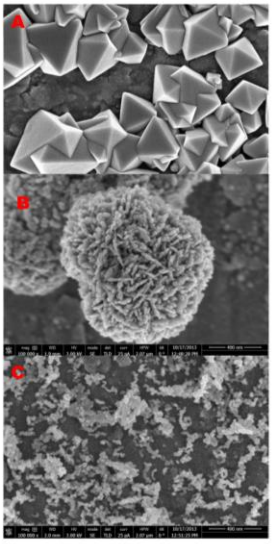

Figure 3. Top-side FESEM views of crystallites formed onto the thermally oxidized Ti substrate by AC deposition at $U_{p\text{-}to\text{-}p}$ = 1.3 V and room temperature for 10 min in the same way as in Figure 2 with the solution kept at the pH: (A) 5.0; (B) 7.0 and (C) 10.0

The purity tests for AC-deposited Cu_2O pyramidal crystals were further performed in a 0.1 mol L^{-1} KOH de-aerated solution by potential sweep from the open circuit potential, e.g. 0.75 V *versus* RHE, to -0.25 V and backwards. Voltammograms obtained for different contents of deposited species are shown in Figure 6. As seen, only a sharp reduction peak at ~-0.1 V, attributable to Cu_2O reduction is characteristic for all specimens. According to [36], such a reduction plot indicates the presence of pure Cu_2O.

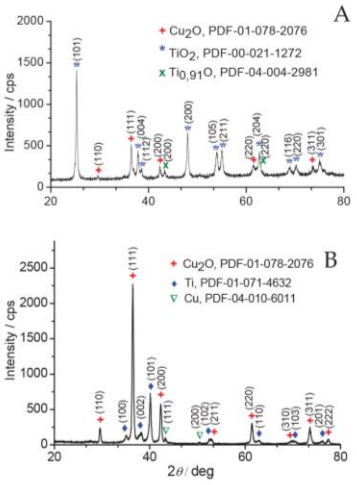

Figure 4. Typical XRD patterns (A) (B) of Cu_2O species deposited inside the TiNT film (A) and on the heat-treated TiO_2 substrate (B) by AC (100 Hz) treatment in the solution as in Figure 2 at $U_{p\text{-}to\text{-}p}$ = 1.2 V for 15 min

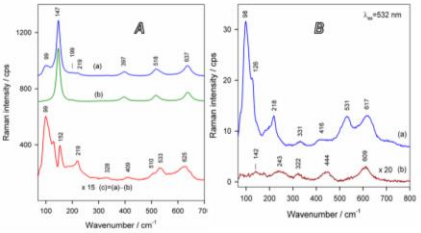

Figure 5. In (A): the Raman spectra of Cu_2O-in-TiNT (a), pure TiNT (b) and their difference (c) in wavenumber region from 65 to 700 cm^{-1}. In (B): the same for the Cu_2O deposited on the thermally oxidized Ti surface (a) and pure heat-treated Ti (b). Excitation wavelength is 532 nm. The same conditions as in Figure 4 were used for sample preparation.

3.2 Antimicrobial properties

The antibacterial activity results revealed that the pyramidal-shaped Cu_2O crystals encasing both the inside of the TiNT film tubes and deposited onto the rutile TiO_2 surface acted as excellent antimicrobial agents against all tested fungi as well as Gram-positive and Gram-negative bacterial strains. It should be noted that in the case of Cu_2O-on-rutile a fungistatic effect was observed for *A. versicolor* and *C.parapsilosis* fungi, whereas in the case of Cu_2O-in-TiNT the fungistatic effect was obtained in the Petri dishes with *A. versicolor, C. parapsilosis and C. krusei* strains. Figures 7 and 8 show the zones of inhibition produced by Cu_2O-in-

TiNT and Cu_2O-on-rutile TiO_2 against various eukaryotic and prokaryotic microorganism strains, respectively. Based on these results, some stronger fungicidal effects are characteristic for Cu_2O-on-rutile TiO_2 specimens showing the inhibition zones up to 25-27 mm after 48 h incubation (Table 1).

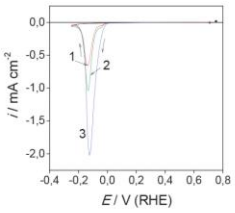

Figure 6. Reduction profiles of Cu_2O species deposited on the TiO_2 substrate by AC (100 Hz) treatment in the solution as in Figure 2, kept at a pH = 5.25 and $U_{p\text{-}to\text{-}p}$ = 1.2 V for 5 (1), 10 (2) and 15 min (3). Voltammograms were recorded in the O_2-free 0.1 mol L^{-1} KOH solution at v = 1.0 mV s^{-1} and 20°C.

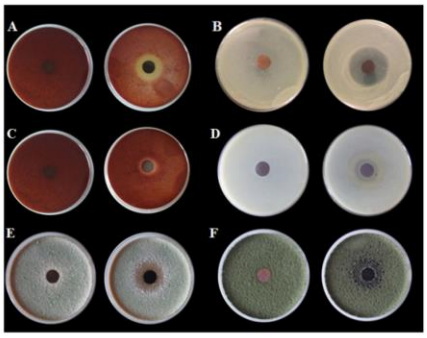

Figure 7. Zone of inhibition produced by Cu_2O-on-rutile (A, B, D) and TiO_2 Cu_2O-in-TiNT (C) specimens against the lawns of eukaryotic microorganisms: (A, C) *A. versicolor*, (B) *S. cerevisiae*, (D) *C. krusei*. In the left side - control specimen.

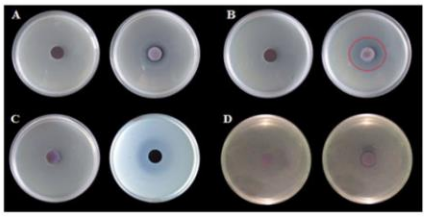

Figure 8. Zone of inhibition produced by Cu_2O-on-rutile (A, B, D) and Cu_2O-in-TiNT (C) specimens against the lawns of prokaryotic microorganisms: (A) *M. luteus*, (B, C) – *P. aeruginosa* and (D) *E. coli*. In the left side - control specimen.

Microorganism	Antimicrobial agent	Disc potency (μg)	Diameter of disc (d) (mm)	Diameter of zone (z) (mm)	z/d
Saccharomyces cerevisiae[a]	Cu_2O-in-TNT	33	14	25	1.8 ± 0.1
	Cu_2O-on-TiO_2	114	14	27	1.9 ± 0.1
Aspergillus versicolor[b]	Cu_2O-in-TNT	33	14	19	1.3 ± 0.2
	Cu_2O-on-TiO_2	114	14	24	1.7 ± 0.2
Candida parapsilosis[c]	Cu_2O-in-TNT	33	14	17	1.2 ± 0.1
	Cu_2O-on-TiO_2	114	14	18	1.3 ± 0.1
Candida krusei[d]	Cu_2O-in-TNT	33	14	18	1.3 ± 0.1
Pseudomonas aeruginosa[e]	Cu_2O-in-TNT	33	14	25	1.8 ± 0.2
	Cu_2O-on-TiO_2	114	14	24	1.7 ± 0.1
Escherichia coli[f]	Cu_2O-in-TNT	33	14	15.5	1.1 ± 0.1
	Cu_2O-on-TiO_2	114	14	15.5	1.1 ± 0.1
Micrococcus luteus[g]	Cu_2O-in-TNT	33	14	16	1.1 ± 0.1
	Cu_2O-on-TiO_2	114	14	17	1.2 ± 0.1
[a-d] Cultured in Sabouraud CAF agar (Liofilchem, Italy) at 27°C.					
[e-g] Cultured in Nutrient agar (Liofilchem, Italy) at 27°C.					

Table 1. Comparison of antimicrobial activities of Cu_2O-in-TNT and Cu_2O-on-rutile TiO_2

The antimicrobial efficiencies of pyramidal-shaped Cu_2O species attached to various TiO_2 substrates were also assessed against typical Gram-negative (*E. coli* and *P.aeruginosa*) and Gram-positive (*M. luteus*) bacteria. Note that *P. aeruginosa* was found to be more sensitive both for Cu_2O-on-TiO_2 and Cu_2O-in-TiNT surfaces: the average inhibition zone in this bacteria lawn was 1.5 to 1.6 times wider than in *E. coli* and *M. luteus* bacteria lawns (see Table 1). We note that in contrast to Li et al.'s indication that *E. coli* is resistant to cubic and spherical Cu_2O nanocrystals [37], our Cu_2O-TiO_2 heterostructures demonstrated a strong antibacterial activity against *E. coli*. We hypothesized that differences in the antimicrobial efficacy of Cu_2O-TiO_2 heterostructures and Cu_2O nanoparticles could be explained by synergetic behaviour of p-n heterojunction between Cu_2O and TiO_2 possessing a remarkable visible light photoresponse creating $OH^{\cdot}$ and H_2O_2 oxidative species [15] in the aqueous bacteria lawns. On the other hand, as reported by Ren et al. [23], Cu_2O octahedral single crystals bounded by {111} facets, as in our case, exhibited higher activity in killing *E. coli* than cubic ones. We also note that a similar result has been obtained under visible light illumination for *E. coli* inactivation by Cu_2O loaded on TiNT film *via* direct deposition from alkaline $CuSO_4$ and lactic acid solution [15].

3.3 Stability tests

To examine deterioration in photosensivity of Cu_2O pyramidal-shaped crystals deposited from the slightly acidic Cu(II) acetate solution on the thermally oxidized Ti substrate, the stability tests were performed in a 0.5 mol L^{-1} Na_2SO_4 solution at -0.35 V (*vs.* Ag/AgCl, sat.) and 100 W tungsten lamp illumination for up to 50 h. In these experi-

ments the tungsten lamp was placed in front of a quartz glass window of an electrochemical cell at a 12 cm distance from the socket of the lamp to the specimen. Figure 9 shows the variations in the open circuit potential of the Cu_2O-on-TiO_2 specimen after light switching before and after the stability test which lasted for 50 h. As can be seen, the Cu_2O-coated-TiO_2 specimen remained quite photosensitive to bright light even after prolonged 50 usage. It is noteworthy that the contamination of copper ions was not detected in the tested solution even after 50 h. These results imply the prospective application of the Cu_2O-on-TiO_2 antimicrobial coatings in food and healthcare industries.

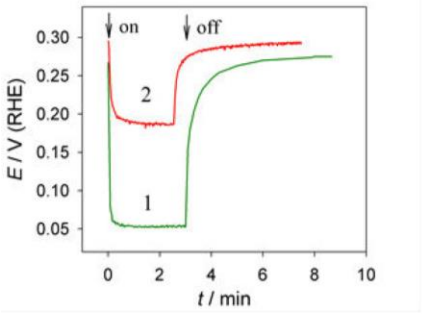

Figure 9. Variation in the open circuit potential for as formed (1) and deteriorate Cu_2O-on-TiO_2 heterostructure (2) in 0.5 mol L^{-1} Na_2SO_4 solution after switching of light. The stability test was performed in the same solution at -0.35 V (*vs* Ag/AgCl, sat) under 100 W tungsten lamp illumination for 50 h.

4. Conclusions

Pyramidal-shaped pure Cu_2O crystallites were successfully deposited both in/on the TiO_2 nanotube film and onto the thermally oxidized Ti substrate by using the alternating current deposition approach from the slightly acidic copper acetate solution. Both anodized and thermally oxidized Ti surfaces after covering with pyramidal-shaped Cu_2O crystallites possess strong antimicrobial properties against the tested fungi (*A. versicolor*, *C. parapsilosis*, *C. kruseiandS.cerevisiae*), Gram-negative (*E. coli* and *P.aeruginosa*) and Gram-positive (*M. luteus*) bacteria. In all cases, the Cu_2O-on-rutile TiO_2 surface demonstrated higher antimicrobial efficiency which could be linked with 2-3 times larger amounts of attached Cu_2O species. The antimicrobial effect of the Cu_2O species tethered to the TiO_2 surface was linked with the semiconducting properties of cuprous oxide capable of absorbing visible light and through synergetic coupling with TiO_2 produced oxidative species of OH^- and H_2O_2 destroying the walls of microorganism cells. The Cu_2O-coated-TiO_2 specimen remained quite photosensitive to bright light even after prolonged 50 h exploitation.

5. Acknowledgements

We would like to thank Dr. V. Pakštas for XRD and Dr. Habil. G. Niaura for Raman spectra collection and comments.

6. References

[1] Mor G K, Grimes C A (2009) TiO_2 nanotube arrays-Synthesis, Properties and Applications. Springer, New York.

[2] Keller V, Keller N, Ledoux MJ, Lett MC (2005) Biological agent inactivation in a flowing air stream by photocatalysis. Chem. Commun. 23: 2918-2920.

[3] Hashimoto K, Irie H, Fujishima A (2005) TiO_2 photocatalysis: a histerical overview and future prtospects. Jpn. J. Appl. Phys. 44: 8269-8285.

[4] Matsunaga T, Tomoda R, Nakajima T, Wake H (1985) Photoelectrochemical sterilization of microbial-cells by semiconductor powders. FEMS Microbial Lett. 29: 211-214.

[5] Li G Y, Liu X L, Zhang H M, An T C, Zhang S Q, Carroll A R, Zhao H J (2011) In situ photoelectrocatalytic generation of bactericide for instant inactivation and rapid decomposition of Gram-negative bacteria. J. Catal. 277: 88-94.

[6] Gholami M R, Elahifard M R, Rahimnejad S, Haghighi S (2007) Apatite-coated Ag/AgBr/TiO_2 visible-light photocatalyst for destruction of bacteria. J. Am. Chem. Soc. 129: 9552-9553.

[7] Pulgarin C, Rengifo-Herrera J A, Kiwi J N (2009) S-co-doped and N-doped Degussa P-25 powders with visible light response prepared by mechanical mixing of thiourea and urea. Reactivity towards *E. coli* inactivation and phenol oxidation. J. Photoch. Photobio. 205: 109-115.

[8] Wu P G, Xie R C, Imlay K, Shang J K (2010) Visible-light-induced bactericidal activity of titania dioxide codoped with nitrogen and silver. Environ. Sci. Technol. 44: 6992-6997.

[9] Wu T S, Wang K X, Li G D, Sun S Y, Sun J, Chen J S (2010) Montmorillonite-supported Ag/TiO_2 nanoparticles: an efficient visible-light bacteria photodegradation material. ACS Appl. Mater. Inter. 2: 544-550.

[10] Pang H, Gao, Lu Q (2009) Morphology effect on antibacterial activity of cuprous oxide. Chem. Commun. 1076-1078

[11] Akhavan O, Azimirad R, Safa S, Larijani M M (2010) Visible light photo-induced antibacterial activity of CNT-doped TiO_2 thin films with various CNT contents. J. Mater. Chem. 20: 7386-7392.

[12] Mai L X, Wang D W, Zhang S, Xie Y J, Huang C M, Zhang Z G (2010) Synthesis and bactericidal ability of Ag/TiO_2 composite films deposited on titanium plate. Appl. Surf. Sci. 257: 974-978.

[13] Kang Q, Lu Q Z, Liu S H, Wen L X, Luo S L, Cai Q Y (2010) A ternary hybrid CdS/Pt-TiO_2 nanotube structure for photoelectrocatalytic bactericidal effects on *Escherichia coli*. Biomaterials 31: 3317-3326.

[14] Hayden S C, Allam N K, El-Sayed M A (2010) TiO_2 nanotube/CdS hybrid electrodes: extraordinary enhancement in the inactivation of *Escherichia coli*. J. Am. Chem. Soc. 132: 14406-14408.

[15] Hou Y, Li X Y, Zhao Q D, Quan X, Chen G H (2009) Fabrication of Cu_2O/TiO_2 nanotube heterojunction arrays and investigation of its photoelectrochemical behavior. Appl. Phys. Lett. 95: 093108-093111.

[16] Zhang S, Liu C, Liu X, Zhang H, Liu P, Zhang S, Peng F, Zhao H (2012) Nanocrystal Cu_2O-loaded TiO_2 nanotube arrays films as high-performance visible-light bactericidal photocatalyst. App. Microbiol. Biotechnol. 96: 1201-1207.

[17] Li H G, Dimitrevich N M, Chen L, Rajh T, Gray K A (2008) Role of surface/interfacial Cu^{2+} sites in the photocatalytic activity of coupled CuO TiO_2 nanocomposites. J. Phys. Chem. C. 112: 19040-19044.

[18] Mills A, Hunte S Le (1997) An overview of semiconductor photocatalysis. J. Photochem. Photobiol. A: Chemistry 108: 1-35.

[19] Garuthara R, Siripala W (2006) Photoluminescence characterization of polycrystalline n-type Cu_2O films. J. Luminesc. 121: 173-178.

[20] Yang Q, Yan P X, Chang J B, Feng J J, Yue G H (2007) Growth of bicrystal CuO microsheets from aqueous solution. Phys. Lett. A 361: 493-496.

[21] Zhao W Y, Fu W Y, Yang H B, Tian C J, Li M H, Li Y X, Zhang L N, Sui Y M, Zhou X M, Chen H, Zou G T (2011) Electrodeposition of Cu_2O films and their photoelectrochemical properties. Crys. Eng. Comm. 13: 2871-2877.

[22] Huh A J, Kwon Y J (2011) "Nanoantibiotics": a new paradigm for treating infectious diseases using nanomaterials in the antibiotics resistant era, J. Contr. Release 156: 128-145.

[23] Ren J, Wang W, Sun S, Zhang L, Wang L, Chang J (2011) Crystallography Facet-Dependent Antibacterial Activity: The Case of Cu_2O. Ind. Eng. Chem. Res. 50: 10366-10369.

[24] Gerischer J H (1977) On the stability of semiconductor electrodes against photodecomposition. J. Electroanal. Chem. 82: 133-143.

[25] Takeuchi M, Weichman F L, Morosawa K, Kowakami M, Nagasaka N (1988) Photoelectrochemical behavior of Cu_2O single crystals in liquid electrolytes. Appl. Surf. Sci. 33-34: 972-979.

[26] De Jongh P E, Vanmaekelbergh D, Kelly J J (1999) Cu_2O: Electrodeposition and characterization. Chem. Mater. 11: 3512-3517.

[27] Engel C J, Polson T A, Spado J R, Bell J M, Fillanger A (2008) Photoelectrochemistry of Porous p-Cu_2O Films. J. Electrochem. Soc. 155: F37-F42.

[28] Sowers K L, Fillanger A (2009) Crystal face dependence of *p*-Cu_2O stability as photocatode. J. Electrochem. Soc. 156: F80-F85.

[29] Jagminas A (2002) Influence of magnesium and aluminium ions on the copper a.c. deposition into aluminium anodic oxide film nanotubes. J. Appl. Electrochem. 32(11): 1201-1209.

[30] Jagminas A, Kovger J, Rėza A, Niaura G, et. al. (2014) Decoration of the TiO_2 nanotube arrays with copper suboxide by AC treatment, Electrochim. Acta 125: 516-523.

[31] Mikami M, Nakamura S (2002) Dynamics and dielectric properties or TiO_2 anatase: A first-principles study. Phys. Rev. B 66: 155213.

[32] Ohsaka T, Izumi F, Fujiki Y (1978) Raman spectrum of anatase, TiO_2. J. Raman Spectr. 7: 321-325.

[33] Yu P Y, Shen Y R (1975) Resonance Raman studies in Cu_2O. I. The phonon-assisted 1s yellow excitonic absorption edge. Phys.Rev. B 12: 1377-1380. Soc. 127: 10982–10990.

[34] Yu P Y, Shen Y R (1975) Resonance Raman studies in Cu_2O. I. The phonon-assisted 1s yellow excitonic absorption edge. Phys.Rev. B 12: 1377-1381.

[35] Carabatos C, Prevot B (1971) Rigid ion model lattice dynamics of cuprite (Cu_2O). Phys. Status Solidi B 44: 701-705.

[36] Strehblow H H, Maurice V, Marcus P (2001) Initial and lateral stages of anodic oxide formation on Cu, chemical aspects, structure and electronic properties. Electrochim. Acta 46: 3755-3766.

[37] Li B, Li Y, Zhao Y, Sun L (2013) Shape-controlled synthesis of Cu_2O nano/microcrystals and their antibacterial activity. J. Phy. Chem. Solids 74:1842-1847.

2nd publication / 2 publikacija

Design, optical and antimicrobial properties of extremely thin alumina films colored with silver nanospecies

Jagminas A., Žalnėravičius R., Rėza A., Paškevičius A., Selskienė A.
Dalton Transactions, 44 (2015)
DOI: 10.1039/c4dt03644a

Dalton Transactions

PAPER

Cite this: *Dalton Trans.*, 2015, **44**, 4512

Design, optical and antimicrobial properties of extremely thin alumina films colored with silver nanospecies

A. Jagminas,*[a] R. Žalnėravičius,[a] A. Rėza,[a] A. Paškevičius[b] and A. Selskienė[a]

Received 27th November 2014,
Accepted 23rd January 2015

DOI: 10.1039/c4dt03644a

www.rsc.org/dalton

In this study, conditions for the fabrication of extremely thin and flexible anodic films decorated with silver nanowire arrays by alternating current treatments for the finishing of high purity and commercial aluminium foils were developed. For characterization of these porous films with a thickness of ≤1.0 μm and encased silver species, inductively coupled plasma optical emission spectroscopy, X-ray diffraction and field emission scanning electron microscopy were used. Variable angle spectroscopic ellipsometry in the wavelength range of 200–1700 nm was also used to determine the influence of the deposited Ag content and the film thickness on the optical constants (*n*, *k*) of the fabricated alumina films. It is shown that due to surprisingly low *k* values of nano-Ag-in-alumina films in the visible and near IR regions these films could be applied as transparent films with an extremely low refractive index. In addition, the antimicrobial activity of the obtained films was assessed for the as-deposited and fully-encapsulated silver nanowire arrays against several widespread fungi and bacteria. The results obtained from *in vitro* tests indicated that the as-formed Ag-in-alumina films containing ≥19 μg cm^{-2} of silver possessed antimicrobial properties and could be promising as foodstuff packaging materials.

Introduction

Nanoscale materials frequently demonstrate unique physical and chemical properties due to their high surface area as well as quantum-sized effects.[1,2] In recent years, these effects have stimulated a rapid growth in studies devoted to fabrication of various nanostructured architectures and composites. Among others, silver nanoparticle-containing materials[3–5] and silver-based composites[6–11] with antimicrobial activity have been synthesized. These materials can reduce infections during burn treatment[12,13] and prevent bacterial colonization of dental materials,[14] catheters,[15,16] stainless steel instruments,[17] textile products,[18,19] and human skin.[20,21] Note that silver nanoparticle-containing materials frequently demonstrate greater antimicrobial activity than silver ions alone, whose bactericidal properties have been known for centuries.[22] The smaller the Ag^0 particles are, the greater are their antimicrobial effects.[4,5,23] The bactericidal efficacy of silver-containing materials is frequently linked to the interaction of silver ions[24] or free radicals[25] with the liquid watery phase, resulting in membrane damage. As also reported, silver nanoparticles can exhibit genotoxic and cytotoxic effects in human tissues, causing DNA and cell damage if they are directly applied above a certain concentration.[26] However, little is known about the antibacterial and fungicidal properties of nm-scaled silver species encased inside the alumina pores although decoration processes of porous alumina films of a thickness of ≥6.0 μm with nanowired silver arrays for the finishing of the aluminium surface have been patented four decades ago.[27] It is also worth noting that usual anodic coatings are brittle and unsuitable for surface finishing of foodstuff packaging aluminium foils.

In this study, extremely thin porous alumina films were decorated in gold tints by alternating current deposition of silver in various contents and their antimicrobial activity against various microorganisms were tested. Variations in the ellipsometric parameters Ψ (psi) and Δ (delta) data with angle of incidence were also evaluated to determine the influence of the deposited Ag content and film thickness on the optical constants (*n*, *k*) of the fabricated alumina films.

Experimental

Milli-Q water (18 MΩ) was used for the preparation of all solutions. Aluminium (99.7% purity) foil was purchased from Russia whereas high-purity foil with a thickness of 0.127 mm

[a]*State Research Institute Center for Physical Sciences and Technology, Institute of Chemistry, Gostauto 9, LT-01108 Vilnius, Lithuania. E-mail: jagmin@ktl.mii.lt*
[b]*Institute of Botany of Nature Research Centre, Zaliuju ezeru 49, LT-08406 Vilnius, Lithuania*

(99.99% purity) was purchased from Sigma-Aldrich. The highest purity sulfuric, nitric and boric acids were purchased from Labochem Ltd, and analytical grade $AgNO_3$, $MgSO_4$ and triethanolamine (TEA) were from Sigma-Aldrich. *Saccharomyces cerevisiae*, *Micrococcus luteus*, *Escherichia coli*, *Aspergillus fumigatus*, and *Geotrichum candidum* cultures were obtained from the Botany Institute of Nature Research Centre. For the preparation of the YEPD medium, analytical grade peptone and galactose were purchased from Aldrich.

Aluminum samples, 40 mm × 40 mm × 0.05 mm, were cut from pure 50 μm thick, commercial Al foil (Al: 99.7%). The samples were chemically cleaned by etching in 1.5 mol L^{-1} NaOH at ~60 °C for 15 s, rinsed for ~3 min with running water and desmutted for 60 s in a 1.5 mol L^{-1} HNO_3 solution at ambient temperature. After careful rinsing in distilled water, the specimens were dried in a stream of argon gas. The surface of high purity aluminium samples devoted to ellipsometric investigations was polished in the $HClO_4$–ethanol solution at 17 V and 7–10 °C.

Anodizing was carried out in a thermostated 15 ± 0.1 °C glass cell where an aluminium foil was used as a working electrode and two platinum (45 mm × 70 mm × 0.5 mm) sheets were used as the counter electrodes. For anodizing an aqueous solution containing 1.2 mol L^{-1} of H_2SO_4 was used. To obtain a thin and flexible porous film, the specimens were anodized at 15 °C and 10 V for 10 min. For comparison, some specimens were anodized under the same conditions for 2 h, obtaining a porous alumina film with an average thickness of 9.5 μm. The as-anodized sample was rinsed with distilled water for 2 min and placed in the silver deposition bath containing 10 mmol L^{-1} $AgNO_3$.

To obtain uniform deposition of silver within the extremely short alumina pores and uniform colouring of the alumina film in gold tints, the composition of the electrolyte was modified by the addition of H_3BO_3, H_2SO_4, $MgSO_4$ and TEA. The counter-electrode consisted of eight graphite strips connected together. Due to the rectifying properties of the alumina barrier layer,[25] the depositions were carried out in alternating current (ac, 50 Hz) at either a constant effective ac current density or constant peak-to-peak voltage ($U_{p\text{-}to\text{-}p}$) modes. Anodized and coloured specimens were individually sealed in boiling distilled water for 10 min.

The content of deposited silver was determined by inductively coupled plasma optical emission spectroscopy analysis of solutions obtained *via* etching of a 4.5 cm^2 Ag-in-alumina film in a hot $HNO_3 : H_2O$ (1 : 1) solution followed by careful rinsing and sonication in Milli-Q water. A high-resolution scanning electron microscope (SEM, Helios Nanolab 650) was used to examine the morphology of alumina films as well as the filling uniformity of alumina pores by the silver. For these observations, cross-sections of alumina films were obtained by cutting the film perpendicular to the substrate with a FIB focused Ga^+-ion beam.

The phase composition of coloured alumina films was studied by X-ray powder diffraction (XRD) using a D8 diffractometer (Bruker AXS, Germany), equipped with a Göbel mirror as a primary beam monochromator for Cu Kα radiation. A step-scan mode was used in the 2Θ range from 30 to 80° with a step-length of 0.02° and a counting time of 8 s per step. The size of crystallites was determined from the broadening of all diffraction peaks using software PDXL and Halder–Wagner (H–W) approximation.

The optical properties of the as-grown and decorated alumina films were investigated by means of spectroscopic ellipsometry in the wavelength range of 200–1700 nm by measuring the change in the polarization states (Ψ and Δ) of the light reflected off the surface of the film with an ellipsometer RC2. The Bruggeman Effective Medium Approximation (EMA) was applied to calculate the optical constants of the mixed transparent Ag-in-alumina layer on the aluminium substrate using the specified Cauchy dispersion, which comprised of an oxide, empty nanochannels and encased silver. The optical constants, *e.g.* the refractive index n and the extinction coefficient k, as well as the thickness of a film d were evaluated by fitting the model functions to the measured data using the CompleteEASE software program.

The antibacterial effects of the fabricated films were assessed by the *Saccharomyces cerevisiae* (*S. cerevisiae*) colony-forming unit assay (CFU) where Ag-in-alumina film pellets were incubated for various times in the YEPD (1% yeast extract + 2% bacto peptone + 2% galactose) medium and the effects on colony-forming units were analysed. An aqueous solution of methylene blue (0.01%) was applied for detection of killed yeast cells.

The antimicrobial activity of Ag-in-alumina samples against *Micrococcus luteus* SK4 (*M. luteus*), *Escherichia coli* SK 1.10 (*E. coli*), *Aspergillus fumigatus* BTL KO-5 (*A. fumigatus*), *Geotrichum candidum* BTL 2.1 (*G. candidum*) and *Candida parapsilosis* BTL C.7.2 (*C. parapsilosis*) was also investigated by the zone inhibition method. Following this method, pieces of alumina films decorated with silver were pressed gently onto Sabouraud CAF agar or Nutrient-agar ("Liofilchem", Italy) plates inoculated with ≅10^6 CFU mL^{-1} microorganisms and analysed after 48 h incubation at 27 ± 1 °C.

All experiments were performed in triplicate. Data from triplicate counts were averaged and the resulting values were applied for building the corresponding diagrams.

Results

Fig. 1 shows surface and cross-sectional SEM images of alumina films fabricated by short-time (10 min) anodizing of aluminum at 10 V in 1.2 mol L^{-1} H_2SO_4 at 15 °C after ac treatment in a silver deposition bath. The images show a porous anodic oxide film with an average pore diameter ($\varnothing_{pore}$) of 10 ± 0.5 nm and a pore length of ~0.8 ± 0.1 μm. SEM (inset in Fig. 1C) also revealed that the diameter and shape of the silver nanowires encased within the pores of such films by subsequent ac deposition were close to those of alumina pores. The mean size of the silver crystallites was 8–10 nm as assessed from the full width at half maximum of the peaks *via*

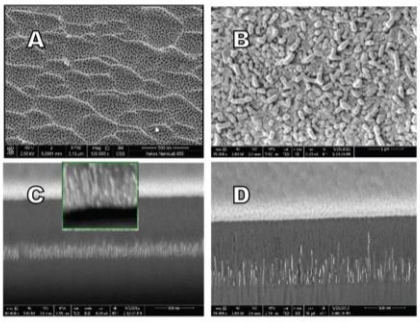

Fig. 1 Surface (A, B) and cross-sectional (C, D) SEM views of a 0.8 μm thick porous alumina film after ac deposition of silver at a constant peak-to-peak voltage of 7.0 V mode for 600 (B), 40 (C) and 150 s (D).

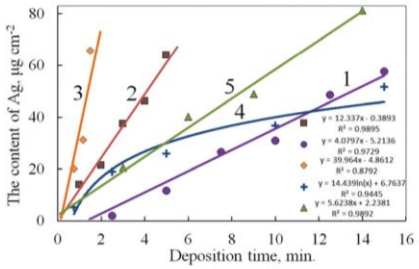

Fig. 3 Variations in the content of silver deposited inside the pores of the alumina film from a solution containing 10 $AgNO_3$ and 50 mmol L^{-1} $MgSO_4$ at constant ac current densities (A dm^{-2}): 0.15 (1), 0.2 (2) and (5), 0.3 (3) and a peak-to-peak voltage of 5.0 ± 0.3 V (4) with a processing time. $\varnothing_{pore} \approx 10$ nm and the thickness of the alumina film (in μm) was: 0.8 (1–4) and 9.5 (5).

the Debye–Scherrer formula. The deposition of silver at the bottom of tiny pores was observed from about 0.15 A dm^{-2}. The cross-sectional SEM observations also indicated that at 0.15 to 0.3 A dm^{-2} ac current density (j_{ac}) most of the alumina pores were filled to a height of ~200–250 nm. With further processing, an uneven growth of silver nanowires prevailed (Fig. 1D).

Further ac treatments resulted in the deposition of silver onto the film surface (Fig. 1A) covering it with rod-shaped Ag^0 crystals (Fig. 1B). However, with a precise control of the ac treatment conditions, a wide spectrum of uniform colours from light gold to bright brown could be obtained by this process (inset in Fig. 2).

From the XRD patterns (Fig. 2), the as-deposited silver nanowires within the alumina pores had a polycrystalline structure with the prevailing orientation along the [110] direction.

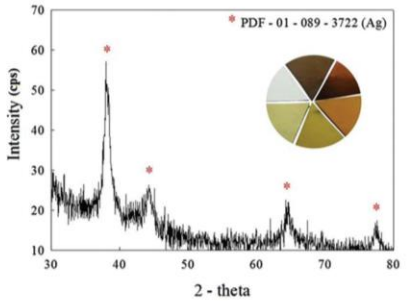

Fig. 2 Typical XRD patterns of porous alumina films formed by anodizing aluminum in 1.2 mol L^{-1} H_2SO_4 at 10 V and coloured *via* electrodeposition (ac treatments) of densely packed silver nanowire arrays. In the inset – the diagram of alumina colours can be obtained by this finishing method.

Quantitative results of silver deposition inside the pores of the alumina film with a thickness of ≤1.0 μm grown under the study conditions are presented in Fig. 3. At a constant j_{ac} within the 0.15 to 0.3 A dm^{-2} range, the deposition of silver inside the alumina pores proceeded at a constant rate strongly dependent on the j_{ac} value, while increasing the j_{ac} resulted in an increased silver deposition rate. It was interesting that at low current densities, the deposition started after some time possible required to re-construct the high-resistant barrier layer of alumina at the film oxide interface.[28] It was also surprising that deposition of silver inside the small, *ca.* 0.8 μm, pores at a constant j_{ac} proceeded at a significantly higher rate (Fig. 3, plot 2) than in the pores of the same diameter in much thicker films (Fig. 3, plot 5).

Variability in the silver content deposited inside the pores of an extremely thin alumina film in constant ac voltage $U_{p\text{-}to\text{-}p}$ mode is shown in a representative plot (4) of Fig. 3. As seen, in this case, the filling of alumina pores proceeded at a decreasing deposition rate which indicated that longer ac treatment times than at a constant current density are required for the deposition of the same amount of silver. These data suggest that the constant voltage ac regime was more suitable for achieving uniform colouring of alumina films in the same tint.

In this study, the optical constants (n, k) and the film thickness were determined by fitting the ellipsometric data (Ψ and Δ) using the specified Cauchy dispersion, comprising of aluminium oxide, empty nanochannels and silver nanowires (Fig. 4). Ten angles of incidence within the 30° to 75° range with 5° step were used to obtain the dependencies of Ψ and Δ on the wavelength length (λ) at each angle (Fig. 5). It was determined that the variations of $\Psi(\lambda)$ and $\Delta(\lambda)$ at each angle calculated using the applied model match well with the experimental both for pure (Fig. 6a and b) and Ag-coloured (Fig. 6c

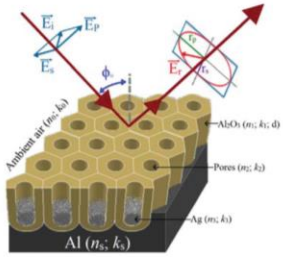

Fig. 4 The scheme corresponding to the model used for the fitting of experimental $\Psi(\lambda)$ and $\Delta(\lambda)$ dependencies.

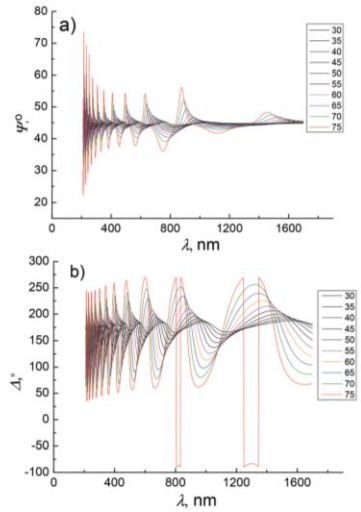

Fig. 5 The typical variations of ellipsometric parameters (a) Ψ and (b) Δ with wavelength λ at indicated angles of incidence for pure alumina films with a thickness of 899.2 nm.

and d) films within the entire spectral interval. In this scenario, the optical constants for alumina samples were further evaluated for each angle of incidence within the tested wavelength range. Fig. 7a shows typical variations of $k(\lambda)$ and $n(\lambda)$ for an alumina film of 900 ± 0.7 nm thickness grown under the conditions of this study before and after the deposition of ~8.0 μg silver, which colors it in gold. Evidently, the variations of the refractive index n and the extinction coefficient k with λ for pure alumina and the same alumina film decorated with a silver nanowire array differ significantly; both $k(\lambda)$ and $n(\lambda)$ for

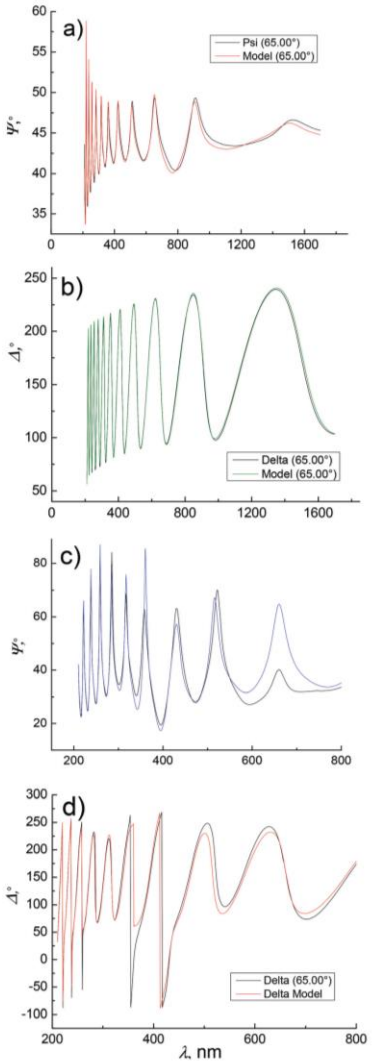

Fig. 6 Spectral ellipsometric data (Ψ, Δ) of the aluminium sample anodized in 1.2 mol L^{-1} H_2SO_4 at 15 °C and 10 V for 12 min (a, b) and then decorated with silver nanospecies by alternating current deposition at $U_{p\text{-}to\text{-}p}$ = 5.0 V for 30 s (c, d). The measurements were realized at an angle of incidence of 65°. The curves in colour were calculated using the model system.

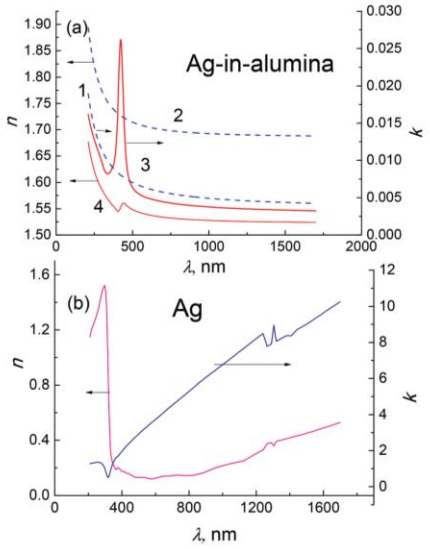

Fig. 7 (a) The spectral dependencies of the extinction coefficient k and the refractive index n of pure alumina film with a thickness of 899.3 nm (1, 2) and the same film decorated with silver nanospecies in the content of 8.3 μg cm^{-2} (3, 4). Film roughness of 5.09 nm. (b) Same dependencies for the bulk silver surface.

the Ag-in-alumina film show a sharp peak in a vicinity of 400–420 nm.

It is worth noting that increase in the content of deposited silver results in the increase of k and n values in this peak region (Fig. 8), whereas a twofold increase in the alumina thickness leads to approximately four times lower k and n values at each angle of incidence for the same content of encased silver.

In order to evaluate the antimicrobial activity of silver nanowires encased inside the extremely thin alumina pores, *in vitro* tests were performed with *S. cerevisiae* colonization in the YEPD medium with and without exposure to Ag-in-alumina pellets. Films sealed in boiling water and unsealed films containing defined amounts of deposited silver were investigated. For comparison, similar tests were performed by incubation of yeast cells (*S. cerevisiae*) in the YEPD medium containing 1.0, 2.5, and 5.0 ppm of Ag^+ ions, pure alumina film, and silver-coated alumina film pellets, respectively. The results obtained from these antimicrobial activity assays against *S. cerevisiae* are shown in Fig. 9.

It is seen that when the silver was fully encapsulated inside the alumina pores, fungicidal activity was insignificant and independent of the content of encased silver (Fig. 9A) which

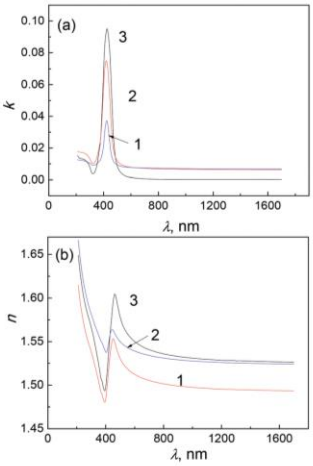

Fig. 8 The spectral dependencies of the extinction coefficient k (a) and the refractive index n (b) of the alumina film decorated with silver nanospecies in contents: (1) 8.0, (2) 13.0 and (3) 15.0 μg cm^{-2}.

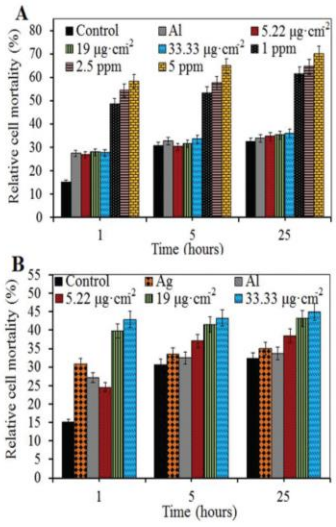

Fig. 9 Percentage of dead *S. cerevisiae* cultured in the YEPD medium in the absence and presence of various as-grown (B) and sealed (A) Ag-in-alumina samples (silver contents indicated) after 1, 5, and 25 h incubation. Error bars represent standard deviation.

Table 1 The results of fungi growth inhibition by as-deposited silver nanowire arrays in alumina pores and Ag^+ ions

Culture	Contacting materials	The content of Ag^0 in μg or $[Ag^+]$	Effect	Zone of inhibition (in mm)
A. fumigatus lawns	Ag-in-alumina film	7.5	—	—
		28.5	Fungistatic	19–24
		50	Fungistatic	21–24
	$AgNO_3$	From 1 to 5 mg L^{-1}	Fungicidic	1.5
G. candidum lawns	Ag-in-alumina film	7.5	—	—
		28.5	Fungistatic	15–36
		50	Fungistatic	21–25
	$AgNO_3$	From 1 to 5 mg L^{-1}	—	—

Table 2 The results of bacteria growth inhibition by various Ag-in alumina nanowire arrays and Ag^+ ions

Culture	Contacting materials	The content of Ag^0 in μg or $[Ag^+]$	Effect	Zone of inhibition (in mm)
E. coli (−)	As-grown Ag-in-alumina film	7.5	—	—
		28.5	Bacteriocidic	3
		50	Bacteriocidic	2–4
	$AgNO_3$	From 1 to 5 mg L^{-1}	—	—
M. luteus (+)	As grown Ag-in-alumina film	7.5	Bacteriocidic	1.7
		28.5	Bacteriocidic	1.1–1.3
		50	Bacteriocidic	1.5–1.7
	$AgNO_3$	From 1 to 5 mg L^{-1}	—	—

could be explained by the slow release and diffusion of Ag^+ ions through the surface layer of the sealed alumina film. For unsealed Ag-in-alumina films (Fig. 9B), the silver content contributed to the fungicidal effect. It is also interesting to note that nanowired Ag^0 species had a higher inhibitory activity towards *S. cerevisiae* than the silver-coated alumina film. These results are corroborated by other studies which indicate that the antimicrobial activity of nanostructured particles, such as Fe_3O_4,[29] ZnO,[30] MgO,[31] and Ag^0,[4,5,23] increased with decreasing particle size.

The antimicrobial activity of Ag-in-alumina samples was also investigated by the zone inhibition method. Following this method, pieces (~1.5 cm^2) of alumina decorated with silver nanowire arrays were pressed gently onto the surface of agar plates, incubated with 10^6 CFU mL^{-1} of uniformly dispersed bacteria, yeast or fungi, and analyzed after 5, 10 and 48 h incubation at 27 °C. We note that all of the tested microorganisms are prevailing in the human's nitty-gritty. Table 1 displays the representative zone inhibition for Ag-in-alumina samples in the *A. fumigatus* plates and $AgNO_3$ (100 μL) solutions. These results suggest that all Ag^+ solutions tested had a fungicidal influence effect at some distances from the drop centre. For the as-deposited Ag-in-alumina samples tested against *A. fumigatus*, a wide zone of inhibition could be seen for films containing ≥19 μg cm^{-2} of silver, suggesting the fungi-static activity for the silver nanowires encased inside the thin alumina pores. A similar effect was seen against *G. candidum* (Table 1) but not against *C. parapsilosis*.

No fungistatic activity was seen for sealed (boiling in water) Ag-in-alumina films against all fungi tested. This effect could be attributed to the lack of direct contact between fungi and silver molecules, as well as the decreased content of the silver ions diffusing through the compact alumina surface layer.

In the next setup, Ag-in-alumina specimens containing various silver contents were tested against Gram negative (*E. coli*) and Gram positive (*M. luteus*) organisms in Mueller-Hinton agar by the standard well diffusion method[32] and the results are presented in Table 2. Data indicate that Ag-in-alumina films containing ≥19 μg cm^{-2} of silver exhibited antimicrobial properties against both bacterial species. However, the zone of inhibition around the as-grown Ag-in-alumina samples was ~90% wider for the Gram-negative *E. coli* than for the Gram-positive *M. luteus*. This behavior is similar to previously reported data where a significantly higher bactericidal activity was seen for silver nanocomposite materials against Gram-negative bacteria,[33] attributed to differing structures of their cell walls.

Discussion

Aluminium foils as nontoxic and quite inexpensive materials have been used for decades for packaging of sweets and chocolates. Chemical stability of aluminium is linked to spontaneous oxidation of this metal at the damaged places even under ambient conditions. To increase chemical stability, the thickness of the naturally formed Al oxide can simply be increased by thermal, chemical or electrochemical oxidation. In fact, the short-time anodizing of Al in aqueous solutions of sulfuric acid at lower bath concentrations and voltages, *ca.*

1.2 M and 10 V, respectively, instead of typical 1.8–2.0 M and 17–18 V, have been chosen in this study in order to form a nanoporous oxide layer with a thickness less than 1.0 μm. We note that such films of approximately (1.5–1.7) × 10^{11} pores cm^{-2} are densely packed and oriented perpendicularly to the substrate, while still retaining elasticity, which is particularly crucial for packaging materials. It is also noteworthy that a decrease in the anodizing voltage down to 10 V resulted in the formation of a thinner barrier layer at the alumina film Al interface. We report that this circumstance allowed us to uniformly deposit silver inside the short (<1.0 μm) and tiny ($Ø_{pore}$ ≤ 10 nm) channels by ac treatment. To the best of our knowledge, this is the first demonstration of uniform coloring of extremely thin alumina films by an electrochemical approach. The first reason for deposition of silver inside the alumina pores was the fact that only nm-scaled Ag species dispersed uniformly in the clear matrices even in the contents of less than 0.1 g m^{-2} color them in esthetic gold tints. Besides, we expected that densely packed silver nanowires, as small as ~10 nm in diameter and 50–200 nm in length, encased in porous alumina films, as thin as ≤1.0 μm, could exhibit antimicrobial activity even after full encapsulation of Ag species. On the other hand, it is also likely that silver will not be able to penetrate through the layer of aluminium oxide formed at the top-side during sealing in boiling water. Therefore, the antibacterial as well as antifungal activities of Ag-in-alumina films, both sealed and unsealed, were studied herein using several wide-spread microorganisms including *S. cerevisiae*, *M. luteus*, *E. coli*, *A. fumigatus*, *G. candidum*, and *C. parapsilosis*. Our results have indicated that in contrast to unsealed alumina, fully encapsulated silver species had significantly weaker or no antimicrobial effects most likely due to the absence of direct contact between microorganisms and Ag species. The results of the present study are in agreement with other reports that indicate a greater activity of silver nanoparticles against Gram-negative microorganisms.[33]

It was also determined that optical parameters of the alumina film changed significantly after deposition of silver at the bottom part of alumina pores. Both $k(\lambda)$ and $n(\lambda)$ for the Ag-in-alumina film show a sharp peak in a vicinity of 400–420 nm. The height of these peaks is related to the content of deposited silver. Increase in the content of deposited silver results in the increase of k and n parameter values in this peak region. Surprisingly a low dispersion extinction coefficient k of Ag-in-alumina films in the wavelength range of 500–1700 nm, *e.g.* 0.004–0.0015 and $dk/d\lambda$ = l–2 × 10^{-6} 1/nm, with respect to those of the bulk silver, where $k \cong$ 2.0–10.0 and $dk/d\lambda = 6 \times 10^{-3}$ 1/nm (see Fig. 7b) implies the prospective applications of alumina films decorated with silver nanospecies in the optoelectronic devices for fabrication of transparent films with a low refractive index.

Conclusions

In this study, conditions were established for finishing aluminium foils in uniform gold-tints *via* formation of a thin (<1 μm) porous anodic film and the subsequent ac deposition of silver nanowire arrays. The antimicrobial properties of as-grown and sealed Ag-in-alumina films were tested *in vitro* against several fungi, bacteria, and yeast. Results indicated that as-deposited Ag-in-alumina films, in contrast to fully encapsulated Ag-in-alumina films, possessed antimicrobial activity against most of the organisms tested in this study, suggesting the potential use in aluminium foil finishing and foodstuff packaging materials.

Variations of the optical parameters, *e.g.* the refractive index n and the extinction coefficient k, with λ of the Ag-in-alumina film demonstrate the sharp peaks in the vicinity of 400–420 nm contrary to the pure film. The height of these peaks is related to the content of deposited silver and increases with loading. Extremely low k values of nano-Ag-in-alumina films in the visible and near IR regions within the λ range from 500 to 1700 nm suggest the possible application of these films in fabrication of transparent films with a low refractive index.

Notes and references

1 A. Huczko, *Appl. Phys.*, 2000, **70**, 365–376.
2 X. Battle and A. J. Labarta, *Appl. Phys.*, 2002, **35**, 15–42.
3 I. Sondi and B. Salopek-Sondi, *J. Colloid Interface Sci.*, 2004, **275**, 177–182.
4 J. R. Morones, J. L. Elechiguerra, A. Camacho, K. Holt, J. B. Kouri, J. T. Ramirez and M. J. Yacaman, *Nanotechnology*, 2005, **16**, 2346–2353.
5 C. Baker, A. Pradhan, L. Pakstis, D. J. Pochan and S. I. Shah, *J. Nanosci. Nanotechnol.*, 2005, **5**, 244–249.
6 L. Z. Zhang, J. C. Yu, H. Y. Yip, Q. Li, K. W. Kwong, A. W. Xu and P. K. Wong, *Langmuir*, 2003, **19**, 10372–10380.
7 Z. Zheng, W. Yin, J. N. Zara, W. Ji, J. Kwak, R. Mamidi, *et al.*, *Biomaterials*, 2010, **31**, 9293–9300.
8 D. Lee, R. E. Cohen and M. F. Rubner, *Langmuir*, 2005, **21**, 9651–9659.
9 P. L. Taylor, A. L. Ussher and R. E. Burrell, *Biomaterials*, 2005, **26**, 7221–7229.
10 S. P. Chen, G. Z. Wu and H. Y. Zeng, *Carbohydr. Polym.*, 2005, **60**, 33–38.
11 S. Shanmugam, B. Viswanathan and T. K. Varadarajan, *Mater. Chem. Phys.*, 2006, **95**, 51–55.
12 E. Ulkur, O. Oncul, H. Karagoz, E. Yeniz and B. Celikoz, *Burns*, 2005, **31**, 874–877.
13 D. V. Parikh, T. Fink, K. Rajasekharan, N. D. Sachinvala, A. P. S. Sawhney, T. A. Calamari and A. D. Parikh, *J. Text. Res.*, 2005, **75**, 134–138.
14 S. Ohashi, S. Saku and K. Yamamoto, *J. Oral Rehabil.*, 2004, **31**, 364–367.
15 M. E. Rupp, T. Fitzgerald, N. Marion, V. Helget, S. Puumala, J. R. Anderson and P. D. Fey, *Am. J. Infect. Contr.*, 2004, **32**, 445–450.
16 U. Samuel and J. P. Guggenbichler, *Intern. J. Antimicrob. Agents*, 2004, **23**, 75–78.

17 M. Bosetti, A. Masse, E. Tobin and M. Cannas, *Biomaterials*, 2002, **23**, 887–892.
18 T. Yuranova, A. G. Rincon, A. Bozzi, S. Parra, C. Pulgarin, P. Albers and J. Kiwi, *J. Photochem. Photobiol.*, 2003, **161**, 27–34.
19 S. H. Jeong, S. Y. Yeo and S. C. Yi, *J. Mater. Sci.*, 2005, **40**, 5407–5411.
20 A. Gauger, M. Mempel, A. Schekatz, T. Schafer, J. Ring and D. Abeck, *Dermatology*, 2003, **207**, 15–21.
21 H. J. Lee and S. H. Jeong, *Text. Res. J.*, 2005, **75**, 551–556.
22 D. Wei, W. Sun, W. Qian, Y. Ye and X. Ma, *Carbohydr. Res.*, 2009, **344**, 2378–2382.
23 A. Panaček, L. Kvitek, R. Prucek, M. Kolar, R. Večerova, N. Pizurova, *et al.*, *J. Phys. Chem.*, 2006, **110**, 16248–16253.
24 R. Kumar and A. Münstedt, *Polym. Int.*, 2005, **54**, 1180–1186.
25 J. S. Kim, E. Kuk, K. N. Yu, J.-H. Kim, S. J. Park, H. J. Lee, *et al.*, *Nanomed. Nanotechnol. Biol. Med.*, 2007, **3**, 95–101.
26 I. Papageorgiou, C. Brown, R. Schins, *et al.*, *Biomaterials*, 2007, **28**, 2946–2958.
27 E. Herrmann, *Galvanotechnik*, 1971, **62**, 867–901.
28 A. Jagminienė, G. Valinčius, A. Riaukaitė and A. Jagminas, *J. Cryst. Growth*, 2005, **247**, 622–631.
29 N. Tran, A. Mir, D. Mallik, A. Sinha, S. Nayar and T. Webster, *Int. J. Nanomed.*, 2010, **5**, 277–283.
30 O. Yamamoto, *et al.*, *Carbon*, 2001, **39**, 1643–1651.
31 S. Makhluf, R. Dror, Y. Nitzan, Y. Abramovich, R. Jelinek and A. Gedanken, *Adv. Funct. Mater.*, 2005, **15**, 1708–1715.
32 R. Thomas, A. Viswan, J. Mathew and R. Ek, *Nano Biomed. Eng.*, 2012, **4**, 139–143.
33 S. Egger, R. P. Lehmann, M. J. Height, M. J. Loessner and M. Schuppler, *Appl. Environ. Microbiol.*, 2009, **75**, 2973–2976.

3rd publication / 3 publikacija

Size-dependent antimicrobial properties of the cobalt ferrite nanoparticles

Žalnėravičius R., Paškevičius A., Kurtinaitienė M., Jagminas A.
Journal of Nanoparticle Research, 18 (2016)
DOI: 10.1007/s11051-016-3612-x

The article could be find online at https://10.1007/s11051-016-3612-x

J Nanopart Res (2016)18:300
DOI 10.1007/s11051-016-3612-x

RESEARCH PAPER

Size-dependent antimicrobial properties of the cobalt ferrite nanoparticles

Rokas Žalnėravičius · Algimantas Paškevičius · Marija Kurtinaitiene · Arūnas Jagminas

Received: 16 June 2016 / Accepted: 28 September 2016

Abstract The growing resistance of bacteria to conventional antibiotics elicited considerable interest to non-typical drugs. In this study, antimicrobial investigations were performed on low-size dispersion cobalt ferrite nanoparticles (Nps) fabricated by co-precipitation approach in several average sizes, in particular, 15.0, 5.0, and 1.65 nm. A variety of experimental tests demonstrated that the size of these Nps is determinant for antimicrobial efficiency against *S. cerevisiae* and several *Candida* species, in particular, *C. parapsilosis, C. krusei*, and *C. albicans*. The small and ultra-small fractions of $CoFe_2O_4$ Nps possess especially strong antimicrobial activity against all tested microorganisms. The possible reasons are discussed. Nps were characterized by means of transmission and high-resolution transmission electron microscopy, *X*-ray diffraction, energy dispersive *X*-ray spectroscopy and atomic force microscopy, chemical analysis and magnetic measurements.

Keywords Antimicrobial · Ferrites · Nanoparticles · Characterization · Microbiology

R. Žalnėravičius · M. Kurtinaitiene · A. Jagminas (✉)
State Research Institute Center for Physical Sciences and Technology, Sauletekio av. 3, LT-10257 Vilnius, Lithuania
e-mail: arunas.jagminas@ftmc.lt

A. Paškevičius
Laboratory of Biodeterioration Research, Nature Research Centre, Akademijos 2, LT-08412 Vilnius, Lithuania

Published online: 10 October 2016

Introduction

The use of metals and their oxide-based nanoparticles (Nps) as antimicrobial units is attractive, as some of them offer high efficacy against resistant microorganisms. Silver is probably the only chemical element that literally every adult has heard about its antimicrobial properties. During past two decades, hundreds of papers have been also reported on the bactericidal efficacy of Ag^0 and Ag-containing species, films, and coatings (Campoccia et al. 2013). It has been reported that silver-based Nps also exhibit strong antimicrobial activity against human pathogens (Rai et al. 2009; Baker et al. 2005) by disturbing the cell membrane (Jena et al. 2012; Butkus et al. 2003) without harming the host cells. This effect was also linked with interaction of silver ions, released from nanoparticle (Np), with disulphide or sulfhydryl enzyme groups (Lok et al. 2007), as well as with membrane damage by free radicals derived from the surface of Ag Nps (Kim et al. 2007). Note that small-sized Nps of other zero-valent metals, such as Zn and Fe, can also exhibit bactericidal effect, being non-active in the bulk size (Lee et al. 2008), whereas Cu^0 Nps demonstrate antimicrobial properties even after covering with polymeric shells (Cioffi et al. 2005). From the previous reports, ZnO (Yamamoto 2001), MgO (Makhluf et al. 2005), Cu_2O (Li et al. 2013), CuO (Ren et al. 2009; Azam et al. 2012), and Co_3O_4 (Pandey et al. 2015) Nps also demonstrate selective

and size-dependent antibacterial activity (Li et al. 2013).

Antimicrobial activity of iron oxide Nps against *S. aureus* bacteria has been reported by Tran et al. (2010), suggesting that 9 nm-sized Fe_2O_3 Nps can penetrate in the cell and generate reactive oxygen species. However, this effect was observed only at relatively high Np concentrations presumably due to the negative zeta potentials of Fe_2O_3 Np ($\xi = -19.09$ mV). Quite similar result has been obtained for *S. epidermidis* and 8 nm-sized iron (III) oxide Nps inoculated in the suspension comprised of 2 mg mL^{-1} bacteria and from 0.1 to 2.0 mg mL^{-1} of Nps (Taylor and Webster 2009). However, in these cases after 48-h treatment the cell population was reduced only to 65 % of controls. From the previous report, iron oxide (Fe_2O_3) Nps could have a dual therapeutic function, particularly, enhance bone growth and inhibit bacterium infection (Pareta et al. 2008). Cobalt ferrite ($CoFe_2O_4$) Nps, exhibiting a high coercivity of more than 5 kOe, a moderate saturation magnetization (~ 80 emu g^{-1}) and excellent chemical stability have been reported as a promising material for magnetic resonance imaging (Zheng et al. 2008), biomedical drug delivery and hyperthermia of cancer (Kim et al. 2008). From the recent report (Sanpo et al. 2013), $CoFe_2O_4$ Nps, 40–50 nm-sized, exhibit antimicrobial activity against *E. coli* and *Staphylococcus aureus*. This property can be strongly enhanced by the partial substitution of Co^{2+} ions with Cu^{2+} and Zn^{2+}. However, the bactericidal behaviour of $CoFe_2O_4$ Nps against other targets, such as *Candida* strain microorganisms, has not been studied yet.

More than 200 different *Candida* species are known in the world, but only 17 are recognized as etiological agents of human infection. However, most of the invasive infections are caused by *Candida albicans, Candida glabrata, Candida lusitaniae, Candida tropicalis, Candida parapsilosis, and Candida krusei* (Pfaller 2012). *Candida* species affect nail, skin, and mucosal surfaces and cause the opportunistic yeast infection widely known as candidiasis. The growing population of immunocompromised patients that use intravenous catheters, total parenteral nutrition, invasive procedures and the increasing use of broad-spectrum antibiotics, cytotoxic chemotherapies, and transplantation are factors that contribute to the increase in these infections (Ortega et al. 2011). Besides, in recent years, the cases of onychomycosis, especially of those caused by *Candida*, greatly increased. Onychomycosis due to *Candida* species accounted for 44.9 % of culture-positive cases. Among *Candida* species, *C. krusei* was isolated most often and made up 38.0 %. *C. albicans* made up 29.0 %, *C. tropicalis*—17.0 %, and *C. parapsilosis*—14.0 % (Paškevicius and Švediene 2013). This is the principal reason for investigations performed for creation of new effective antimicrobial surfaces, particles, or liquids which could help to decrease the count of these pathogenic microorganisms.

In this study, we designed experiments to synthesize Co ferrite Nps in average size of 15.0, 5.0, and 1.65 nm using co-precipitation synthesis and subsequently tested their antimicrobial activities against *S. Cerevisiae* and several *Candida* species, in particular, *C. parapsilosis, C. krusei*, and *C. albicans* strains.

Materials and methods

All the reagents in this study were at least analytical grade and, except NaOH, were used without further purification. $CoCl_2$, $Fe_2(SO_4)_3$, and citric acid were purchased from Aldrich Chemicals Inc. NaOH was purified by preparation of a saturate solution resulting in the crystallization of others sodium salts. Deionized distilled water was used throughout all experiments.

Small (mean size, $Ø_{mean} = 5.0$ nm) and ultra-small (mean size, $Ø_{mean} = 1.65$ nm) Co ferrite particles were synthesized in the thermostated glass reactor from the complex-assisted alkaline solutions containing 45 mmol L^{-1} of $CoCl_2$ and $Fe_2(SO_4)_3$ salts and 75 mmol L^{-1} citric acid, as chelating agent, and NaOH up to pH $\cong$ (12.5 $\pm$ 0.1) at 80 °C for 3 h by co-precipitation way (Massart 1981). Larger cobalt ferrite Nps in average size of $\cong$ 15 nm were synthesized by hydrothermal treatment in the same solution by autoclaving at 130 °C for 10 h with 10 °C min^{-1} ramp. All solutions were deoxygenated with argon before mixing. The synthesis in the thermostated reactor was conducted under a continuous argon gas bubbling. For 5 nm-sized Nps, the crude products were centrifuged at 7500 rpm for 5 min and carefully rinsed/centrifuged five times with pure 12 mL H_2O probes, then isopropyl alcohol and water. For collection of ultra-small Nps, the supernatants of last three centrifugations were connected and rinsed further twice with isopropyl alcohol and finally again with water obtaining Np suspension pH $\cong$ 7.4.

The composition of synthesized products was investigated by energy dispersive *X*-ray spectroscopy (EDX). Besides it, nanoparticles were dissolved in HCl (1:1) solution and analysed by inductively coupled plasma optical emission (ICP-OE) spectrometry using OPTIMA 7000DV (Perkin Elmer). Measurements were performed on emission peaks at $\lambda_{Co} = 238.89$ nm and $\lambda_{Fe} = 259.94$ nm. A calibration graph was plotted using a series of calibration standard solutions within 1–50 ppm concentrations in the same acid matrix as the unknown solutions. The calibration standard solutions and unknown solutions were analysed at least four times. The detection limits based on three standard deviations result in ±3.5 % error.

X-ray powder diffraction experiments were performed on a D8 diffractometer (Bruker AXS, Germany), equipped with a Göbel mirror as a primary beam monochromator for CuK_α radiation ($\lambda = 1.5418$ Å).

The morphology of as-grown products was investigated using a transmission electron microscope (TEM, model MORGAGNI 268) operated at an accelerating voltage of 72 keV. The nanoparticles subjected to TEM observations were dispersed in ethanol and drop-cast onto carbon-coated copper grid. The average size of nanoparticles was estimated from at least 100 species observed in their TEM images. High-resolution transmission electron microscopy (HRTEM) studies of as-synthesized products were performed using a LIBRA 200 FE at an accelerating voltage of 200 keV. The morphology of Co ferrite nanoparticles, spin coated onto the mica surface, was also investigated with the atomic force microscope Veeco AFM diInnova under a tapping mode. Hydrodynamic size of nanoparticles in water was determined by dynamic light scattering (DLS) tests at 25 °C under ambient conditions using Zetasizer Nano S (Malvern Instruments, UK) equipment.

Magnetization measurements were accomplished using the vibrating sample magnetometer calibrated by Ni sample of similar dimensions as the studied sample. The magnetometer was composed of the vibrator, the lock-in-amplifier, and the electromagnet. The magnetic field was measured by the teslameter FH 54 (Magnet-Physics Dr. Steingroever GmbH).

Antimicrobial activities of the synthesized cobalt ferrite nanoparticles were tested against *S. cerevisiae* M-99 and several *Candida* species, particularly *C. parapsilosis* 0561, *C. krusei* 0145, and *C. albicans* M-7. The microorganisms of *Candida* species were isolated from nail specimens in the Laboratory of Microbiology of the Centre of Laboratory Medicine, Vilnius University Hospital, Santariškių Clinics (VUH SC) and identified by use of Vitek 2 systems (bioMérieux, France). All microorganisms were propagated in Sabouraud CAF (Liofilchem, Italy) agar medium (10 g L^{-1} peptomycol, 40 g L^{-1} glucose, 0.5 g L^{-1} chloramphenicol and 15 g L^{-1} agar) at 27 ± 1 °C for 48 h. The fresh cultures were harvested and diluted in sterile distilled water to yield 1–5 × 10^6 colony-forming units CFU mL^{-1} inoculum, based on optical density at 530 nm (OD_{530}). The range of OD_{530} was obtained between 0.12 and 0.15 using a UV–VIS spectrophotometer (Thermo Scientific, USA). Then, 1 mL of the indicator strain suspension was poured into Petri dishes and overlaid with a soft Sabouraud CAF agar medium cooled to 45 °C and mixed. Following a modified Kirby Bauer method (Wikins et al. 1972), an equal amount of cobalt ferrite was coated on filter paper disc (∅ = 14 mm) and placed on the agar plate inoculated with ~10^6 CFU mL^{-1} microorganisms. The pure filter paper was used as a negative control, whereas the antifungal agent (fluconazole) was run as a positive control. Growth inhibition zones were analysed after 48 h incubation at 27 ± 1 °C. All tests were triplicated.

Quantitative analyses were performed to inspect *S. cerevisiae* and *C. parapsilosis* microorganism colonies growth. The diluted overnight culture was seeded into 19 mL of liquid medium (in a 50-mL glass flask) and incubated at 27 ± 1 °C with shaking (200 rpm) until OD_{530} achieved 0.14. For quantitative estimation of the number of viable microorganisms assay, 1 mL of $CoFe_2O_4$ suspension, containing 20 mg Nps was added to the medium of microorganisms and further incubated for 25 h. Isolation of the pure yeast strain from the growing culture was done via the serial dilution technique. Finally, 100 µL of this mixture was spread on Sabouraud agar medium plates using stainless steel spreader and the growth of yeast was tested after incubation at 27 ± 1 °C for 2–3 days.

The minimum inhibitory concentrations (MICs) were determined by a microdilution method of the antimicrobial agent in standardized RPMI-1640 medium with L-glutamine. The *S. cerevisiae* and *C. parapsilosis* inocula were prepared by suspension of cells in Sabouraud liquid medium to a final concentration of 10^4 CFU mL^{-1}. The MIC was defined as the

lowest Co^{2+} ions concentration at which there was no visible fungal growth. MICs were determined after incubation for 25 h at 27 ± 1 °C. All tests were performed in duplicate.

Results

Characterization of tested Co ferrite Nps

Figure 1 depicts AFM and TEM images of all cobalt ferrite Nps designed in this study by co-precipitation ways for subsequent antimicrobial tests. The size distribution histograms calculated from these images revealed their average size equalled to 1.65 (a), 5.0 (b) and 15.0 nm (c). Note that for all samples, both EDX and ICP-OE spectrometry analyses indicated that the $CoFe_2O_4$ composition was close to stoichiometric (Table 1). The crystalline nature of cobalt ferrite Nps was verified further by *X*-ray diffraction tests. The representative XRD patterns of ultra-small and small Nps are shown in Fig. 2a, b, respectively. It should be emphasized that the position and relative intensity of all diffraction peaks match well with standard $CoFe_2O_4$ diffraction data, implying the polycrystalline inverse spinel structure of these Nps. The XRD pattern (Fig. 2c) and HRTEM image of Nps synthesized by hydrothermal way at 130 °C for 10 h also implayed on the formation of polycrystalline 15 nm-sized Nps with Co:Fe atomic ratio close to 1:2 (Fig. 3c). The zeta potential measurements performed by phase analysis light scattering method, for the synthesized cobalt ferrite Nps in stainless steel Teflon line autoclave in an average size of 15 nm, indicated −43.78 mV value, allowing for making a conclusion on their partial stability without aggregation.

Antimicrobial tests

In the first set-up, the antimicrobial activity of cobalt ferrite Nps was investigated against *S. cerevisiae*, *C. parapsilosis*, *C. krusei*, and *C. albicans* yeasts using lysis zone method. For these tests, the discs made from filter papers in size of 1.5 cm^2 were covered with 1.0 mg of 15 nm-sized or 0.5 mg of smaller ferrite Nps and placed gently on a lawn of microorganisms in an agar plate. The antimicrobial property was ascertained by determination of the clear zone of inhibition around the disc after 48-h incubation. The obtained results are presented in Table 2, demonstrating the highest antimicrobial activity of all tested cobalt ferrite Nps against *S. cerevisiae*. For this yeast, the largest lysis zones approximated to 11–13 mm in diameter were created. For comparison, the inhibition zone around the discs impregnated with the commercial antimicrobial agent—fluconazole, used in this study as a positive control on *S. cerevisiae* lawn, was almost 30 % less than that around our samples impregnated with 1.65 and 5.0 nm-sized $CoFe_2O_4$ NPs. Moreover, antimicrobial effects against three other *Candida* species were approximately fourfold weaker (Figs. 4, 5, 6c) than *S. cerevisiae*, reaching only 2–5 mm the size of their lysis zones in agar-diffusion assay. Besides, for *C. parapsilosis*, the fungistatic effect was observed around the filter papers only partially covered with 5 nm-sized $CoFe_2O_4$ Nps (Fig. 5c).

It is worth noticing that for 1.65 and 5.0 nm-sized $CoFe_2O_4$ Nps, a fungicidal effect was greater than that for 15 nm-sized cobalt ferrite Nps creating a narrower zone of inhibition (Figs. 4, 5, 6). These results agree with reported ones on the size-dependent antimicrobial activity of other metal oxide nanoparticles, such as ZnO (Yamamoto et al. 2001), MgO (Makhluf et al. 2005), and CuO (Azam et al. 2012). However, obvious significant differences in the width of inhibition zones were established between the samples encased with the same content of 5.0 and 1.65 nm-sized $CoFe_2O_4$ Nps. On the lawns of *C. parapsilosis*, *C. krusei*, and *C albicans*, the fungicidal zone caused by 1.65 nm Nps was by 20, 20 and 40 %, respectively, higher than that caused by 5.0 nm Nps.

In order to evaluate the size-dependent antimicrobial activity of cobalt ferrite Nps, in vitro tests were performed further with two different yeast cells' colonization in the Sabouraud CAF medium. The results obtained from these investigations against *S. cerevisiae* and *C. parapsilosis* are shown in Fig. 7. In this way, it was found that results obtained using modified Kirby Bauer technique agree with the ones obtained via quantitative analysis of microorganisms inactivation, implying also on the more effective antimicrobial action of 1.65 and 5.0 nm-sized cobalt ferrite Nps against yeast cells than that on 15 nm-sized Nps. However,

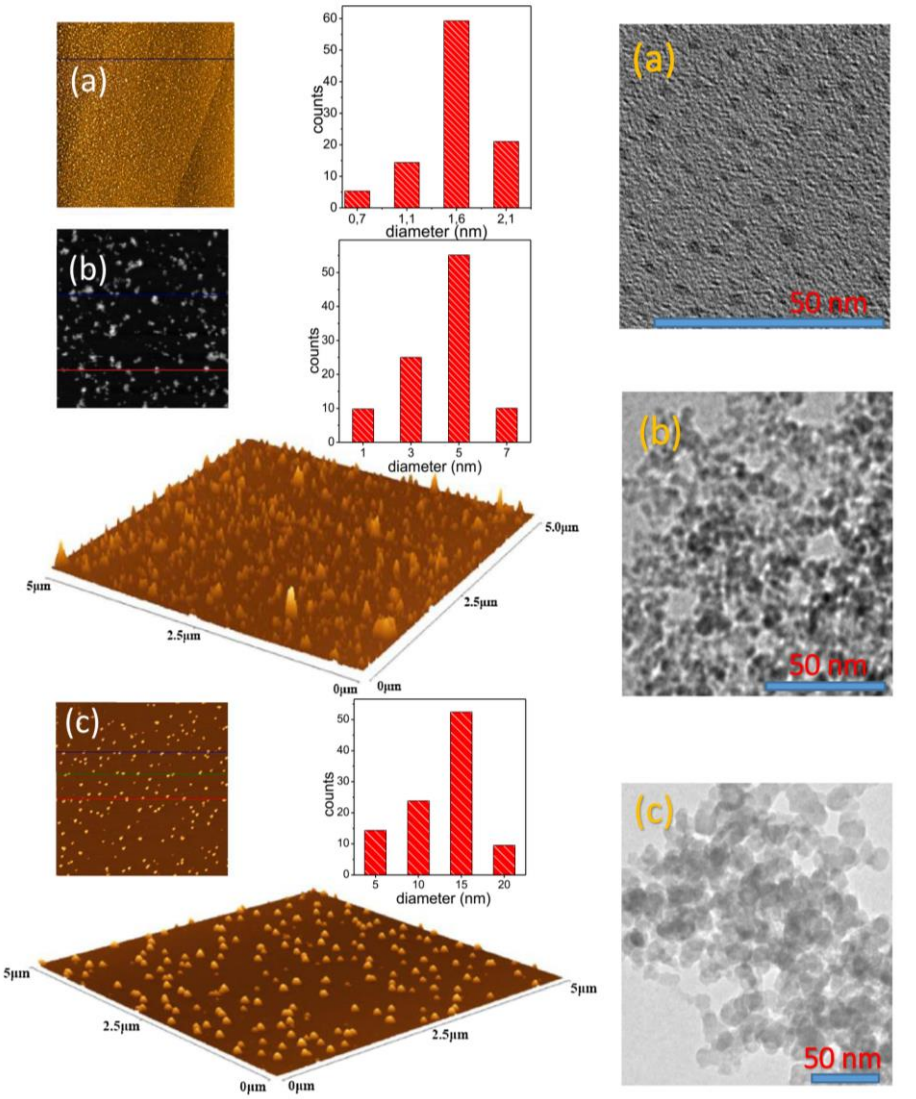

Fig. 1 Size distribution profiles calculated from the presented AFM and SEM images of the tested $CoFe_2O_4$ nanoparticles in average size of 1.65 (**a**), 5.0 (**b**), and 15.0 nm (**c**)

Table 1 Average ratio of iron and cobalt in the synthesized cobalt ferrite nanoparticles determined by EDX and inductively coupled plasma optical emission (ICP-OE) spectrometry analysis

Np size, $\varnothing_{mean}$ (nm)	Fe:Co at% ratio	
	By EDX	By ICP-OE
1.65	1.99	1.97
5.0	2.01	2.05
15.0	1.97	1.96

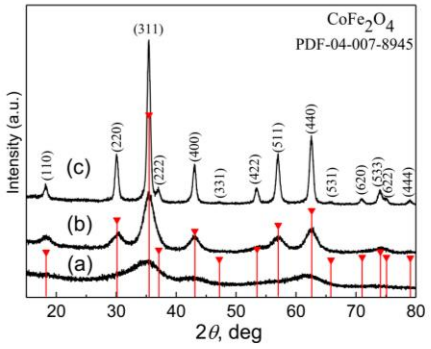

Fig. 2 Typical XRD patterns of cobalt ferrite Nps synthesized under conditions of this study

it should be noted that colonization of *S. cerevisiae* and *C. parapsilosis* colonies with 15 nm-sized $CoFe_2O_4$ Nps decreased their count (Fig. 8).

Comparing the control sample of pure *S. cerevisiae* yeast solution with the one containing 1.65 nm-sized Nps, one can see that killing efficiency of 1.65 nm-sized Nps is by 12 % higher than that of 5.0 nm-sized Nps and their killing rate is improved by 25 % than that of 15 nm-sized Nps. Similar results were obtained for the *C. parapsilosis*. For this yeast, 1.65 nm-sized $CoFe_2O_4$ Nps demonstrated 15 % higher killing efficiency than 5.0 nm-sized Nps did and 44 % higher killing rate than 15 nm-sized Nps did. Moreover, half volume of the smallest Nps ($\varnothing_{mean}$ = 1.65 nm) provided the same effective killing rate against *S. cerevisiae* as 5.0 nm-sized Nps did; and 10 % higher killing efficiency than 5.0 nm-sized Nps against *C. parapsilosis*.

Discussion

As reported above, the fabricated cobalt ferrite nanoparticles with average size ranging between 1.65 and 15 nm have size-dependent antimicrobial activity against several kinds of yeasts. Significantly, higher aggression of small and ultra-small-sized $CoFe_2O_4$ Nps was observed. It is not possible to discuss the

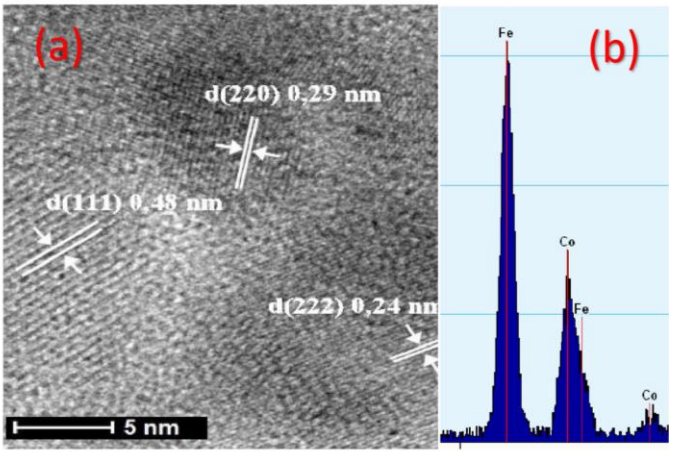

Fig. 3 HRTEM image (**a**) and EDX spectrum (**b**) of Nps formed by hydrothermal treatment at 130 °C for 10 h

Table 2 Antimicrobial activity of cobalt ferrite ($CoFe_2O_4$) nanoparticles against *S. cerevisiae* and three different *Candida* species

Microorganism	Size of $CoFe_2O_4$ Nps (nm)	Diameter of disc (d) (mm)	Diameter of zone (z) (mm)	z/d
Saccharomyces cerevisiae[a]	15	11	22	2.0 ± 0.2
	5	11	24	2.4 ± 0.1
	<2	11	24	2.4 ± 0.1
Candida parapsilosis[b]	15	11	13	1.2 ± 0.05
	5	11	15	1.4 ± 0.1
	<2	11	16	1.4 ± 0.1
Candida krusei[c]	15	11	13	1.3 ± 0.05
	5	11	15	1.4 ± 0.1
	<2	11	16	1.4 ± 0.1
Candida albicans[d]	15	11	13	1.2 ± 0.05
	5	11	14	1.3 ± 0.1
	<2	11	16	1.4 ± 0.1

[a,b,c,d] Cultured in Sabouraud CAF agar (Liofilchem, Italy) at 27 °C

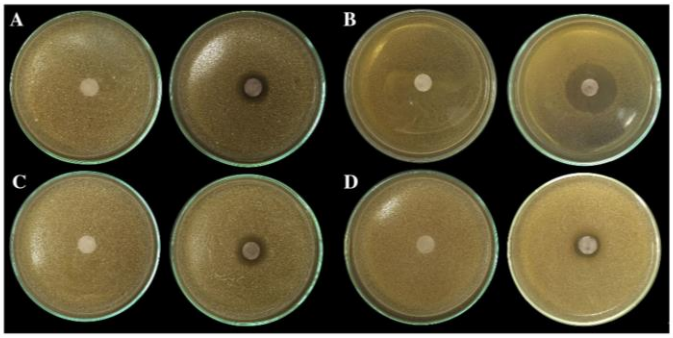

Fig. 4 Inhibitory activity of cobalt ferrite nanoparticles ($Ø_{mean}$ = 1.65 nm) loaded filter paper specimens against the lawns of microorganisms: **a** *C. krusei*, **b** *S. cerevisiae*, **c** *C. parapsilosis*, **d** *C. albicans*. In the *left side*—control specimen

origin of this effect. However, some suggestions can be outlined. Regarding the bactericidal activity of magnetic Co Nps, there is suggestion that 7–8 nm-sized Co_2O_3 Nps can diffuse inside the cell interacting with cell membrane, producing oxidative stress and finally—DNA damage (Pandey et al. 2015). As for crystalline cobalt ferrite Nps, it is commonly accepted that their surface, similar to other iron oxide Nps, is covered with a thin magnetically disordered shell of about 1 nm thickness (Millan et al. 2007). Therefore, the saturation magnetization of small Nps decreases with the decrease in their size approaching zero for 3 nm-sized and smaller Nps (Millan et al. 2007), as one can also see from the results presented in Fig. 9 and for our ultra-small Nps. In fact, the surface spins have some saturation arising from the clustering of surface ions (Silva et al. 2005). For ultra-small Nps, the core disappears and disordered part becomes prevalent, what changes the chemical and binding properties of such Nps. It is also worth noticing that the cationic distribution in the shell region depends significantly on the size of Nps. According to the report (Peddis et al. 2008), $(Co_{0.8}Fe_{0.2})[Co_{0.2}Fe_{1.8}]O_4$ distribution is characteristic to $Ø_{mean}$ = 2.8 nm $CoFe_2O_4$ Nps, whereas $(Co_{0.48}Fe_{0.52})[Co_{0.52}Fe_{1.48}]O_4$ cationic distribution prevails in 6.7 nm-sized Nps. Therefore, it can be

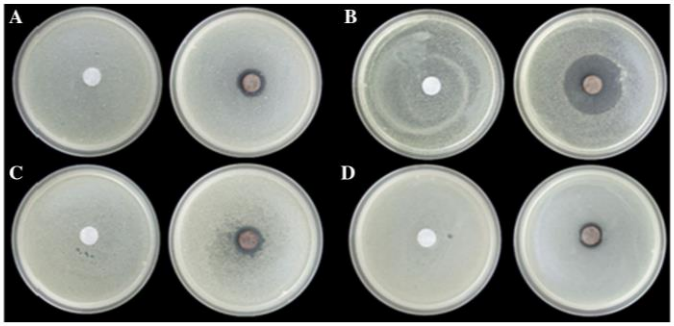

Fig. 5 Inhibitory activity of cobalt ferrite nanoparticles ($Ø_{mean}$ = 5.0 nm) loaded filter paper specimens against the lawns of microorganisms: **a** *C. krusei*, **b** *S. cerevisiae*, **c** *C. parapsilosis*, **d** *C. C albicans*. In the *left side*—control specimen

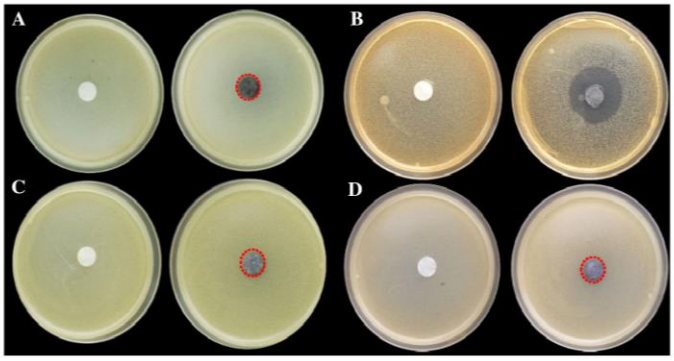

Fig. 6 Inhibitory activity of cobalt ferrite ($Ø_{mean}$ = 15 nm) loaded filter paper specimens against the lawns of microorganisms: **a** *C. krusei*, **b** *S. cerevisiae*, **c** *C. parapsilosis*, **d** *C. albicans*. In the *left side*—control specimen

expected that in the Nps size window tested herein continuous increase in the content of cobalt ions in the outer part of cobalt ferrite Np shell with size decrease could be the main reason of higher antimicrobial activity of small and ultra-small Nps. To verify this assumption, we have performed the experiments seeking to determine the bactericidal behaviour as well as minimum inhibitory concentrations (MICs) of cobalt ions sufficient to prevent the visible *S. cerevisiae* and *C. parapsilosis* yeasts growth after 10^4 CFU mL^{-1} their amount incubation for 25 h at 27 ± 1 °C. Thus, it was found that the killing rate of cobalt ions for *S. cerevisiae* is higher than for *C. parapsilosis* and this effect is attributed to concentration of Co^{2+}, as shown in Fig. 8. The MIC of Co^{2+} ions for *S. cerevisiae* and *C. parapsilosis* was 21 and 25 mmol L^{-1}, respectively. These results are in accordance with the report by Wan et al. (2012) that Co^{2+} ions released from Nps induce oxidative stress in cells eventually causing DNA damage. This may also be happening in the case of the tested yeasts in our experiments. In addition, it should be noticed that the surface to volume ratio of Nps, $S_{\varnothing}/V_{Np}$, increases significantly with their size decrease. For 15, 5.0, and 1.65 nm-sized spherical Nps, $S_{\varnothing}/V_{Np}$ is approximated to 4.8, 10.8, and 33.4, respectively, allowing to predict the possible toxicity increase with Np size decrease due to an increase in area contacting with microorganisms.

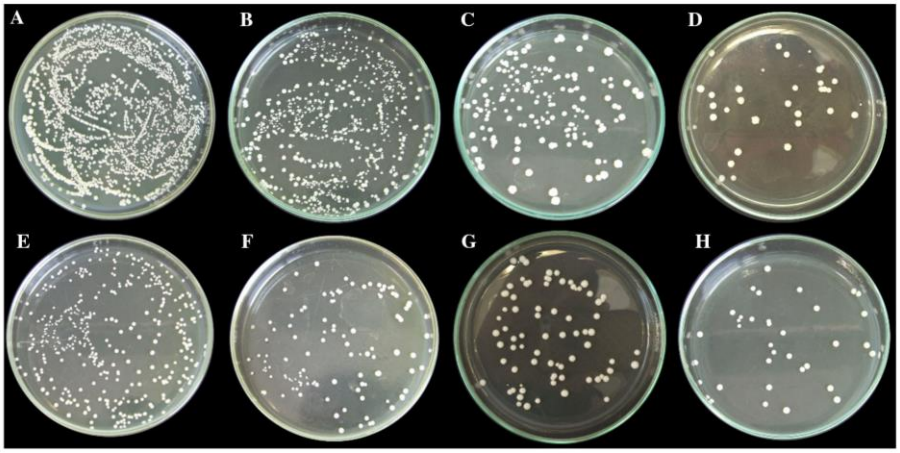

Fig. 7 Photographs showing the size-dependent antimicrobial activity of $CoFe_2O_4$ Nps for growth inhibition of *C. parapsilosis* (*top row*) and *S. cerevisiae* (*bottom row*) microorganism probes incubated in the Sabouraud agar plates. All microorganisms were cultivated in liquid medium without (**a**, **e**) and with 15 nm-sized (**b**, **f**); with 5.0 nm-sized (**c**, **g**) or with 1.65 nm-sized (**d**, **h**) Nps for 48 h

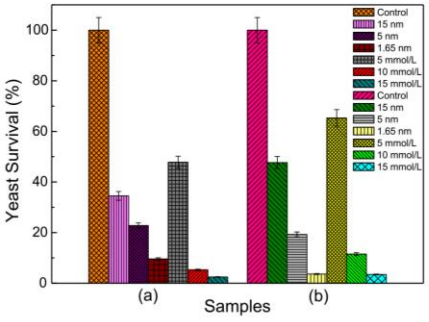

Fig. 8 Comparative antimicrobial activities of 1.65 nm-, 5.0 nm-, and 15 nm-sized cobalt ferrite nanoparticles and Co^{2+} ions at indicated concentrations against *S. cerevisiae* (**a**) and *C. parapsilosis* (**b**)

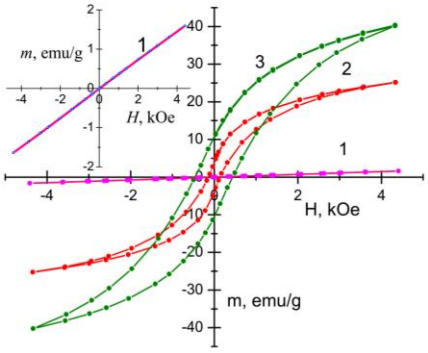

Fig. 9 Magnetization curves of $CoFe_2O_4$ *Nps* in average size of 1.65 (1), 5.0 (2) and 15.0 nm (3)

Conclusion

In summary, we have fabricated stoichiometric, crystalline cobalt ferrite Nps in average size of 1.65, 5.0, and 15 nm from the same solution via co-precipitation synthesis and post-fractionation way. Antimicrobial activity of as-synthesized Nps was studied against *C. krusei*, *S. cerevisiae*, *C. parapsilosis*, and *C. albicans* yeasts by quantitative analysis and modified Kirby Bauer methods, both indicating on the significant higher antimicrobial activity of small and ultra-small $CoFe_2O_4$ Nps in comparison with 15 nm-sized ones. This effect we linked herein with variation in the composition of magnetically disordered shell around Np core, ~1 nm thick, expecting that increase in the content of cobalt ions in the shell side with Np size

decrease should change the binding capability of small Nps to yeast membrane, destroying it.

Acknowledgments We appreciate Drs. V. Pakštas for powder XRD collection, J. Vaičiūniene for chemical analysis, K. Mažeika for magnetic measurements, and V. Karabanovas for AFM observations.

References

Azam A, Ahmed AS, Oves M, Khan MS, Memic A (2012) Size-dependent antimicrobial properties of CuO nanoparticles against Gram-positive and -negative bacterial strains. Int J Nanomed 7:3527–3535

Baker C, Pradhan A, Pakstis L, Pochan DJ, Ism at Shah S (2005) Synthesis and antimicrobial properties of silver nanoparticles. J Nanosci Nanotechnol 5:244–249

Butkus MA, Edling L, Labare MP (2003) The efficacy of silver as a bactericidal agent: advantages, limitations and considerations for future use. J Water Supply Res Technol-Aqua 52:407–416

Campoccia D, Montanaro L, Arciola CR (2013) A review of the biomaterials technologies for infection-resistant surfaces. Biomaterials 34:8533–8554

Cioffi N, Torsi L, Ditaranto N, Ghibelli G, Sabbatini L et al (2005) Copper nanoparticle/polymer composites with antifungal and bacteriostatic properties. Chem Mater 17:5255–5262

Jena P, Mohanty S, Mallick R, Jacob B, Sonawane A (2012) Toxicity and antibacterial assessment of chitosan-coated silver nanoparticles on human pathogens and macrophage cells. Int J Nanomedicine 7:1805–1818

Kim JSK, Kuk E, Xu KN, Kim-H J, Park SJ et al (2007) Antimicrobial effects of silver nanoparticles. Nanomed Nanotechnol Biol Med 3:95–101

Kim D-H, Nikles DE, Johnson DT, Brazel CS (2008) Heat generation of aqueously dispersed $CoFe_2O_4$ nanoparticles as heating agents for magnetically activated drug delivery and hyperthermia. J Mag Mag Mater 320:2390–2396

Lee C, Kim JY, Lee WI, Nelson KL, Yoon J, Sedlak DL (2008) Bactericidal effect of zero-valent iron nanoparticles on *Escherichia coli*. Environ Technol 42:4927–4933

Li B, Li Y, Zhao Y, Sun L (2013) Shape-controlled synthesis of Cu_2O nano/microcrystals and their antibacterial activity. J Phys Chem Solids 74:1842–1847

Lok CN, Ho C-M, Chen R, He Q-Y, Yu W-Y, Sun H, Tam PK-H, Chiu J-F, Che C-M (2007) Silver nanoparticles: partial oxidation and antibacterial activities. J Biol Inorg Chem 12:527–534

Makhluf S, Dror R, Nitzan Y, Abramovich Y, Gedanken A (2005) Microwave-assisted synthesis of nanocrystalline MgO and its use as a bactericide. Adv Func Mater 15:1708–1715

Massart R (1981) Preparation of aqueous magnetic liquids in alkaline and acidic media. IEEA Trans Magn 17:1247–1248

Millan A, Urtizberea A, Silva NJO, Palacio F, Amaral VS, Snoeck E, Serin V (2007) Surface effects in maghemite nanoparticles. J Mag Mag Mater 312:L5–L9

Ortega M, Marco F, Soriano A, Almela M, Martinez JA, Lopez J, Pitart C, Mensa J (2011) *Candida* species bloodstream infection: epidemiology and outcome in a single institution from 1991 to 2008. J Hosp Infect 77:157–161

Pandey BK, Shahi AK, Srivastava N, Kumar G, Gopal R (2015) Synthesis and cytogenic effect of magnetic nanoparticles. Adv Mater Lett 6:954–960

Pareta RA, Taylor E, Webster TJ (2008) Increased osteoblast density in the presence of novel calcium phosphate coated magnetic nanoparticles. Nanotechnology 19:265101

Paškevičius A, Švedienė J (2013) Distribution and species composition causative agents of dermatophytosis in Lithuania. Acta Dermatovenerol Croatica 21:99–104

Peddis D, Mannilla MV, Morup S, Cannos C, Masinu A, Piccaluga G, Orazio FD, Lucari F, Fiorani D (2008) Spin-canting and magnetic anisotropy in ultrasmall $CoFe_2O_4$ nanoparticles. J Phys Chem B 112:8507–8513

Pfaller MA (2012) Antifungal drug resistance: mechanisms, epidemiology, and consequences for treatment. Am J Med 125:3–13

Rai M, Yadav A, Gade A (2009) Silver nanoparticles as a new generation of antimicrobials. Biotechnol Adv 27:76–83

Ren G, Hu D, Cheng EWC, Vargas-Reus MA, Reip P, Allaker RP (2009) Characterization of copper oxide nano-particles for antimicrobial applications. Int J Antimicrob Agents 33:587–590

Sanpo N, Berndt CC, Wen C, Wang J (2013) Transition metal-substituted cobalt ferrite nanoparticles for biomedical applications. Acta Biomater 9:5830–5837

Silva NJO, Amaral VS, Carlos LD (2005) Relevance of magnetic moment distribution and scaling law methods to study the magnetic behavior of antiferromagnetic nanoparticles: application to ferritin. Phys Rev B 71:184408

Taylor EN, Webster TJ (2009) The use of superparamagnetic nanoparticles for prosthetic biofilm prevention. Int J Nanomed 4:145–152

Tran N, Mir A, Mallik D, Sinha A, Nayar A, Webster TJ (2010) Bactericidal effect of iron oxide nanoparticles on *Staphylococcus aureus*. Int J Nanomed 5:277–283

Wan R, Mo Y, Feng L, Chien S, Tollerud DJ, Zhang Q (2012) DNA damage caused by metal nanoparticles: involvement of oxidative stress and activities of ATM. Chem Res Toxicol 25:1402–1411

Wikins TD, Holdeman LV, Abramson IJ, Moore WE (1972) Standardized single-disc method for antibiotic susceptibility testing of anaerobic bacteria. Antimicrob Agents Chemother 1:451–459

Yamamoto O (2001) Influence of particle size on the antibacterial activity of zinc oxide. Int J Inorg Mater 3:643–646

Yamamoto O, Nakakoshi K, Sasamoto T, Nakagawa H, Miura K (2001) Adsorption and growth inhibition of bacteria on carbon materials containing zinc oxide. Carbon 39:1643–1651

Zheng L, He K, Xu CY, Shao WZ (2008) Synthesis and characterization of single crystalline $MnFe_2O_4$ nanorods via a surfactant-free hydrothermal route. J Mag Mag Mater 320:2672–2675

4th publication / 4 publikacija

Fe(II)-substituted cobalt ferrite nanoparticles against multidrug resistant microorganisms

Žalnėravičius R., Paškevičius A., Mažeika K., Jagminas A.

Applied Surface Science, 435 (2018)
DOI: 10.1016/j.apsusc.2017.11.028

Applied Surface Science 435 (2018) 141–148

Contents lists available at ScienceDirect

Applied Surface Science

journal homepage: www.elsevier.com/locate/apsusc

Full Length Article

Fe(II)-substituted cobalt ferrite nanoparticles against multidrug resistant microorganisms

Rokas Žalnėravičius[a], Algimantas Paškevičius[b], Kęstutis Mažeika[a], Arūnas Jagminas[a,*]

[a] State Research Institute Centre for Physical Sciences and Technology, Sauletekio av. 3, LT-10257 Vilnius, Lithuania
[b] Laboratory of Biodeterioration Research, Nature Research Centre, Akademijos 2, LT-08412 Vilnius, Lithuania

ARTICLE INFO

Article history:
Received 22 June 2017
Received in revised form
29 September 2017
Accepted 5 November 2017
Available online 9 November 2017

Keywords:
Antimicrobial
Cobalt ferrite nanoparticles
Fe(II) doping
L-Lysine
Characterization

ABSTRACT

The present study is focused on the determination the influence of cobalt content in the magnetic cobalt ferrite nanoparticles (Nps) on their antibacterial efficiency against gram-negative *Escherichia coli* and gram-positive *Staphylococcus aureus* bacteria and several *Candida* species, in particular *C. parapsilosis* and *C. albicans*. For the synthesis of Fe(II) substituted cobalt ferrite Nps by co-precipitation way, the L-lysine was used as the capping biocompatible agent and the particle size was successfully controlled to be in the range of 5–6.4 nm. The antimicrobial efficiencies of the $Co_xFe_{1-x}Fe_2O_4$@Lys Nps, where x varies from 0.2 to 1.0, were evaluated through the quantitative analysis by comparing with that of Fe_3O_4@Lys Nps and L-lysine. In this way, it was evidenced that increase in the Co^{2+} content in the similar sized cobalt ferrite Nps resulted in an increase in their antimicrobial potency into 93.1–86.3 % for eukaryotic and into 96.4–42.7 % for prokaryotic strains. For characterization the composition, structure, and morphology of the tested herein Nps inductively coupled plasma optical emission spectrometry, X-ray diffraction, high-resolution transmission electron microscopy, Mössbauer, and FTIR spectroscopy techniques were conferred.

1. Introduction

Magnetic iron oxide-based nanoparticles (Nps) have become the focus of many studies in the last two decades because of their capability to mediate heat induction [1,2], transfer targeting drugs [3,4], separate cells [5], conduct magnetic resonance imaging [6], and sense [7]. Besides, it has been shown that in contrast to eco-friendly magnetite, Fe_3O_4, some ferrite Nps, $MeFe_2O_4$, where Me is Co, Zn, Mn, Cu, or Ni, can demonstrate antimicrobial properties against multidrug resistant bacteria and fungi [8,9]. Recently, we have shown that cobalt ferrite Nps display in-vitro size-dependent antimicrobial activity against a range of pathogenic bacteria [10]. As reported, decrease in the size of Nps down to ~2 nm resulted in the dramatic increase in their bactericidal efficiency. Observed effect has been linked with an increase in the content of active cobalt ions at the surface of ultra-small cobalt ferrite Nps [10]. As reported by Wang et al. [11], the substitution of the Co^{2+} ion in cobalt ferrite Nps with Zn^{2+}, Ni^{2+}, Cr^{2+}, and Cu^{2+} allows variation in their magneto-optical characteristics as well as antimicrobial properties and efficiency. The substitution of zinc and cobalt in cobalt ferrite Nps significantly improved antibacterial activity against *E. coli* and *S. aureus*. Unfortunately, these publications do not reflect the influence of active Me^{2+} content in the ferrite Nps on bactericidal efficacy. Consequently, the main task of this study was to synthesize cobalt ferrite Nps similar in size but differing in the Co(II) content. To achieve this goal, we focused on the synthesis and investigation of the Nps where Co(II) is substituted by Fe(II) with the general formula $Co_xFe(II)_{1-x}Fe(III)_2O_4$ for several x values. The bactericidal activity of four synthesized Nps, namely Fe_3O_4, $CoFe_2O_4$, $Co_{0.5}Fe(II)_{0.5}Fe_2O_4$ and $Co_{0.2}Fe(II)_{0.8}Fe_2O_4$ with of average size 5.0–6.4 nm, has been studied against several kinds of bacteria and fungi that are well-known as typical pathogens for many skin, tissue, blood, and respiratory infections. Therefore gram-negative *Escherichia coli* (*E. coli*), gram-positive *Staphylococcus aureus* (*S. aureus*) bacteria and two *Candida* line fungi, namely *C. parapsilosis* and *C. albicans*, were tested. It is worth noticing that *C. parapsilosis* and *C. albicans* are significant clinical pathogens and almost the most common species causing candidemia. While azoles are the most commonly used drugs for the treatment of *Candida* infections, short generation time and mutations in nucleic acids lead the drug resistance [12]. Again, *E. coli* bacteria have the ability to cause diverse and serious diseases, such as urinary tract infections (UTIs) and bacteremia [13]. *S. aureus*, is one of the common causes of severe nosocomial infections, because of its capacity to adapt fast to the different environmental conditions [14]. Both of

* Corresponding author.
E-mail address: jagmin@ktl.mii.lt (A. Jagminas).

https://doi.org/10.1016/j.apsusc.2017.11.028
0169-4332/

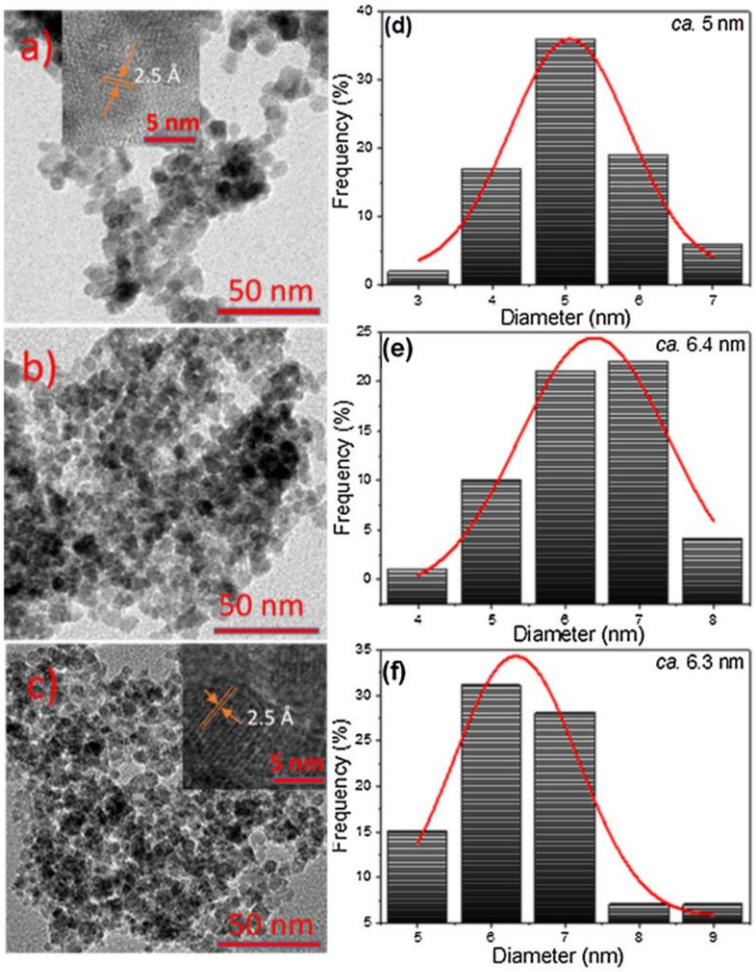

Fig. 1. TEM and HRTEM (Insets) images of synthesized transition metal-substituted cobalt ferrite nanoparticles: (a) $Co_{0.2}Fe_{0.8}Fe_2O_4$@Lys, (b) $Co_{0.5}Fe_{0.5}Fe_2O_4$@Lys and (c) $CoFe_2O_4$@Lys. Histograms of particle size distribution with the average diameter of (d) 5 nm, (e) 6.4 nm and (f) 6.3 nm.

these microorganisms have garnered substantial public attention due to increasing mortality associated with multidrug resistance [15].

Magnetic iron oxide-based particles of the nm size can be formed by several methods [16,17]. As reported, co-precipitation of Me(II) and Fe(III) species in the aqueous alkaline solutions is one of the simplest and most efficient chemical pathway to form magnetic Nps. By this approach, varying the nature of precursors, concentration of solution and pH, the synthesis temperature, pressure, and time it is possible to form Nps with average size ranging from 3 to 20 nm. Driven by this idea, in this study we have successfully used co-precipitation approach for the synthesis of uniformly sized magnetite, Fe_3O_4, cobalt ferrite $CoFe_2O_4$, and Fe(II)-doped cobalt ferrite Nps. Based on the recent reports on the prospective applications of biocompatible ligand for formation of uniformly sized Nps [18,19],

L-lysine amino acid was applied as the Np growth and stabilizing agent.

2. Experimental

2.1. Materials and reagents

All of the reagents were used as received without further purification unless otherwise stated. Iron(II) chloride tetrahydrate ($FeCl_2{\cdot}4H_2O$, 99 %), iron(III)chloride hexahydrate ($FeCl_3{\cdot}6H_2O$, 99%), cobalt(II)chloride hexahydrate ($CoCl_2{\cdot}6H_2O$, 97%) and L-lysine (98 %) were supplied by Sigma-Aldrich Chemical Co. Sabouraud CAF (10 g L^{-1} peptomycol, 40 g L^{-1} glucose and 0,5 g L^{-1} chloramphenicol) and Nutrient Broth (1 g L^{-1} glucose, 15 g L^{-1} peptone, 6 g L^{-1} sodium chloride and 3 g L^{-1} yeast extract) were obtained from Liofilchem. Sodium hydroxide was purified by preparation of a saturate solution resulting in the crystallization of others sodium salts. Milli-Q water (18 MΩ) as well as a rinse was used for the preparation of all solutions.

Gram-positive and gram-negative bacteria strain *Staphylococcus aureus* (ATCC 29213), *Escherichia coli* (ATCC 25922) and several *Candida* species, particularly *Candida parapsilosis* (CBS 8836) and *Candida albicans* (CBS 2730) were obtained from Nature Research Centre collection of microbial strains.

2.2. Synthesis of metal substituted cobalt ferrite nanoparticles

L-Lysine coated Fe-substituted magnetic cobalt ferrite Nps with compositions of $Co_xFe_{1-x}Fe_2O_4$ (where x varies from 0.2 to 1.0) were synthesized by co-precipitation method. Co^{2+}, Fe^{2+}, Fe^{3+} salts with molar ratios of 1:1:4 for $Co_{0.5}Fe_{0.5}Fe_2O_4$, 1:4:10 for $Co_{0.2}Fe_{0.8}Fe_2O_4$, 1:2 for $CoFe_2O_4$, and 1:2 for Fe_3O_4 were dissolved in 25 mL deionized water under magnetic stirring and Ar gas bubbling for 30 min. The total concentration of metal salts was fixed at 75 mmol L^{-1}. Then 1.14 g of L-lysine was dissolved in 12 mL of distilled water and rapidly added to the mixture. Finally, 3 mL of 5 M NaOH was drop-by-drop added to the black solution to get pH ≅ 12.35. The slurry mixture was put into a Teflon-lined stainless steel autoclave and the reaction was conducted at 130 °C with a 10 °C/min ramp for 10 h and then cooled to the room temperature. Prepared black nanopowders, were separated magnetically, washed from reaction fluid several times with deionized water and dried in air overnight.

2.3. Characterization

The morphology and inter-planar spacing of the as-growth Nps were investigated by transmission electron microscope FEI Tecnai F20 X-TWIN at an accelerating voltage of 200 kV. TEM images were recorded using a Gatan Orius CCD camera. A drop of Nps was placed on a carbon-coated nickel grid. Fe-substituted cobalt ferrite Np size distribution and mean particles size were determined using Image J software. In this case, the average diameter of particles was obtained by processing of TEM images. For this, one hundred Nps were randomly selected and measured.

Phase analysis of Fe-doped cobalt ferrite nanopowders was carried out using a diffractometer SmartLab (Rigaku) with rotating Cu anode. CuK_α radiation (λ = 0.154183 nm) was separated by multilayer bent graphite monochromator. The XRD patterns were measured in Bragg-Brentano scan mode with a step 0.02° (in 2θ scale) and counting time 8 s per step. Phase identification was performed using the powder diffraction database PDF4+ (2015). The size of Nps was determined by the Halder-Wagner (H-W) approximation.

The composition of Fe-substituted cobalt ferrite Nps was investigated by inductively coupled plasma optical emission spectrometer ICP-OES OPTIMA 7000DV (Perkin Elmer). Firstly a small pinch of nanopowders were dissolved in HCl (1:1 by volume) solution. Then a calibration curve was drawn using a series of calibration standard solutions in the same acidic matrix as the unknown solutions. All measurements were carried out on emission peaks at λ_{Co} = 238.89 nm and λ_{Fe} = 259.94 nm.

Infrared spectra were recorded in the transmission mode on an ALPHA FTIR spectrometer (Bruker, Inc., Germany) equipped with a room temperature detector DLATGS. The spectral resolution was set at 2 cm^{-1}. Spectra were acquired from 100 scans. Samples were dispersed in KBr tablets. Parameters of the bands were determined by fitting the experimental spectra with Gaussian-Lorentzian shape components using GRAMS/A1 8.0 (Thermo Scientific) software.

Electrokinetic measurements were performed with Zetasizer Nano ZS (Malvern) at 25 °C. The $CoFe_2O_4$ Nps at a concentration of 0.1 mg mL^{-1} were dispersed in $1{\cdot}10^{-3}$ M NaCl. The pH was adjusted with 0.1 M HCl and 0.1 M NaOH respectively.

Mössbauer spectra were collected in transmission geometry using ^{57}Co(Rh) source. The hyperfine field *B* distributions and the doublets (singlets) were fitted to the Mössbauer spectra using WinNormos (Dist) software. Isomer shifts are given relatively to α-Fe.

2.4. Antimicrobial activity

Antimicrobial assessment of the synthesized Fe-substituted cobalt ferrite nanoparticles were tested against prokaryotic (*E. coli, S. aureus*) and eukaryotic (*C. parapsilosis, C. albicans*) microorganisms using the serial dilution method. Followed by these investigations bacteria and yeast strains had been propagated in Nutrient and Sabouraud CAF agar medium at 30 ± 1 °C for 24 h and 27 ± 1 °C for 48 h, respectively. The fresh cultures had been harvested and diluted in sterile nutritional media to yield colony-forming units (CFU) inoculum of $1 - 5 \times 10^6$ for yeast and $6.4 - 8 \times 10^8$ for bacteria cells, based on optical density at 530 nm (OD_{530}) and 600 nm (OD_{600}). The range of OD_{530} and OD_{600} was obtained between 0.12–0.15 and 0.08–0.1, respectively. Then 19 mL of the diluted microorganisms suspensions were collected at the logarithmic stage of growth and transferred in a 50-mL glass flask. Finally, 1 mL of distilled water, containing 20 mg black Nps was added to the liquid medium and further incubated at room temperature for 72 h with 150 rpm shaking. L-Lysine and magnetite (Fe_3O_4) Nps were used as a negative control. During the cultivation, 1 mL of suspensions was taken from each reaction mixture, diluted in glass tubes *via* broth dilution method and spread on Nutrient Broth and Sabouraud agar media plates using stainless steel spreader. The growth of microorganisms was tested after incubation at 30 ± 1 °C and 27 ± 1 °C for 2–3 days.

The field emission scanning electron microscope (FE-SEM, Quanta 250, FEI, Netherland) was employed to analyze the morphological features of microorganism exposed to nanoparticles. Following these investigations, the probes of yeast cell suspension with and without 1 g/L $CoFe_2O_4$@Lys nanoparticles were taken from reaction mixture after 24 h incubation, washed several times with distilled water and mixed with 1% uranyl acetate solution, to enhance the sample contrast. Then 10 μL of solution was dropped on a carbon tape and left to dry in the laboratory box at room temperature and investigated.

3. Results and discussion

3.1. Synthesis and characterization of Fe(II)-doped cobalt ferrite nanoparticles

In an attempt to develop biocompatible magnetic Nps possessing a narrow size distribution, first we applied L-lysine amino acid

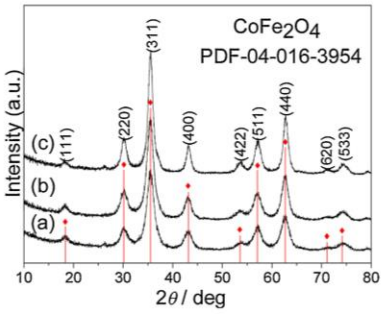

Fig. 2. X-ray diffraction patterns of Fe(II)-doped cobalt ferrite Nps: (a) $Co_{0.2}Fe_{0.8}Fe_2O_4$, (b) $Co_{0.5}Fe_{0.5}Fe_2O_4$, and (c) $CoFe_2O_4$.

as Np growth and stabilizing agent in the hydrothermal synthesis conducted by co-precipitation approach [19]. TEM observations of the as-prepared nanoparticles showed that Fe_3O_4, $CoFe_2O_4$ and Fe(II)-substituted cobalt ferrite Nps are mainly spherical with average diameters 5.0–6.4 nm and quite narrow size distribution (Fig. 1). HRTEM images (Fig. 1, *Insets*) clearly demonstrate that the Nps grow preferentially along the (311) direction with a lattice interatomic distance 0.25 nm. According to analysis of numerous images, the decrease in the cobalt content results in the formation of smaller Nps. Similarly sized magnetite Nps were also formed under the same hydrothermal synthesis conditions (130 °C; 10 h) using $FeCl_2$ and $FeCl_3$ precursors at 1:2 molar ratio with 0.2 mol L^{-1} L-lysine. HRTEM observations agree with the XRD data (Fig. 2), confirming a face-centered cubic (fcc) crystal structure (PDF card No. 04-016-3954, space group *Fd-3m*, $\alpha = \beta = \gamma = 8.385$ Å) of all cobalt ferrite Nps. Notably that the positions and relative intensities of all diffraction peaks of cobalt ferrite and Fe(II)-doped cobalt ferrite Nps: (a) – $CoFe_2O_4$, (b) – $Co_{0.5}Fe_{0.5}Fe_2O_4$ and (c) – $Co_{0.2}Fe_{0.8}Fe_2O_4$ matched well with each other and the standard $CoFe_2O_4$ diffraction data.

The size of Nps estimated from the corresponding XRD patterns using Halder-Wagner approximation equaled to 3.8, 3.1, and 3.6 nm for $CoFe_2O_4$, $Co_{0.5}Fe_{0.5}Fe_2O_4$, and $Co_{0.2}Fe_{0.8}Fe_2O_4$, respectively, complementing the fact, that our synthesized Nps are quite uniformly-sized. The content of cobalt encased in ferrite Nps was determined by chemical analysis of iron and cobalt after Nps probe dissolution in HCl (1:1) using ICP-OES and the composition of Np was calculated assuming that $M_{Fe(II)} + M_{Co(II)} = ½\ M_{Fe(III)}$, as crystalline phases of cobalt oxide were not detected by the XRD analysis.

To explore the influence of substitution of cobalt with divalent iron in the ferrite lattices, the Mössbauer spectra of the Np arrays were collected. As seen, the Mössbauer spectra collected under transmission mode at an ambient temperature differ (Fig. 3) because variations in the composition and possibly in the size of Nps. Two methods of evaluation of Fe(II) content were used. The spectra collected at the room temperature can be fitted using two hyperfine field distribution having different isomer shift values 0.23–0.26 and 0.53–0.58 mm/s, respectively. Attributing the area covered by hyperfine distribution with larger isomer shift to Fe(II) + Fe(III) cations as in magnetite we obtain that approximately 17–20 % of all Fe cations are divalent. However, it should be noted that isomer shift of B sublatice of magnetite is larger (about 0.67 mm/s), subspectra strongly overlap because of superparamagnetic relaxation, and Co cations also have an influence on the isomer shift of iron in A (tetrahedral) and B (octahedral sublatices) of Co ferrite.

While comparing the isomeric shift values of Fe(II)-doped Nps with the corresponding values measured for magnetite and maghemite samples, some errors associated with fitting model of Mössbauer spectra can be avoided. According to these data the amounts of Fe(II) (blue points in Fig. 3d for $Co_zFe_x^{2+}Fe_2^{3+}O_{6+2(x+z)}$) should be approximately four times lower than expected for $Co_{0.5}Fe_{0.5}^{2+}Fe_2^{3+}O_4$ and $Co_{0.2}Fe_{0.8}^{2+}Fe_2^{3+}O_4$ compositions. At the same time, the Mössbauer spectra of the same Nps collected at a cryogenic temperature of 10 K are not quite informative because of charge redistribution below Verway temperature. Whereas spectra taken at the enhanced temperatures vary due to further oxidation of Nps. To the end, the compositions of Fe(II)-doped cobalt ferrite Nps are likely to be better presented by calculations performed on the basis of analytical results presented in Table 1.

Fig. 4 compares the FTIR spectra of L-lysine modified cobalt ferrite Nps and L-lysine hydrochloride powder. The intense and broad absorption band near 592 cm^{-1} corresponds to Fe—O/Co—O stretching vibration in tetrahedral metal complex [20]. Several broad bands of lower intensity are visible in the higher frequency fingerprint spectral region of cobalt ferrite Nps stabilized with L-lysine (Fig. 4a). These bands might be associated with vibrations of both carboxylate and amino groups of adsorbed L-lysine amino acid used for the stabilization of cobalt ferrite Nps. The most intense band in the FTIR spectrum of crystalline L-lysine is located at 1581 cm^{-1} (Fig. 4b). This feature can be assigned to antisymmetric COO^- group stretching vibration, $\nu_{as}(COO)$. The shoulder near 1603 cm^{-1} belongs to the antisymmetric deformation vibration of proximal and distal NH_3^+ groups, $\delta_{as}(NH_3)$. The clearly resolved bands near 1515 and 1406 cm^{-1} can be associated with NH_3^+ symmetric deformation vibration, $\delta_s(NH_3)$, and symmetric stretching vibration of COO^- group, $\nu_s(COO)$, respectively. The bands in the wavenumber region from 1321 to 1356 cm^{-1} are due to the coupled vibrations of $\delta_{as}(CH_2)$ and $\delta(CH)$ [21,22].

The FTIR spectrum of L-lysine-modified cobalt ferrite Nps (see Fig. 4a) exhibit broad band near 1595 cm^{-1} which is associated with the mixed $\nu_{as}(COO)/\delta_{as}(NH_3)$ vibrational modes. The broad band at 1510 cm^{-1} belongs to $\delta_s(NH_3)$ mode and indicates the presence of charged amino group at the interface. The frequency of $\nu_s(COO)$ mode downshifts from 1406 to 1381 cm^{-1} upon adsorption of L-lysine on the Np surface. Previous SERS studies have demonstrated that such frequency downshift is a signature of direct interaction of carboxylate group with the metal surface [23,24]. Thus, FTIR spectroscopy data suggest that L-lysine amino acid binds to cobalt ferrite Nps through the carboxylate group; while the amine group remains protonated. These results agree with those obtained by Zeta potential measurements, which we have performed to determine the surface charge of Nps.

Fig. 5 illustrates variations of Zeta potential *versus* the pH for the L-lysine coated cobalt ferrite Np suspensions. As seen, all particles are positively charged in the acidic solutions if pH ≤ 7.0. Significantly, the ζ-potential of the $CoFe_2O_4$@Lys Nps is in 40–50 % larger within (5.0–7.0) pH range than Fe(II)-doped Nps, emphasizing to the role of Co(II) substitution with Fe(II).

These observations can be attributed to the larger content of the tethered L-lysine molecules at the particle surface, exposing more amino groups in the protonated form [25].

3.2. Antimicrobial activity of Fe(II)-substituted cobalt ferrite Nps

It has been determined by a modified Kirby-Bauer method that all $CoFe_2O_4$ Nps showed a fungicidal effect against the tested pathogens after 48 h lasted incubation. The biggest inhibition zone has been obtained around the discs impregnated with L-lysine functionalized $CoFe_2O_4$ Nps (Fig. 6).

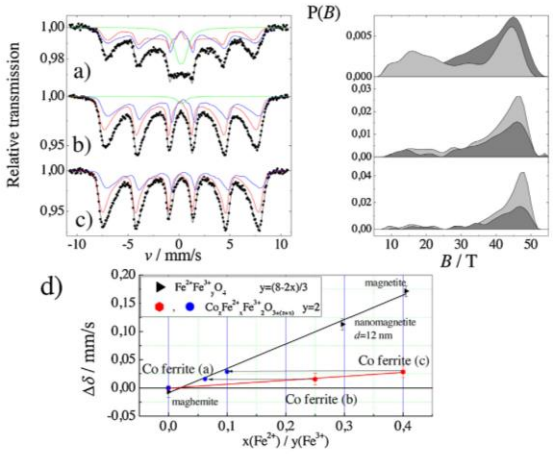

Fig. 3. Room temperature Mössbauer spectra of $CoFe_2O_4$ (a), and Fe(II)-doped cobalt ferrite Nps, presumably $Co_{0.5}Fe_{0.5}^{2+}Fe_2^{3+}O_4$ (b), and $Co_{0.2}Fe_{0.8}^{2+}Fe_2O_4$ (c), while hyperfine distributions are presented on the right. The dependence of an average Mössbauer spectrum centrum shift (d) is relative to pure cobalt ferrite.

Table 1
ICP-OES analysis data and calculated composition of the synthesized $CoFe_2O_4$ and Fe- substituted ferrite nanoparticles.

Expected sample	The probe Co^{2+}, mg/L	composition[a] Fe^{3+}, mg/L	Fe^{2+}/Co^{2+} ratio	Calculated formula
$CoFe_2O_4$	45.7	91.17	1.95[b]	$CoFe_2O_4$
$Co_{0.5}Fe_{0.5}Fe_2O_4$	17.8	79.56	1.23	$Co_{0.52}Fe_{0.48}Fe_2O_4$
$Co_{0.2}Fe_{0.8}Fe_2O_4$	5.64	70.53	3.50	$Co_{0.21}Fe_{0.79}Fe_2O_4$

[a] ±0.03 mg/L.
[b] Fe^{3+}/Co^{2+} ratio.

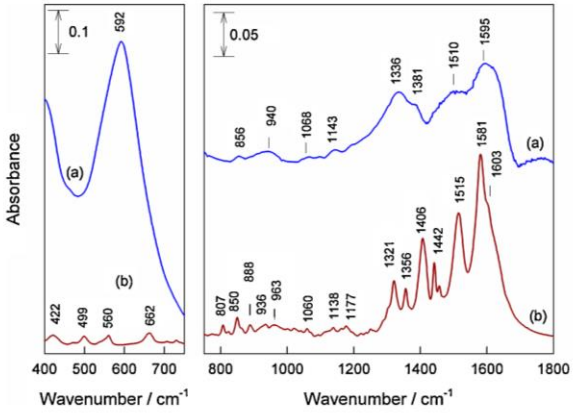

Fig. 4. FTIR absorbance spectra of (a) L-lysine modified Co-Fe nanoparticles, and (b) L-lysine powder in the wavenumber range 400–750 (left panel) and 750–1800 cm^{-1} (right panel).

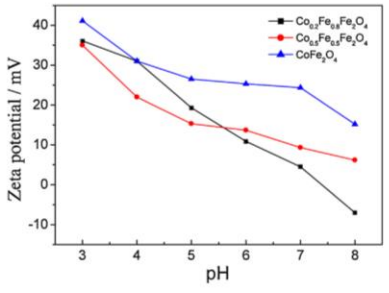

Fig. 5. Variations in the Zeta potential of L-lysine-functionalized Fe(II)-doped cobalt ferrite Nps with solution pH.

These results agree with those obtained by quantitative analysis. It has been determined that Fe(II)-doped cobalt ferrite Nps also demonstrate high killing efficiency against all tested microorganisms. Consequently, antimicrobial activity of doped $CoFe_2O_4$ Nps were further investigated against multidrug-resistant clinical pathogens *Staphylococcus aureus* (ATCC 29213), *Escherichia coli* (ATCC 25922), *Candida parapsilosis* (CBS 8836), and *Candida albicans* (CBS 2730) by assessing the colony forming units (CFU). To quantify the bactericidal and fungicidal potencies, the microorganisms were incubated in the liquid medium with the same content of tested Nps under shaking for 24 and 72 h. The results obtained from these investigations are shown in Fig. 7. Besides, 100 mg L^{-1} of L-lysine and 1 g L^{-1} of Fe_3O_4@Lys Np probes were also incubated and investigated as the negative control samples. In this way, a good correlation was found between the amount of overall Co^{2+} in Nps and the microorganisms survival. It can be easily seen that $CoFe_2O_4$ Nps showed the highest antimicrobial potency against all tested microorganisms. If compare with control sample, these Nps have showed the killing efficiency of 93.1–86.3 % for eukaryotic and 96.4–42.7 % for prokaryotic strains. It should be noted that both Fe(II)-doped cobalt ferrites, namely $Co_{0.5}Fe_{0.5}Fe_2O_4$ and $Co_{0.2}Fe_{0.8}Fe_2O_4$, show 11–24 % and 21–70 % decrease in the antimicrobial activity, respectively, after 24 h incubation with respect to $CoFe_2O_4$. One of the most striking result obtained from the data comparison tests was that the same amount of both $CoFe_2O_4$ and $Co_{0.5}Fe_{0.5}Fe_2O_4$ Nps killed a huge part of *C. parapsilosis* microorganisms after 72 h cultivation. Furthermore, in the case of *E. coli* and *S. aureus* incubation with a pure L-lysine for 24 h contact time, it shows surprisingly bactericidal potency at a level of 9% and 6%, respectively.

However, the number of microorganisms has increased after 72 h incubation with in a pure L-lysine, in comparison with control sample. In the case of L-lysine coated magnetite Nps, the same amount of colony forming units, as for the control sample (Fig. 7), has been obtained implying on the no toxically behavior of magnetite Nps. In addition, Fig. 8 shows the quantity of eukaryotic and prokaryotic microorganisms grown on the Sabouraud and Nutrient agar plates as a function of Co^{2+} content in the cobalt ferrite Nps demonstrating a significant reduction of colonies count with an increase in the content of Co(II) species in the Fe(II)-substituted cobalt ferrite Nps. Only two to three dozens of bacteria *C. albicans* and *S. aureus* instead of thousands remain viable after incubation with 10 μg mL^{-1} amount of $CoFe_2O_4$ Nps for 24 h.

Considerable alternations of the *C. parapsilosis* cells were observed by SEM inspection of these microorganisms before and after incubation with cobalt ferrite Nps (Fig. 9). In this study, the interaction of $CoFe_2O_4$@Lys Nps with yeast cells was also confirmed using Energy-dispersive X-ray spectroscopy (EDX) results (see Inset in Fig. 9). The EDX spectrum of cobalt ferrite treated *C. parapsilosis* surface in the damaged sites shows the presence of Fe and Co, confirming the interaction of nanoparticles with yeast cell.

The mechanism of interaction between the cobalt ferrite Nps and bacteria is not clear and demands for further investigations. Nevertheless, some suggestions can be derived from the FESEM results obtained in this study. First, due to biocompatible L-lysine

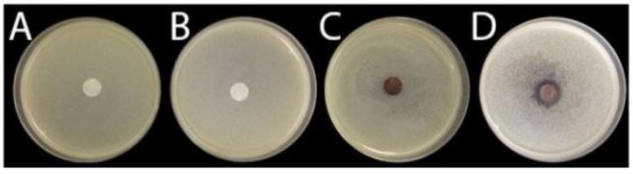

Fig. 6. Inhibitory activity of L-lysine (D) functionalized cobalt ferrite Nps loaded filter paper specimens against *C. albicans* microorganisms. In the left side – control specimens: A – filter paper, B – L-lysine and C – Fe_3O_4, D – $CoFe_2O_4$ NPs.

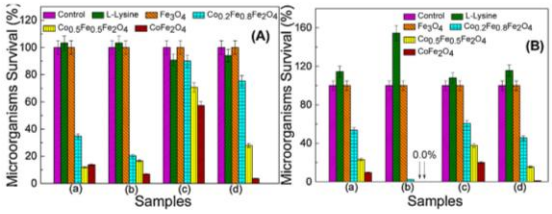

Fig. 7. Antimicrobial activities of the synthesized pure and Fe(II)-substituted cobalt ferrite Nps after (A) 24 h and (B) 72 h incubation with *C. albicans* (a), *C. parapsilosis* (b), *E. coli* (c) and *S. aureus* (d). For comparison, the behavior of pure L-lysine and magnetite Nps is presented.

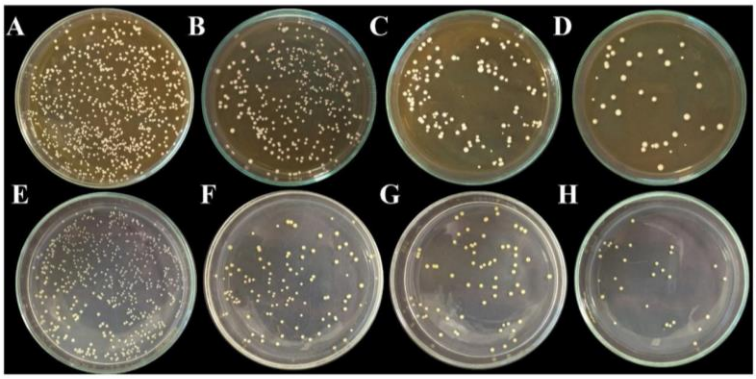

Fig. 8. Photographs showing the antimicrobial activity of various Fe(II)-substituted cobalt ferrite Nps for growth inhibition of *C. albicans* (top row) and *S. aureus* (bottom row) microorganisms incubated in the Sabouraud and Nutrient agar plates, respectively. All microorganisms were cultivated in liquid medium without (a and e) and with $Co_{0.2}Fe_{0.8}Fe_2O_4$ (b and f); $Co_{0.5}Fe_{0.5}Fe_2O_4$ (c and g) or $CoFe_2O_4$ (d and h) Nps for 24 h. The loading was 10 μg mL^{-1}.

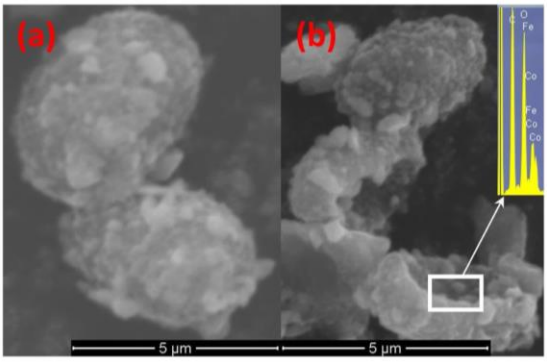

Fig. 9. Scanning electron micrographs of *C. parapsilosis* cells before (a) and after (b) incubation with L-lysine coated $CoFe_2O_4$ Nps showing the cell biomass destruction due to interaction with cobalt ferrite nanoparticles. *Inset*: EDX spectrum taken from the surface of *C. parapsilosis* after incubation with $CoFe_2O_4$ Nps.

shell and the positive ζ-potential $CoFe_2O_4$@Lys Nps can readily interact electrostatically with the negatively bacterium cell wall and damage it, as shown in Fig. 9b. We also suspect, as in [25], this effect can be attributed to amino acid-induced generation of negative curvature at the surface of membrane due to a specific interaction, where the cationic amine group induces negative curvature wrapping of anionic membranes leading to micellization/vesiculation and disrupt of membrane integrity causing the thinning of membranes. Secondly, it is likely the content of cobalt in the Fe(II)-doped cobalt ferrite Nps to be determined by the amount of L-lysine molecules bind to the Np surface through the carboxylate link. A less cobalt is encased, less L-lysine molecules are attached, and, thus, a lower ζ-potential value of Nps is created.

3.3. Conclusions

In summary, we have developed L-lysine capped magnetite, cobalt ferrite and partially Co(II) substituted with Fe(II) cobalt ferrite Nps, quite similar in size and narrow size distribution. We also have found that synthesized $Co_{1-x}Fe(II)_x$ $Fe(III)_2O_4$@Lys Nps in contrast to Fe_3O_4@Lys and L-lysine alone had strong antimicrobial effect against gram-negative as well as gram-positive and *Candida* line fungal pathogens. Notably that an increase in the cobalt content in the nanoparticles resulted in an increase in bactericidal activity of Nps. This effect could be linked with the determined higher positive Zeta potential value of pure cobalt ferrite Nps than Fe(II)-doped ones in the neutral and slightly acidic environments.

Conflict of interest

The authors declare that they have no conflict of interest.

Acknowledgements

This work was funded by Research Council of Lithuania (student research fellowship No. DOC-17095). The authors gratefully acknowledge Dr. Jurate Vaičiūniene, Hab. Dr. Gediminas Niaura, Mr. Martynas Skapas and Mr. Laurynas Šiliauskas for ICP–OES technical support, Raman spectra, TEM and SEM observations, respectively.

References

[1] B. Thiesen, A. Jordan, Clinical applications of magnetic nanoparticles for hyperthermia, Int. J. Hyperthermia 24 (2008) 467–474.
[2] M. Koneracka, P. Kočansky, M. Antalik, M. Timko, C.N. Ramchand, D. Lobo, R.V. Mehta, R.V. Upadhyay, Immobilization of proteins and enzymes to fine magnetic particles, J. Magn. Magn. Mater. 201 (1999) 427–430.
[3] M. Arruebo, R. Fernandez-Pacheco, M.R. Ibarra, J. Santamaria, Magnetic nanoparticles for drug delivery, Nano Today 2 (2007) 22–32.
[4] J.S. Basuki, H.T.T. Duong, A. Macmillan, R.B. Erlich, L. Esser, M.C. Akerfeldt, R.M. Whan, M. Kavallaris, C. Boyer, T.P. Davis, Using fluorescence lifetime imaging microscopy to monitor theranostic nanoparticle uptake and intracellular doxorubicin release, ACS Nano 11 (2013) 10175–10189.
[5] A.K. Gupta, M. Gupta, Synthesis and surface engineering of iron oxide nanoparticles for biomedical applications, Biomaterials 26 (2005) 3995–4021.
[6] T.K. Jain, J. Richey, M. Strand, D.L. Leslie-Pelecky, C.A. Flask, V. Labhasetwar, Magnetic nanoparticles with dual functional properties: drug delivery and magnetic resonance imaging, Biomaterials 29 (2008) 4012–4021.
[7] Z. Liu, Y. Liu, H. Yang, Y. Yang, G. Shen, R. Yu, A phenol biosensor based on immobilizing tyrosinase to modified core-shell magnetic nanoparticles supported at a carbon paste electrode, Anal. Chim. Acta 533 (2005) 3–9.
[8] N. Sanpo, C.C. Berndt, J. Wang, Microstructural and antibacterial properties of zinc-substituted cobalt ferrite nanopowders synthesized by sol-gel methods, J. Appl. Phys. 112 (2012) 1–6.
[9] A. Samavati, A.F. Ismail, Antibacterial properties of copper-substituted cobalt ferrite nanoparticles synthesized by co-precipitation method, Particuology 30 (2017) 158–163.
[10] R. Žalnėravičius, A. Paškevičius, M. Kurtinaitienė, A. Jagminas, Size-dependent antimicrobial properties of the cobalt ferrite nanoparticles, J. Nanopart. Res. 18 (2016) 1–10.
[11] N. Sanpo, C.C. Berndit, C. Wen, J. Wang, Transition metal-substituted cobalt ferrite nanoparticles for biomedical applications, Acta Biomater. 9 (2013) 5830–5837.
[12] N. Dunkel, J. Blass, P.D. Rogers, J. Morschhauser, Mutations in the multi-drug resistance regulator MRR1, followed by loss of heterozygosity, are the main cause of MDR1 overexpression in fluconazole-resistant *Candida albicans* strains, Mol. Microbiol. 69 (2008) 827–840.
[13] F. Alhashash, V. Weston, M. Diggle, A. McNally, Multidrug-resistant *Escherichia coli* bacteremia, Emerg. Infect. Dis. 19 (2013) 1699–1701.
[14] K. Hiramatsu, Y. Katayama, M. Matsuo, T. Sasaki, Y. Morimoto, A. Sekiguchi, T. Baba, Multi-drug-resistant *Staphylococcus aureus* and future chemotherapy, J. Infect. Chemother. 20 (2014) 593–601.
[15] J.Y. Park, E.S. Choi, M.J. Baek, G.H. Lee, Colloidal stability of amino acid coated magnetite nanoparticles in physiological fluid, Mater. Lett. 63 (2009) 379–381.
[16] M.A. Willard, I.K. Kurihara, F.F. Carpenter, S. Calvin, V.G. Harris, in: H.S. Nalwa (Ed.), Encyclopedia of Nanoscience and Nanotechnology, vol. 1, American Scientific Publishers, Valencia, CA, 2004, pp. 815–848.
[17] P. Tartaj, M.P. Morales, S. Veintemillas Verdagner, T. Gonzalez Carreno, C.J. Serna, Synthesis, properties and biomedical applications of magnetic nanoparticles Handbook of Magnetic Materials, 16, 2006, pp. 403–482.
[18] J. Lyczak, H. Gu, B. Xu, Multifunctional magnetic nanoparticles: design, synthesis, and biomedical applications, Acc. Chem. Res. 42 (2009) 1097–1107.
[19] S. Laurent, D. Forge, M. Port, A. Roch, C. Robic, L. Vande Elst, R.N. Muller, Magnetic iron oxide nanoparticles: synthesis, stabilization, vectorization, physicochemical characterization, and biological applications, Chem. Rev. 108 (2008) 2064–2110.
[20] F.M. Paiva, J.C. Batista, F.S.C. Rego, J.A. Lima, P.T.C. Freire, F.E.A. Melo, J. Mendes Filho, A.S. de Menezes, C.E.S. Nogueira, Infrared and Raman spectroscopy and DFT calculations of DL amino acids: valine and lysine hydrochloride, J. Mol. Struct. 1127 (2017) 419–426.
[21] A.D. Roddick-Lanzilotta, P.A. Connor, A.J. McQuillan, An in situ infrared spectroscopic study of the adsorption of lysine to TiO_2 from an aqueous solution, Langmuir 14 (1998) 6479–6484.
[22] S. Martusevicius, G. Niaura, Z. Talaikyte, V. Razumas, Adsorption of L-histidine on copper surface as evidenced by surface-enhanced Raman scattering spectroscopy, Vib. Spectrosc. 10 (1996) 271–280.
[23] M. Dagys, P. Lamberg, S. Shleev, G. Niaura, I. Bachmatova, L. Marcinkeviciene, R. Meskys, J. Kulys, T. Arnebrant, T. Ruzgas, Comparison of bioelectrocatalysis at *Trichaptum abietinum* and *Tramates hirsuta* laccase modified electrodes, Electrochim. Acta 130 (2014) 141–147.
[24] A. Lopez-Cruz, C. Barrera, V.L. Calero-DdelC, C. Rinaldi, Water dispersible iron oxide nanoparticles coated with covalently linked chitosan, J. Mater. Chem. 19 (2009) 6870–6876.
[25] M.T. Hyldgaard, T. Mygind, B.S. Vad, M. Stenvang, D.E. Otzen, R.L. Meyer, The antimicrobial mechanism of action of epsilon-poly-L-lysine, Appl. Environ. Microbiol. 80 (2014) 7758–7770.

5th publication / 5 publikacija

Shell-dependent antimicrobial efficiency of cobalt ferrite nanoparticles

Ramanavičius S., Žalnėravičius R., Drabavičius A., Jagminas A.

Nano-Structures & Nano-Objects, 15 (2018)
DOI: 10.1016/j.nanoso.2018.03.007

Nano-Structures & Nano-Objects 15 (2018) 40–47

Contents lists available at ScienceDirect

Nano-Structures & Nano-Objects

journal homepage: www.elsevier.com/locate/nanoso

Shell-dependent antimicrobial efficiency of cobalt ferrite nanoparticles

Simonas Ramanavičius [1], Rokas Žalnėravičius [1], Gediminas Niaura, Audrius Drabavičius, Arūnas Jagminas *

State Research Institute Center for Physical Sciences and Technology, Department of Electrochemical Materials Science, Sauletekio Ave. 3, LT-10222, Vilnius, Lithuania

HIGHLIGHTS

- Cobalt ferrite nanoparticles against multidrug resistance pathogens.
- Synthesis and characterization of L-lysine and oleic acid stabilized cobalt ferrite nanoparticles.
- While $CoFe_2O_4$@Ole Nps are more efficient antimicrobial agents than $CoFe_2O_4$@Lys Nps.

ARTICLE INFO

Article history:
Received 10 July 2017
Received in revised form 9 March 2018
Accepted 10 March 2018

Keywords:
Magnetic nanoparticles
Antimicrobial efficiency
Cobalt ferrite
Co-precipitation
Thermal decomposition

ABSTRACT

Uniformly shaped and sized superparamagnetic nanoparticles (NPs) have recently received increasing attention due to their prospective applications in theranostics, sensing and as antimicrobials. However, utilization of magnetic NPs in nanomedicine largely depends on their properties, which, in turn, are influenced by the size, structure and composition of the core and the nature of stabilization shell. This paper highlights the significant influence of stabilizing shell of superparamagnetic cobalt ferrite NPs on the antimicrobial efficacy against several kinds of pathogenic microorganisms. Two very popular preparation methods of biocompatible magnetic NPs, namely, co-precipitation from alkaline solutions containing Co(II) and Fe(III) salts and L-lysine (Lys) as well as thermal decomposition of organometallic Co(II) and Fe(III) precursors in the presence of oleic acid were applied. The properties of resulting NPs are characterized and discussed herein. Surprisingly, highly efficient bactericidal behaviour of cobalt ferrite NPs capped with oleine shell compared to that of $CoFe_2O_4$@Lys, was ascribed to the differences in their surface charge and more grained structure of the former.

1. Introduction

Current research in fabrication of nano-sized materials is motivated by the idea that unique, considerably changed physical, chemical or biological properties of materials can be obtained when their size is reduced to nanometre dimensions [1,2]. According to the recent publications, except for well-known antimicrobial behaviour of silver nanoparticles (Nps) [3–5], the Nps of some metal oxides such as TiO_2, ZnO, MgO [6,7], Cu_2O [8], and ferrite, $MeFe_2O_4$, where Me = Co, Zn, Cu, Ni [9,10], are capable to fight human pathogens more effectively than antibiotic agents do [11]. The toxicity of nanosized TiO_2, ZnO, and CuO Nps have been studied by Heinlaan et al. [12]. Wang's group reported that the shape of Cu_2O crystals affects their antimicrobial activity: octahedral Cu_2O crystals bounded by {111} facets exhibited higher activity in killing *Escherichia coli* than cubic ones bounded by {100} facets, presumably due to stronger electrostatic interaction of the former [13]. As reported, the antimicrobial properties of NPs can easily be altered by changing their size, shape, and crystallinity. Size-dependent interaction of silver [14–16], ZnO [17], as well as cobalt ferrite NPs [18] has been reported emphasizing effectiveness of ultra small-sized species due to 4 times higher efficacy of ultra-small NPs against *S. cerevisiae* and several kinds of Candida microorganisms in comparison with the 15-nm sized ones [18].

Recently, the emphasis has been placed onto understanding the role of the NP stabilizing shell because the specific properties can be rendered *via* smart functionalization of NP surface. For example, it has recently been reported that $CoFe_2O_4$ NPs capped with folic acid and hematoporphyrin fragments are effective anticancer reagent [19]. Moreover, the surface composition of silver NPs

* Corresponding author.
E-mail address: arunas.jagminas@ftmc.lt (A. Jagminas).
[1] These authors contributed equally to this work.

https://doi.org/10.1016/j.nanoso.2018.03.007
2352-507X/

strongly influences their interaction with bacteria membrane [20]. Nevertheless, according to review of Soenen et al. [21], surface functionalization of NPs does not alter the intrinsic NP toxicity, but may reduce the extent of cell-NP interaction. However, to the best of our knowledge, until now no studies have been devoted to investigation of the effect of the shell of magnetic NP on their antimicrobial properties.

Therefore, the objective of this study is to investigate and compare antimicrobial behaviour of cobalt ferrite NPs, grown by both the co-precipitation [22,23] and by thermal decomposition [24,25] methods, considering the role of their stabilizing shells. In order to form biocompatible and superparamagnetic NPs, co-precipitation synthesis was performed hydrothermally using L-lysine amino acid, as stabilizing and capping surfactant. To the best of our knowledge, the application of L-lysine has been reported earlier only for fabrication of monodisperse magnetite NPs [26]. An important finding of this study is that the antimicrobial properties are strongly dependent on the nature of the ligands capped on the Np surface, even though they have similar size. The surprisingly enhanced antimicrobial behaviour of $CoFe_2O_4$@Ole NPs with respect to $CoFe_2O_4$@Lys ones is likely to be due to the negative ζ-potential of these NPs.

2. Experimental section

2.1. Chemical reagents and equipment

In this study, all the reagents were of analytical grade at least and, except for NaOH, were used without further purification. $CoCl_2$, $FeCl_3$, $FeCl_2$, L-lyzine, Co(II) acetylacetonate, $Co(acac)_2$, (≥97.0%), oleic acid, C_8H_{18}=C_8H_{15}–COOH, (72%), and Trimethylamine-N-oxide (98.0%) were purchased from Aldrich Chemicals Inc. Dibenzyl ether (≥98.0%) and iron (III) acetylacetonate, $Fe(acac)_3$ (≥97.0%) were obtained from Fluka Analytical. NaOH was purified by preparation of a saturated solution resulting in the crystallization of others sodium salts. After analysis, this solution was diluted to 2.0 mol L^{-1} concentration and used. Deionized/distilled water was used in all experiments.

2.2. Synthesis of NPs

Hydrophilic cobalt ferrite nanoparticles were synthesized hydrothermally at 130 °C with 10 °C min^{-1} ramp for 10 h in alkaline solution containing 25 mmol L^{-1} of $CoCl_2$, 50 mmol L^{-1} of $FeCl_3$ salts, 0.2 mol L^{-1} of L-lyzine amino acid, as chelating agent, and NaOH up to pH ≅ 12.35 ± 0.1. As-grown NPs were centrifuged at 7500 rpm for 5 min, carefully rinsed with pure H_2O/centrifuged several times, and finally dried at 60 °C. Similarly, magnetite (Fe_3O_4) NPs caped with L-lysine were synthesized in an alkaline solution containing $FeCl_2$ and $FeCl_3$ salts and 0.2 mol L^{-1} of L-lyzine. Hydrophobic cobalt ferrite NPs were fabricated *via* thermal decomposition of $Co(acac)_2$ and $Fe(acac)_3$ salts dissolved in the dibenzyl ether deoxygenated by bubbling with nitrogen gas. For stabilization of NPs size, oleic acid and Trimethylamine-N-oxide were used. Briefly, to form small NPs, 18 mmol L^{-1} $Co(acac)_2$, 36 mmol L^{-1} $Fe(acac)_3$, 15 mmol L^{-1} (0.051 g) Trimethylamine-N-oxide and 41.7 g L^{-1} oleic acid were dissolved in 45 mL of dibenzyl ether under the stirring and nitrogen gas purge. The temperature was increased to 230 °C and the synthesis was conducted under reflux, N_2 gas flow and stirring for 2 h followed by temperature increase to 280 °C and processing further under reflux and N_2 bubbling for 1 h. After cooling to room temperature, the crude products were centrifuged, rinsed with acetone/ethanol mixture (2:1) for several times, collected with permanent magnet and dried in air at 60 °C. For the synthesis of larger cobalt ferrite NPs, more than 15 nm in diameter, the same synthesis protocol was repeated using already synthesized NPs in a double diluted solution, compared to the first one, under the same conditions.

2.3. Nanoparticle characterization

The morphology of the as-grown products was investigated using a transmission electron microscope (TEM, model MORGAGNI 268) operated at 72 kV. The NPs subjected to TEM observations were dispersed in ethanol, drop-casted onto a carbon-coated copper grid, and dried naturally. The average size of NPs was estimated from at least 150 species observed in their TEM images. High resolution transmission electron microscopy (HRTEM) studies of the as-grown products were performed using a LIBRA 200 FE at an accelerating voltage of 200 kV. Hydrodynamic size of NPs in water was determined by dynamic light scattering (DLS) tests at 25 °C under ambient conditions using Zetasizer Nano S (Malvern Instruments, UK) equipment. Magnetization measurements were conducted using the vibrating sample magnetometer calibrated by Ni sample of similar dimensions as the studied sample of NPs placed in the plastic tube. The magnetometer was composed of the vibrator, lock-in-amplifier, and electromagnet. The magnetic field was measured by the teslameter FH 54 (Magnet-Physics Dr. Steingrover GmbH). *X*-ray powder diffraction experiments were performed on a D8 diffractometer (Bruker AXS, Germany), equipped with a Göbel mirror as a primary beam monochromator for CuK_α radiation (λ = 1.5418 Å).

Infrared spectra were recorded in transmission mode on an ALPHA FTIR spectrometer (Bruker, Inc., Germany) equipped with a room temperature detector DLATGS. The spectral resolution was set at 2 cm^{-1}. Spectra were acquired from 100 scans. Samples were dispersed in KBr tablets. Parameters of the bands were determined by fitting the experimental spectra with Gaussian–Lorentzian shape components using GRAMS/A1 8.0 (Thermo Scientific) software.

2.4. Antimicrobial tests

Antimicrobial assessment of the synthesized cobalt ferrite NPs against prokaryotic (*E. coli, Staphylococcus aureus*) and eukaryotic (*Candida parapsilosis, Candida albicans*) microorganisms was performed using the serial dilution method. Antimicrobial tests against eukaryotic microorganisms *C. albicans* and *C. parapsilosis* were done in sterile Sabouraud CAF media composed of 10 g L^{-1}peptomycol, 40 g L^{-1} glucose, and 0.5 g L^{-1} chloramphenicol; pH = 5.6 ± 0.2 at 25 °C. Antimicrobial assessment of the synthesized cobalt ferrite NPs against prokaryotic microorganisms *E. coli* and *S. aureus* was carried out in sterile Nutrient Broth (1 g L^{-1} glucose, 15 g L^{-1} peptone, 6 g L^{-1} sodium chloride and 3 g L^{-1} yeast extract); pH = 7.5 ± 0.2 at 25 °C. Following these investigations bacteria and yeast strains were propagated in Nutrient and Sabouraud CAF agar medium at (30 ± 1) °C for 24 h and (27 ± 1) °C for 48 h, respectively. The fresh cultures were harvested and diluted in sterile nutritional media to yield colony-forming units (CFU) inoculum of 1–5 × 10^6 for yeast and (6.4–8.0) × 10^8 for bacterium cells, based on optical density at 530 nm (OD_{530}) and 600 nm (OD_{600}). The range of OD_{530} and OD_{600} was obtained between 0.12–0.15 and 0.08–0.1, respectively. Then 19 mL of the diluted microorganism suspensions, which were collected at the logarithmic stage of growth, were transferred in a 50-mL glass flask. Finally, 1 mL of distilled water, containing 20 mg black NPs was added to the liquid medium and further incubated at room temperature for 72 h with 150 rpm shaking. L-lysine and magnetite (Fe_3O_4) NPs were used as a negative control. Tween 80 was used as a solvent for oleic acid. During the cultivation, 1 mL of the suspension was taken from each reaction mixture, diluted in the glass tubes *via* broth dilution method and spread on the Nutrient Broth and Sabouraud agar media plates using the stainless steel spreader. The growth of microorganisms was tested after incubation at 30 ± 1 °C and 27 ± 1 °C for 2–3 days.

2.5. Confocal scanning laser microscopy investigations

Information about the *C. parapsilosis* cells structure before and after incubation with cobalt ferrite NPs was obtained using the confocal scanning laser microscope Nicon eclipse TE2000 C1 Plus (Plan Apo VC, Nikon, Japan). For these investigations mid-log-phase of *C. parapsilosis* cells (10^6 CFU/mL) were incubated with 1 g/L of $CoFe_2O_4$ NPs and the MIC of Co^{2+} ions, as reported in our previous work [18]. The suspensions were centrifuged, washed and re-suspended in the distilled water. Then, 1 mL of prepared sample was dropped on the Petri dish with the coverslip embedded in the bottom and examined with a confocal scanning microscope equipped with argon laser for 488 nm excitation. Microorganism cells were always included as auto-fluorescence controls. Image acquisition was done by utilizing the FV10-ASW1.6 imaging software. Laser scanning was controlled by the Nikon EZ-C1 software. The images were further processed using the EZ-C1 Bronze version 3.80 (Nikon, Japan) and ImageJ 1.41 software (National Institute of Health, USA).

3. Results and discussion

3.1. Evaluation of morphology and structure of formed NPs

Fig. 1 shows a representative TEM and HRTEM micrographs comparing $CoFe_2O_4$@Lys NPs (a, b) with the ones obtained by thermal decomposition of organometallic precursors in the presence of oleic acid (c, d). As expected, the size and uniformity of evolved NPs are dependent on the synthesis scenario. As also evidenced from the Np spacing and its uniformity, the $CoFe_2O_4$@Ole NPs are individually more isolated than $CoFe_2O_4$@Lys NPs. The calculated size distribution histograms of the corresponding NPs are depicted in the right side of Fig. 1. As seen, the most uniform and finely grained NPs with a main diameter of 7.5 nm have been formed by thermal decomposition of $Co(acac)_2$ and $Fe(acac)_3$ mixture in the presence of oleic acid and Trimethylamine-N-oxide. In the case of repeated decomposition of $Co(acac)_2$ and $Fe(acac)_3$ onto the as-formed cobalt ferrite NPs by an adapted protocol, significantly larger NPs with a mean size of 17.3 nm (Fig. 2) have been formed. Moreover, these NPs seem to be cubic rather than spherical. HRTEM inspection implied a well-expressed crystalline structure of NPs (see Inset of Fig. 2a).

Fig. 3 A depicts the room temperature magnetization curves for 7.2 nm-sized $CoFe_2O_4$@Lys and 7.5 nm-sized $CoFe_2O_4$@Ole NPs indicating their superparamagnetic behaviour. Note, that NPs capped with oleic acid have higher saturation magnetization value (52 emu/g) than similar in size NPs capped with L-Lyzine (46 emu/g). The XRD patterns of the both types of the tested herein $CoFe_2O_4$ NPs stabilized with L-lyzine (Fig. 3B-a) and oleic acid (Fig. 3B b,c) proved their highly crystalline nature because of the strong peak intensities ascribed to (311), (440), (511), (220), (400), and (422) planes of this material. According to the calculations obtained by a Sherrer approach, the crystallite dimension of smaller NPs equalled to 4.03 nm whereas the larger ones—had the diameter of 14.0 nm. It is worth to notice that observed diffraction peaks and their relative intensities for the both types of the cobalt ferrite samples matched well with standard $CoFe_2O_4$ reflections, reported in the PDF card no. 00-022-1086. Several wider diffraction peaks of the small NPs (Fig. 3B-a and b) agree with the TEM observations (Fig. 1) and indicate the significantly smaller crystallite size than 17.3 nm. Quite similar XRD spectrum has been obtained for cobalt ferrite NPs stabilized with L-lysine (Fig. 3B-a). In this case, the mean size of crystallites approximated 4.0 nm that is somewhat smaller than the size value determined by TEM observations. This difference most likely should be due to NP sub-grains structure not detectable by XRD as has been also reported recently for the synthesized magnetite NPs [27].

3.2. The influence of composition on the properties of NPs

Fig. 4A compares the infrared spectra of oleic acid stabilized cobalt ferrite NPs and bulk oleic acid. It is clear that two broad and well-defined bands around 401 and 591 cm^{-1} belong to Fe-O/Co-O stretching vibrations of $CoFe_2O_4$ NPs (Fig. 4A-a) [28–30]. The higher frequency band ν_1 is associated with metal-oxygen vibration of complexes in tetrahedral sites, while the lower frequency component ν_2 corresponds to vibrations in octahedral sites. FTIR observation of these two modes confirms the cubic spinel structure of synthesized $CoFe_2O_4$ NPs. Two strong high frequency bands near 1562 and 1603 cm^{-1} belong to asymmetric stretching vibration of COO^- group [31]. Appearance of these two vibrational bands indicates the presence of two distinct adsorption sites at the surface of $CoFe_2O_4$ NPs. The broad band near 1406 cm^{-1} contains contribution from symmetric stretching vibration of carboxylate group.

As the characteristic for the bulk oleic acid C=O stretching band around 1710 cm^{-1} is absent, there is no spectroscopic evidence for the presence of oleic acid at the interface of NPs (Fig. 4A-b). Thus FTIR analysis indicate that studied magnetic $CoFe_2O_4$ nanoparticles are stabilized by adsorbed oleate anions.

Fig. 4B compares the infrared spectra of L-lysine stabilized cobalt ferrite NPs and L-lysine hydrochloride powder. The intense and broad absorption band around 592 cm^{-1} corresponds to the Fe-O/Co-O stretching vibrations in tetrahedral metal complex [32]. Several broad bands of lower intensity are visible in the higher frequency fingerprint spectral region of cobalt ferrite NPs stabilized with L-lysine (Fig. 4B-a). These bands might be associated with vibrations of carboxylate and/or amino groups of adsorbed L-lysine amino acid used for stabilization of cobalt ferrite nanoparticles. The most intense band in the infrared spectrum of pure L-lysine is located at 1581 cm^{-1} (Fig. 4B-b). This feature was assigned to antisymmetric COO^- group stretching vibration, $\nu_{as}(COO)$ [33,34]. The shoulder near 1603 cm^{-1} belongs to the antisymmetric deformation vibration of proximal and distal NH_3^+ groups, $\delta_{as}(NH_3)$. The clearly resolved bands near 1515 and 1406 cm^{-1} are associated with NH_3^+ symmetric deformation vibration, $\delta_s(NH_3)$, and symmetric stretching vibration of COO^- group, $\nu_s(COO)$, respectively, whereas the bands in the spectral region from 1321 to 1356 cm^{-1} are due to the coupled vibrations of CH_2 antisymmetric deformation and CH deformation modes [35,36].

The infrared spectrum of L-lysine stabilized cobalt ferrite NPs (Fig. 4B-a) exhibit broad band near 1595 cm^{-1} attributable to the mixed $\nu_{as}(COO)/\delta_{as}(NH_3)$ vibrational modes, whereas the broad band at 1510 cm^{-1} belongs to $\delta_s(NH_3)$ mode and indicates the presence of charged amino group at the surface of NPs. The frequency of $\nu_s(COO)$ mode downshifts from 1406 to 1381 cm^{-1} upon adsorption of L-lysine on ferrite nanoparticles. Previous SERS studies have demonstrated that this shifting is the main sign of the direct interaction of carboxylate group with the metal surface [33,34]. Thus, infrared spectroscopy data suggest that L-lysine amino acid binds to cobalt ferrite nanoparticles through the carboxylate group while the amine group remains protonated.

Typical ς-potential variations with the pH of suspensions containing 10 mmol L^{-1} NaCl and 0.25 g L^{-1} either $CoFe_2O_4$@Ole (1) or $CoFe_2O_4$@Lys (2) NPs are shown in Fig. 5. As seen, in the pH region from 3.0 to 8.0 $CoFe_2O_4$@Lys NPs are positively charged due to the exposed protonated amino groups of L-lysine molecules attached to the NPs surface. The decrease in pH results in the decrease in ς-potential value although its variation is insignificant and equals (23 ± 1) mV within the pH 5.0–7.2, characteristic to antimicrobial experiments. The NPs grown *via* thermal decomposition of $Co(acac)_2$ and $Fe(acac)_3$ in the presence of oleic acid are hydrophilic [37] what can be seen from solution of NP probe (A)

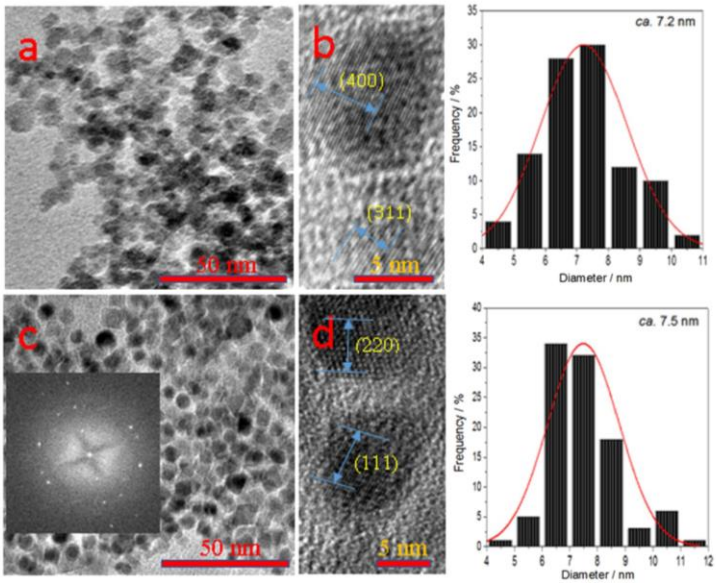

Fig. 1. TEM (a, c) and high resolution TEM (b, d) images of $CoFe_2O_4$@Lys (a, b) and $CoFe_2O_4$@Ole (c, d) nanoparticles. In the *Inset*, typical SAED pattern of cobalt ferrite NPs formed by thermal decomposition.

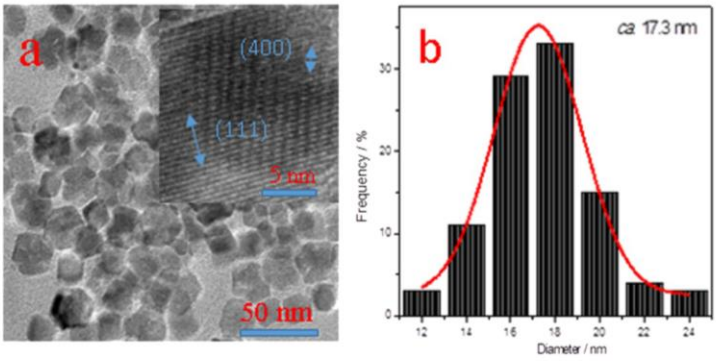

Fig. 2. TEM (a), high resolution TEM *(Inset)* images and size distribution histogram (b) of $CoFe_2O_4$@Ole nanoparticles grown by repeated synthesis.

(*Inset* of Fig. 5). To make NPs hydrophobic and soluble in water for the subsequent antimicrobial tests, we have used the prolonged ultrasound agitation of these NPs in an aqueous solution containing 10 mmol L^{-1} NaCl and some HCl or NaOH added to adjust the required pH of suspension. It is noteworthy that upon the 4–6 h agitation quite stable black-coloured suspensions of $CoFe_2O_4$@Ole NPs have been obtained (see probe (C) in the *Inset* of Fig. 5). Significantly, these NPs possess a negative ς-potential values within all tested pH range, namely between 3.0 and 8.0 (Fig. 5). With an increase in pH from 5.0 to 7.0, the ς-potential of $CoFe_2O_4$@Ole increased from −33 to −44 mV.

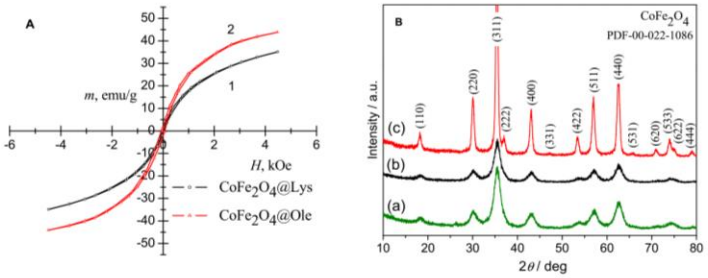

Fig. 3. A: Magnetic hysteresis loops of 7.2 nm-sized $CoFe_2O_4$@Lys (1) and 7.5 nm-sized $CoFe_2O_4$@Ole (2) NPs. In B: XRD patterns of 7.2 nm-sized $CoFe_2O_4$@Lys (a), 7.5 nm-sized (b) and 17.3 nm-sized (c) $CoFe_2O_4$@Ole nanoparticles.

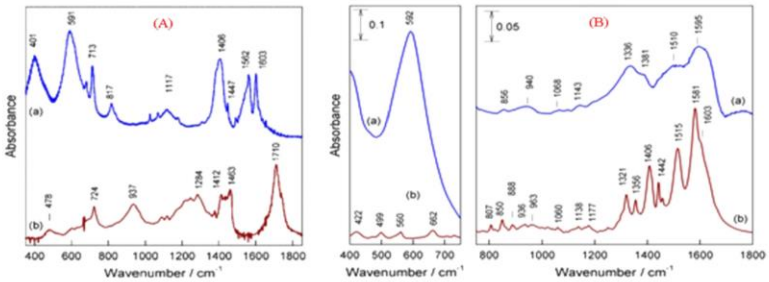

Fig. 4. (A): FTIR absorbance spectra of (a) oleic acid modified cobalt ferrite nanoparticles, and (b) pure oleic acid in the spectral region of 350–1850 cm^{-1}. In (B): the same of L-lysine stabilized cobalt ferrite nanoparticles (a), and (b) L-lysine powder in the spectral regions of 400–750 (left panel) and 750–1800 cm^{-1} (right panel).

Table 1
Viability of bacteria after 24 h incubation with the indicated species.

Viability of bacteria, %							
Microbes	Control	Fe_3O_4	L-lysine	Oleic acid	$CoFe_2O_4$@Lys	7.5 nm $CoFe_2O_4$@Ole	17.3 nm $CoFe_2O_4$@Ole
C. albicans	100	100	103.28	102.24	13.71	9.34	10.16
C. parapsilosis	100	100	103.29	100.83	6.98	0.29	0.009
E. coli	100	100	90.71	133.36	57.30	1.18	4.65
S. aureus	100	100	93.99	143.42	3.64	0.50	1.18

Table 2
Viability of bacteria after 72 h incubation with the indicated species.

Viability of bacteria, %							
Microbes	Control	Fe_3O_4	L-lysine	Oleic acid	$CoFe_2O_4$@Lys	7.5 nm $CoFe_2O_4$@Ole	17.3 nm $CoFe_2O_4$@Ole
C. albicans	100	100	114.39	133.10	9.52	3.33	3.51
C. parapsilosis	100	100	154.47	165.06	0	0	0
E. coli	100	100	108.01	132.14	20.03	0.51	0.67
S. aureus	100	100	115.57	148.39	1.04	0	0

3.3. Antimicrobial activity of NPs

In this study, antimicrobial activity of $CoFe_2O_4$ NPs has been investigated against multidrug-resistant clinical pathogens *S. aureus* (ATCC 29213), *E. coli* (ATCC 25922), *C. parapsilosis* (CBS 8836), and *C. albicans* (CBS 2730) by assessing the colony forming units (CFU). To quantify the bactericidal and fungicidal potencies, all microorganisms were incubated in liquid medium containing NPs under shaking for 24 and 72 h. The results obtained in these investigations are shown in Fig. 6. The control sample consisting of pure L-lysine and oleic acid at the concentrations of 0.1 mg mL^{-1} and 5 *v*/*v* %, respectively, showed no antibacterial activity suggesting no toxicity. Furthermore, in the case of 24 h exposure of oleic acid with *E. coli* and *S. aureus*, the content of bacteria increased by approximately 33% and 43%, respectively, relative to the control sample (Table 1). In the case of incubation of oleic acid with all tested microorganisms for 72 h, their content increased at least by 32% with respect to the control sample (Table 2). These observations implied that 0.1 mg mL^{-1} of L-lysine as well as oleic acid added

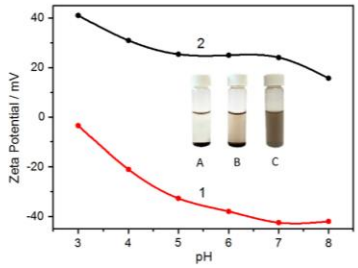

Fig. 5. Variations of the ς-potential values with the pH of aqueous suspension containing 10 mmol L^{-1} NaCl for $CoFe_2O_4$@Ole (1) and $CoFe_2O_4$@Lys (2). In the *Inset*, $CoFe_2O_4$@Ole NP ($\varnothing = 7.5$ nm) suspensions in water before (A) and following 3 (B) and 6 h ultrasound agitation (C) are shown.

into the tested bacteria medium alone significantly increased viability of microorganisms with extending incubation time. It is also noteworthy that pure L-lysine after 24 h incubation with *E. coli* and *S. aureus* demonstrated statistically light antibacterial activity, e.g. ~9 and ~6%, respectively. In contrast, after 72 h incubation of L-lysine with *C. parapsilosis* the number of these bacteria increased by more than 54%, whereas in the case of L-lysine incubation with other bacteria lawns their vitality increased by 8%–15% (Table 2). These observations implied that 0.1 mg mL^{-1} of L-lysine as well as 5 v/v % of oleic acid added to the tested bacterium medium alone increased vitality of bacteria with extending incubation time. It is worth mentioning that incubation of all bacteria tested herein with 1 g L^{-1} of Fe_3O_4 NPs stabilized with L-lysine also did not show any antimicrobial efficacy (Fig. 6). This observation was further supported by a modified Kirby–Bauer method for 48 h incubation of magnetite NPs stabilized with L-lysine (Fig. 7b). Contrary, all cobalt ferrite NPs have shown a fungistatic effect against the tested pathogens. The largest inhibition zone was obtained around the disc impregnated with oleic acid-functionalized $CoFe_2O_4$ NPs (Fig. 7d). These results are in good agreement with those obtained by quantitative analysis (Fig. 6), which is more precise and shows that cobalt ferrite NPs functionalized with oleine shell possess a higher killing efficiency for all tested microorganisms. Both 7.5 nm and 17.3 nm-sized $CoFe_2O_4$@Ole NPs demonstrated the surprisingly high inhibition of almost all microorganisms growth. Consequently, after 72 h incubation, the number of survived microorganisms was only 0.06%–3.3% (Fig. 8).

The mechanism of antimicrobial behaviour of cobalt ferrite NPs formed and investigated herein is not clear and needs to be studied further. However, some suggestions can be derived from the results obtained in this study. Firstly, due to the positive ς-potential of $CoFe_2O_4$@Lys NPs they can readily interact electrostatically with negatively charged bacterium cell walls, such as *S. aureus* and *E. coli*, causing destruction and lysis of the cytoplasm. Secondly, there seem to be different mechanisms of positively charged $CoFe_2O_4$@Lys NPs and negatively charged $CoFe_2O_4$@Ole NPs by which they can affect bacteria cell homoeostasis [20]. A strong interaction of negatively charged bacterium walls, such as *S. aureus* and *E. coli*, can be expected only for L-lysine stabilized cobalt ferrite NPs possessing a positive ς-potential of about 23 mV. This process could facilitate the release of Co^{+2} ions from the NP surface resulting in antimicrobial effect, as in the case of Ag NPs [38,39]. Exceptionally high antimicrobial efficiency of oleine-stabilized cobalt ferrite NPs against all tested bacteria could probably be ascribed either to their higher stability than that of $CoFe_2O_4$@Lys NPs or to a negative curvature wrapping of anionic membranes by a specific interaction with cationic amine groups causing the thinning of membranes, as reported in [40]. Besides, NP-based toxic effects could be associated also with their surface area available for communication with microorganism cultured in a given medium [41]. As can be judged from the XRD data, the surface area of finely grained $CoFe_2O_4$@Ole NPs can be significantly larger than that of $CoFe_2O_4$@Lyz NPs of the same average size. To get a better understanding of the mechanism by which $CoFe_2O_4$@Ole NPs kill bacteria new experiments, except for Co^{2+} release, need to be performed. This issue, however, was beyond the scope of present study.

3.4. Structural observations

Due to the differences in the auto-fluorescence of live and dead eukaryotic microorganisms it is reasonable to investigate them with confocal microscopy. As seen (Fig. 9a), the untreated *C. parapsilosis* yeast cells are oval and cylindrical shaped displaying the intact cell walls. After incubation with MIC of Co^{2+} ions, however, the considerable alterations on cell walls were detected (Fig. 9b). Similar damages of yeast cell walls were also observed after 24 h-long treatment with $CoFe_2O_4$@Lys NPs (Fig. 9a). Furthermore, the agglomeration of these NPs on the surface of microorganism (Fig. 9c) confirms the interaction of $CoFe_2O_4$@Lys NPs with yeast cell. Similar damages of *C. parapsilosis* yeast cells were also visualized after their incubation with $CoFe_2O_4$@Ole NPs.

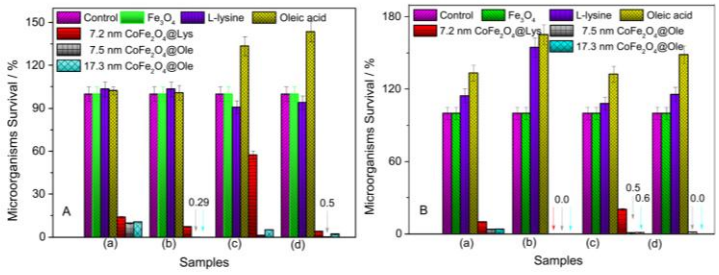

Fig. 6. Antimicrobial activities of the synthesized L-lysine and oleic acid-functionalized cobalt ferrite nanoparticles against *C. albicans* (a), *C. parapsilosis* (b), *E. coli* (c), and *S. aureus* (d) after (A) 24 h and (B) 72 h incubation. Except for the control tests, the efficacies of magnetite (Fe_3O_4@Lys) NPs, L-lysine and oleic acid are also presented.

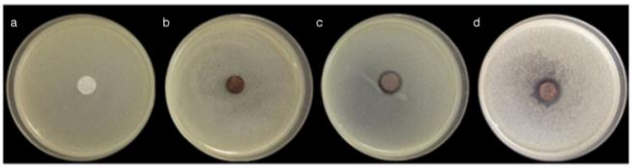

Fig. 7. Inhibitory activity of L-lysine (c) and oleic acid (d) functionalized cobalt ferrite NPs loaded filter paper specimens against *C. albicans* microorganisms. In the left side – control specimens: a – filter paper and b – Fe_3O_4 NPs.

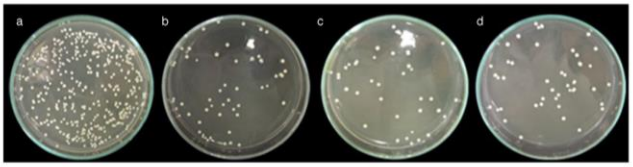

Fig. 8. Photographs showing the antimicrobial activity of the cobalt ferrite NPs for growth inhibition of *C. albicans* microorganisms incubated in the Sabouraud agar plates. All microorganisms were cultivated in liquid medium without (a) and with $CoFe_2O_4$@Lys NPs (b), 7.5 nm-sized $CoFe_2O_4$ (c), or 17.3 nm-sized $CoFe_2O_4$ (d) NPs for 24 h.

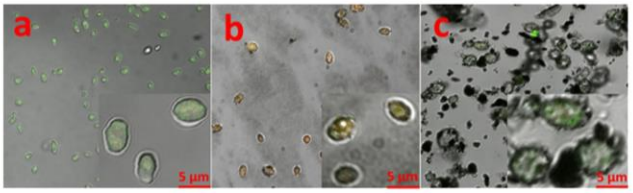

Fig. 9. Laser confocal microscopy images showing *C. parapsilosis* strains before (a) and after incubation with MIC of Co^{2+} ions (b) and $CoFe_2O_4$ nanoparticles (c).

4. Conclusions

Altogether, the analysis of bacterium viability results after incubation with magnetic NPs, presented in this study, leads to the conclusion that $CoFe_2O_4$@Ole NPs are more efficient antimicrobial agents than $CoFe_2O_4$@Lys NPs. Antimicrobial efficiency of cobalt ferrite NPs depends on the bacterium type. For $CoFe_2O_4$@Lys case, the antimicrobial efficiencies increase in the following sequence: *E. coli* < *C. albicans* < *C. parapsilosis* < *S. aureus*, whereas for $CoFe_2O_4$@Ole the sequence is: *C. albicans* < *E. coli* < *S. aureus* < *C. parapsilosis*. The influence of $CoFe_2O_4$@Ole NPs size on the antimicrobial efficiency is not significant between ∅ 7.5 nm and ∅ 17.3 nm. The L-lysine coated magnetite NPs show the same amount of colony forming units as the control sample. The exceptional antimicrobial efficiency of $CoFe_2O_4$@Ole NPs against *C. parapsilosis*, *E. coli*, and *S. aureus* pathogens was attributed to the differences in the surface charge of the tested NPs and finely grained structure.

Acknowledgements

The authors are grateful to Dr. Algimantas Paškevičius from the Laboratory of Biodeterioration Research, Nature Research Centre and Dr. Vitalijus Karabanovas from the National Cancer Centre for the help in antimicrobial and confocal microscopy investigations, respectively.

Author Contributions

Simonas Ramanavičius performed the synthesis work, prepared samples, analysed and characterized products. Rokas Žalnėravičius performed the antimicrobial activity tests, Audrius Drabavičius and Dr. Gediminas Niaura conducted TEM and FTIR investigations, respectively. Dr. Arunas Jagminas designed the research and wrote the manuscript. All authors discussed, edited, and approved the final version.

Conflict of interest

The authors declare no conflict of interest.

References

[1] D.W. Grainger, D.G. Castner, Adv. Mater. 20 (2008) 867.
[2] J. Zheng, P.R. Nicovich, R.M. Dickson, Anuu. Rev. Phys. Chem. 58 (2007) 409.
[3] M. Rai, A. Yadov, A. Gade, Biotechnol. Adv. 27 (2009) 76.
[4] S. Maleki, F. Lotfipour, M. Barrzegar, M. Hossein, K. Adibkia, Mater. Sci. Eng. C 44 (2014) 278.
[5] N. Duran, M. Duran, M.B. de Jesus, A.B. Scabra, W.J. Favaro, G. Nakazato, Nanomedicine 12 (2016) 789.
[6] S. Stankic, S. Suman, F. Haque, J. Vidic, J. Nanobiotechnol. 14 (2016) 73.
[7] G.D. Venkatasubbu, R. Baskar, T. Anusuya, C.A. Seshan, Colloids Surf. B 148 (2016) 600.
[8] H. Pang, F. Gao, Q.Y. Lu, Chem. Commun. 9 (2009) 1076.
[9] N. Sanpo, C.C. Berndt, C. Wen, J. Wang, Acta Biomater. 9 (2013) 5830.
[10] G. Vaidyanathan, S. Sendhilnathan, Phys. B Condens. Matter. 403 (2008) 2157.

[11] L. Yildirimer, N.T. Thanh, M. Loizidou, A.M. Seifalian, Nano Today 6 (2011) 585.
[12] M. Heinlaan, A. Ivasj, I. Blinova, H.-C. Dubouguier, A. Kahru, Chemosphere 71 (2008) 1308.
[13] J. Ren, W. Wang, S. Sun, L. Zhang, L. Wang, J. Chang, Ind. Eng. Chem. Res. 50 (2011) 10366.
[14] J.R. Morones, J.L. Elechiguerra, A. Camacho, K. Holt, J.B. Kouri, J.T. Ramirez, M.J. Yacaman, Nanotechnology 16 (2005) 2346.
[15] S. Shrivastava, T. Bera, A. Ray, G. Singh, P. Ramachandrarao, D. Dash, Nanotechnology 18 (2007) 225103.
[16] S. Pal, Y.K. Tak, J.M. Song, Appl. Environ. Microbiol. 73 (2007) 1712.
[17] K.R. Raghupati, R.T. Kaodali, A.C. Manna, Langmuir 27 (2011) 4020.
[18] R. Žalneravičius, A. Paškevičius, M. Kurtinaitiene, A. Jagminas, J. Nanopart. Res. 18 (2016) 300.
[19] K.-H. Choi, K.C. Nam, U.-H. Kim, G. Chao, J.-S. Jung, B.J. Park, Nanomaterials 7 (2017) 144.
[20] M.S. Palencia, M.E. Berrio, S.L. Palencia, J. Nanosci. Nanotechnol. 17 (2017) 5197.
[21] S.J. Soenen, P. Rivera-Gil, J.-M. Montenegro, W.J. Parak, S.C. De Smedt, K. Braechmans, Nano Today 6 (2011) 446.
[22] S. Laurent, D. Forge, M. Port, A. Roch, C. Robic, L.V. Elst, R.N. Muller, Chem. Rev. 108 (2008) 2064.
[23] M. Vadivel, R.R. Babu, K. Ramamurthi, M. Arivanandhan, Nano Struct. Nano Objects 11 (2017) 112.
[24] J. Park, K. An, Y. Hwang, J.G. Park, H.J. Noh, J.Y. Kim, J.H. Park, N.M. Hwang, T. Hyeon, Nature Mater. 3 (2004) 891.
[25] J.E. Macdonald, C.J. Brooks, J.G. Veinot, Chem. Commun. 32 (2008) 3777.
[26] Z. Durmus, H. Kavas, M.S. Toprak, A. Baykal, T.G. Altinçekiç, A. Aslan, A. Bozkurt, S. Coşgun, J. Alloys Compd. 484 (2009) 371.
[27] N. Belachew, D.R. Devi, K. Basavaiah, J. Mol. Liq. 224 (2016) 713.
[28] P.K. Selvan, C.O. Augustin, L.J.R. Berchmans, Mater. Res. Bull. 38 (2003) 41.
[29] M.A. Gabal, Y.M. Al Angari, M.W. Kadi, Polyhedron 30 (2011) 1185.
[30] H.S. Mund, B.L. Ahuja, Mater. Res. Bull. 85 (2017) 228.
[31] P.J. Thistlethwaite, M.L. Gee, D. Wilson, Langmuir 12 (1996) 6487.
[32] R. Safi, A. Ghasemi, R. Shoja-Razavi, M. Tavousi, J. Magn. Magn. Mater. 396 (2015) 288.
[33] F.M. Paiva, J.C. Batista, F.S.C. Rego, . Jr.J.A. Lima, P.T.C. Freire, F.E.A. Melo, J. Mendes Filho, A.S. de Menezes, C.E.S. Nogueira, J. Mol. Struct. 1127 (2017) 419.
[34] A.D. Roddick-Lanzilotta, P.A. Connor, A.J. McQuillan, Langmuir 14 (1998) 6479.
[35] S. Martusevicius, G. Niaura, Z. Talaikyte, V. Razumas, Vibr. Spectrosc. 10 (1996) 271.
[36] M. Dagys, P. Lamberg, S. Shleev, G. Niaura, I. Bachmatova, L. Marcinkeviciene, R. Meskys, J. Kulys, T. Arnebrant, T. Ruzgas, Electrochim. Acta 130 (2014) 141.
[37] S. Laurent, D. Forge, M. Port, A. Roch, C. Robic, L.V. Elst, R.N. Muller, Chem. Rev. 108 (2008) 2064.
[38] V. Sambhy, M.M. MacBride, B.R. Peterson, A. Sen, J. Am. Chem. Soc. 128 (2006) 9798.
[39] W.J. Ye, M.F. Leung, J. Xin, T.L. Kwong, D.K.L. Lu, P. Li, Polymer 46 (2005) 10538.
[40] M.T. Hyldgaard, T. Mygind, B.S. Vad, M. Stenvang, D.E. Otzen, R.L. Meyer, Appl. Environ. Microbiol. 80 (2014) 7758.
[41] L. Kvitek, A. Panaček, J. Soukupova, M. Kolar, R. Večerova, R. Prucek, M. Holecova, R. Zboril, J. Phys. Chem. C 112 (2008) 5825.

6th publication / 6 publikacija

Ultra-small methionine-capped Au^0/Au^+ nanoparticles as efficient drug against the antibiotic-resistant bacteria

Žalnėravičius R., Mikalauskaite A., Niaura G., Paškevičius A., Jagminas A.

Materials Science and Engineering C-Materials for Biological Applications, 102 (2019)

DOI: 10.1016/j.msec.2019.04.062

Materials Science & Engineering C 102 (2019) 646–652

Contents lists available at ScienceDirect

Materials Science & Engineering C

journal homepage: www.elsevier.com/locate/msec

Ultra-small methionine-capped Au^0/Au^+ nanoparticles as efficient drug against the antibiotic-resistant bacteria

Rokas Žalnėravičius[a], Agnė Mikalauskaitė[a], Gediminas Niaura[a], Algimantas Paškevičius[b], Arūnas Jagminas[a,*]

[a] State Research Institute Centre for Physical Sciences and Technology, Sauletekio av. 3, LT-10257 Vilnius, Lithuania
[b] Laboratory of Biodeterioration Research, Nature Research Centre, Akademijos 2, LT-08412 Vilnius, Lithuania

ARTICLE INFO

Keywords:
Gold species
Antimicrobial behavior
Magnetite nanoparticles
Methionine

ABSTRACT

In this study we examined the influence of ultra-small gold and magnetite-gold nanoparticles (NPs) stabilized with D,L-methionine, Fe_3O_4@Au@Met, on their antibacterial efficacy against three of twelve the worst bacterial family members included in the World Health Organization (WHO) list. In particular, gram-negative *Acinetobacter baumannii*, *Salmonella enterica* and gram-positive methicillin-resistant *Staphylococcus aureus* and *Micrococcus luteus* were tested. Apart from the synthesis, gold species reduction and NP stabilization, an excess of methionine has been used herein to detach ultra-small gold NPs from the Fe_3O_4@Au@Met surface, collect them and investigate. The antimicrobial efficiency of the ultra-small (Ø ~ 1.8 nm) Au@Met NPs and Fe_3O_4@Au@Met NPs was evaluated through the quantitative analysis by comparing with that of naked magnetite NPs, D,L-Met and BSA. It has been determined that compared with the control sample, 70 mg L^{-1} probe of Au@Met NPs exhibited the killing efficiency of 84.4–58.5% against gram-negative bacteria and 89.1–75.7% against gram-positive bacteria. The composition, structure, and morphology of the synthesized and tested herein NPs were investigated by inductively coupled plasma optical emission spectrometry, magnetic measurements, FTIR, XRD, XPS, AFM and HRTEM.

1. Introduction

It is commonly accepted that contrary to silver, gold in the metallic state is highly stable, biocompatible, and not cytotoxic even in the nanoparticulated size [1]. Au^0 nanoparticle (NP) antimicrobials render the grafted drug molecules, such as ampicillin, peptides or zwitterionic ligands [2–6]. On the other hand, antimicrobial behavior of gold ions is well-known, has been widely investigated, and well-reviewed in Djuran and Glišic paper [7]. According to the some recent reports, Au^0 NPs reduced down to the nanocluster size, *e.g.* ≤ 2.0 nm in diameter, may also exhibit the antimicrobial activity against some fungi and bacteria strains. For example, Zheng et al. [8] synthesized and tested 6-nm sized Au^0 NPs and ≤ 2.0-sized gold nanoclusters both templated and protected with the 6-mercaptohexanoic acid. Although these NPs possessed quite similar surface *zeta*-potential, a remarkable antimicrobial efficacy has been established just for nanoclusters against *S. aureus* and *E. coli* killing roughly from 95 to 96% of their population. Besides, it was concluded that the antimicrobial effect is not derived from the surface ligand and its content. On the contrary, Zhang et al. [9] reported that cationic ligands of gold NPs contributed to their antimicrobial activity. This effect has been attributed to the strong ionic interaction with the bacteria indicating that positively charged ligand molecules of Au NPs are responsible for the bacteria membrane permeability increase. Eventually, Chen et al. have synthesized gold clusters in lysozyme template and demonstrated their significant antimicrobial efficacy against two strains of multidrug-resistant bacteria [10].

Inspired by these works, in this study, we synthesized and tested ultra-small gold and gold-functionalized magnetite NPs comprised of Au^0/Au^+ for possible inactivation of multi-drug resistant bacteria. To the best of our knowledge, the antimicrobial behavior of ultra-small gold NPs stabilized with the amino acid has not been investigated against the most dangerous microorganism such as methicillin-resistant *Staphylococcus aureus*, *Acinetobacter baumannii*, and *Salmonella enterica*. For comparison, the antimicrobial efficacy of the magnetite NPs decorated with Au^0/Au^+ species as well as typical red-luminescent gold clusters formed and templated in a bovine serum albumin (BSA) matrix was also tested herein. It should be noted that *Salmonella* serotypes are associated with three distinct human disease syndromes: bacteremia, typhoid fever, and enterocolitis, whereas enterocolitis is the second most frequently bacterial food-borne disease causing roughly 1.4

* Corresponding author.
E-mail address: arunas.jagminas@ftmc.lt (A. Jagminas).

https://doi.org/10.1016/j.msec.2019.04.062
Received 15 November 2018; Received in revised form 14 March 2019; Accepted 20 April 2019
Available online 22 April 2019

million illnesses [11] and approximately 550 annual deaths per year just in the United States [12]. Consequently, the interest in *Acinetobacter* serotypes has risen sharply over the recent years from both the scientific and public community since they cause a wide spectrum of infections that include pneumonia, bacteremia, meningitis, urinary tract infection, and wound infection [13,14].

2. Experimental

2.1. Chemical reagents and materials

All the reagents in this study were at least of the analytical grade and, except NaOH, were used as received. Iron(III) chloride hexahydrate ($FeCl_3{\cdot}6H_2O$, ≥99%), iron(II) chloride tetrahydrate ($FeCl_2{\cdot}4H_2O$, ≥99%), tetrachloroauric(III) acid tetrahydrate ($HAuCl_4{\cdot}4H_2O$, ≥99.9%) D,L-methionine (≥99%), M9 5× minimal microbial growth medium (33.9 g L^{-1} Na_2HPO_4, 15 g L^{-1} KH_2PO_4, 5 g L^{-1} NH_4Cl and 2.5 g L^{-1} NaCl, pH = 7) and bovine serum albumin (BSA, 96%) were supplied by Sigma-Aldrich Chemical Co. Nutrient agar (3 g L^{-1} beef extract, 15 g L^{-1} peptone and 15 g L^{-1} agar) and Nutrient Broth (1 g L^{-1} glucose, 5 g L^{-1} peptone, 6 g L^{-1} sodium chloride and 3 g L^{-1} yeast extract) were obtained from Liofilchem. Sodium hydroxide was purified by preparation of a saturate solution resulting in the crystallization of other sodium salts. Following the analysis, this solution was diluted to the 2.0 mol L^{-1} concentration and applied. Milli-Q grade water was used (18 MΩ) for preparation of all solutions.

Gram-positive methicillin-resistant *Staphylococcus aureus* (MRSA) (ATCC 433300), *Micrococcus luteus* (GTC-BTL, B-30S) and gram-negative *Acinetobacter baumannii* (ATCC BAA-747), *Salmonella enterica* (GTC-BTL, B-25) bacteria strains were obtained from the Nature Research Centre collection of microbial strains.

2.2. Synthesis of NPs

In this study, the synthesis of ultra-small gold NPs was carried out in the following way (Fig. 1). In the first step, magnetite NPs were synthesized from the alkaline solution containing 15 mmol L^{-1} $FeSO_4$, 30 mmol L^{-1} $FeCl_3$, and 0.2 mol L^{-1} D,L-methionine (Met) amino acid, as chelating agent, and NaOH up to pH ≅ 12.35 ± 0.1 at 130 °C for 10 h hydrothermally using the 10 °C min^{-1} ramp. Then, as-grown NPs were collected by centrifugation at 7500 rpm for 5 min, carefully rinsed several times with water and dried at 60 °C. In the second step, the surface of magnetite NPs was loaded with ultra-small gold nanocrystals *via* Met-induced chemical reduction of the chloroauric acid according to our previous work [15]. Briefly, Fe_3O_4@Met NP probe (3.5 mg) was dispersed in 5 mL of water under ultrasound agitation until the mixture became bright mustard-coloured. Then, 3.5 mL of this suspension was transferred into a glass reactor along with 5 mL of Met (10 mM) and $HAuCl_4$ (4 mM) solutions under stirring. The solution pH was adjusted to ≅12.4 with 2 M NaOH drop-wise and the synthesis was conducted at 37 °C for 4 h under mild stirring. The products identified as Fe_3O_4@Au@Met NPs were washed thoroughly with water and ethanol for further examination. In the third step, ultra-small gold NPs were detached from the surface of Fe_3O_4@Au@Met NPs by chemical means. To achieve this result, Fe_3O_4@Au@Met NPs were sonicated in the 0.3 M Met solution under ultra-sound agitation for 7 min resulting in Fe_3O_4 removal from the surface of magnetite NPs viewed from the suspension colour changes from bright brown to light pink. Finally, Au@Met NPs were separated from the magnetic ones using a permanent magnet, rinsed and stored at 4 °C for characterization and further experiments.

2.3. Measurements and equipment

The morphology of the as-growth NPs was investigated with the transmission electron microscope (TEM) FEI Tec-nai F20 X-TWIN operated at an accelerating voltage of 200 kV. TEM images were recorded using a Gatan Orius CCD camera. The nanoparticles subjected to TEM observations were dispersed in ethanol and drop-cast on a carbon-coated nickel grid. The size distribution histograms of Fe_3O_4@Met, Fe_3O_4@Au@Met and Au@Met NPs were estimated using the Image J software. The average diameter of particles was estimated by analyzing high resolution TEM images. For this purpose, at least one hundred of NPs were randomly selected and measured.

Phase analysis of magnetite and Fe_3O_4@Au@Met NPs was carried out using a diffractometer SmartLab (Rigaku) with rotating Cu anode. CuK_α radiation (α = 0.154183 nm) was separated with the multilayer bent graphite monochromator. The XRD patterns were performed in the Bragg-Brentano scan mode in the 2theta range from 10 o to 80° with the step size of 0.02° and a counting time of 8 s per step. Phase identification was performed using the powder diffraction database PDF4 + (2015). The size of NPs was determined by the Halder-Wagner (H-W) approximation.

X-ray photoelectron spectroscopy (XPS) experiments were carried out in order to obtain information about the chemical state of ultra-small gold NPs deposited as well as detached from the magnetite surface on the upgraded Vacuum Generator "VG ESCALAB MK II" (VG Scientific) spectrometer fitted with a new XR4 twin anode. The non-monochromatised MgKα X-ray source was operated at $h\nu$ = 1253.6 eV with the 300 W power (20 mA/15 kV). During the spectral acquisition, the pressure in the analysis chamber was lower than 5·107 Pa. The spectra were acquired with the electron analyzer pass energy of 20 eV and resolution of 0.05 eV.

Infrared spectra were recorded in the transmission mode on an ALPHA FTIR spectrometer (Bruker, Inc., Germany) equipped with a room temperature detector DLATGS. The spectral resolution was set at 4 cm^{-1}. Spectra were acquired from 64 scans. Samples were dispersed in the KBr tablets. Parameters of the bands were determined by fitting the experimental spectra with Gaussian-Lorentzian shape components using GRAMS/A1 8.0 (Thermo Scientific) software.

The amount of gold in the Fe_3O_4@Au@Met and ultra-small Au@Met NP probes was estimated using an inductively coupled plasma optical emission spectrometer ICP-OES OPTIMA 7000DV (Perkin Elmer). In this way, a small pinch of nanopowders was dissolved in the aqua regia solution. Then, a calibration curve was drawn using a series of calibration standard solutions in the HCl:HNO_3 (3:1 by volume) acidic matrix as the unknown solutions. All measurements were carried

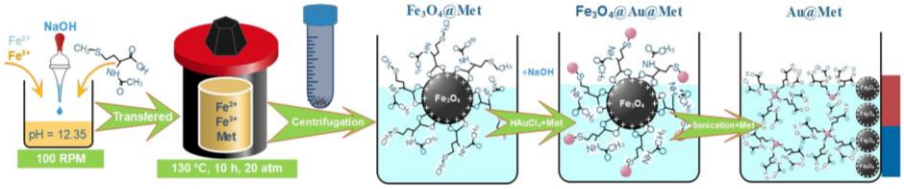

Fig. 1. The scheme illustrating fabrication of Fe_3O_4@Met, Fe_3O_4@Au@Met, and ultra-small Au@Met NPs.

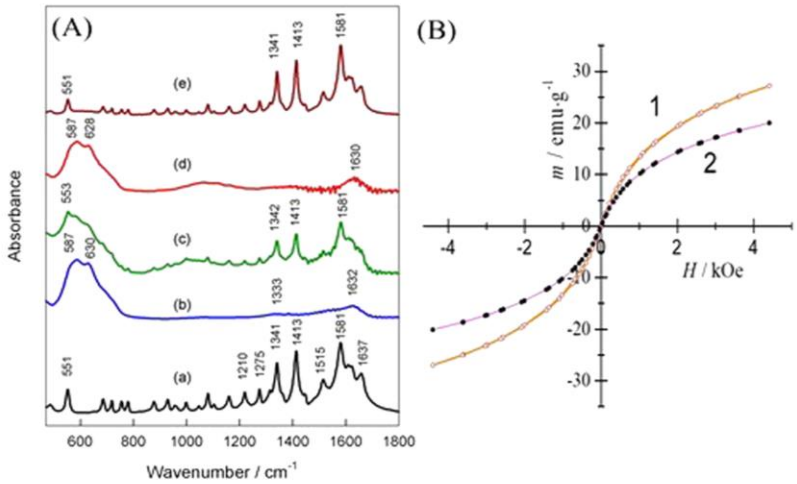

Fig. 2. (A): The FTIR spectra of pure Met (a) and as-synthesized NP samples "b, c, d and e" corresponding to Fe_3O_4, Met-caped Fe_3O_4, gold-capped Fe_3O_4 and gold species detached from the magnetite, respectively. In (B): the magnetic response plots of magnetite NPs before (1) and after (2) gold deposition.

out at emission peaks λ_{Au} = 267.595 nm and λ_{Au} = 242.795 nm.

The morphology of ultra-small gold NPs, spin coated onto the mica surface, was also investigated with the atomic force microscope (AFM) Veeco AFM diInnova (Veeco Instruments Inc.) in a tapping mode. TESPA-V2 cantilevers (Veeco Instruments Inc.) with a tip curvature of 8 nm were used. Images were acquired at the scan rate of 1 Hz per line with the 512 × 512 pixel image resolution. Image processing included flattening to remove the background slope caused by the irregularities of the piezoelectric scanner. The analysis was performed using the SpmLabAnalysis software (Veeco Instruments Inc.).

Magnetization measurements were accomplished using a vibrating-sample magnetometer calibrated by a Ni sample of similar dimensions as the studied sample. The magnetometer was composed of the vibrator, the lock-in amplifier, and the electromagnet. The magnetic field was measured with a test meter FH 54 (Magnet-Physics Dr. Steingrover GmbH).

2.4. Antimicrobial activity of as-grown nanoparticles

Antimicrobial assessments of the synthesized Fe_3O_4@Au@Met NPs and ultra-small gold nanocrystals were tested against gram-negative *A. baumannii* and *S. enterica* and gram-positive *S. aureus* (MRSA) and *M. luteus* bacteria strains using the serial dilution method. Following these investigations bacteria strains were propagated in the Nutrient agar medium at 37° ± 1 °C for 24 h. The fresh cultures were harvested and diluted in the sterile M9 minimal microbial growth medium to yield colony-forming units (CFU) inoculum of 6.4–8 × 108 for bacteria cells, based on the optical density at 600 nm (OD600). The range of OD600 was obtained to be between 0.08 and 0.1. Then, 100 μL probe of the diluted microorganism suspension was collected at the logarithmic stage of growth and transferred in a 96 well cell culture plate. Finally, 100 μL of water containing 140 mg L^{-1} or 60 mg L^{-1} of Fe_3O_4@Au@Met or ultra-small gold NPs was added to the liquid medium, resulting in their final concentration of 70 and 30 mg L^{-1}, respectively, and incubated further for 24 h with 150 rpm shaking. In these investigations, D,L-methionine and magnetite NPs were used as negative controls. During the cultivation, 100 μL of suspension was taken from each reaction mixture, diluted in the glass tube *via* the broth dilution method and spread on the Nutrient Broth agar media plate using a stainless steel spreader. The growth of microorganisms was tested after incubation at 37° ± 1 °C for one day. Each assay was performed in triplicate with three independent experiments.

3. Results and discussion

3.1. Synthesis and characterization of Fe_3O_4@Met nanoparticles

In this study, gold NPs, ultra-small, quite uniform in size, and containing zero-valent gold were synthesized on the surface of magnetite NPs by reducing the gold acid with Met molecules capped at the surface of Fe_3O_4. For this purpose, magnetite NPs were synthesized hydrothermally employing both Fe^{2+} and Fe^{3+} salts at the 2:1 molar ratio as precursors and Met amino acid as the stabilizing agent for control over the uniformity of the NPs growth. The adapted concentration of iron salts (45 mmol L^{-1}) and Met (0.2 mol L^{-1}), synthesis temperature (130 °C) and duration (10 h) allowed us to grow the spherical NPs (Fig. 1S). The morphology of NPs synthesized *via* this hydrothermal approach was investigated further by high-resolution TEM and is depicted in Fig. 1S, part B revealing that as-grown NPs possess mainly an average diameter of roughly 11 nm and quite narrow size distribution (Fig. 2S). Besides, from the HRTEM image inspection (Fig. 1S, part B) as-grown NPs are single crystalline as clearly indicated by atomic lattice fringes and most probably they grow preferentially along the (311) direction with a lattice interatomic distance of *ca.* 0.252 nm. It should be noted that the XRD pattern taken from the scope of these NPs (Fig. 3S) demonstrated a set of diffraction peaks clearly seen at 2Θ positions: 18.28, 30.08, 35.43, 43.06, 53.42, 56.94, 62.53, 70.94, 73.97, 74.97, and 78.93. These peaks matched well with the diffraction peaks characteristic of polycrystalline Fe_3O_4 planes (111), (220), (311), (400), (422), (511), (440), (620), (533), (622), and (444),

respectively, (PDF Card No. 04-005-4319), and confirmed the formation of a face-centered cubic (fcc) crystal structure (space group *Fd-3m*, $a = \beta = \gamma = 8.396$ Å). It is also seen that the average size of Fe_3O_4 NPs estimated from the XRD pattern using Halder-Wagner approximation equaled to *ca.* 11.9 ± 0.15 nm was consistent with the data obtained from the HRTEM observations complementing the fact that our synthesized NPs are quite uniformly-sized.

To probe the Met adsorption on the NPs surface, the FTIR spectra of pure D,L-Met, as well as the synthesized and chemically modified Fe_3O_4 NPs were collected and are depicted in the part (A) of Fig. 2. The FTIR spectrum of pure Met (a) shows a set of numerous peaks most intense at the 1413 and 1581 cm^{-1} which according to the literature [16–19] are due to the symmetric and asymmetric stretching vibrations of $-COO^-$ group. The two peaks located at 1515 and 1637 cm^{-1} correspond to symmetric and asymmetric deformation vibrations of NH_3^+ group, respectively [16,17]. Thus, infrared spectrum confirms zwitterionic structure of studied compound. The intense band near 1341 cm^{-1} is associated with symmetric CH_3 deformation vibration with contribution from deformation vibration of CH group, δ(CH) [17]. The clearly defined band at 551 cm^{-1} belongs to out-of-plane deformation of carboxylate group, $\gamma(COO^-)$ [17].

According to the literature [20–22], the vibration band with the peaks at 628 and 587 cm^{-1} in the spectrum of as-grown Fe_3O_4 NPs should be assigned to the stretching modes of the Fe—O bond both at the tetrahedral sites and on the surface of magnetite NPs. Besides, the FTIR spectrum of as-grown Fe_3O_4 NPs has an additional broad shoulder peaked at 1630 cm^{-1} attributable to the asymmetric C=O stretching vibration of deprotonated carboxyl group $-(COO^-)$ [23] in the Met molecule bound to the surface of Fe_3O_4. The intense bands from both Fe_3O_4 and Met species are visible in the spectrum of Met-capped Fe_3O_4 (curve c of Fig. 2A) indicating presence of adsorbed Met in zwitterionic form.

3.2. Fe_3O_4@Met NPs decoration with ultra-small gold nanoparticles

Fig. 3 shows the formation of numerous gold species on the surface of methionine-stabilized Fe_3O_4 NPs after their sonication in the $HAuCl_4$ solution under adapted herein conditions. From the TEM inspection, however, it was difficult to determine the size distribution of attached gold species, although most of them seem to be spherical and ≤ 2.0 nm-sized (Fig. 3B). From the literature the attachment of gold seeds [24] and functionalization of magnetite Nps with gold-containing shells [25] resulted in the saturation magnetization (M_s) decrease although in the case of gold nanograins attachment onto magnetite nanocrystals with an amino-terminated silane [26] M_s decrease was insignificant. Therefore, the attachment of gold species to the magnetite surface was verified by EDX and FTIR spectra and magnetization investigations. Fig. 2A shows the room-temperature magnetization plots as a function of the applied magnetic field for Fe_3O_4@Met NPs before (1) and after (2) their sonication in the chloroauric acid solution. From these measurements, the saturation magnetization value of magnetite NPs decreased from 27 to 21 emu·g^{-1} (at H_{max} = 4.4 kOe) supporting the proposition that gold species were deposited although NPs remained superparamagnetic. The deposition of gold onto the surface of Fe_3O_4@Met NPs has also been certified by EDX spectra (see Fig. 4S). In addition, the FTIR spectrum of gold-decorated Fe_3O_4@Met NPs (Fig. 2B, sample d) clearly evidenced the bond with Met molecules even after the careful NP rinse.

3.3. Detachment and characterization of Au@Met NPs

To remove ultra-small gold NPs from the surface of magnetite NP for the first time we have used the same methionine amino acid as a detaching agent. This procedure was conducted *via* ultrasound agitation of gold-coated magnetite NPs in methionine solution attributing the detachment effect to the stronger interaction of the amino acid with gold nanocrystals compared to the Au-Fe_3O_4 bond. The obtained light-pink solution due to dispersion of ultra-small gold NPs was further investigated by sampling on the Lacey grid followed by AFM and TEM observations for the particle size inspection. As seen from Fig. 4 images, the detached ultra-small gold nanocrystals exhibit mainly the spherical particle morphology with an average diameter of 1.8 nm and a quite narrow size distribution. It is noteworthy, that they seems to be not aggregated.

3.4. Antimicrobial activity of Au@Met and Fe_3O_4@Au@Met NPs

For these investigations, we have chosen three the worst bacterial family members included in the World Health Organization (WHO) list of the drug-resistant bacteria that pose the greatest threat to human health and for which new antibiotics are desperately needed [27]. Therefore, the antimicrobial activity of ultra-small gold and Fe_3O_4@Au@Met NPs was investigated against gram-negative *A. baumannii* (ATCC BAA-747), *S. enterica* (GTC-BTL, B-25) and gram-positive methicillin-resistant *S. aureus* (ATCC 433300), and *M. luteus* (GTC-BTL,

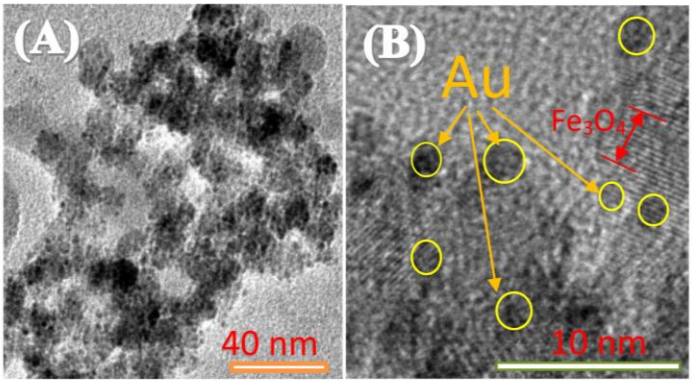

Fig. 3. TEM (A) and HRTEM (B) images of magnetite NPs after decoration with gold nanocrystals *via* methionine-induced $HAuCl_4$ reduction.

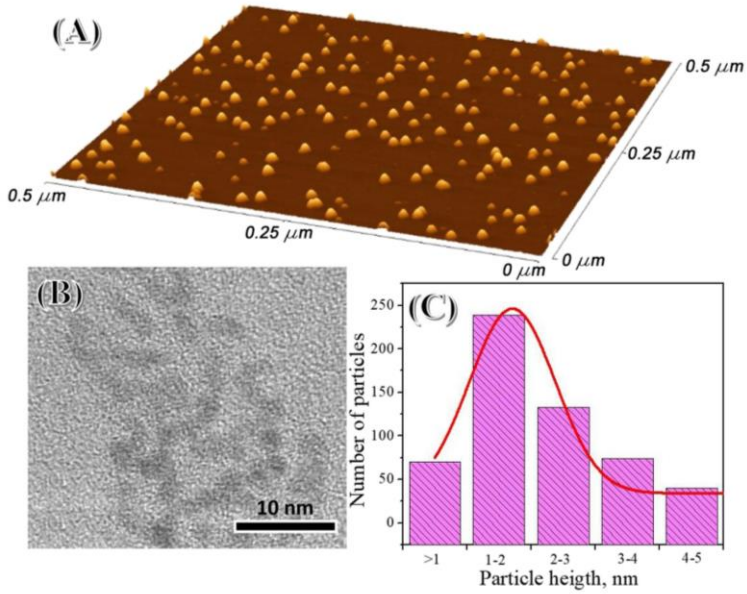

Fig. 4. AFM 3D view of magnetite Nps (A), whereas TEM image and size distribution histogram of gold NPs detached from magnetite nanoparticles are shown in the (B) and (C) parts, respectively.

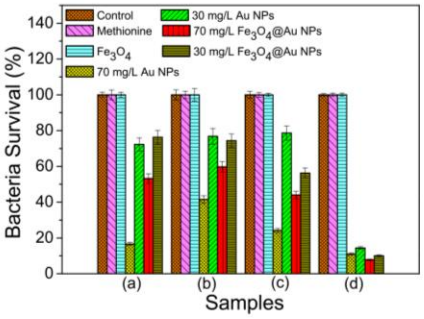

Fig. 5. Antimicrobial activities of the synthesized Au@Met and Fe_3O_4@Au NPs after 24 h incubation with gram-negative *A. baumannii* (a), *S. enterica* (b), and gram-positive *S. aureus* (MRSA) (c), *M. luteus* (d). For comparison, the behavior of pure D,L-methionine and magnetite NPs is presented.

B-30S) by assessing the colony forming units (CFU). During this investigation, the microorganisms were incubated in the M9 liquid medium together with 70 or 30 mg L^{-1} of Au@Met either Fe_3O_4@Au@Met NP probes, respectively, under shaking for 24. The percentage ratios of bacteria survival obtained from these assays are shown in Fig. 5. Moreover, 100 mg L^{-1} of D,L-methionine and 1 g L^{-1} of Fe_3O_4@Met NP probes were also investigated as the negative control samples. It can be easily seen that Au@Met and Fe_3O_4@Au@Met NPs show the highest killing efficiency against the *M. luteus* bacteria strain. These results further support the idea that human pathogenic microorganisms are more virulent and resistant than antibiotic-susceptible microbes such as *M. luteus* [28]. A positive correlation was also found between the concentration of Au in NPs and bacteria survival. In comparison with the control sample, 70 mg L^{-1} of Au@Met NP probe exhibits the killing efficiency of 84.4–58.5% against gram-negative bacteria and 89.1–75.7% against gram-positive bacteria. In addition, Fig. 6 shows the quantity of gram-negative and gram-positive microorganisms grown on the Nutrient agar plates demonstrating a significant reduction of the colonies count. From these tests, one unanticipated finding was that the decreasing of the concentration of gold NPs approximately in the 2.3 times results in the weakening of bacteria assessment by 3.05, 2.52, 1.35, and 1.04 fold against *A. baumannii*, *S. enterica*, *S. aureus* (MRSA), and *M. luteus* bacteria, respectively. These results seem to be consistent with other investigation which determined that 6 nm-sized AuNPs showed no concentration dependent antibacterial effect against *B. subtilis* and *E. coli* microorganisms [8]. It should be noted that *S. enterica* demonstrated the strongest resistance against the ultra-small gold and Fe_3O_4@Au@Met NPs.

It is noteworthy, however, that in the case of Fe_3O_4@Met NPs, as well as D,L-methionine amino acid, the same amount of colony forming units as for the control sample was grown. From the antimicrobial activity tests of methionine, this stabilizing agent of gold species and magnetite Nps is nontoxic because this is an amino acid and can be easily metabolized by bacteria [29]. Having in mind the biocompatibility and non-toxicity of gold materials even in the nm-scaled dimensions, the established antimicrobial behavior of the synthesized Au@Met nanocrystals as well tethered to the surface of Fe_3O_4 NPs

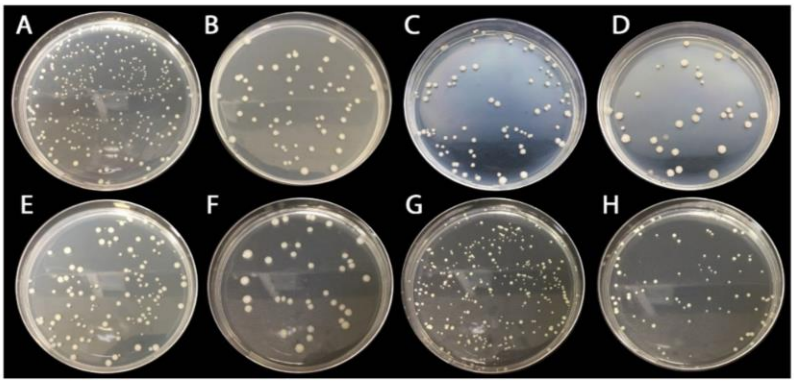

Fig. 6. Photographs showing the antimicrobial activity of Au@Met nanocrystals for growth inhibition of gram-negative (a–b) *A. baumannii*, (c–d) *S. enterica* (top row) and gram-positive (e–f) methicillin-resistant *S. aureus*, (g–h) *M. luteus* (bottom row) microorganisms incubated in the Nutrient agar plates. All the microorganisms were cultivated in liquid M9 medium without (a, c, e, g) and with (b, d, f, h) 70 mg L^{-1} Au@Met species for 24 h.

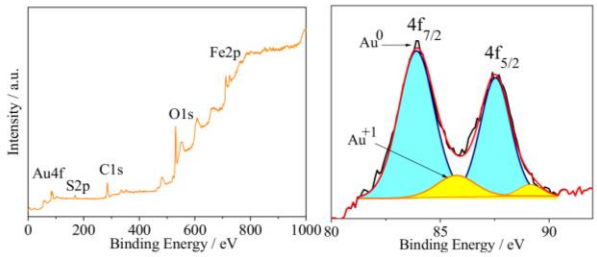

Fig. 7. XPS survey of gold-coated magnetite NPs (A) and high-resolution deconvoluted XP spectrum of Au 4f (B).

required explanation. We hypothesized that one possible explanation of such behavior should be ascribed to the composition and structure of ultra-small gold species because the methionine shell showed no cytotoxicity and antimicrobial efficacy. In an attempt to shed light on the reasons for the strong bactericidal effect of Au@Met nanocrystals and Fe_3O_4@Au@Met NPs, X-ray photoelectron spectroscopy (XPS) investigations of these species were further performed. Fig. 7A displays the XPS survey spectrum of the tested Fe_3O_4@Au@Met NP sample revealing the clear signals from Fe, O, C, S, and Au. The carbon and sulfur peaks were tentatively assigned mainly to the methionine molecules attached to the magnetite and gold NPs. The deconvoluted

Au 4f XP spectrum taken from the scope of Fe_3O_4@Au@Met NPs is presented in Fig. 7B. It is clear that the main Au $4f_{7/2}$ photoelectron peak is located at a binding energy (BE) 83.94 eV characteristic of the pure metallic Au^0 [30]. The fitting of this spectrum was further performed using the two spin-orbit split Au $4f_{7/2}$ and Au $4f_{5/2}$ components, separated by 3.56 eV. In addition, the Au 4f plot fitting revealed an additional shoulder peaked at 85.74 eV indicating the presence of Au^+ [23,31]. Based on the relative contents of Fe, O, N, C, S, and Au measured by high-resolution XPS, the average content of the deposited gold was estimated roughly to be 1.67 at.% of the total NP mass. We suggest that the main reason for the antimicrobial activity of our Fe_3O_4@Au@Met NPs as well as Au@Met nanocrystals should be ascribed to the presence of Au^+ ions on the surface of gold species. Therefore, we attributed this effect to the small gold species size coupled to their composition, particularly Au^0/Au^+, capable to interact with bacteria cell walls and membranes. The interaction between ultra-small gold Nps containing Au^+ and bacteria is expected induce a metabolic imbalance in bacterial cells and protein denaturation that kills bacteria. Note that metallic gold (Au^0) is inert, highly stable, and not easily dissociate into ions [32] remaining highly biocompatible even in the few-nm size [33].

4. Conclusions

Antimicrobial properties of ultra-small gold species as well as tethered to the surface of magnetite NPs have been studied against multidrug-resistant gram-negative A. baumannii, *S. enterica* and gram-positive *S. aureus* (MRSA), *M. luteus* bacteria strains using the serial dilution method. Uniformly sized gold species were formed by reduction of the gold acid with the Met capped to the surface of superparamagnetic magnetite NPs of the average size of 11.9 ± 0.15 nm. Both the attached to magnetite surface (Fe_3O_4@Au@Met) and alone (Au@Met) gold species were tested. It was determined that 70 mg L^{-1} Au@Met NPs probe exhibited the killing efficiency of 84.4–58.5% against gram-negative bacteria and 89.1–75.7% against gram-positive

acteria. Numerous methods have been applied for characterization of he synthesized gold species shown to be spherical, average sized ≤1.8 nm) and composed of $Au^0 + Au^+$. The strong antimicrobial ef- iciency of Met-capped gold species against several most dangerous acteria was related to the presence of single-valent gold on the surface ide.

cknowledgements

We appreciate Drs. V. Pakštas for powder XRD collection, J. aičiūniene for chemical analysis, and V. Jasulaitiene for XPS spectra ollection.

ppendix A. Supplementary data

Supplementary data to this article can be found online at https://oi.org/10.1016/j.msec.2019.04.062.

eferences

[1] N. Lewinski, V. Colvin, R. Drezek, Small 4 (2008) 426–449.
[2] T. Pellegrino, S. Kureda, T. Liedl, A.M. Javier, L. Manna, W.J. Parak, Small 1 (2005) 48–63.
[3] P. Juzenas, W. Chen, Y.P. Sun, M.A.N. Coelho, R. Generalov, N. Generalova, I.L. Chistensen, Adv. Drug Deliv. Rev. 60 (2008) 1600–1614.
[4] M.A. Walling, J.A. Novak, J.R.E. Shepard, Int. J. Mol. Sci. 10 (2009) 441–491.
[5] G.L. Burygin, B.N. Khlebtsov, A.N. Shantrokha, L.A. Dykman, V.A. Bogatyrev, N.G. Khlebtsov, Nanoscale Res. Lett. 4 (2009) 794–801.
[6] A.M. Allahverdiyev, K.V. Kon, E.S. Abamor, M. Bagirova, M. Rafailovich, Expert Rev. Anti-Infect. Ther. 9 (2011) 1035–1052.
[7] B.D. Glišic, M.I. Djuran, Dalton Trans. 43 (2014) 5950–5969.
[8] K. Zheng, M.I. Setyawati, D.T. Leong, J. Xie, ACS Nano 11 (2017) 6904–6910.
[9] Y. Zhang, H. Peng, W. Huang, Y. Zhou, D. Yan, J. Colloid Interface Sci. 325 (2008) 371–376.
[10] W.Y. Chen, J.Y. Lin, W.J. Chen, L. Luo, E.W.G. Diau, Y.C. Chen, Nanomedicine 5 (2010) 755–764.
[11] P.S.L. Mead Slutsker, V. Dietz, L.F. McCaig, J.S. Bresee, C. Shapiro, P.M. Griffin, R.V. Tauxe, Emerg. Infect. Dis. 5 (1999) 607–625.
[12] F.C. Fang, J. Fierer, Medicine (Baltimore) 70 (1991) 198–207.
[13] A.T. Bernards, H.I. Harinck, L. Dijkshoorn, T.J. van der Reijden, P.J. van den Broek, Infect. Control Hosp. Epidemiol. 25 (2004) 1002–1004.
[14] P.E. Fournier, H. Richet, Clin. Infect. Dis. 42 (2006) 692–699.
[15] A. Jagminas, A. Mikalauskaitė, V. Karabanovas, J. Vaičiūnienė, Beilstein J. Nanotechnol. 8 (2017) 1734–1741.
[16] E. Cooper, F. Krebs, McD. Smith, R. Raval, J. Electron Spectrosc. Relat. Phenom. 64/65 (1993) 469 – 475.
[17] M. Wolpert, P. Hellwig, Spectrochim. Acta A 64 (2006) 987 – 1001.
[18] N.B. Colthup, L.H. Daly, S.E. Wiberley, Introduction to Infrared and Raman Spectroscopy, Academic Press, New York, 1990.
[19] Z. Wang, H. Zhu, F. Wang, X. Yang, Nanotechnology 20 (2009) 465606.
[20] A. Barth, Prog. Biophys. Mol. Biol. 74 (2000) 141–173.
[21] K. Basavaiah, P.Y. Kumar, A.V. Prasada Rao, Appl. Nanosci. 3 (2013) 409–415.
[22] N. Belachew, D. Rama Devi, K. Basavaiah, J. Mol. Liq. 224 (2016) 713–720.
[23] R.M. Cornell, S. Chwertmann, The Iron Oxides: Structures, Properties, Reactions, Occurrences and Uses, Willey-VCH, Weinheim, 2003.
[24] S. Sabale, P. Kandesar, V. Jadhav, R. Komorek, R.K. Motkuri, X.-Y. Yu, Biomater. Sci. 5 (2017) 2212–2225.
[25] S. Karamipour, M.S. Sadjadi, N. Farhadyar, Spectrochim. Acta A Mol. Biomol. Spectrosc. 148 (2015) 146–155.
[26] D. Caruntu, B.L. Cushing, G. Caruntu, C.J. O'Connor, Chem. Mater. 17 (2005) 3398–3402.
[27] C. Willyard, Nature 543 (2018) 15–16.
[28] F. Rozgonyi, E. Kocsis, K. Kristof, K. Nagy, Clin. Microbiol. Infect. 13 (2007) 843–845.
[29] M.S. Palencia, M.E. Berrio, S.L. Palencia, J. Nanosci. Nanotechnol. 17 (2017) 5197–5204.
[30] J.F. Moulder, W.F. Sticker, P.E. Sobol, K.D. Bomben, R.C. King (Eds.), Physical Electronics, Eden Prairee, MN, U.S.A., 1995.
[31] A.M. Venezia, G. Pantaleo, A. Longo, G. Di Carlo, M.P. Casaletto, L. Liotta, G. Deganello, J. Phys. Chem. B 109 (2005) 2821–2827.
[32] B. Hammer, J. Norskov, Nature 376 (1995) 238.
[33] N. Lewinski, V. Colvin, R. Drezek, Small 4 (2008) 26–49.

NOTES

Vilniaus universiteto leidykla
Universiteto g. 1, LT-01513 Vilnius
El. p. info@leidykla.vu.lt,
www.leidykla.vu.lt
Tiražas 15 egz.